

Risk modeling, analysis and control of multi-energy systems

Preface

The large-scale consumption of fossil fuels has brought about numerous issues, e.g. environmental pollution and climate change, which call for technological innovations to improve energy efficiency and reduce harmful emissions. Nowadays, the energy systems are undergoing a pivotal transition, especially the increasing interactions across multiple energy carriers. Through the coordination between various energy subsystems, more clean, efficient, and sustainable energy can be supplied to consumers. The multi-energy systems, which couple gas systems, power systems, and heating systems through coupled components, e.g., gas-fired power plants and combined heat and power (CHP) plants, have gained rapid technological development globally.

Despite the high efficiency and sustainability of multi-energy systems in energy production and transportation, the interplay between different energy subsystems can introduce new risk factors, i.e. cross-sectorial failure propagation. For example, gas source outages or pipeline contingencies occurring in NGS may cause the interruption of gas supply to gas-fired power plants. The power plants that cannot obtain sufficient gas will dramatically reduce their power output, jeopardizing the risk to the power system. The practical blackouts in Texas, USA on 16th February 2021 resulted from such a failure propagation issue. Due to unexpected cold weather, the production decline of gas sources and pipeline shutdowns significantly reduced the transportation of gas from production areas to gas-fired power plants. Simultaneously, numerous electric-driven gas compressors failed due to the interruption of the power supply. In addition, other blackouts around the world, such as the massive outages in Taiwan, China on 15th August 2017 and the outages in the Southwestern United States in February 2011, are all correlated to the failure propagation features. Therefore, unsuccessfully dealing with the risk issues of failure propagation will threaten the reliable and secure operation of the whole system, further hindering the development of multi-energy systems.

This book focuses on the risk modeling, analysis, and control of multi-energy systems considering cross-sectorial failure propagation. Proposed

models and methods have been addressed with engineering practice. This is achieved by providing an in-depth study on the modeling of system physics and reliabilities in both long-term and short-term phases. Different models and methods to evaluate the risk of multi-energy systems considering various disturbances, e.g., component failures, load uncertainties, and extreme weather, are studied in detail. Moreover, different risk control methods, including long-term capacity planning and integrated demand response, of multi-energy systems are also analyzed in this book, which is particularly suited for the readers who are interested in risk management of systems. The book can benefit researchers, engineers, and graduate students in the fields of electrical and electronic engineering, energy engineering, complex network and control engineering, etc.

There are ten chapters in this book.

- Chapter 1 introduces the development and risk issues of multi-energy systems. The typical risk evaluation techniques and the challenges in the risk assessment of multi-energy systems are also illustrated in this chapter.
- Chapter 2 proposes a generalized framework for long-term reliability modeling and evaluation of integrated electricity and gas systems utilizing the universal generating function technique. The analysis mentality of “individual components, gas system, coupling components, and power system” is developed. Nodal risk indices are defined to quantify the regional risk levels of power and gas systems.
- Chapter 3 proposes a short-term risk evaluation technique for integrated electricity and gas systems considering gas flow dynamics. Firstly, the short-term risk models of gas sources and gas-fired units are developed. Then, the multi-stage contingency management scheme is proposed, where gas flow dynamics are analyzed for determining the time-varying load curtailments of electricity and gas. Moreover, a time-sequential Monte Carlo simulation technique is developed with the finite-difference scheme to tackle the gas flow dynamics during the short-term risk evaluation.
- Chapter 4 is devoted to operational risk evaluation of integrated electricity and gas systems considering the impacts of cascading effects. Considering different dynamic behaviors between the power system and gas system, a dynamic cascading effect analysis model is proposed to describe the temporal and spatial process of failure

propagation. Based on the Monte Carlo simulation technique, the bi-directional failure propagation is incorporated into the operational system risk evaluation framework.

- Chapter 5 introduces the definitions and risk modeling methods of two-interdependent-performance multi-state systems (TIP-MSS) and their application to CHP units. An object, i.e., the performance trade-off curve, is utilized to represent the performance rates. The universal generating function method is extended to represent the performance distribution of a TIP-MSS. Moreover, different composition operators are defined for analyzing the reliability of TIP-MSS with parallel/series structures. The availability criterion based on the TIP-UGF method is also proposed.
- Chapter 6 proposes the operational reliability assessment method of the integrated electricity and heating systems with CHP units. The scenario-based combined heat and power dispatch (CHPD) model is proposed to calculate the nodal reliability indices. Several techniques are utilized to improve the computation efficiency of the reliability assessment technique. First, the traditional universal generating function method is extended for combining the coupling device states and consequently reducing the number of scenarios that need to be considered. Second, a hydraulic-thermal decomposition technique is proposed to decompose the CHPD model into two linear programming models that can be iteratively solved.
- Chapter 7 studies the operational risk of multi-energy customers considering service-based self-scheduling. An optimal self-scheduling model for multi-energy customers is developed with the consideration of chronological service curtailment, service shifting, and possible failures during service shifting. In the optimal self-scheduling model, the costs of service curtailment and shifting are formulated based on the proposed evaluation method. The time-sequential Monte Carlo simulation approach is applied to model the chronological volatilities of multi-energy demands over the entire study period. Taking account of the possible scenarios, the quantitative risk indices of the multi-energy customers are obtained.
- Chapter 8 is devoted to the risk analysis and quantification of multi-energy systems under windstorms. The multi-phase performance curve is utilized to describe the response behavior of multi-energy systems at different phases under the impacts of windstorms. Besides, a service-based optimal energy flow model is developed to minimize the consequences caused by windstorms through coordination among different energy subsystems. Furthermore, nodal risk

metrics for different energy carriers are proposed to quantify the risk performance.

- Chapter 9 proposes the long-term reserve expansion model of integrated electricity and gas systems for risk mitigation. The novel multifactor-influenced reliability indices are defined considering the synthetic effects of multiple uncertainties, including failure propagation, load uncertainties, and generation failures. In the reliability index formulation, the contribution of failure propagation on system reliability is analytically expressed. To effectively solve the planning model, the decomposition approach is introduced to decompose the original problem into a master problem and two correlated reliability sub-problems.
- Chapter 10 presents the outlook of incorporating integrated demand response in risk control of multi-energy systems. Taking industrial loads as an example, integrated flexibility is defined and characterized by the feasible region. The integrated model based on the energy hub is proposed to couple the material flows in the industry load and the energy flows in the distributed energy systems. Incorporating the above method with the mathematical expression of the integrated flexibility, the integrated flexible region can be calculated by the poly-topic projection. On this basis, the process for incorporating the integrated flexible region of industrial loads in the risk control of multi-energy systems is proposed.

The authors shared the work in writing this book.

It was a pleasure with Springer Associate Editor, .

Macau/Hangzhou, China
 Hangzhou, China
 Hangzhou, China
 Hangzhou, China
 Chongqing, China

Yonghua Song
 Yi Ding
 Minglei Bao
 Sheng Wang
 Changzheng Shao

Acknowledgments

Yi Ding would like to acknowledge the financial support from the National Science Fund for Distinguished Young Scholars under Grant 52125702 and the China NSFC under Grant 71871200.

1 Multi-energy systems and risk evaluation

1.1 Descriptions of multi-energy systems

Energy is the foundation and engine for the progress of human society. Faced with the challenges of global climate change and environmental issues, low-carbon and high-efficiency have become the most important topics in nowadays energy utilization [1]. Coordinately using multiple energies, including electricity, gas, and heating, provides a promising pathway toward a low-carbon energy system. Under this circumstance, the concept of multi-energy systems (MESs) is emerging and has become one of the most discussed topics recently. MESs aim to coordinate multiple energies in the production, transportation, and consuming processes in terms of operation, planning, etc.

According to different geographic scales, the MESs can be divided into two parts: the generation & transmission side and the distribution side, as illustrated in Fig 1.1. On the generation & transmission side, the electricity and gas transmission systems are linked by the gas-fired units (GFU), which gives birth to the concept of integrated electricity and gas systems (IEGS). Compared with the traditional coal-fired units, the GFU is cleaner with less harmful emissions. In addition, it is more flexible in assisting the peak regulation of the power systems. Therefore, natural gas has become one of the most appealing fossil fuels to generate electricity in many countries and regions. For example, till Jan 2021, the gas consumption from the electric power sector has increased by 22.03% in the USA in the last three years [2]. The electricity generated by natural gas takes 38.42 % of all the electricity generation, which is the highest among all the fuels. In China, despite the high spot price for natural gas, the electricity generation from gas reaches 215.5 TWh, which is increased by 6.1% [3]. Apart from the GFU, the main components in the IEGS also include traditional fossil generating units, renewable generating units, high-voltage electricity transmission lines, gas pipelines, gas compressors, etc.

On the distribution side, the distributed energy systems consume the electricity and gas from the IEGS on the transmission side and satisfy the electricity, heating, and cooling demands of end-users. The energies are delivered by the integrated electricity and heating systems (IEHS), consisting of electricity distribution systems, and district pipeline systems. The components mainly include distributed renewable generations, micro turbines, combined heat and power (CHP) units, electric and gas boilers, heat pumps, absorption chillers, etc. It is reported in China that the centralized heat supplying area reaches about 9 trillion m², where the CHP is responsible for 51 % of the total area [4]. The primal fuel they consumed is coal now and is currently under a transition toward electric heating and gas heating. Therefore, the tight integration of multiple energies in different spatial scales is one of the most important features of future energy systems.

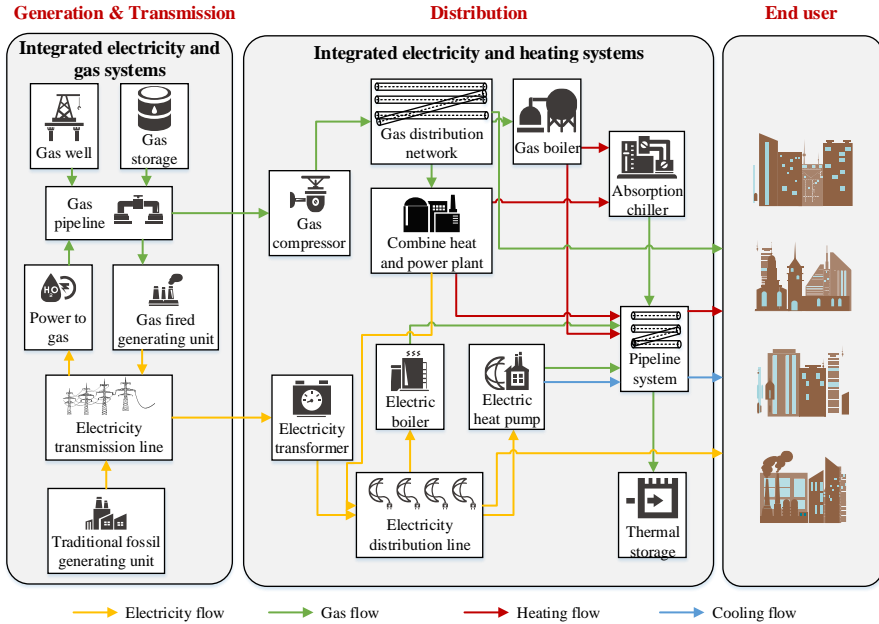


Fig. 1.1 Structure of the multi-energy systems

1.2 Risk issues of multi-energy systems

Despite the high efficiency and sustainability of MESs in energy generation, transmission, storage, and use, the interplay between different energy subsystems can bring about diverse emerging risk issues. On the one hand, as the scale of MESs expands, the external disturbances originating from extreme weather, cyber failures, intentional attacks, and policy uncertainties can increase significantly. On the other hand, random failures occurring in one energy system may propagate to the other system due to energy interactions, threatening the reliable operation of the whole system. Considering the impacts of various external disturbances and internal features of failure propagation, several blackouts have happened during the past decades, as summarized in Table 1.1. This section includes review related to the analysis of Texas blackout from the perspective of multi-energy coupling by [5].

Taking the Texas blackout as an example, the impacts of failure propagation on the reliability of MESs are illustrated here. In Texas, natural gas ranks first in the primary energy types for electricity generation. GFUs supplied more than half the electricity in Texas in 2020 [6], resulting in the tight interdependency between power system and gas system. During the extreme cold weather in February 2021, the outputs of nearly all types of power plants have suffered a dramatic decline, as shown in Fig 1.2, mounting at 48.6% with respect to the total installed capacity [7]. It should be illustrated that Fig. 1.2 is repainted according to the data and fig-

ures in [7]. Therefore, the outage capacity of gas-fired plants was approximately 26.5GW, accounting for 51% of the maximum generation out of all generation types [7]. Large-scale GFU outages mainly resulted from the shortage supply of natural gas, and the reasons can be summarized as follows:

Table 1.1 Practical blackouts in the multi-energy systems around the world

Time	Location	Cause	Consequence
Sep 2011	USA	Failure of transformer substation, and cascading failure of GFUs	Interruption of electricity supply for 7 million people [8]
Sep 2016	Australia	Volatility of the gas market, large penetration of wind generating units	Interruption of electricity supply for 50 hours [9]
Aug 2017	Taiwan, China	Gas supply interruption due to the misoperation of GFUs	4 GW interruption of electricity supply [10]
Aug 2018	UK	Shutdown of little Barford GFUs, wind turbine off-grid	Interruption of electricity supply for 1 million people for 1.5 hours [11]
Feb 2021	Texas, US	Freezing of gas well valves	20 GW electric load shedding, influence on over 4.8 million people [12]
May 2021	Taiwan, China	Shutdown of Xingda GFUs	Rolling blackouts for over 4 million people [13]

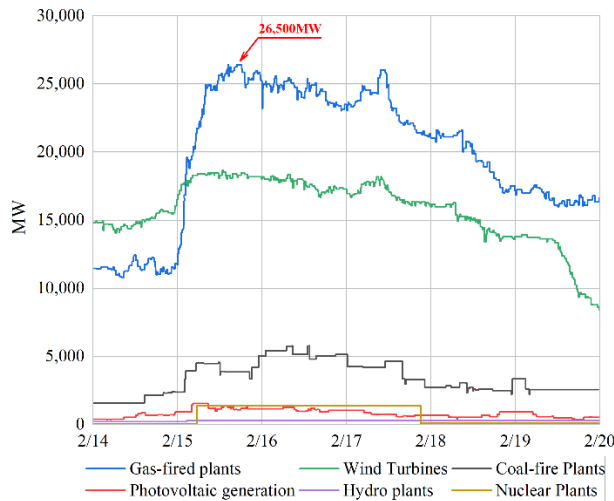


Fig. 1.2 Generation capacity losses for different generation types

The absence of anti-freezing measures for natural gas production and transportation facilities. Unlike the colder northern regions of the U.S., natural gas production and refinement facilities located in Texas, including boilers, turbines, and other auxiliary equipment, are directly exposed to the ambient environment. This design could effectively prevent these pieces of equipment from overheating due to fatigue during the hot summer [14]. Nevertheless, this design

routine can lead to devoid freeze protections that make it difficult for natural gas systems to withstand extremely cold temperatures outside. Suffering from the extreme freezings combined with the deficient anti-freezing means, the normal supply of natural gas was largely threatened [14]. Firstly, frigid ambient temperature possibly caused the congestion of the gas flow for several reasons during all processes of gas extraction, refinement, and transportation [15]: i) water mixed with raw gas frozen in the pipeline and valve tree atop the wellhead. ii) water frozen in the scrubber/sePARATOR which splits the product streams. iii) natural gas liquids (NGLs) or hydrates condensed before the gas can exit the gathering system. Beyond the congestion of gas flow, malfunctions of some field equipment rooted in the frigid weather are also reasons for the interrupted supply of natural gas [16].

The insufficient capacity of gas storage and gas reserve. Enough and reliable natural gas storage is vital to both natural gas systems and power systems under contingency states. There are about 30 active natural gas underground storage facilities within the border of Texas[17]. The average daily gas withdrawal of underground gas storage facilities in seven south-central U.S. states, including Texas, reached a record high (22.3 billion cubic feet [18]) during the whole February. The average daily withdrawal of natural gas at Texas underground storage is about 7.8 billion cubic feet on February 19th, 2021[18]. Even so, this was insufficient to compensate for the 10 billion cubic feet gap due to the reduction of natural gas production. According to the calorific conversion formula [19], this gas shortfall is equivalent to a power shortfall of about 1430 GWh (assuming that all electricity is generated by high-efficiency combined-cycle gas-fired units).

The neglect of failure propagation from gas systems to power systems. With the significant development of renewable energy capacity in Texas and the increasing frequency of extreme weather events, the operation uncertainties in the power system are prominent. ERCOT usually evaluates the adequacy of system capacity and arranges reserve resources every quarter [20]. However, due to the separate operation and management of power systems and natural gas systems in Texas, the reliable gas supply to GFUs is out of the jurisdiction of ERCOT. In this case, ERCOT lacks a coordination mechanism with the natural gas system operator. Besides, ERCOT cannot acquire timely information about the operation conditions of natural gas systems. Hence, the adequacy assessment of the power system capacity is usually based on the complete reliability of the primary energy supply, e.g. natural gas supply. Consequently, the impact of extreme weather on the electricity supply is underestimated [20].

Based on the descriptions of practical blackouts around the world, it is essential to evaluate and control the risks of MESs to guarantee the reliable operation of multi-energy systems.

1.3 Challenges in risk modeling and analysis of multi-energy systems

As a section of MES, the risk modeling of power systems has been studied extensively in recent years [21, 22]. The multi-state system model is a widely-used technique to evaluate the risk levels of power system [23]. In specific, the components (e.g. generating units) in power system can have multiple states, such as complete failure, partial failure and well-being [24]. For different states, the performance rates of components, e.g. generating capacity, can vary due to various extents of failure conditions. Hence, the power system composed of numerous multi-state components can certainly be a multi-state system. Based on the multi-state system theory, the risk models of power system have been proposed to describe its ability to provide consumers with electricity within accepted standards [25].

In the traditional multi-state model for power systems, the performance of components and system can be characterized by one single measure, i.e. electricity. Nevertheless, the MESs can simultaneously have different types of performances, including power, gas and heating. Besides, there exists interdependence between different performances in MESs [26]. Taking the CHP unit as an example, the power and heating outputs are usually constrained by a two-dimension feasible operation region [26]. Considering the dependence between different performance types, the MESs can be abstracted into multi-state multi-performance systems (MPMMSS), as shown in Fig. 1.3. Compared to traditional multi-state systems, the main feature of MPMMSS is that the state of system and components has different types of performance and can be represented by a performance vector. Hence, the traditional multi-state model ought to be extended to multi-dimensional space.

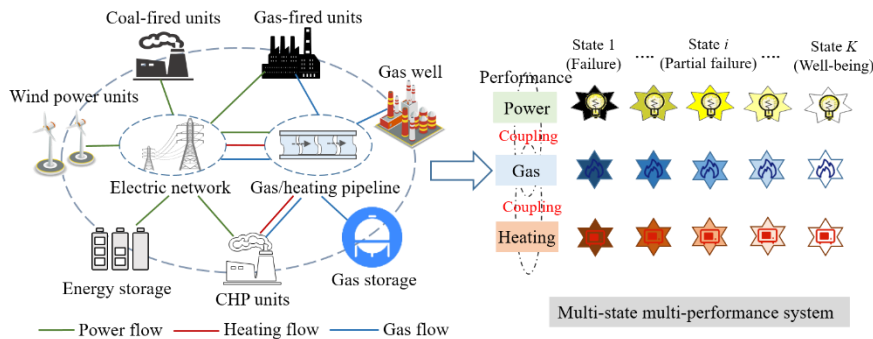


Fig. 1.3 Multi-state multi-performance features of MESs

The existing risk modeling and evaluation methods for multi-state systems mainly include two categories, i.e. analytical techniques and simulation methods. Analytical techniques mainly represent multi-state systems in an analytical way and therefore the risk indices could be evaluated using mathematical solutions [27]. The analytical techniques can effectively help the deep understanding of risk

evaluation and modeling for multi-state systems. Several analytical techniques have been proposed to evaluate the risk of multi-state systems, including the state enumeration method [28], failure tree method [29], and universal generating function (UGF) technique [30].

Compared with the analytical method, the simulation approach is more flexible by simulating the operating state of energy system, which is more efficient and effective in the risk evaluation [31]. On the one hand, with the development of system scale, the number of components can be increased. As a result, the number of the possible system states, as a state combination of components state, grows exponentially [32]. If we still apply the analytical-based approach, the computation complexity and the computation time will also grow exponentially. In contrast, the simulation approach is less sensitive to the system scale. It can conveniently achieve a balance between the accuracy and the computation time by preference[33]. Several simulation approaches have been proposed to analyze the risk of multi-state systems, including non-sequential Monte Carlo simulation[34], pseudo-sequential Monte Carlo simulation[35] and time-sequential Monte Carlo simulation[36].

Though the risk modeling techniques for power systems have been well developed, the multi-performance features of MESs can make the traditional modeling and evaluation approaches not applicable. Therefore, a generalized modeling approach needs to be developed for analyzing the risk levels of MPMMSS and components considering multi-performance features. Moreover, the basic definition of system risk should be given to evaluate the risk features of MPMMSS for different performances, which are of great importance to further studies of MES risk.

Besides multi-performance features, the significant differences between power systems and MESs from transmission sides to demand sides can challenge the traditional risk analysis techniques. The major challenges can be summarized as follows:

1) Energy transmission dynamics: Owing to the distinguishing physical characteristics among electricity, gas, and heating systems, there exist a few main obstacles to directly applying the traditional risk evaluation technique to the MESs. On the one hand, different from the traditional electricity system which is described by algebraic equations during the operational phase, the physical characteristics of gas flow and heating flow are described by the partial derivative equations [37]. That means the time constant and dynamic response of the gas systems are larger and slower. When there is a sudden change in the system state, e.g., a failure of a gas well, the transient process can last for hours, which becomes an unnegelectable factor during the operational risk evaluation [38]. On the other hand, the gas flow and heating models have strong nonlinearity and nonconvexities [39]. The load shedding calculation in the risk evaluation can be difficult and time-costly, and not robust in convergence. Considering that, it is not suitable for the numerous state simulations during risk evaluation.

2) Increasing uncertainty categories: The current research mainly focuses on studying the impacts of internal uncertainties on the risk of power systems, such as

load variation and wind power fluctuation. Considering energy interactions, the disruptions occurring in one system can have impacts on the operation of the other system, which may further feedback to the original system [40]. Therefore, the traditional evaluation models of power systems cannot consider the external uncertainties, i.e. failure propagation process in the risk analysis of MESs. A comprehensive evaluation model needs to be proposed to quantify the multiple uncertainties on the risk levels of MESs.

3) Multi-energy conversion of demand sides: The integration of multiple energies on the demand side increases its flexibility. In the traditional electricity system, the electric demand can only be satisfied by using electricity. While in the MESs, the demands of end-users contain electricity, heating, and cooling simultaneously, and are deeply interconnected. For example, the heating demands can either be met by using air conditioners or electric heat pumps that consume electricity, or by using CHPs that consume natural gas. This kind of energy substitution effect can bring additional flexibilities to the multi-energy customers in the normal operation, demand response, or contingency management, as well as uncertainties[41].

4) Time-varying risk features during operation: The current research on the risk evaluation of MESs mainly focuses on the long-term risk mostly. On the one hand, the traditional risk model and evaluation method usually consider the steady-state probability of components. this method is usually used in the long-term, e.g., in the planning stage. While in the operational phase, due to the commitment and maintenance of the devices, the steady-state probability-based risk model may cause inaccuracies [42]. On the other hand, compared with traditional electricity systems, the MESs have distinguished energy flow dynamics and the flexibilities on the transmission and demand sides, respectively, which are strongly time-related and have great impacts on the operational phase[38]. Currently, this factor has rarely been considered in the risk evaluation of MESs.

Faced with the existing challenges, it is essential to develop new risk evaluation theories and methods for MESs. The proposed method can help system operators and planners accurately understand the risk levels of MESs, which can guide the formulation of risk control measures.

1.4 Organization of this book for risk analysis and control of multi-energy systems

In order to deal with the challenges of risk modeling and analysis in MESs, the organization of this book is shown in Fig.1.4. Firstly, the illustration of MESs and the corresponding risk issues is presented in Chapter 1. In this chapter, the research motivation of this book is answered. Moreover, the risk modeling and analysis of MESs are given in Chapters 2-8 considering multi-performance features under multiply uncertainties. In specific, the long-term and short-term risk modeling and analysis of IEGS are illustrated in Chapters 2-4 considering failure propagation. The risk modelling of CHP units and IEHS considering multi-state multi-performance features are proposed in Chapters 5-6. On this basis, the detailed il-

lustrations about the risk analysis of MESs considering multi-energy conversion of demand sides and the impacts of windstorms are given in Chapters 7 and 8, respectively. Finally, the risk control measures of MESs are presented in Chapters 9-10, including long-term reserve expansion and integrated demand response.

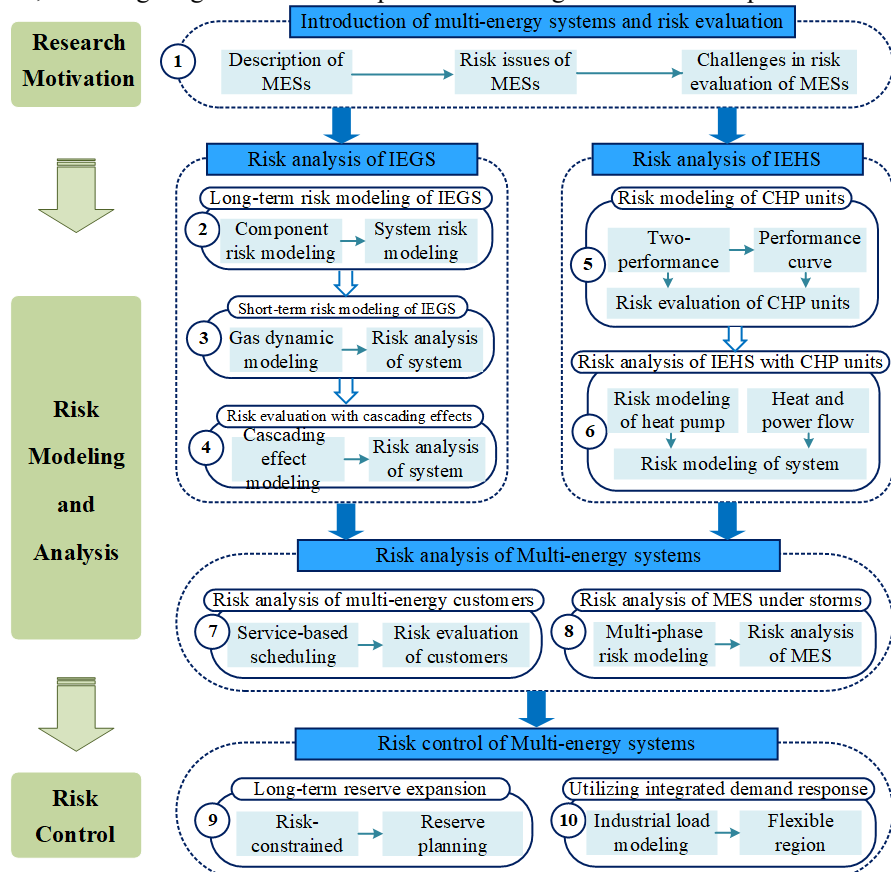


Fig. 1.4 Organization of this book for risk analysis and control of MESs

References

- [1] Y. K. Lei, K. Hou, Y. Wang *et al.*, "A new reliability assessment approach for integrated energy systems: Using hierarchical decoupling optimization framework and impact-increment based state enumeration method," *Applied Energy*, vol. 210, pp. 1237-1250, Jan, 2018.
- [2] U. S. E. I. Administration. "Monthly Energy Review," Nov, 2019; [Online]. Available: <http://www.eia.gov/totalenergy/data/monthly/#naturalgas/>.
- [3] P. I. R. Institute, "Current development of natural gas in China," 2020.

- [4] J. Wang, H. Zhong, Z. Yang *et al.*, "Exploring the trade-offs between electric heating policy and carbon mitigation in China," *Nature Communications*, vol. 11, no. 1, pp. 6054, 2020/11/27, 2020.
- [5] Y. Hou, Y. Ding, M. Bao *et al.*, "Analysis of Texas Blackout From the Perspective of Electricity-Gas Coupling and Its Enlightenment to the Development of China's New Power System," *Proceedings of the CSEE*, 2022.
- [6] U. S. E. I. Administration. "Profile analysis," <https://www.eia.gov/state/analysis.php?sid=TX> (accessed Aug. 23, 2021).
- [7] B. Magness, "Review of February 2021 Extreme Cold Weather Event – ERCOT Presentation," ERCOT, ed., 2021.
- [8] A. Mao, G. Zhang, L. Yuechun *et al.*, "Analysis on largescale blackout occurred in South America and North Mexico interconnected power grid on Sept. 8, 2011 and lessons for electric power dispatching in China," vol. 36, no. 4, pp. 74-78, 2012.
- [9] R. Yan, N. Masood, T. K. Saha *et al.*, "The Anatomy of the 2016 South Australia Blackout: A Catastrophic Event in a High Renewable Network," *IEEE Transactions on Power Systems*, vol. 33, no. 5, pp. 5374-5388, 2018.
- [10] H. Hui, Y. Ding, K. Luan *et al.*, "Analysis of "8•15" Blackout in Taiwan and the Improvement Method of Contingency Reserve Capacity Through Direct Load Control." pp. 1-5, Aug, 2018.
- [11] drax, "Britain's Blackout," 2019.
- [12] Wikipedia, "2021 Texas power crisis," 2021.
- [13] Reuters, "Taiwan power resumes after outage, TSMC hit by brief dip," 2021.
- [14] FERC, "Report on outages and curtailments during the southwest cold weather event of February 1-5," 2011.
- [15] B. V. H. company, "Long-term assessment of natural gas infrastructure to serve electric generation needs within ERCOT: Appendix A," *Texas : ERCOT*, 2011.
- [16] B. V. H. Company, *Long-term assessment of natural gas infrastructure to serve electric generation needs within ERCOT: Appendix A*, Texas : ERCOT, 2011.
- [17] U. S. E. I. Administration, "Underground natural gas storage capacity," W. U. E. I. Administration, ed., 2021.
- [18] U. S. E. I. Administration, "Cold weather results in near-record withdrawals from underground natural gas storage," *Washington : USA : Energy Information Administration*, 2021.
- [19] U. S. E. I. Administration. "Spark spread," https://www.eia.gov/todayinenergy/includes/sparkspread_explain.php (accessed Aug. 23, 2021).

- [20] ERCOT, "Resource adequacy," Texas: ERCOT, ed., 2021.
- [21] Y.-F. Li, and E. Zio, "A multi-state model for the reliability assessment of a distributed generation system via universal generating function," *Reliability Engineering & System Safety*, vol. 106, pp. 28-36, 2012.
- [22] J. S. Contreras-Jiménez, F. Rivas-Dávalos, J. Song *et al.*, "Multi-state system reliability analysis of HVDC transmission systems using matrix-based system reliability method," *International Journal of Electrical Power & Energy Systems*, vol. 100, pp. 265-278, Sep, 2018.
- [23] A. Lisnianski, I. Frenkel, and Y. Ding, *Multi-state system reliability analysis and optimization for engineers and industrial managers*, London: Springer Science & Business Media, 2010.
- [24] G. Yingkui, and L. Jing, "Multi-State System Reliability: A New and Systematic Review," *Procedia Engineering*, vol. 29, pp. 531-536, 2012/01/01/, 2012.
- [25] R. N. Allan, *Reliability evaluation of engineering systems: concepts and techniques*, Boston: Pitman Advanced Pub. Program, 1983.
- [26] C. Shao, and Y. Ding, "Two-interdependent-performance multi-state system: Definitions and reliability evaluation," *Reliability Engineering & System Safety*, vol. 199, pp. 106883, 2020/07/01/, 2020.
- [27] R. Billinton, and N. R. Allan, *Reliability evaluation of power systems*, 2nd ed. New York, NY, USA: Plenum, 1996.
- [28] X. ZHANG, C. Wang, and X. Cheng, "Reliability analysis model for protective relaying system of UHV power network based on Markov state-space method," *power system technology*, vol. 32, no. 13, pp. 94-99, 2008.
- [29] I. Akhtar, and S. Kirmani, "An application of fuzzy fault tree analysis for reliability evaluation of wind energy system," *IETE Journal of Research*, pp. 1-14, 2020.
- [30] G. Levitin, "Universal generating function and its applications," *Springer, Berlin, Germany*, vol. 159, no. 3, pp. 307-324, 2005.
- [31] R. Billinton, and W. Li, "A system state transition sampling method for composite system reliability evaluation," *IEEE Transactions on Power Systems*, vol. 8, no. 3, pp. 761-770, 1993.
- [32] A. M. L. d. Silva, L. A. D. F. Manso, J. C. D. O. Mello *et al.*, "Pseudo-chronological simulation for composite reliability analysis with time varying loads," *IEEE Transactions on Power Systems*, vol. 15(1), no. 1, pp. 73-80, 2000 Feb.
- [33] R. Billinton, and W. Peng, "Teaching distribution system reliability evaluation using Monte Carlo simulation," *IEEE Transactions on Power Systems*, vol. 14(2), no. 2, pp. 397-403, 1999.
- [34] C. L. T. Borges, and J. A. S. Dias, "A Model to Represent Correlated Time Series in Reliability Evaluation by Non-Sequential Monte Carlo Simulation," *IEEE Transactions on Power Systems*, vol. 32, no. 2, pp. 1511-1519, 2017.

- [35] J. C. O. Mello, M. V. F. Pereira, and A. M. L. d. Silva, "Evaluation of reliability worth in composite systems based on pseudo-sequential Monte Carlo simulation," *IEEE Transactions on Power Systems*, vol. 9, no. 3, pp. 1318-1326, 1994.
- [36] R. Billinton, and A. Jonnavithula, "Application of sequential Monte Carlo simulation to evaluation of distributions of composite system indices," *IEE Proceedings - Generation, Transmission and Distribution*, 144, https://digital-library.theiet.org/content/journals/10.1049/ip-gtd_19970929, 1997.
- [37] A. Zlotnik, M. Chertkov, and S. Backhaus, "Optimal control of transient flow in natural gas networks." pp. 4563-4570, 15-18 Dec. 2015, 2015.
- [38] T. Xueyong, W. Sheng, S. Bin *et al.*, "Contingency Management in Integrated Electricity and Gas Systems Considering Gas Flow Dynamics," *EnerarXiv*, 2020/10/24, 2020.
- [39] A. Seungwon, L. Qing, and T. W. Gedra, "Natural gas and electricity optimal power flow," in 2003 IEEE PES Transmission and Distribution Conference and Exposition, 2003, pp. 138-143.
- [40] M. Bao, Y. Ding, C. Shao *et al.*, "Nodal Reliability Evaluation of Interdependent Gas and Power Systems Considering Cascading Effects," *IEEE Transactions on Smart Grid*, vol. 11, no. 5, pp. 4090-4104, Mar, 2020.
- [41] S. Wang, C. Shao, Y. Ding *et al.*, "Operational reliability of multi-energy customers considering service-based self-scheduling," *Applied Energy*, vol. 254, pp. 113531, Nov, 2019.
- [42] Z. Bao, D. Chen, L. Wu *et al.*, "Optimal inter- and intra-hour scheduling of islanded integrated-energy system considering linepack of gas pipelines," *Energy*, vol. 171, pp. 326-340, Mar, 2019.

2 A Framework for Risk Modeling of Integrated Electricity and Gas Systems Utilizing Universal Generating Function Techniques

2.1 Introduction

As illustrated in Chapter 1, the energy interaction can cause failure propagation between gas and electricity systems, which can have great impacts on the risk levels of integrated electricity and gas systems (IEGS). In the previous studies, risk assessment techniques of power systems have been well developed during the past few decades [1, 2]. However, these conventional techniques are more focused on studying the risk of the power system itself and usually ignore the coupled relationship between the power system and NGS. The integration of NGS and power system can bring complexities in risk evaluation and management. Firstly, the risk and performances of IEGS are affected by the random failures either in NGS or in the power system. The NGS contains many different components with various operating characteristics. It is important to develop a risk model of NGS considering the stochastic performances of its components and the corresponding operating constraints. Moreover, because of the coupled relationship between NGS and the power system, the impacts of NGS on the risk of the power system must be modeled in the risk analysis. Additionally, the effects of random failures on the risk of the power system can differ at various nodes because of the transmission constraints and uneven distributions of generators and demands [3-5]. Nodal risk, therefore, has been adopted to evaluate the locational risk performances of the power system. When considering the integration of NGS and the power system, customers' nodal reliabilities must be thoroughly analyzed and quantitatively evaluated.

To model the operating characteristics and random failures of components, a multi-state system model is used to represent the stochastic performances of IEGS [6]. However, with regard to IEGS consisting of numerous components, the number of system states can be relatively large. Enormous efforts must be spent to develop a stochastic model for IEGS and solve it [7]. It can be a difficult process for the state-space diagram building or model construction, even for a relatively small IEGS. Hence, the universal generating function (UGF) technique, which has been widely used in multi-state system risk and performance evaluation, is adopted in this chapter. The proposed technique [6-8], first introduced by Ushakov [7] and greatly extended by Lisnianski [6] and Levitin [8], has proved as an effective method to evaluate the reliabilities of the power system [9-11]. References [9] and [10] have adopted the UGF technique to study the impacts of high wind penetration on the risk evaluation and management of the power system. In reference [11], the UGF technique has also been utilized to evaluate the reliabilities of the distributed generation system with different energy sources. The UGF technique provides us an effective tool to obtain the performance distribution of the entire

system based on the given performance distributions of its elements [9]. Moreover, it can represent the various risk models of individual components in IEGS and describe the coupled relationship between NGS and power system.

In this chapter, a UGF-based framework is proposed to evaluate the nodal risk of IEGS considering the random failures of components, as well as the coupled relationship between NGS and the power system. Firstly, the UGFs for different components in NGS are developed to represent their stochastic performances. The multi-state model of NGS is obtained by aggregating these UGFs utilizing the proposed gas flow calculation (GFC) operator. Moreover, the multi-state model of gas injection at each node is converted into the power output models of GPPs, which is based on the gas-to-power calculation (GTP) operator. In this manner, the impacts of NGS could be incorporated into the risk evaluation of the power system. Moreover, to evaluate the locational risk performances of IEGS, nodal risk indices for both the NGS and power system are proposed. This chapter includes research related to the general framework for risk modeling of IEGS considering failure propagation by[12].

2.3 Risk modeling of the natural gas system

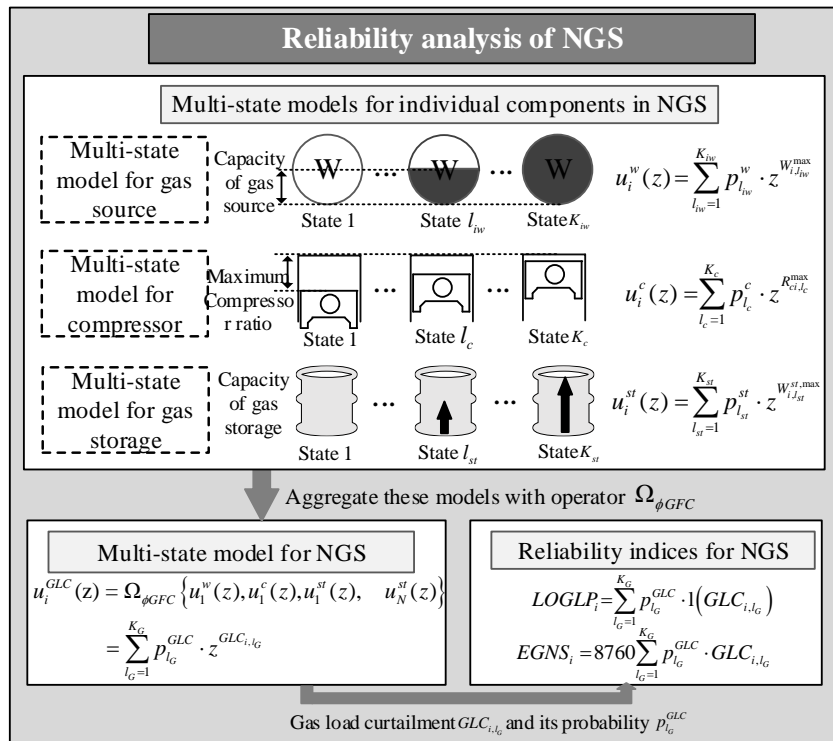


Fig. 2.1 Framework for risk modeling of NGS.

According to the coupling features, the risk analysis of NGS is conducted firstly, as shown in Fig. 2.1. The multi-state models of key components in NGS, such as gas sources, compressors, and gas storages, are developed to represent their stochastic performances utilizing the UGF method. The GFC operator is developed for aggregating these UGFs to obtain the multi-state model of NGS. Using this model, the possible gas load curtailment in contingency states can be obtained, with which the nodal risk indices for the NGS are determined.

2.3.1 Risk model for gas source

The gas source on one node could consist of multiple gas wells using directional and horizontal drilling technology [13]. Hence, the multi-state model of the gas source could be represented by the aggregation of gas wells. Regarding an individual gas well, the gas production is affected by many factors, such as geological conditions and extraction techniques, etc.

Generally, the risk model of a gas well can be represented as a two-state model. The maximum gas production is zero when the well fails and is W_{is}^{\max} when the well is in operation. Therefore, the corresponding UGF used to represent the risk model of gas well s at node i is defined as:

$$u_{is}^r(z) = p_{is}^{Ar} \cdot z^{W_{is}^{\max}} + p_{is}^{Ur} \cdot z^0 \quad (2.1)$$

where p_{is}^{Ar} and p_{is}^{Ur} are the availability and unavailability of gas well s at node i , respectively.

The risk model of the gas source at node i is composed of several gas-well subsystems and can be represented as a multi-state gas source (MGS_i) using UGF equivalent as shown in Fig. 2.2. The parallel operator Ω_{ϕ_w} over UGF representations of n_{iw} wells is used to obtain the multi-state model for MGS_i :

The risk model of the gas source at node i is composed of several gas-well subsystems and can be represented as a multi-state gas source (MGS_i) using UGF equivalent. The parallel operator Ω_{ϕ_w} over UGF representations of n_{iw} wells is used to obtain the multi-state model for MGS_i :

$$\begin{aligned} u_i^w(z) &= \Omega_{\phi_w} \left\{ u_{i1}^r(z), K, u_{i,n_{iw}}^r(z) \right\} \\ &= \Omega_{\phi_w} \left\{ p_{i1}^{Ar} \cdot z^{W_{i1}^{\max}} + p_{i1}^{Ur} \cdot z^0, K, p_{i,n_{iw}}^{Ar} \cdot z^{W_{in_{iw}}^{\max}} + p_{i,n_{iw}}^{Ur} \cdot z^0 \right\} \\ &= \prod_{s=1}^{n_{iw}} p_{is}^{Ar} \cdot z^{\sum_{s=1}^{n_{iw}} W_{is}^{\max}} + K + \prod_{s=1}^{n_{iw}} p_{is}^{Ur} \cdot z^0 \\ &= \sum_{l_{iw}=1}^{K_{iw}} p_{l_{iw}}^w \cdot z^{W_{l_{iw}}^{\max}} \end{aligned} \quad (2.2)$$

where $p_{l_w}^w$ and W_{l,l_w}^{\max} are the probability and maximum gas production of the gas source at node i for the state l_w . There are K_{l_w} states of the gas source considering random failures.

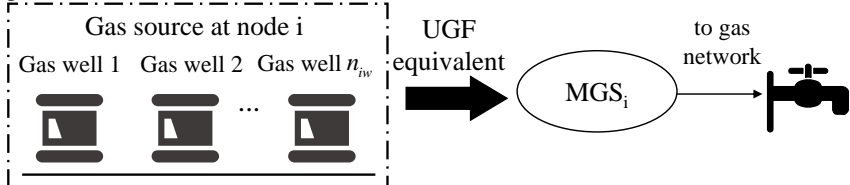


Fig. 2.2 Gas source UGF equivalent.

2.3.2 Risk model for gas compressor

To maintain the pressures on the pipeline at desired values, the compressor will modify the suction pressure or discharge pressure. The compressor ratio R_{ci} is used to represent the compression capability of compressor c between node i and node j , which is defined as:

$$R_{ci} = \frac{\pi_j}{\pi_i} \quad (2.3)$$

where π_i and π_j are the pressures of suction node i and discharge node j , respectively.

Generally, the maximum compressor ratio is affected by both characteristics and the risk of compressors. Hence, the maximum compressor ratio of compressor c can be viewed as a multi-state model. The corresponding UGF to represent the compression capability of compressor c between node i and node j can be defined as a polynomial:

$$u_i^c(z) = \sum_{l_c=1}^{K_c} p_{l_c}^c \cdot z^{R_{ci,l_c}^{\max}} \quad (2.4)$$

where $p_{l_c}^c$ and R_{ci,l_c}^{\max} are the probability and maximum compressor ratio of compressor c with its inlet at node i for state l_c , respectively, and K_c is the number of states.

2.3.3 Risk model for gas storage

During operation, the gas storage could adjust the operating status between the charge state and discharge state, which can be modeled as a gas supplier or a load. The different operating statuses of gas storage could be represented by the signs of gas storage output. Generally, due to physical characteristics and random failures, the capacity of gas storage could be regarded as a multi-state model, which is defined as the polynomial:

$$u_i^{st}(z) = \sum_{l_{st}=1}^{K_{st}} p_{l_{st}}^{st} \cdot z^{W_{i,l_{st}}^{st,\max}} \quad (2.5)$$

where $p_{l_{st}}^{st}$ and $W_{i,l_{st}}^{st,\max}$ are the probability and capacity of gas storage st at node i for state l_{st} , respectively. There are K_{st} states of gas storage.

As significant gas reserves, the change of capacity for gas storage will have an influence on the risk of NGS. To measure the average capacity of gas storage in NGS, the indicator C_{st} is introduced in this chapter. C_{st} is a weighted average value of gas storage capacity at each node over gas loads, which can be represented as:

$$C_{st} = \frac{\sum_{i=1}^N \sum_{l_{st}}^{K_{st}} p_{l_{st}}^{st} \cdot W_{i,l_{st}}^{st,\max}}{\sum_{i=1}^N W_{i,L}} \quad (2.6)$$

where $W_{i,L}$ is the gas load in the normal state at node i and N represents the number of gas nodes in NGS.

2.3.4 Risk analysis of natural gas system

Failures of gas sources and variations of gas storage output may result in a change in gas supply to GPPs. After evaluating the $u_i^w(z)$, $u_i^c(z)$ and $u_i^{st}(z)$, the multi-state model of NGS could be obtained by GFC operator $\Omega_{\phi GFC}$ to calculate the gas load curtailment at each node.

$$\begin{aligned} u_i^{GLC}(z) &= \Omega_{\phi GFC} \left\{ u_1^w(z), u_1^c(z), u_1^{st}(z), K, u_i^w(z), u_i^c(z), \right. \\ &\quad \left. u_i^{st}(z) K u_N^w(z), u_N^c(z), u_N^{st}(z) \right\} \\ &= \sum_{i=1}^N \sum_{l_w=1}^{K_{iw}} \sum_{l_c=1}^{K_c} \sum_{l_{st}=1}^{K_{st}} p_{l_w}^w \cdot p_{l_c}^c \cdot p_{l_{st}}^{st} \cdot z^{\phi GFC \{ W_{i,l_w}^{\max}, R_{c,1,l_c}^{\max}, W_{i,l_{st}}^{st,\max}, L, W_{N,l_{Nw}}^{\max}, R_{cN,l_c}^{\max}, W_{N,l_{st}}^{st,\max} \}} \quad (2.7) \\ &= \sum_{l_G=1}^{K_G} p_{l_G}^{GLC} \cdot z^{GLC_{i,l_G}} \end{aligned}$$

where $p_{l_G}^{GLC}$ and GLC_{i,l_G} are the probability and the gas load curtailment at node i for state l_G , respectively. There are K_G states of gas load curtailment at node i .

Hence, the UGF representing the gas injection at node i for different states compared to the load $W_{i,L}$ in the normal state can be obtained as:

$$\begin{aligned} u_i^{GS}(z) &= \sum_{l_G=1}^{K_G} p_{l_G}^{GLC} \cdot z^{W_{i,L} - GLC_{i,l_G}} \\ &= \sum_{l_G=1}^{K_G} p_{l_G}^{GLC} \cdot z^{GS_{i,l_G}} \quad (2.8) \end{aligned}$$

where GS_{i,l_G} refers to gas injection at node i for state l_G .

The GFC operator used in (2.7) is defined as an optimization model to determine the gas load curtailment at node i for state l_G , which is described in (2.9)-(2.19). The objective function is to minimize the total gas load curtailment for state l_G :

$$\text{Min } f_{l_G} = \sum_{i=1}^N GLC_{i,l_G} \quad (2.9)$$

Subject to the following constraints:

Gas flow through pipelines: The gas flow f_{ij,l_G} through the pipeline from node i to node j for state l_G can be calculated according to Weymouth equation [14]. The gas flow is a quadratic function of the pressures on both sides of nodes, which is expressed as:

$$\text{sgn}(\pi_{i,l_G}, \pi_{j,l_G}) f_{ij,l_G}^2 = M_{ij}^2 (\pi_{i,l_G}^2 - \pi_{j,l_G}^2) \quad (2.10)$$

where $\text{sgn}(\pi_{i,l_G}, \pi_{j,l_G}) = 1$ if $(\pi_{i,l_G}^2 - \pi_{j,l_G}^2) > 0$ or $\text{sgn}(\pi_{i,l_G}, \pi_{j,l_G}) = -1$ if $(\pi_{i,l_G}^2 - \pi_{j,l_G}^2) < 0$. M_{ij} refers to the constant pipeline flow coefficient, which is related to the diameter of the pipeline, temperature, and gas pressure. π_{i,l_G} and π_{j,l_G} are the pressures of node i and node j for state l_G , respectively.

The pressure levels at each node are bounded by:

$$\pi_i^{\min} \leq \pi_{i,l_G} \leq \pi_i^{\max} \quad (2.11)$$

where π_i^{\min} and π_i^{\max} represent the minimum and maximum limits of the pressure at node i , respectively.

The gas flow through each pipeline is restricted by pipeline capacity:

$$|f_{ij,l_G}| \leq f_{ij}^{\max} \quad (2.12)$$

where f_{ij}^{\max} represents the maximum gas flow of the pipeline between node i to node j .

Compressor model: In general, the work function of the compressor is complex and closely associated with the compressor type. In this chapter, we use centrifugal compressors, whose key characteristic is that horsepower needs to be consumed to drive the turbine [14]. The horsepower consumption H_{cij,l_G} of compressor c between node i and node j for state l_G is a function of the gas flow f_{ij,l_G} through the compressor, which can be expressed as:

$$H_{cij,l_G} = B_{ij} f_{ij,l_G} (R_{i,l_G}^{z_c(1-1/\alpha)} - 1) \quad (2.13)$$

where B_{ij} is the constant horsepower consumption coefficient, which depends on the heat ratio, suction temperature and efficiency of a compressor. R_{i,l_G} represents

the compressor ratio for state l_G . z_c and α refer to gas compressibility factor and specific heat ratio, respectively. Hence, the amount of gas τ_{cij,l_G} supplied to the turbine in compressor c for state l_G can be calculated via horsepower consumption H_{cij,l_G} . For simplicity, τ_{cij,l_G} is a quadratic function of H_{cij,l_G} , which can be calculated as:

$$\tau_{cij,l_G} = \alpha_{T_c} + \beta_{T_c} H_{cij,l_G} + \gamma_{T_c} H_{cij,l_G}^2 \quad (2.14)$$

where α_{T_c} , β_{T_c} and γ_{T_c} are compressor gas consumption coefficients.

The compressor ratio of each compressor is bounded by:

$$R_{i,l_G} \leq R_{i,l_G}^{\max} \quad (2.15)$$

where R_{i,l_G}^{\max} represents the maximum compressor ratio of the compressor with its inlet at node i for state l_G .

Gas flow balance on each node: Similar to the power system, the NGS also needs to follow the nodal supply-demand balance. The amount of the gas leaving node i for state l_G is equal to that of gas injected at that node. The gas flow equation at node i can be given by:

$$W_{i,l_G} - (W_{iL} - GLC_{i,l_G}) + W_{i,l_G}^{st} - \sum_{j=1}^N \tau_{cij,l_G} - \sum_{j=1}^N f_{ij,l_G} = 0 \quad (2.16)$$

where W_{i,l_G} is the production of gas source and W_{i,l_G}^{st} is the output of gas storage at node i for state l_G .

The production of each gas source is restricted by its capacity, which can be modeled as:

$$0 \leq W_{i,l_G} \leq W_{i,l_G}^{\max} \quad (2.17)$$

where W_{i,l_G}^{\max} represent the maximum production of the gas source at node i for state l_G .

The output of each gas storage is restricted by the maximum level:

$$W_{i,l_G}^{st} \leq W_{i,l_G}^{st,\max} \quad (2.18)$$

where $W_{i,l_G}^{st,\max}$ represents the maximum output of gas storage at node i for state l_G .

The gas load curtailment at each node is bounded by:

$$GLC_{i,l_G}^{\min} \leq GLC_{i,l_G} \leq GLC_{i,l_G}^{\max} \quad (2.19)$$

where GLC_{i,l_G}^{\min} and GLC_{i,l_G}^{\max} represent the minimum and maximum limits of gas load curtailment at node i for state l_G , respectively.

2.3.5 Risk indices for gas system

In a composite system, many indices are defined to evaluate the risk of the energy system, including the expected values and nodal reliabilities. In this chapter, the loss of gas load probability ($LOGLP_i$) and the expected gas not supplied ($EGNS_i$) are introduced to evaluate the nodal risk of NGS.

After calculating the $p_{l_G}^{GLC}$ and GLC_{i,l_G} at node i for each state from (2.7), the risk indices $LOGLP_i$ and $EGNS_i$ at node i can be calculated as:

$$LOGLP_i = \sum_{l_G=1}^{K_G} p_{l_G}^{GLC} \cdot 1(GLC_{i,l_G}) \quad (2.20)$$

$$EGNS_i = 8760 \sum_{l_G=1}^{K_G} p_{l_G}^{GLC} \cdot GLC_{i,l_G} \quad (2.21)$$

where $1(\text{True})=1$ and $1(\text{False})=0$.

2.4 Risk modeling of power system considering the impacts of the gas system

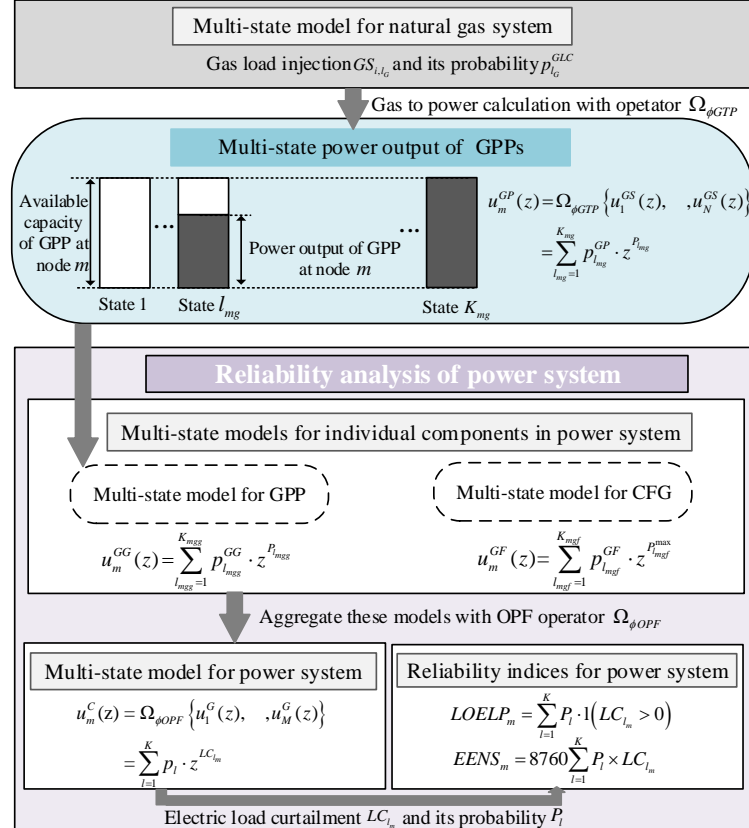


Fig. 2.3 Framework for risk modeling of the power system.

Based on the multi-state model of NGS in (2.7), the framework for risk analysis of the power system considering the impacts of NGS is shown in Fig. 2.3. The gas-to-power calculation (GTP) operator is first developed to convert the multi-state model of gas injection at each node to the power output models of GPPs in the power system. Moreover, the optimal power flow (OPF) composition operator is developed to aggregate the multi-state models for GPPs and other generators (such as coal-fired generators) to obtain the multi-state model for the power system. Based on this, possible electric load curtailment in contingency states can be obtained, with which the nodal risk indices for the power system are evaluated.

2.4.1 Risk model for GPP based on GTP operator

The coupled relationship between the power system and NGS could be described by the model of GPPs. Each GPP acts as an energy converter, which is

simultaneously connected to the load node i in the NGS and generation node m in the power system. According to [14], there is a conversion relationship between the output of GPPs and the gas injection at corresponding nodes. Hence, the power output of a GPP at electric node m could be obtained by the GTP operator $\Omega_{\phi GTP}$ after evaluating the $u_i^{GS}(z)$:

$$\begin{aligned} u_m^{GP}(z) &= \Omega_{\phi GTP} \left\{ u_1^{GS}(z), L, u_i^{GS}(z), L, u_N^{GS}(z) \right\} \\ &= \Omega_{\phi GTP} \left\{ \sum_{l_G=1}^{K_G} p_{l_G}^{GLC} \cdot z^{GS_{i,l_G}}, L, \sum_{l_G=1}^{K_G} p_{l_G}^{GLC} \cdot z^{GS_{N,l_G}} \right\} \\ &= \sum_{l_G=1}^{K_G} p_{l_G}^{GLC} \cdot z^{\phi GTP \{ GS_{i,l_G}, L, GS_{N,l_G} \}} \\ &= \sum_{l_{mg}=1}^{K_{mg}} p_{l_{mg}}^{GP} \cdot z^{P_{l_{mg}}} \end{aligned} \quad (2.22)$$

where $p_{l_{mg}}^{GP}$ and $P_{l_{mg}}$ are the probability and power output of a GPP at node m for state l_{mg} , respectively. There are K_{mg} states of a GPP considering the impacts of NGS.

The GTP operator used in (2.22) is a conversion relationship to calculate the power output of a GPP $P_{l_{mg}}$ based on the corresponding nodal gas injection GS_{i,l_G} in NGS, which is described in (2.24). However, according to the heating rate curve [14], the amount of natural gas consumed by a GPP at electric node m is a quadratic function of the power generation, which is expressed as:

$$GS_{i,l_G} = (\alpha_{mg} + \beta_{mg} \cdot P_{l_{mg}} + \gamma_{mg} \cdot P_{l_{mg}}^2) / GHV \quad (2.23)$$

where α_{mg} , β_{mg} and γ_{mg} are the heat rate coefficients of GPP at node m . GHV refers to the gas gross heating value.

Hence, $P_{l_{mg}}$ is the solution to equation (2.23):

$$P_{l_{mg}} = \frac{-\beta_{mg} + \sqrt{\beta_{mg}^2 - 4 \cdot \gamma_{mg} \cdot (\alpha_{mg} - GS_{i,l_G} \cdot GHV)}}{2\gamma_{mg}} \quad (2.24)$$

As seen from the computation procedure from $u_i^{GS}(z)$ to $u_m^{GP}(z)$, the impacts of NGS on the risk of the power system could be embodied in the multi-state model of GPP.

The power output of a GPP also depends on its risk. The power output is zero when the GPP fails and $P_{l_{mg}}$ when the GPP is in the operation state. The UGF for a GPP at electric node m considering random failures is defined as:

$$u_{mg}^{GK}(z) = p_{mg}^{AK} \cdot z^{P_{l_{mg}}} + p_{mg}^{UK} \cdot z^0 \quad (2.25)$$

where p_{mg}^{AK} and p_{mg}^{UK} are the availability and unavailability of a GPP at electric node m , respectively.

Considering both the impacts of NGS and the risk of GPPs, the combination of (2.22) and (2.25) is used to obtain the power output of multi-state GPP (MGG_m).

The series operator $\Omega_{\phi s}$ is applied to calculate the UGF for MGG_m :

$$\begin{aligned} u_m^{GG}(z) &= \Omega_{\phi s} \left\{ u_m^{GP}(z), u_m^{GK}(z) \right\} \\ &= \Omega_{\phi s} \left\{ \sum_{l_{mg}=1}^{K_{mg}} p_{l_{mg}}^{GP} \cdot z^{P_{l_{mg}}}, p_{mg}^{AK} \cdot z^{P_{mg}} + p_{mg}^{UK} \cdot z^0 \right\} \\ &= \sum_{l_{mg}=1}^{K_{mg}} p_{l_{mg}}^{GP} \cdot p_{mg}^{AK} \cdot z^{P_{l_{mg}}} + \sum_{l_{mg}=1}^{K_{mg}} p_{l_{mg}}^{GP} \cdot p_{mg}^{UK} \cdot z^0 \\ &= \sum_{l_{mg}=1}^{K_{mg}} p_{l_{mg}}^{GG} \cdot z^{P_{l_{mg}}} \end{aligned} \quad (2.26)$$

where $p_{l_{mg}}^{GG}$ and $P_{l_{mg}}$ are the probability and power output of MGG_m at node m for state l_{mg} , respectively. There are K_{mg} states of MGG_m considering the impacts of NGS and the risk of GPPs.

2.4.2 Risk model for coal-fired generators

Considering random failures, the risk model for a coal-fired generator (CFG) can be represented as a two-state model. The UGF of CFG c at node m is defined as the polynomial:

$$u_{mc}^{CK}(z) = p_{mc}^{AK} \cdot z^{P_{mc}^{\max}} + p_{mc}^{UK} \cdot z^0 \quad (2.27)$$

where p_{mc}^{AK} and p_{mc}^{UK} are the availability and unavailability of CFG c , respectively. P_{mc}^{\max} refers to the available capacity of CFG c at node m .

Since there are also several CFGs installed at one node, the multi-units at node m can be represented as a multi-state coal-fired generator (MCG_m) using the UGF method. The corresponding UGF for MCG_m can be obtained by using the parallel operator $\Omega_{\phi g}$ over UGF representations of n_{mc} CFGs:

$$\begin{aligned} u_m^{GF}(z) &= \Omega_{\phi g} \left\{ u_{m1}^{CK}(z), K, u_{mn_{mc}}^{CK}(z) \right\} \\ &= \Omega_{\phi g} \left\{ p_{m1}^{AK} \cdot z^{P_{m1}^{\max}} + p_{m1}^{UK} \cdot z^0, K, p_{mn_{mc}}^{AK} \cdot z^{P_{mn_{mc}}^{\max}} + p_{mn_{mc}}^{UK} \cdot z^0 \right\} \\ &= \prod_{c=1}^{n_{mc}} p_{mc}^{AK} \cdot z^{\sum_{c=1}^{n_{mc}} P_{mc}^{\max}} + K + \prod_{c=1}^{n_{mc}} p_{mc}^{UK} \cdot z^0 \\ &= \sum_{l_{mgf}=1}^{K_{mgf}} p_{l_{mgf}}^{GF} \cdot z^{P_{l_{mgf}}^{\max}} \end{aligned} \quad (2.28)$$

where $p_{l_{mgf}}^{GF}$ and $P_{l_{mgf}}^{\max}$ are the probability and total available capacity of MCG_{*m*} at node *m* for state l_{mgf} , respectively. There are K_{mgf} states of the MCG_{*m*} considering random failures.

2.4.3 Risk model for generation provider

The GPPs and CFGs could coexist at node *m*. The combination of MCG_{*m*} and MGG_{*m*} is represented as a multi-state generation provider at node *m* (MGP_{*m*}). The parallel operator $\Omega_{\phi P}$ over the UGF representations of MCG_{*m*} and MGG_{*m*} is used to obtain the UGF of MGP_{*m*}, which can be expressed as:

$$\begin{aligned} u_m^G(z) &= \Omega_{\phi P} \left\{ u_m^{GG}(z), u_m^{GF}(z) \right\} \\ &= \Omega_{\phi P} \left\{ \sum_{l_{mgg}=1}^{K_{gg}} p_{l_{mgg}}^{GG} \cdot z^{P_{l_{mgg}}}, \sum_{l_{mgf}=1}^{K_{mgf}} p_{l_{mgf}}^{GF} \cdot z^{P_{l_{mgf}}^{\max}} \right\} \\ &= \sum_{l_{mgg}=1}^{K_{mgg}} \sum_{l_{mgf}=1}^{K_{mgf}} p_{l_{mgg}}^{GG} \cdot p_{l_{mgf}}^{GF} \cdot z^{\left(P_{l_{mgg}} + P_{l_{mgf}}^{\max} \right)} \\ &= \sum_{l_{mg}=1}^{K_{mg}} p_{l_{mg}}^G \cdot z^{P_{l_{mg}}^{\max}} \end{aligned} \quad (2.29)$$

where $p_{l_{mg}}^G$ and $P_{l_{mg}}^{\max}$ are the probability and total available capacity of MGP_{*m*} at node *m* for state l_{mg} , respectively. The generation provider MGP_{*m*} has K_{mg} states.

2.4.4 Risk analysis of power system

The stochastic failures in both NGS and the power system can result in transmission line congestion or customer interruptions. The influence of random failures in NGS on the power system has been embodied in the multi-state model in (2.22). For an *M*-electric-node system with κ states, the multi-state model for the power system could be obtained by the OPF composition operator $\Omega_{\phi OPF}$ after evaluating the $u_m^G(z)$.

$$\begin{aligned} u_m^C(z) &= \Omega_{\phi OPF} \left\{ u_1^G(z), K, u_i^G(z), K, u_M^G(z) \right\} \\ &= \sum_{m=1}^M \sum_{l_{mg}=1}^{K_{mg}} p_{l_{mg}}^G \cdot z^{\phi OPF \left\{ P_{l_{ig}}^{\max}, L, P_{l_{ig}}^{\max}, L, P_{l_{Me}}^{\max} \right\}} \\ &= \sum_{l=1}^K p_l \cdot z^{LC_{l_m}} \end{aligned} \quad (2.30)$$

where p_l and LC_{l_m} are the probability and electric load curtailment at node *m* for state *l*, respectively.

The OPF operator used in (2.30) is defined as a linear optimization model to determine the electric load curtailment for state l at node m , which is described in (2.31)-(2.35). The objective function is to minimize the total cost of electric load curtailment for state l [15].

$$\text{Min } f_l = \sum_{m=1}^M OC(LC_{l_m}) \quad (2.31)$$

Subject to the following constraints:

Power balance constraints:

$$\mathbf{B}_l \cdot \boldsymbol{\Theta}_l = \mathbf{P}_l - \mathbf{D}_l \quad (2.32)$$

Generating unit limits:

$$0 \leq P_{l_m} \leq P_{l_m}^{\max} \quad (2.33)$$

Load curtailment constraints:

$$0 \leq LC_{l_m} \leq LC_{l_m}^{\max} \quad (2.34)$$

Line flow constraints:

$$\left| \frac{1}{x_{l_{mn}}} (\theta_{l_m} - \theta_{l_n}) \right| \leq |S_{l_{mn}}^{\max}| \quad (2.35)$$

where LC_{l_m} is load curtailment at node m for state l ; $OC(LC_{l_m})$ is load curtailment cost which is modeled as a linear function; \mathbf{B}_l is the admittance matrix of transmission network; $\boldsymbol{\Theta}_l = [\theta_{l_1}, \dots, \theta_{l_m}, \dots, \theta_{l_M}]^T$ is phase angle vector of the node voltages; $\mathbf{P}_l = [P_{l_1}, \dots, P_{l_m}, \dots, P_{l_M}]^T$ is the vector of power generations for state l ; $\mathbf{D}_l = [D_{1,l}, \dots, D_{m,l}, \dots, D_{M,l}]^T$ is the vector of node loads for state l ; P_{l_m} is the power generation of MGP _{m} and θ_{l_m} is the phase angle of voltage at node m ; $x_{l_{mn}}$ and $|S_{l_{mn}}^{\max}|$ are the reactance and power flow limits of the line between node m and n , respectively.

2.4.5 Risk indices for power system

Similar to the risk indices in NGS, the loss of electric load probability ($LOELP_m$) and the expected energy not supplied ($EENS_m$) are introduced to evaluate the nodal risk of the power system [1]. After calculating the p_l and LC_{l_m} at node m for each state from (2.30), the risk indices $LOELP_m$ and $EENS_m$ at node m can be calculated as:

$$LOELP_m = \sum_{l=1}^K p_l \cdot \mathbb{1}(LC_{l_m} > 0) \quad (2.36)$$

$$EENS_m = 8760 \sum_{l=1}^K p_l \cdot LC_{l_m} \quad (2.37)$$

2.6 System studies

The proposed techniques and models are applied to analyze the risk of the test system composed of the modified IEEE 30-bus power system from [16] and the Belgian 20-node gas system detailed in [17], as shown in Fig. 2.4. The Belgian 20-node gas system is composed of seven gas wells, three centrifugal compressors, 19 pipelines, and three gas storages. On the other hand, the power system has 6 generating nodes, 27 load nodes, 41 transmission lines, and 9 generating units. It is assumed that there are three GPPs at electric nodes 1, 13, and 5 which are supplied from the gas flow at gas nodes 10, 16, and 7 of NGS through connections C1, C2, and C3, respectively.

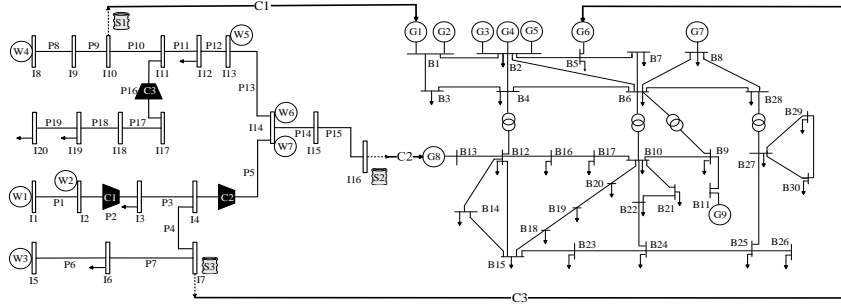


Fig. 2.4 Test system composed of the modified IEEE 30-bus power system and the 20-node Belgian gas system

The physical parameters of gas compressors (such as heat ratio, suction temperature, compressor ratio, etc.), pipelines (such as diameter and length) and gas gross heating value can be found in [18]. The risk parameters of CFGs and GPPs can be found in [19]. The customers in the power system are divided into industrial, commercial, and residential, whose interruption costs per unserved MWh [20] are presented in Table 2.1. According to references [21] and [22], the unavailability of gas compressors and gas storage is 4% and 5%, respectively. Hence, the maximum compressor ratio of gas compressors and the capacity of gas storage are assumed to have three states, as shown in Table 2.2 and Table 2.3, respectively. Based on this, the capacity level of gas storages is 0.1.

Table 2.1 The interruption costs for different customers

Customer sector	Location (bus)	Interruption costs (\$/unserved MWh)
Residential	3,4,8,10,12,17,19,20,24,26,27	1000
Commercial	5,6,14,15,21,22,28,29	10000
Industrial	2,7,9,16,18,23,25,30	5000

Table 2.2 Maximum compressor ratio for different states

Gas compressor	State 1 ($R_{ci}^{\max} / p_{l_c}^c$)	State 2 ($R_{ci}^{\max} / p_{l_c}^c$)	State 3 ($R_{ci}^{\max} / p_{l_c}^c$)
----------------	---	---	---

C1	1.9/0.96	1.4/0.03	1/0.01
C2	1.7/0.96	1.3/0.03	1/0.01
C3	1.8/0.96	1.4/0.03	1/0.01

Table 2.3 The capacity of gas storages for different states ($10^3 \text{m}^3/\text{h}$)

Gas storage	State 1 ($W_{i,l_s}^{\text{sr},\max} / p_{l_s}^{\text{sr}}$)	State 2 ($W_{i,l_s}^{\text{sr},\max} / p_{l_s}^{\text{sr}}$)	State 3 ($W_{i,l_s}^{\text{sr},\max} / p_{l_s}^{\text{sr}}$)
S1	1.6/0.92	0.9/0.04	0/0.04
S2	1.4/0.91	0.8/0.04	0/0.05
S3	1.2/0.92	0.7/0.05	0/0.03

To illustrate the effectiveness of the proposed technique, three cases are modeled to evaluate the nodal risk of IEGS.

Case 1: The impacts of the coupling degree between the power system and NGS on the risk of IEGS are evaluated in this case. Three scenarios are considered in case 1: scenario A is the base case without considering the coupling between the two systems, where the connections C1, C2, and C3 are broken. Compared to scenario A, the connection C3 between electric node 5 and gas node 7 is considered in scenario B, and all the connections C1, C2, and C3 are considered in scenario C. Besides, the capacity levels of gas storage C_{st} are set as zero for three scenarios in this case.

The risk indices $EGNS$ ($10^3 \text{ m}^3/\text{yr}$), $LOGLP$ in NGS and $EENS$ (MWh/yr), $LOELP$ in the power system at different nodes from three scenarios are shown in Table 2.4 and Table 2.5, respectively.

Regarding the NGS, both $EGNS$ and $LOGLP$ are relatively constant with the increase of coupling degree between NGS and the power system. Moreover, it can be noted that there are huge differences between the risk indices at different nodes. The $EGNS$ at gas node 10 is the largest among all nodes, with values of $4.9758 \times 10^6 \text{ m}^3/\text{yr}$, $4.9752 \times 10^6 \text{ m}^3/\text{yr}$, and $4.9761 \times 10^6 \text{ m}^3/\text{yr}$ for scenarios A, B, and C, respectively. In contrast, the $EGNS$ at gas node 12 is relatively small for all scenarios. This is mainly because that gas node 12 is close to gas source nodes 13 and 14 compared to other gas nodes. The customers at gas node 12 are easier to obtain gas supply in contingency states.

Table 2.4 Risk indices in gas systems for case 1

Gas node	SCENARIO A		SCENARIO B		SCENARIO C	
	LOGLP	EGNS	LOGLP	EGNS	LOGLP	EGNS
3	0.1048	1505.34	0.1048	1504.28	0.1048	1505.21
6	0.1258	1917.94	0.1258	1918.95	0.1258	1918.21
7	0.1597	2182.41	0.1597	2182.31	0.1597	2182.56
10	0.1134	4975.84	0.1134	4975.24	0.1134	4976.11
12	0.0373	794.20	0.0373	794.15	0.0373	794.40
15	0.0587	947.32	0.0587	947.21	0.0587	947.23
16	0.1708	3707.44	0.1708	3707.23	0.1708	3707.42
19	0.0539	558.24	0.0539	559.11	0.0539	558.21

20	0.1286	1568.32	0.1286	1567.21	0.1286	1568.29
----	--------	---------	--------	---------	--------	---------

Table 2.5 Risk indices in power systems for case 1

Electric node	SCENARIO A		SCENARIO B		SCENARIO C	
	LOELP	EENS	LOELP	EENS	LOELP	EENS
2	0.0000	0.11	0.0000	0.78	0.0006	13.41
4	0.0101	250.52	0.0272	837.70	0.0951	3010.05
6	0.0001	1.82	0.0005	8.55	0.0039	78.39
8	0.0030	95.73	0.0139	318.77	0.0323	865.80
10	0.0101	264.85	0.0273	761.59	0.0833	2603.17
12	0.0060	203.63	0.0263	781.29	0.0833	2761.29
14	0.0048	107.05	0.0223	362.84	0.0540	1410.77
16	0.0000	0.00	0.0000	0.00	0.0000	0.09
18	0.0000	0.09	0.0000	0.54	0.0005	8.66
20	0.0101	204.78	0.0281	602.45	0.0833	1837.46
22	0.0001	1.48	0.0004	6.55	0.0030	57.11
24	0.0095	140.75	0.0225	439.78	0.0609	1570.04
26	0.0091	185.74	0.0192	486.50	0.0612	1451.22
28	0.0031	68.35	0.0138	210.00	0.0251	579.39
30	0.0000	0.00	0.0000	0.00	0.0000	0.08

Regarding the power system, it can be seen from Table 2.5 that the *EENS* at most nodes increase sharply with the increase of coupling degree. For example, the value of *EENS* at node 12 is only 203.63 MWh/yr for scenario A and increases to 2761.29 MWh/yr for scenario C. Likewise, there exist some nodes whose *EENS* values are close to zero for all scenarios. This is mainly because these nodes with low loads are relatively close to generators. The power is easier to be transported from generators to consumers in contingency states, considering the operating constraints of the power system. Moreover, the variation trend of *LOELP* at each node is in accordance with that of *EENS*. The *LOELP* at node 12 are relatively large, which are 0.0060, 0.0263, and 0.0833 for scenarios A, B, and C, respectively.

Based on the results in Table 2.4 and Table 2.5, we can draw the conclusion that the increase of coupling degree has no impact on the risk of NGS, while can significantly reduce the risk of the power system. Compared to the GPPs which are assumed to obtain sufficient gas in the conventional power system, the output of GPPs in IEGS is determined by both the gas supplied to them and their own reliabilities. In this circumstance, the random failures in NGS will reduce the power output of GPPs connected to it, and further reduce the generating capacity in the power system. That is to say, the total available capacity P_{mg}^{\max} in (2.33) will decrease, leading to the reduction of the feasible region of the OPF model. Besides, with the improvement of the coupling degree, more GPPs in the power system will be affected by the risk of NGS and the feasible region of the OPF model will be

reduced furtherly. Therefore, the impacts of failures in NGS on the power system will certainly increase with the improvement of the coupling degree.

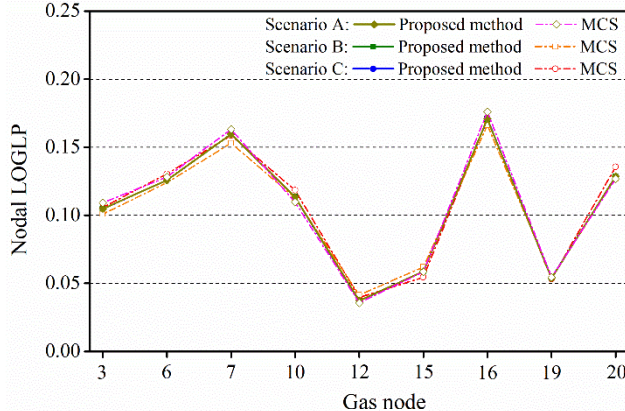


Fig. 2.5 Comparisons of nodal *LOGLP* in NGS for different methods

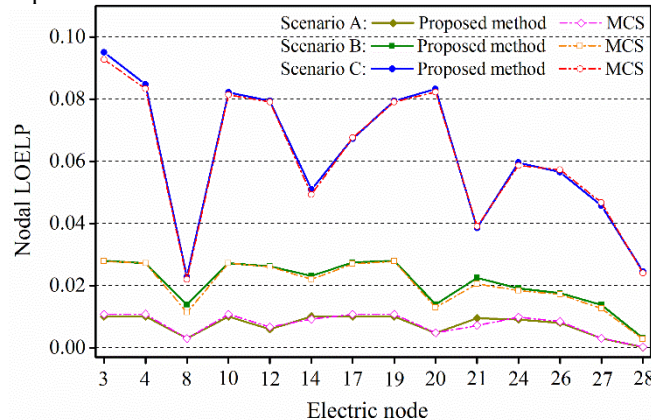


Fig. 2.6 Comparisons of nodal *LOELP* in power system for different methods

For validating the accuracy of the proposed method, the Monte Carlo simulation (MCS) approach is also developed to compare the results obtained by the proposed method. The convergence error is set to be 0.05. The computer programs for the proposed method and MCS were implemented on a PC with a 1.6 GHz processor.

The comparisons of results between the proposed method and MCS for different scenarios are given in Fig. 2.5 and Fig. 2.6. It is illustrated that the results of the proposed method are close to those of the MCS technique. The average percentage error of the proposed method and MCS is 4.82%, which is relatively low.

The computation times of the proposed method and MCS for different scenarios are illustrated and compared in Table 2.6. The average computation time of MCS is 7.67 times that of the proposed approach for obtaining the results. Besides, the

computation time of Scenario A is shorter than that of Scenario B and C since the coupling between NGS and the power system is not considered in Scenario A.

Table 2.6 Comparison of computation time for different methods

Computation time(s)	SCENARIO A	SCENARIO B	SCENARIO C
Proposed method	336.4	641.5	654.3
MCS	3163.5	4640.6	4717.6

Case 2: The impacts of gas storage capacity levels C_{st} on the risk of IEGS are evaluated in this case. As defined in (2.6), C_{st} refers to the capacity levels of gas storage compared to gas loads. In this case, four scenarios are analyzed, including 0, 10%, 20%, and 40% capacity levels. In common with scenario C in case 1, the NGS and power system are connected through connections C1, C2, and C3. The risk indices $EGNS$ ($10^3 \text{ m}^3/\text{yr}$) in NGS and $EENS$ (MWh/yr) in the power system are shown in Fig. 2.7 and Fig. 2.8, respectively.

Fig. 2.7 shows the nodal $EGNS$ in NGS for different storage capacity levels C_{st} . When C_{st} is 0, the values of nodal $EGNS$ are large, which are $2.1826 \times 10^6 \text{ m}^3/\text{yr}$, $4.7961 \times 10^6 \text{ m}^3/\text{yr}$, and $3.7074 \times 10^6 \text{ m}^3/\text{yr}$ at gas nodes 7, 10, and 16, respectively. With the increase of C_{st} , the $EGNS$ at each gas node all decrease sharply. When C_{st} changes from 0 to 20%, the $EGNS$ at gas node 10 decreases from $4.7961 \times 10^6 \text{ m}^3/\text{yr}$ to $1.8392 \times 10^6 \text{ m}^3/\text{yr}$. For the 40% scenario, the values of $EGNS$ are relatively small, which are only $1.3723 \times 10^5 \text{ m}^3/\text{yr}$, $1.7159 \times 10^5 \text{ m}^3/\text{yr}$, and $4.6141 \times 10^5 \text{ m}^3/\text{yr}$ at gas nodes 7, 10, and 16, respectively.

For the power system, the nodal $EENS$ for different storage capacity levels C_{st} are shown in Fig. 2.8. Firstly, in accordance with nodal $EGNS$ in NGS, the nodal $EENS$ in the power system also decreases sharply with the increase of C_{st} . When C_{st} changes from 0 to 20%, the values of $EENS$ at nodes 4, 10, and 12 all decrease from about 2800 MWh/yr to 1500 MWh/yr. Moreover, there are also large differences between $EENS$ at different electric nodes. With regard to the nodes with low loads, such as nodes 6, 16, and 18, the nodal $EENS$ for each scenario are all close to zero. Regarding the nodes with high loads, such as nodes 4, 10, and 12, the nodal $EENS$ are relatively large, especially when C_{st} is 0.

From the simulation results in Fig. 2.7 and Fig. 2.8, we can draw the conclusion that the increase in gas storage capacity levels could significantly improve the risk of IEGS. As significant gas reserves, the gas storages could ensure the uninterrupted gas supply to gas consumers during contingencies. Besides, GPPs can obtain sufficient fuels from NGS instead of reducing their power output in contingency states. Therefore, introducing gas storages to reduce the impacts of failures in NGS on the risk of the power system can be an effective approach.

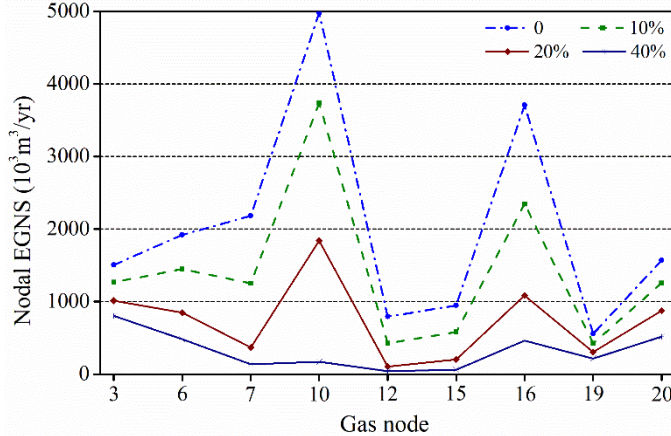


Fig. 2.7 Nodal EGNS for different C_{st} in gas system.

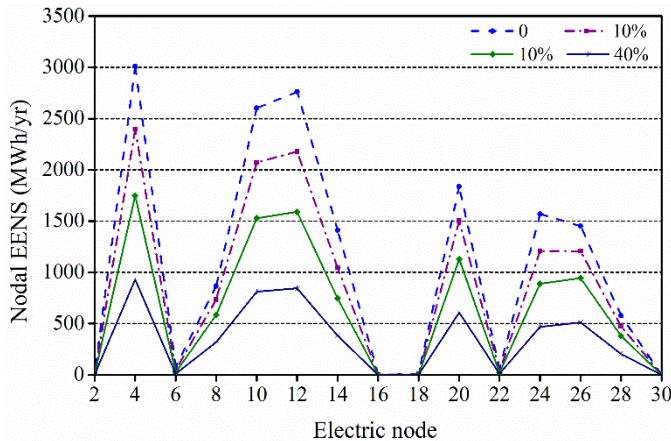


Fig. 2.8 Nodal EENS for different C_{st} in power system.

Case 3: In order to compare the computation time and results of UGF and MCS methods on a larger test system, three scenarios with different dimensions are considered in this case. The power systems used in scenarios A, B, and C are the modified IEEE 57-bus [23], IEEE 118-bus [24], and IEEE 300-bus systems [25], respectively. It is assumed that three GPPs at electric nodes 1, 8, and 12 in scenario A, at electric nodes 4, 54, and 100 in scenario B, and at electric nodes 19, 156, and 222 in scenario C are supplied from the gas flow at gas nodes 10, 16 and 7 of NGS, respectively. The NGS in these three scenarios is the same as that in the previous cases. The risk parameters of CFGs and GPPs can be found in [29]. Moreover, the convergence error of the MCS method is set to be 0.05. The computer programs for UGF and MCS methods were implemented on a PC with a 1.6 GHz processor.

The comparisons of *EENS* between UGF and MCS methods for different scenarios are given in Table 2.7 and Table 2.8. It is illustrated that the results of the UGF method are close to those of the MCS technique. The average percentage errors of the UGF and MCS methods are relatively small, which are 3.3%, 0.9%, and 0.8% for scenarios A, B, and C, respectively. This is an acceptable difference as we know that the results of MCS are only estimates that lie within upper and lower bounds with a given probability.

Table 2.7 Comparisons of *EENS* for different methods in scenarios A and B

SCENARIO A (57-BUS SYSTEM)			SCENARIO B (118-BUS SYSTEM)		
Node	UGF	MCS	Node	UGF	MCS
1	3527.31	3640.75	4	1380.89	1325.81
5	726.37	740.35	12	0.00	0.00
8	68.17	118.16	20	0.00	0.00
12	86.46	126.71	28	0.00	0.00
16	2614.36	2686.42	39	232.09	203.47
21	0.00	0.00	47	0.00	0.00
25	395.84	403.06	51	771..37	688.24
29	937.86	958.20	57	23.50	27.67
32	126.93	129.99	62	0.00	0.00
35	7.66	10.10	67	753.76	818.07
39	0.00	0.00	76	1469.92	1443.94
43	154.38	158.06	86	1697.18	1792.46
47	17.11	26.12	97	2180.94	2191.16
51	13.23	19.20	103	205.39	204.01
55	420.39	427.96	112	1279.10	1253.73

Table 2.8 Comparisons of *EENS* for different methods in scenarios C

SCENARIO A (57-BUS SYSTEM)			SCENARIO B (118-BUS SYSTEM)		
Node	UGF	MCS	Node	UGF	MCS
1	2940.51	2933.29	140	0.00	0.00
20	0.00	0.00	160	0.00	0.00
40	0.00	0.00	181	2086.12	2083.72
60	2482.59	2478.23	200	0.00	0.00
80	0.00	0.00	240	2363.39	2359.68
100	0.00	0.00	260	0.00	0.00
121	2473.94	2469.62	300	245.62	247.28

The computation times of UGF and MCS methods for different scenarios are compared in Table 2.9. It can be noted that the computation time of the UGF method for obtaining the results increases more obviously than the MCS technique with the increase of system size. The computation time of the UGF method is 0.82 times, 1.19 times, and 1.90 times that of the MCS technique for scenarios A, B, and C, respectively. With the increase in system size, the number of system states

increases exponentially and the computation time of the UGF method can be longer [8]. With regard to the MCS technique, the required number of samples for a given convergence error is independent of the size of the system [26]. Therefore, the MCS technique is suitable for a large-scale system whereas the UGF method is more suitable for a relatively smaller system.

Despite the relatively lower computation efficiency in large-scale systems, the UGF method is still an effective tool for risk analysis [6, 8]. Firstly, the UGF method could represent multi-state systems in an analytical way and therefore the risk indices could be evaluated using mathematical solutions [8]. Therefore, the UGF method could give the same numerical results for each calculation, whereas the results obtained by the MCS technique are dependent on the number of simulations [8, 26]. Another major advantage of the UGF method is that it could clearly represent the performance distribution of a system with a complex structure. Based on the UGF method, we can easily obtain the performance distribution of the entire system based on the given performance distributions of its elements using algebraic procedures [8]. Therefore the UGF method can provide an effective tool for analyzing the risk of IEGS.

Table 2.9 Comparison of computation time for different methods

Computation time(s)	SCENARIO A	SCENARIO B	SCENARIO C
UGF	4762.73	13609.9	39557.2
MCS	5742.41	11423.3	20840.9

2.7 Conclusions

The integration of NGS and power system requires evaluation of reliabilities of the power system and NGS simultaneously. This chapter proposes a general framework for the risk evaluation of IEGS considering the tight coupling between NGS and the power system. The multi-state model of NGS is developed utilizing the UGF method considering the stochastic performances of individual components in NGS. The GTP operator is developed to obtain the power output models of GPPs based on the multi-state model of gas injection at each node. Using this multi-state model, the impacts of NGS are incorporated into the risk evaluation of the power system. Moreover, the customers' nodal reliabilities for both the NGS and the power system in three cases are evaluated.

The results show that the improvement of the coupling degree will increase the impacts of failures in NGS on the power system. It is an effective method to introduce gas storage to increase the risk of IEGS. Besides the UGF method, there are several other well-established methods that can be developed to evaluate the risk of IEGS. In this chapter, we also utilized the MCS technique to evaluate the risk of large-scale IEGS. Other methods can also be discussed for future studies in this new research area.

References

- [1] R. Billinton, and N. R. Allan, *Reliability evaluation of power systems*, 2nd ed. New York, NY, USA: Plenum, 1996.
- [2] C. Singh, and R. Billinton, *System reliability, modelling and evaluation*, London: Hutchinson 1977.
- [3] Y. Liu, and C. Singh, "Nodal reliability evaluation of impact of hurricanes on transmission and distribution systems," in Joint International Conference on Power Electronics, Drives and Energy Systems, New Delhi, India, 2010, pp. 1-6.
- [4] P. Wang, Y. Ding, and Y. Xiao, "Technique to evaluate nodal reliability indices and nodal prices of restructured power systems," *IEE Proceedings-Generation, Transmission and Distribution*, vol. 152, no. 3, pp. 390-396, 2005.
- [5] Y. Ding, and P. Wang, "Reliability and price risk assessment of a restructured power system with hybrid market structure," *IEEE Transactions on power systems*, vol. 21, no. 1, pp. 108-116, 2006.
- [6] A. Lisnianski, and G. Levitin, *Multi-state system reliability: assessment, optimization and applications*: World Scientific Publishing Company, 2003.
- [7] B. Gnedenko, and I. Ushakov, *Probabilistic reliability engineering*: John Wiley & Sons, 1995.
- [8] G. Levitin, "Universal generating function and its applications," *Springer, Berlin, Germany*, vol. 159, no. 3, pp. 307-324, 2005.
- [9] Y. Ding, P. Wang, L. Goel *et al.*, "Long-term reserve expansion of power systems with high wind power penetration using universal generating function methods," *IEEE Transactions on Power Systems*, vol. 26, no. 2, pp. 766-774, 2011.
- [10] Y. Ding, C. Singh, L. Goel *et al.*, "Short-Term and Medium-Term Reliability Evaluation for Power Systems With High Penetration of Wind Power," *IEEE Transactions on Sustainable Energy*, vol. 5, no. 3, pp. 896-906, Jul, 2014.
- [11] Y.-F. Li, and E. Zio, "A multi-state model for the reliability assessment of a distributed generation system via universal generating function," *Reliability Engineering & System Safety*, vol. 106, pp. 28-36, 2012.
- [12] M. Bao, Y. Ding, C. Singh *et al.*, "A Multi-State Model for Reliability Assessment of Integrated Gas and Power Systems Utilizing Universal Generating Function Techniques," *IEEE Transactions on Smart Grid*, pp. 1-1, 2019.
- [13] "Horizontal Drilling. [online]," <http://loga.la/louisiana-shale-plays/shale-drilling/>.
- [14] A. Martinez-Mares, and C. R. Fuerte-Esquivel, "A unified gas and power flow analysis in natural gas and electricity coupled networks," *IEEE Transactions on Power Systems*, vol. 27, no. 4, pp. 2156-2166, 2012.

- [15] H. Jia, Y. Ding, Y. Song *et al.*, "Operating Reliability Evaluation of Power Systems Considering Flexible Reserve Provider in Demand Side," *IEEE Transactions on Smart Grid*, 2018.
- [16] C. Shao, Y. Ding, J. Wang *et al.*, "Modeling and integration of flexible demand in heat and electricity integrated energy system," *IEEE Transactions on Sustainable Energy*, vol. 9, no. 1, pp. 361-370, 2018.
- [17] D. De Wolf, and Y. Smeers, "The gas transmission problem solved by an extension of the simplex algorithm," *Management Science*, vol. 46, no. 11, pp. 1454-1465, 2000.
- [18] S. An, Q. Li, and T. W. Gedra, "Natural gas and electricity optimal power flow." pp. 138-1432003.
- [19] P. M. Subcommittee, "IEEE Reliability Test System," *IEEE Transactions on Power Apparatus and Systems*, vol. PAS-98, no. 6, pp. 2047-2054, 1979.
- [20] A. P. Sanghvi, "Measurement and application of customer interruption costs/value of service for cost-benefit reliability evaluation: some commonly raised issues," *IEEE Transactions on Power Systems*, vol. 5, no. 4, pp. 1333-1344, 1990.
- [21] H. P. Barringer, and M. Kotlyar, "Reliability of critical turbo/compressor equipment," in Proceedings of fifth international conference on process plant reliability, Houston, Texas, 1996.
- [22] P. E. Folga Steve, et al, *US natural gas storage risk-based ranking methodology and results*, Argonne National Lab (ANL), Argonne, IL (United States), 2016.
- [23] M. A. Mostafa, M. El-Hawary, G. Mbamalu *et al.*, "A computational comparison of steady state load shedding approaches in electric power systems," *IEEE Transactions on Power Systems*, vol. 12, no. 1, pp. 30-37, 1997.
- [24] Y. Lin, Y. Ding, Y. Song *et al.*, "A Multi-State Model for Exploiting the Reserve Capability of Wind Power," *IEEE Transactions on Power Systems*, vol. 33, no. 3, pp. 3358-3372, 2018.
- [25] S. Chakrabarti, E. Kyriakides, G. Ledwich *et al.*, "Inclusion of PMU current phasor measurements in a power system state estimator," *IET generation, transmission & distribution*, vol. 4, no. 10, pp. 1104-1115, 2010.
- [26] R. Billinton, and R. Karki, "Application of Monte Carlo simulation to generating system well-being analysis," *IEEE Transactions on Power systems*, vol. 14, no. 3, pp. 1172-1177, 1999.

3 Short-Term Risk Evaluation of Integrated Electricity and Gas Systems Considering Dynamics of Gas Flow

3.1 Introduction

The studies in Chapter 2 focus on the long-term (time-independent) risk evaluation of integrated electricity and gas systems (IEGS), where the steady gas flow model is utilized. However, the previous techniques can be not fully applicable for evaluating the short-term risk of IEGS on the operational horizon [1]. Short-term risk is formulated on the time-scale of hours to days, during which the dynamics of gas flow are significantly slower than those of electricity flow. When the gas well fails, the downstream gas-fired units (GFUs) may still be able to generate electricity for a relatively short period by utilizing the gas stored in the pipelines [2]. It can serve as an effective buffer to mitigate the consequences of gas well failures. Consequently, using the steady-state gas flow model will lead to inaccuracies in the short-term risk evaluation.

The dynamics of gas flow were modeled in the traditional natural gas transmission system design and simulation [3, 4]. However, it is not easy to embed it into the electricity system operation. The gas flow dynamics are governed by a set of partial derivative equations. It is difficult to obtain analytical solutions for a set of generally connected gas pipelines. Finite-difference schemes were usually adopted to discretize the partial derivative equations into numerical equations [5]. Recently, the gas flow dynamics have been considered in the unit commitment [6] and economic dispatch [7] in the IEGS under wind uncertainties. The gas flow dynamics were also used in [8] to characterize the interdependency between the electricity and gas systems. However, its effect on the short-term risk of IEGS has not been quantitatively explored yet.

To fill the aforementioned research gaps, this chapter contributes in the following aspects:

- 1) A novel short-term risk evaluation framework for IEGS is proposed. Compared with traditional steady-state based risk evaluation techniques, the proposed technique is more practical in the operational phase by incorporating the gas flow dynamics.
- 2) Multi-state short-term risk models for IEGS components are developed, which are capable of characterizing the time-varying state probabilities. Especially for GFUs, both the inherent failure and constraints from gas flow are considered.
- 3) A multi-stage contingency management scheme is proposed to determine the time-varying load curtailments, considering the interdependency between the electricity and gas systems. Both the optimal dispatch strategy and transient-state analysis (TSA) of gas flow are incorporated.
- 4) For evaluating the short-term risk indices with partial derivative equations, a time-sequential Monte Carlo simulation (TSMCS) technique is developed by em-

bedding the finite-difference scheme into its inner loop. Several practical techniques are also developed to reduce computation time.

This chapter includes research related to short-term risk analysis of IEGS considering the dynamic features of gas flows by [9].

3.2 Short-Term Risk Models of IEGS Components Considering Gas Flow Dynamics

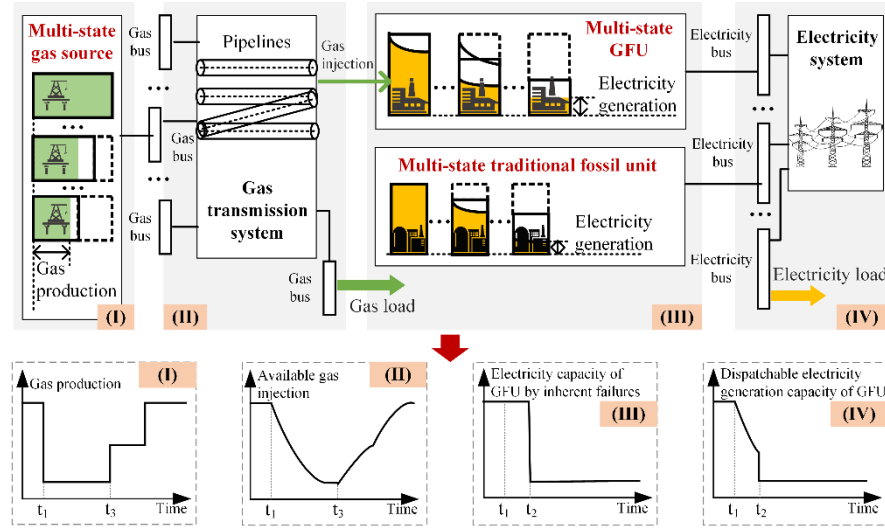


Fig. 3.1 Multi-state short-term risk model of IEGS considering the gas flow dynamics

As illustrated in Fig. 3.1, in the natural gas transmission system, the gas pipelines are responsible for transporting the gas from distant gas sources, e.g. gas wells and storages, to the demands at different gas buses (GB). One of the gas demands is the non-power gas load from residential and industrial users, etc. The other type is the gas consumption from GFUs, through which the electricity system is interconnected with the gas system.

The short-term risk of gas sources, GFUs, and traditional fossil units are represented using multi-state models. The gas source at a bus usually consists of several gas wells using directional and horizontal drilling technology [10]. The GFU is also a complex system comprising many parts, and the failures of these parts may lead to a situation in which the GFU operates in a derated state [11]. Therefore, compared with the traditional binary-state model, multi-state representations are more flexible and accurate for those components in risk evaluations [12]. The effects of gas flow dynamics on the multi-state models are presented in Fig. 3.1. During IEGS operation, the random failures or deratings of gas sources could reduce their gas production capacities. Due to the gas flow dynamics in the transmission, such failures do not reduce the available gas injection to the downstream

GFUs immediately. Incorporating the inherent failures of the GFU, it determines the dispatchable electricity generation capacity of the GFU in real-time. Therefore, comprehensive short-term risk models should be developed to accurately characterize such unique and time-related behavior of those IEGS components.

3.2.1 Short-term risk model of the gas source

Firstly, the multi-state short-term risk model is developed to model the random failures and repairs of multiple gas wells and storages at a GB.

Generally, the risk model of gas well or storage g at bus i uses binary-state representations $W_{i,g}^h$, where $h = 1$ for perfect functioning state and $h = 2$ for complete failure state, respectively [13]. During the operation, the gas well capacity $W_{i,g}(t)$ evolution in its state space produces the stochastic capacity process $W_{i,g}(t) \in \{W_{i,g}^1, W_{i,g}^2\}$ by random failures and repairs. Let $pr_{i,g}^h(t)$ be the probabilities of gas well g at bus i at state h :

$$pr_{i,g}^h(t) = \Pr\{W_{i,g}(t)=W_{i,g}^h\}, h=1,2, t \geq 0 \quad (3.1)$$

The state transition of the gas well is represented as a Markov process [12]. Normally all the components are assumed to be perfect functioning after commitment at the beginning of the simulation period ($W_{i,g}(t)|_{t=0} = W_{i,g}^1$). Then, $pr_{i,g}^h(t)$ can be obtained as [1]:

$$\begin{cases} pr_{i,g}^1(t) = \mu_{i,g} / (\lambda_{i,g} + \mu_{i,g}) + \lambda_{i,g} / (\lambda_{i,g} + \mu_{i,g}) e^{-(\lambda_{i,g} + \mu_{i,g})t} \\ pr_{i,g}^2(t) = \lambda_{i,g} / (\lambda_{i,g} + \mu_{i,g})(1 - e^{-(\lambda_{i,g} + \mu_{i,g})t}) \end{cases} \quad (3.2)$$

where $\lambda_{i,g}$ and $\mu_{i,g}$ denote the failure and repair rates of gas well g at bus i , respectively.

The state of the gas source is determined by the state combination of corresponding gas wells, and therefore its risk can be represented using a multi-state model. The total gas production capacity takes random values from $W_i(t) \in \{W_i^1, \dots, W_i^h, \dots, W_i^{NH}\}$, the value of which in state h can be calculated by:

$$W_i^h = \sum_{g \in NG_i} W_{i,g}^1 \quad (3.3)$$

where NG_i is the set of gas wells or storages in the perfect functioning state at bus i .

3.2.2 Gas flow dynamics in the pipeline

The changes in gas flow after gas source failures are evaluated using the TSA in this chapter. Under the assumption of isothermal gas flow and a constant compression factor in a horizontal pipeline, the following partial derivative equations are typically used to describe the continuity and motion of the gas flow in a pipeline [14]:

$$\frac{4\omega^2}{\pi\varepsilon D^2} \frac{\partial q}{\partial x} + \frac{\partial p}{\partial t} = 0 \quad (3.4)$$

$$\frac{\partial p^2}{\partial x} + \frac{8\varepsilon p}{\pi D^2} \frac{\partial q}{\partial t} + \frac{64\varepsilon^2 \omega^2 q |q|}{\pi^2 F^2 D^5} = 0 \quad (3.5)$$

where p and q are the gas pressure and gas flow, respectively. ω is the isothermal wave speed of gas. ε is the gas density at the standard temperature and pressure, D is the diameter of the pipeline, and F is the *Fanning* transmission factor.

3.2.3 Short-term risk models of the GFU and traditional fossil unit

The dispatchable electricity generating capacities of the GFU and traditional fossil units are both related to their inherent failures and repairs. For GFU, particularly, the capacity further relies on the gas supply from the gas transmission pipelines.

The inherent failure and repair process of GFU or traditional fossil unit is modeled as the Markov process. Considering GFU l at bus i with $NH_{i,l}$ states. The electricity generating capacity for each state h ($h=1, 2, \dots, NH_{i,l}$) is $E_{i,l}^h$. The probability of the GFU being in the state h , $pr_{i,l}^h(t)$, can be obtained by solving the following differential equation set [1]:

$$\left\{ \begin{array}{l} \frac{dpr_{i,l}^h(t)}{dt} = -pr_{i,l}^h(t) \sum_{h'=1}^{NH_{i,l}, h' \neq h} \lambda_{h,h'} + \sum_{h'=1}^{NH_{i,l}, h' \neq h} pr_{i,l}^{h'}(t) \lambda_{h',h}, \\ h = 1, 2, \dots, NH_{i,l} \\ pr_{i,l}^1 \Big|_{t=0} = 1, pr_{i,l}^2 \Big|_{t=0} = \dots = pr_{i,l}^{NH_{i,l}} \Big|_{t=0} = 0 \end{array} \right. \quad (3.6)$$

where $\lambda_{h,h'}$ is the state transition rate of the GFU from state h to h' . The state probability of traditional fossil units can also be calculated correspondingly.

As mentioned, the dispatchable electricity generating capacity of GFU is further limited by the sufficiency of gas at the exact time and location. If the GFU capacity determined by the inherent failure is $E_{i,l}^h$, and the maximum available gas injection determined by TSA is $\bar{gi}_{i,l}(t)$, then the real-time dispatchable electricity generating capacity of GFU $E_{i,l}^{RT}(t)$ can be calculated as [15]:

$$E_{i,l}^{RT}(t) = \min \left\{ \begin{array}{l} E_{i,l}^h \\ (-\beta_{i,l} + (\beta_{i,l}^2 - 4\alpha_{i,l}) \\ ((\gamma_{i,l} - H_g \bar{gi}_{i,l}(t)))^{1/2}) / 2\alpha_{i,l} \end{array} \right\} \quad (3.7)$$

where $\alpha_{i,l}$, $\beta_{i,l}$, and $\gamma_{i,l}$ are the coefficients of heat rate for GFU l at bus i , respectively. H_g is the high heat value of natural gas.

3.3 Multi-stage Risk Management Scheme for IEGS Considering Gas Flow Dynamics

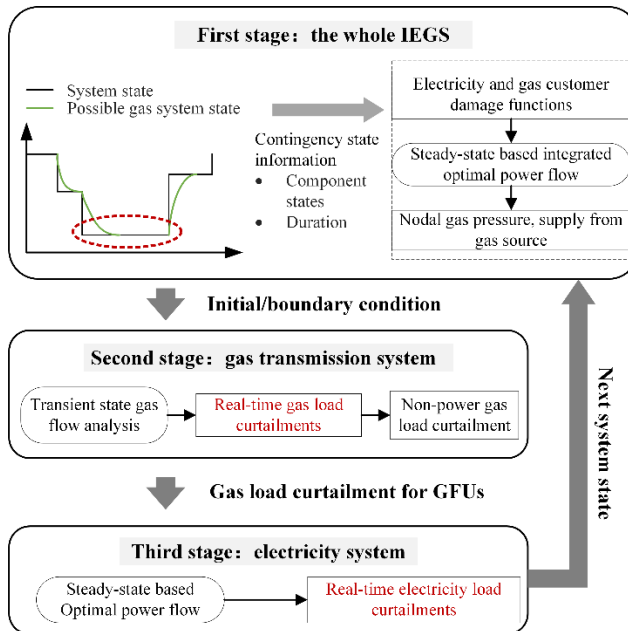


Fig. 3.2 Multi-stage risk management scheme

During IEGS operation, failures or deratings of gas sources, GFUs, and traditional fossil units can reduce the electricity and gas capacities suddenly, and thus transfer the IEGS from the normal operating state to a contingency state. In this circumstance, gas production and electricity generation should be re-dispatched. The electricity or gas loads would be curtailed, even in the worst case, to maintain a balanced operation and manage the system risks.

Due to the slower dynamics of gas flow, the steady-state based optimal power flow that is commonly adopted in the traditional electricity systems, is no longer suitable for evaluating the load curtailment in IEGS directly. Therefore, a multi-stage contingency management scheme is proposed.

3.3.1 Framework of the multi-stage risk management

As outlined in Fig. 3.2, the multi-stage contingency management scheme is developed. The IEGS initially operates in the normal state at the beginning. When failures or derations of gas sources, GFUs, or traditional fossil units occur, the IEGS may be transferred into a contingency state. The contingency management

scheme begins with receiving the contingency state information, e.g., the failed generating units. The desired operating condition in the first stage is evaluated using a steady-state based integrated electricity and gas optimal power flow. Though the load curtailments are not finalized in this stage, it sets the boundary conditions for the TSA in the next stage, i.e., the nodal gas pressure or the quantity of gas supply. In the second stage, the TSA is conducted to determine the real-time operating condition of the gas system, e.g., the real-time gas load curtailment (GLC) and the available gas injection for GFUs. The latter factor is to further impose constraints on the GFU ramping, for evaluating the real-time electricity generation and electricity load curtailment (ELC) in the third stage.

3.3.2 First stage: re-dispatch in the contingency state using integrated electricity-gas optimal power flow

In the first stage, the integrated electricity-gas optimal power flow is conducted for determining the re-dispatch in the contingency state. Based on the total gas production capacities of gas sources, electricity generating capacities of GFUs and traditional fossil units, and other necessary network parameters of IEGS, the following variables in system state sequence k are calculated: 1) gas production of gas sources $w_{i,k}$; 2) active power of GFU l at bus i , $P_{i,l,k}$, and its reactive power $Q_{i,l,k}$; 3) active power of traditional fossil unit m at bus i , $P_{i,m,k}$, and its reactive power $Q_{i,m,k}$; 4) ELCs at bus i , $ec_{i,k}$; 5) GLCs at bus i , $gc_{i,k}$. The objective of the first stage is to minimize the total operating cost TC_k . It includes the gas purchasing cost, the generation cost of traditional fossil units, and the interruption costs of ELCs and GLCs.

$$\begin{aligned} \text{Min } TC_k = & \sum_{i \in GB} \left(\rho_i w_{i,k} + gc_{i,k} CDF_i^g(T_k) \right) \\ & + \sum_{i \in EB} \left(ec_{i,k} CDF_i^e(T_k) + \sum_{m \in NM_i} cst_{i,m}(P_{i,m,k}) \right) \end{aligned} \quad (3.8)$$

Subject to the following constraints:

a) Electricity generation output limits on GFUs and traditional fossil units:

$$\underline{W}_i \leq w_{i,k} \leq \overline{W}_{i,k} \quad (3.9)$$

$$\underline{P}_{i,l} \leq P_{i,l,k} \leq \overline{E}_{i,l,k} \quad (3.10)$$

$$\underline{Q}_{i,l} E_{i,l,k} / E_{i,l}^1 \leq Q_{i,l,k} \leq \overline{Q}_{i,l} E_{i,l,k} / E_{i,l}^1 \quad (3.11)$$

$$\underline{P}_{i,m} \leq P_{i,m,k} \leq \overline{E}_{i,m,k} \quad (3.12)$$

$$\underline{Q}_{i,m} E_{i,m,k} / E_{i,m}^1 \leq Q_{i,m,k} \leq \overline{Q}_{i,m} E_{i,m,k} / E_{i,m}^1 \quad (3.13)$$

b) Electricity/gas load curtailment constraints:

$$[0 \quad 0] \leq [ec_{i,k} \quad gc_{i,k}] \leq [\overline{ec}_i \quad \overline{gc}_i] \quad (3.14)$$

c) AC power flow constraints:

$$\sum_{l \in NL_i} (P_{i,l,k} + jQ_{i,l,k}) + \sum_{m \in NM_i} (P_{i,m,k} + jQ_{i,m,k}) - P_i - jQ_i + ec_{i,k} - \sum_{j \in \Psi_i^e} f_{ij,k} = 0 \quad (3.15)$$

$$f_{ij,k} = V_{i,k} V_{j,k} ((G_{ij} \cos \theta_{ij,k} + B_{ij} \sin \theta_{ij,k}) + j(G_{ij} \sin \theta_{ij,k} - B_{ij} \cos \theta_{ij,k})) \quad (3.16)$$

d) Steady-state gas flow constraints:

$$w_{i,k} - GL_i - \sum_{l \in NL_i} gi_{i,l,k} + gc_{i,k} - \sum_{j \in \Psi_i^g} q_{ij,k} = 0 \quad (3.17)$$

$$q_{ij,k} = C_{ij} \operatorname{sgn}(p_{i,k} - p_{j,k}) \sqrt{|p_{i,k}^2 - p_{j,k}^2|} \quad (3.18)$$

e) Electricity power flow and gas flow limits:

$$[|f_{ij,k}| \quad |q_{ij,k}|] \leq [\overline{f}_{ij} \quad \overline{q}_{ij}] \quad (3.19)$$

where EB , GB , NM_i , and NL_i are the sets of electricity bus (EB), GB, traditional fossil unit, and GFU at bus i , respectively. T_k is the duration of system state sequence k . ρ_i is the gas price at bus i . CDF_i^e and CDF_i^g are the electricity and gas customer damage function [16]. $cst_{i,m}$ is the generation cost function for traditional fossil units. $E_{i,m,k}$ is the electricity generating capacity of traditional fossil unit at system state k . $E_{i,m}^1$ is the electricity generating capacity of traditional fossil unit at perfect functioning state. $f_{ij,k}$ and $q_{ij,k}$ are the electricity and gas flows from bus i to j . P_i and Q_i are the active and reactive power of electricity load. $gi_{i,l,k}$ is the gas consumption of GFU. $V_{i,k}$ and $\theta_{ij,k}$ are the amplitude and phase angle. G_{ij} and B_{ij} are the conductivity and susceptance of the electricity branch. Ψ_i^e and Ψ_i^g are the sets of electricity branches and gas pipelines connected to bus i . $p_{i,k}$ is the nodal natural gas pressure at bus i . C_{ij} is a characteristic parameter of the pipeline, depending on the length, absolute rugosity, and some other properties. $\operatorname{sgn}(x)$ is the signum function, where $\operatorname{sgn}(x)=1$ if $x \geq 0$, and $\operatorname{sgn}(x)=-1$ if $x < 0$.

3.3.3 Second stage: operating condition of the gas system using TSA

The results from the first stage have defined the desired operating condition of IEGS, and meanwhile set the initial and boundary conditions for the second stage.

The two partial derivative equations (3.4) and (3.5) are formulated for each pipeline. Four values are required to characterize the state of a pipeline: the gas pressures and gas flow quantities at the beginning and end of the pipeline, respectively. Two of these four values should be specified as the boundary conditions. They can be either set as a given value, or specified implicitly in the equations associated with adjacent pipelines.

According to the types of expected boundary conditions, GBs can be divided into three categories: gas load bus, gas source bus, and other conjunction GB. For all the GBs, the gas pressures at the connecting point of pipelines are equal, as in

(3.20). For gas load buses, the gas pressures are specified as the values from the first stage, as in (3.21). For gas source buses and other conjunction GBs, Kirchhoff law holds, as in (3.22), where $w_{i,k}$ is set according to the results from the first stage.

$$\begin{aligned} p_{ij} \Big|_{x=0} &= p_{ij_1} \Big|_{x=0} (\forall j_1 \in \Psi_i^g) \\ p_{ij} \Big|_{x=0} &= p_{j_2 i} \Big|_{x=L_{ij}} (\forall j_2 \in \Psi_i^g) \end{aligned} \quad (3.20)$$

$$p_{ij} \Big|_{x=0} = p_{i,k}, p_{ij} \Big|_{x=L_{ij}} = p_{j,k} \quad (3.21)$$

$$w_{i,k} + \sum_{j \in \Psi_i^g} q_{ji} \Big|_{x=L_{ji}} - \sum_{j \in \Psi_i^g} q_{ij} \Big|_{x=0} = 0 \quad (3.22)$$

where L_{ij} is the length of the pipeline from bus i to j .

At the beginning of the study period, the initial condition is set according to the results from the first stage when all the IEGS components are in the perfect functioning state. As the simulation proceeds, the initial condition in system state sequence k is set as the operating condition at the end of system state sequence $k-1$:

$$p_{ij,k}(x, t) \Big|_{t=0} = p_{ij,k-1}(x, t) \Big|_{t=T_{k-1}} \quad (3.23)$$

$$q_{ij,k}(x, t) \Big|_{t=0} = q_{ij,k-1}(x, t) \Big|_{t=T_{k-1}} \quad (3.24)$$

After solving the partial derivative equations, the real-time pressures and quantities of gas flow can be obtained along all the pipelines. In the second stage, the gas loads are not necessarily fully satisfied, and the GFU capacities will be further constrained by the injected gas at the corresponding GB. Note that the real-time GLCs for non-power gas load $gc_i^{np}(t)$ and GFU gas requirement $gc_{i,l}^{RT}(t)$ are also time-varying. The sum of them $gc_i^{RT}(t)$ can be calculated as:

$$\begin{aligned} gc_i^{RT}(t) &= gc_i^{np}(t) + \sum_{l \in NL_i} gc_{i,l}^{RT}(t) \\ &= GL_i + \sum_{l \in NL_i} gi_{i,l,k} - w_{i,k} - \sum_{j \in \Psi_i^g} q_{ji} \Big|_{x=L_{ji}} + \sum_{j \in \Psi_i^g} q_{ij} \Big|_{x=0} \end{aligned} \quad (3.25)$$

The distribution of GLC among the non-power gas load and GFUs depends on the interruptible contracts between gas transport companies and generation utilities. In practical cases, most of the contracts entail that the GFU gas requirement is the first candidate to be curtailed, which is also the case in this chapter [2, 17]:

$$\begin{aligned} \text{If } gc_i^{RT}(t) &\leq \sum_{l \in NL_i} gi_{i,l,k} \\ gc_{i,l}^{RT}(t) &= gc_i^{RT}(t)gi_{i,l,k} / \sum_{l \in NL_i} gi_{i,l,k}, \quad gc_i^{np}(t) = 0 \end{aligned} \quad (3.26)$$

$$\text{If } gc_i^{RT}(t) > \sum_{l \in NL_i} gi_{i,l,k}$$

$$gc_{i,l}^{RT}(t) = gi_{i,l,k}, \quad gc_i^{np}(t) = gc_i^{RT}(t) - \sum_{l \in NL_i} gi_{i,l,k} \quad (3.27)$$

3.3.4 Third stage: operating condition of the electricity system using optimal power flow

The GLC of GFU in the second stage now defines the maximum available gas injection $\bar{gi}_{i,l}$ in(3.7):

$$\bar{gi}_{i,l}(t) = gi_{i,l,k} - gc_{i,l}^{RT}(t) \quad (3.28)$$

Now we can calculate the dispatchable electricity generating capacities of GFUs, $E_{i,l}^{RT}$, according to(3.7). Based on that, the electricity system is rescheduled to assess the actual ELC in the third stage. The objective is to minimize the electricity system operating cost EC , by controlling the GFU and traditional fossil unit generations, and the real-time ELCs ec_i^{RT} for each time t :

$$\text{Min } EC(t) = \sum_{i \in EB} \left(ec_i^{RT}(t) CDF_i^e(T_k) + \sum_{m \in NM_i} cst_{i,m}(P_{i,m}(t)) \right) \quad (3.29)$$

Subject to (9) – (13), (15), (16), and the following (3.30):

$$[0 \quad -\bar{f}_{ij}] \leq [ec_i^{RT}(t) \quad f_{ij}(t)] \leq [\bar{ec}_i \quad \bar{f}_{ij}] \quad (3.30)$$

3.4 Short-Term Risk Evaluation Procedures

3.4.1 Computation time reduction techniques in the TSMCS

The risk evaluation of the IEGS during the operational phase is the process of predicting the risk for the system operator and customers for a given system operating condition. The TSMCS is used to sample the chronological random failures during the operation and calculate the risk indices. In each system state simulated by the TSMCS, the optimization problem in the first stage is a nonlinear programming problem, which is solved using the interior point method [18]. The continuity and motion equations in the second stage are discretized into a set of equations using a finite-difference scheme. It is implicit along the pipeline and explicit in the time dimension [14]. The equation set is solved using the Newton–Raphson method. The gas pressure and gas flow at each time step can thus be obtained.

Nonetheless, directly embedding the finite difference scheme into the TSMCS will introduce tremendous computational burdens. Both the convergence of TSMCS requires many simulations, and each time step entails solving a large-scale equation set. To address this issue we offer the following remarks from a practical point of view:

- 1) Criteria for the completion of a transient process: With the knowledge that each transient process gradually converges to the corresponding steady-state, calculations in each system state can be avoided by setting an appropriate tolerance.

Hence, a relative bound is set as the criteria for determining the completion of the transient process:

$$\|(\mathbf{x}(t) - \mathbf{x}(t - \Delta t)) / (1 + |\mathbf{x}(t - \Delta t)|)\|_{\infty} \leq \xi_1 \quad (3.31)$$

where $\mathbf{x}(t) = [p_{i,j,s}(t), q_{i,j,s}(t), gc_i^{RT}(t)], \forall i, j, s$ is the set of IEGS state variables, and s is the index of the pipeline segment.

2) Offline contingency state database: To avoid redundant calculation of the same system state, storing the TSA results during the first calculation is critical for reducing the computation time. Suppose the operating condition of IEGS is $x_1(t)$ after the failure at t_1 . When the same failure pattern occurs for the second time at t_2 , the operating condition $x_2(t)$ can be pulled out from memories with a little modification $x_2(t)=x_1(t+t_1-t_2)$. However, note that the offline results should only be used when the change of system state happens after the completion of the transient process.

3.4.2 Risk evaluation procedures

The expected demand not supplied (EDNS) and loss of load probability (LOLP) are commonly adopted to characterize the risk of the electricity system. To cope with the short-term risk evaluation of IEGS, EDNS and LOLP are reformed as time-varying indices, and are specified for each bus, as calculated in (3.32) - (3.33). Moreover, they are extended to the gas system, i.e. the expected gas demand not supplied (EGNS), and loss of gas probability (LOGP). They can be calculated using identical equations.

$$EDNS_i(t) = \left(\sum_{n=1}^{NS} ec_i^{RT}(t) \right) / NS \quad (3.32)$$

$$LOLP_i(t) = \left(\sum_{n=1}^{NS} flag(ec_i^{RT}(t)) \right) / NS \quad (3.33)$$

where NS is the sampling times of the simulation. $flag(x)$ is defined as a function where $flag(x)=1$ if $x>0$, and $flag(x)=0$ if $x\leq 0$. The coefficient of variation of EDNS is set as the stopping criterion for the TSMCS:

$$\sqrt{Var(\sum_{i \in EB} EDNS_i(t))} / \sum_{i \in EB} EDNS_i(t) \leq \xi_2 \quad (3.34)$$

where $Var(x)$ is the variance of x .

In summary, the short-term risk evaluation procedure for IEGS is elaborated as follows:

Step 1: Calculate the operating condition of IEGS at $t=0$ with all the IEGS components in the perfect functioning state according to (3.8)-(3.19). Initialize the conditions for the transient gas flow analysis and TSMCS. Initialize the offline contingency database.

Step 2: Generate the state sequences and corresponding total gas capacities for gas sources, and electricity generating capacities for GFUs and traditional fossil units, using the TSMCS sampling technique according to (3.1)-(3.3) and.

Step 3: Set the length of pipeline sections Δx_{ij} and time step Δt for the finite-difference scheme in the TSA.

Step 4: For each system state k , determine if it is in the offline contingency database. If so, use the offline data (according to Section IV. A), and go to Step 9.

Step 5: Conduct the first stage integrated optimal power flow formulated in Section III. B. Obtain the results as the desired operating condition. Set the gas productions of gas sources and pressures at gas load buses as the boundary conditions for TSA according to (3.20)-(3.22).

Step 6: Conduct the second stage TSA for one time step Δt , and the pre-set initial/boundary conditions. Set the solutions as the initial condition for the next step according to (3.23) and (3.24).

Step 7: Calculate the real-time GLCs for non-power gas load and GFU gas requirement according to (3.25)-(3.27).

Step 8: Evaluate the real-time dispatchable electricity generating capacity of GFUs according to (3.28). Conduct the optimal power flow in the electricity system according to Section III. D.

Step 9: Repeat Steps 4-8 until it reaches the duration of system state k .

Step 10: Repeat Steps 4-9 until the whole study period ST is reached.

Step 11: Calculate the short-term risk indices according to (3.32) and (3.33). Evaluate the stopping criterion for TSMCS according to (3.34). If it satisfies $t \in [0, ST]$, output the short-term risk indices as the final results. Otherwise, begin the next simulation from *Step 1*.

3.5 Case Studies

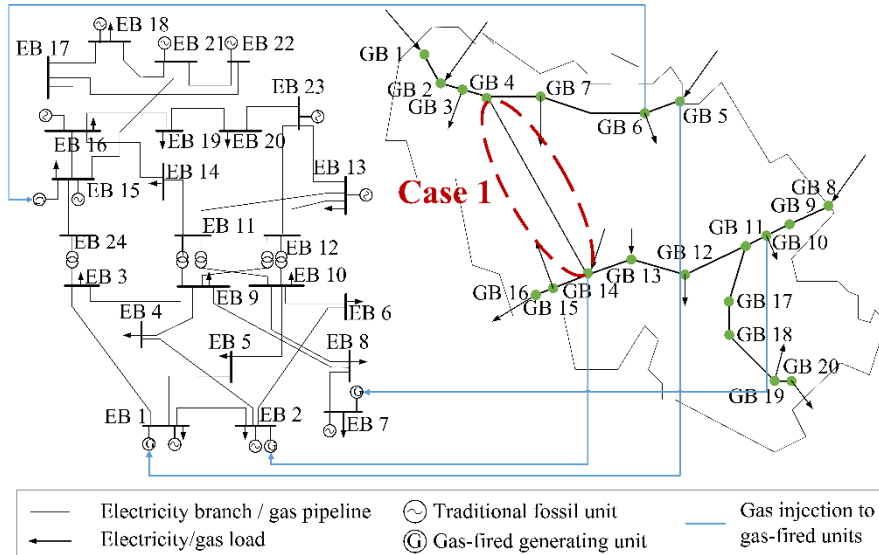


Fig. 3.3 Integrated IEEE RTS and Belgium natural gas transmission system

In this section, an integrated IEEE Risk Test System [19] and the Belgium gas transmission system [20] are studied, as illustrated in Fig. 3.3. The generating units No. 1, 2, 5, 6, 9, 10, 11, 16, 17, 18, 19, and 20 in the electricity system are replaced with the GFUs of the same capacities. The coefficients of heat rate and the gas purchasing price are referred to [15]. Simulations are performed on the following three cases to validate the proposed short-term risk evaluation technique.

3.5.1 Case 1: Illustration of gas flow dynamics in a single pipeline

The first illustrative case is performed on a single pipeline to demonstrate the gas flow dynamics during the contingency state, as well as the necessity to incorporate the gas flow dynamics in the short-term risk evaluation. The pipeline from GB 4 to GB 14 is used, which is assumed to be isolated from the IEGS, as presented in Fig. 3.3. A gas well is connected to GB 4. A gas load and a GFU are connected to GB 14, and an electricity load is further connected to the GFU. The capacities of the gas source and GFU are { 6,4,2,0 } Mm³/day and 200 MW at different states. The gas pressure at GB 14 is a constant of 5.1784×10^6 Pa. The gas and electricity loads are 5 Mm³/day and 100 MW, respectively. The length of a pipeline section $\Delta x = 10$ km, and the time step $\Delta t = 5$ min [6]. The study period is 168 h.

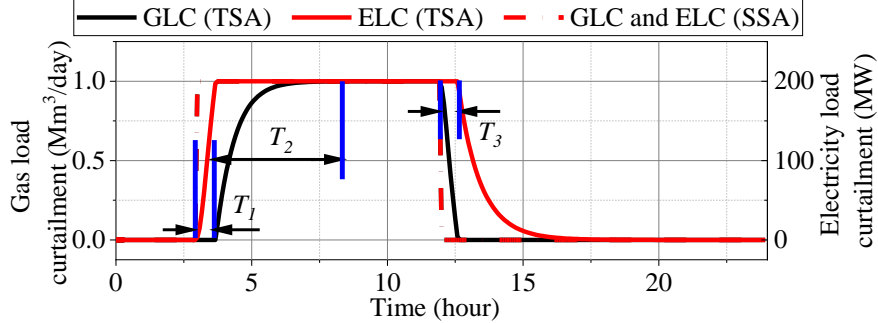


Fig. 3.4 GLCs and ELCs in the TSA and SSA

As observed from the TSA results in Fig. 3.4, the failure of the gas source is triggered at $t=3\text{h}$. Then the ELC begins to increase while the GLC remains zero within T_1 . This is because the GFU's gas requirement is the first to be curtailed compared to the non-power gas load. During T_2 , the insufficient quantity of gas supply exceeds the GFU gas requirement, and the gas load begins to be curtailed. Due to the slower dynamics of gas flow, part of the gas load can still be supplied by the linepack, and therefore the GLC increases gradually. The repair of the gas well completes at $t=12\text{h}$. Similarly, the gas load gradually recovers followed by the electricity load. Noted that due to the higher priority of gas load than the gas requirement of GFUs, the GLC recovers faster than it emerges. The incorporation of gas flow dynamics substantially influences the load curtailments, compared with steady-state analysis (SSA) where the state transition of IEGS can be regarded as an instant process.

Fig. 3.5 and 3.6 show the influences on the short-term reliabilities by gas flow dynamics. It is worth noting in Fig. 3.5(a) that the LOGP in TSA is almost the same as that in SSA, while LOLP in TSA is larger than that in SSA. This can be explained in Fig. 3.4. The duration of $\text{ELC}>0$ in TSA is longer than that in SSA by T_1+T_2 , while the duration of $\text{GLC}>0$ in TSA is the same as that in SSA. Further exploring the first 12 hours in Fig. 3.5(b), a noticeable delay in the occurrence of LOGP can be found. It can also be explained by Fig. 3.4 that the GLC does not occur within T_1 .

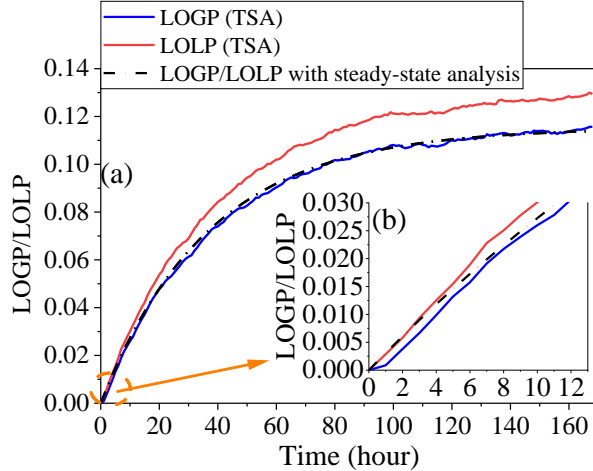


Fig. 3.5 LOGP and LOLP during the operational phase

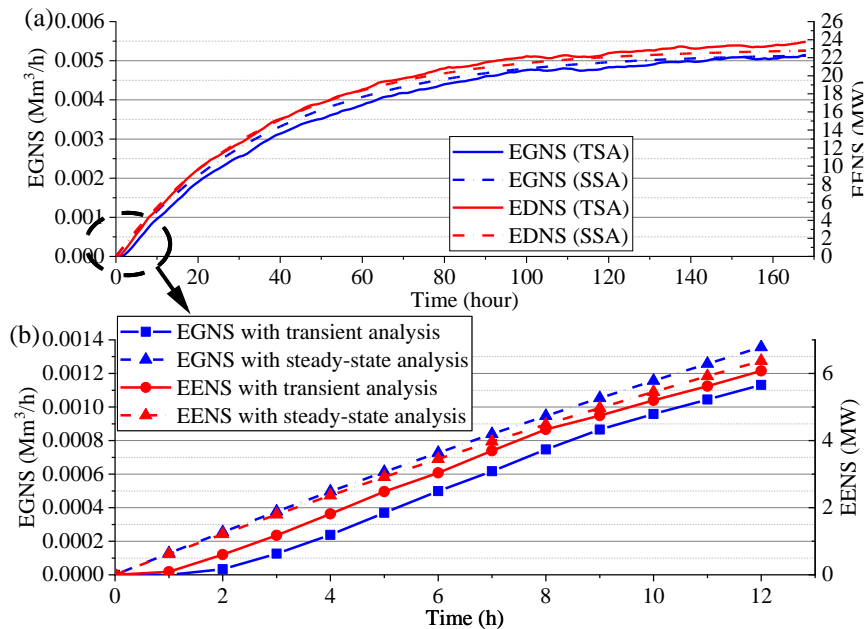


Fig. 3.6 EGNS and EDNS during the operational phase

The EGNS and EDNS in Fig. 3.6 present a slightly different pattern. The EGNS in TSA is smaller than that in SSA, while EDNS in TSA grows higher as time goes on. It can be explained in Fig. 3.4. The GLC accumulated over time in TSA is smaller than that in SSA, while the ELC accumulated over time in TSA is larger than that in SSA. Similarly, as indicated by the simulations of the first 12

hours in Fig. 3.6(b), there also exist noticeable delays for EDNS and EGNS, except that the effect of gas dynamics is more obvious.

In summary, the following conclusions can be drawn from the above simulations: (1) the gas flow in a transmission pipeline takes from minutes to hours to stabilize. (2) With the incorporation of the gas dynamics, the LOLP increases, while the EGNS and EDNS decrease. (3) The occurrences of LOGP, EGNS, and EDNS are delayed to varying degrees, and their increasing trends are also mitigated at the beginning of the simulation.

3.5.2 Case 2: impact of gas flow dynamics on the failure propagation in a representative scenario

In this case, a representative scenario exemplifies the propagation of failures in the gas system to the electricity system. A compound failure of 197 and 400 MW traditional fossil units at EB 13 and 18, and 2 Mm³/day deration of the gas source at GB 1 is triggered at $t=0.83$ h. The length of a pipeline section $\Delta x = 2000$ m, and the time step $\Delta t = 15$ min. The study period is 6 h. Here we define the *delay time* as the difference between the time of failure and the time of load curtailment occurrence. Also, we define the *failure distance* as the minimum distance along the pipeline between the studied GB and the GB where the gas component failure has happened.

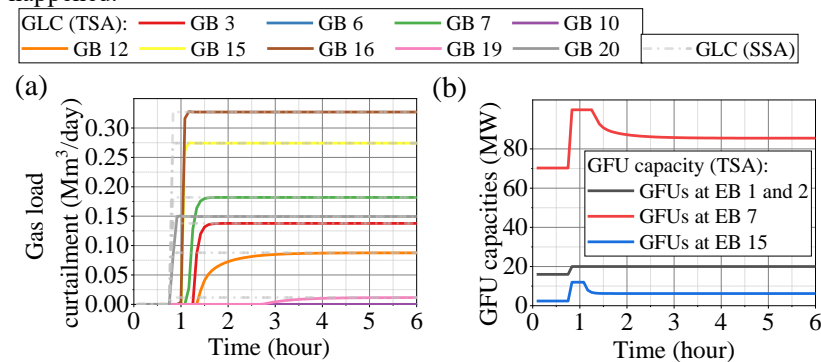


Fig. 3.7 Nodal GLCs and GFU capacities in TSA and SSA

As shown in Fig. 3.7(a), GLCs at GBs present different delay times. For example, the GLC at GB 20 increases immediately right after the failure, while GLC at GB 19 begins to increase at $t=2.83$ h. Note that in this case, the pressures at gas load buses are controlled to be constant in the TSA. There is no monotonicity between the delay time of the GLC and the failure distance. In fact, the feature of GLC is directly determined by the inlet and outlet gas flows of the GB, which can be further determined by the boundary conditions (the optimized pressures and flows at adjacent gas load buses and gas source buses, respectively). Take GB 19 and 20 for example - though they are both at the end of the same gas branch, their GLCs present entirely different temporal patterns. GB 19 and 20 are both gas load

buses. Their pre- and post-fault pressures are controlled as 28.53, 26.11 bar, and 29.50, 27.53 bar, respectively. Hence, the gas flow in the pipeline between GB 19 and 20 can be soon stabilized to its steady-state value, which results in the immediate stabilization of GLC at GB 20. On the contrary, looking at the upstream GBs of GB 19, the closest gas load bus is GB 10 still a long distance away. Hence, the GLC at GB 19 takes more time to stabilize.

It is also worth mentioning that GLCs at almost all the GBs will reach their values in SSA after enough time, except GBs 6 and 10. As can be seen from Fig. 3.3 that GBs 6 and 10 are connected with EBs 15 and 7 through GFUs. Therefore, by observing the difference between corresponding GFU capacities in TSA and the stabilized values in Fig. 3.7(b), it can be concluded that the GLCs at GBs 6 and 10 are reduced by curtailing the gas consumption of GFUs instead.

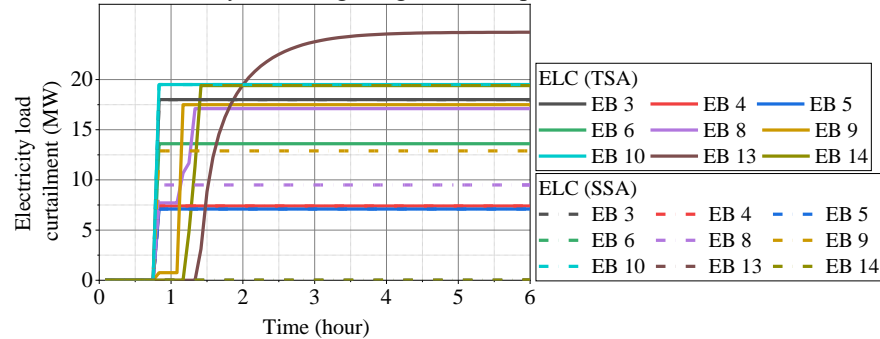


Fig. 3.8 Nodal ELCs in TSA and SSA

The ELCs present a similar transient process, as shown in Fig. 3.8. The increase in ELC is due to the time-varying GFU capacities. The ELC of EB 13 takes the longest time to stabilize since its electricity load is mostly supplied by the GFU at EB 7. Some of the ELCs present a multi-segment feature, such as EBs 8 and 9. It is because the loads at these EBs are jointly supplied by GFUs at EB 1 or 2, and 15.

On the other hand, the stabilized value of ELCs in TSA does not necessarily equal those in SSA. For example, after considering the gas flow dynamics, the ELCs at EBs 8 and 9 have raised from 9.50 and 12.89 MW to 17.1 and 17.5 MW, respectively. This indicates that the consideration of gas dynamics and prior curtailment of GFU gas consumption does lead to worse ELCs at some EBs eventually. Their reliabilities may also be inferior.

3.5.3 Case 3: short-term risk indices

The short-term risk indices for the studied IEGS are obtained in this case using TSMCS. Simulations were performed on a Lenovo laptop with an Intel® Core™ i7-8565U 1.80GHz and a 16GB memory. Observe from Table 3.1 that with the proposed technique, a computation time of 6.74h can be achieved. It allows the system operator to evaluate the short-term risk in the day ahead. Moreover,

TSMCS is perfect for parallel computing. The computation time can be further reduced with the implementation of production codes on a high-performance and parallel-architecture computing platform.

The short-term risk of the IEGS is presented in Fig. 3.9 and 3.10. On account of the same reason in Fig. 3.4, the LOGP in TSA is almost the same as that in SSA, while the EGNS in TSA is much lower. As for the electricity system in Fig. 3.10, the EDNS in TSA is remarkably lower than those in SSA, while the LOLP presents an opposite pattern.

Table 3.1 Computation times

Proposed time reduction technique	TOTAL (s)	For offline contingencies (s)	For TSMCS (s)
With	24261	1747	22514
Without	302170	/	/

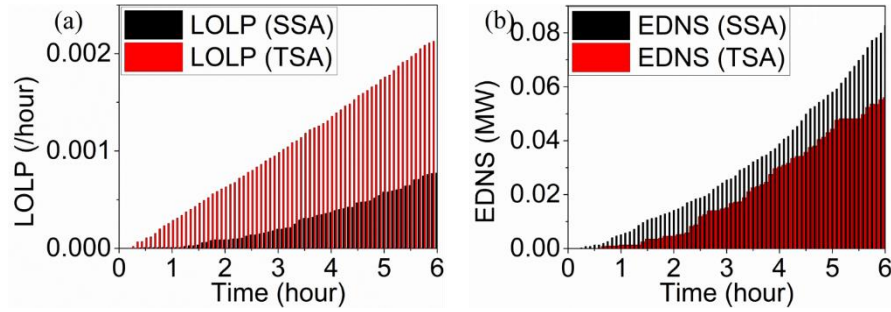


Fig. 3.9 LOGP and EGNS during the operational phase

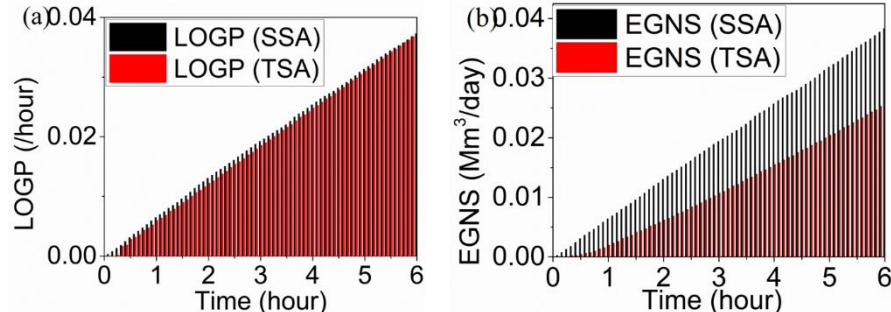


Fig. 3.10 LOLP and EDNS during the operational phase

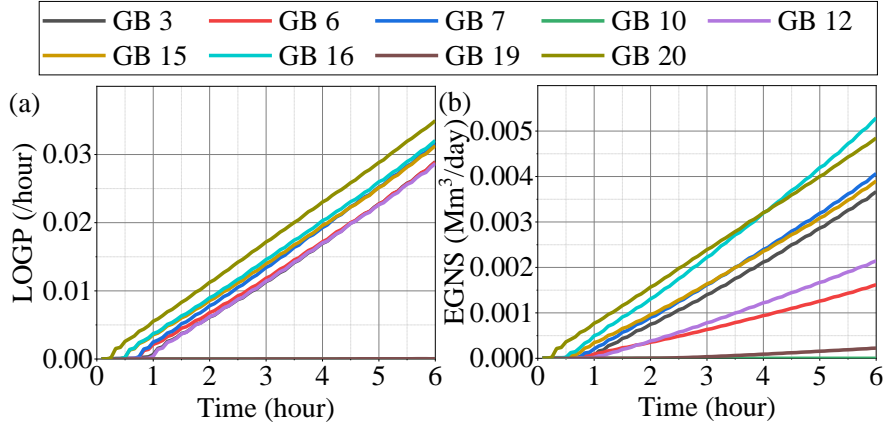


Fig. 3.11 Nodal LOGP and EGNS during the operational phase

Considering that load curtailments vary spatially, the risk indices are further specified into the nodal scale. Observe from Fig. 3.11 that the delay times of LOGP and EGNS at GBs are different. The increase in LOGP begins with GB 20, which is the same as indicated in Fig. 3.7(a). The LOGP of GB 20 also remains the largest among all GBs during the operational phase. However, the EGNS of GB 16 begins to exceed GB 20 at $t = 4.25$ h. Noted that GB 16 is also at the end of another gas pipeline branch. This indicates that, although GB 20 is always most likely to be curtailed, GB 16 is also prone to suffer a more severe gas shortage after a certain time point.

3.6 Conclusion

This chapter proposes a short-term risk evaluation technique considering the gas flow dynamics. The short-term multi-state risk models of gas sources, GFUs, and traditional fossil units are developed, respectively, considering the interdependency between the electricity and gas systems. A multi-stage contingency management scheme is proposed to use the gas flow dynamics to evaluate the time-varying electricity and gas load curtailments during the operation phase. The TSMCS is enhanced by embedding the finite-difference scheme to solve the partial derivative equations of gas flow, as well as to obtain the short-term risk indices. Several practical techniques are adopted to reduce the computation time.

From the simulation results in case studies, we find that by considering the gas flow dynamics in the operational phase, the EDNS and EGNS of the IEGS can be reduced significantly. The proposed risk evaluation technique is more accurate and practical in the operational phase compared with those that use the steady-state gas flow model. It can be further utilized to assist the system operator in the short-term risk management in practical IEGS.

3.7 References

- [1] Y. Ding, C. Singh, L. Goel *et al.*, "Short-Term and Medium-Term Reliability Evaluation for Power Systems With High Penetration of Wind Power," *IEEE Transactions on Sustainable Energy*, vol. 5, no. 3, pp. 896-906, Jul, 2014.
- [2] C. M. Correa-Posada, and P. Sánchez-Martín, "Integrated Power and Natural Gas Model for Energy Adequacy in Short-Term Operation," *IEEE Transactions on Power Systems*, vol. 30, no. 6, pp. 3347-3355, 2015 Nov.
- [3] E. Shashi Menon, "Chapter Five - Fluid Flow in Pipes," *Transmission Pipeline Calculations and Simulations Manual*, E. Shashi Menon, ed., pp. 149-234, Boston: Gulf Professional Publishing, 2015.
- [4] X. Chen, J. Lv, M. B. McElroy *et al.*, "Power System Capacity Expansion Under Higher Penetration of Renewables Considering Flexibility Constraints and Low Carbon Policies," *IEEE Transactions on Power Systems*, vol. 33, no. 6, pp. 6240-6253, 2018.
- [5] Y. Zhou, C. Gu, H. Wu *et al.*, "An Equivalent Model of Gas Networks for Dynamic Analysis of Gas-Electricity Systems," *IEEE Transactions on Power Systems*, vol. 32, no. 6, pp. 4255-4264, Nov, 2017.
- [6] J. Yang, N. Zhang, C. Kang *et al.*, "Effect of Natural Gas Flow Dynamics in Robust Generation Scheduling Under Wind Uncertainty," *IEEE Transactions on Power Systems*, vol. 33, no. 2, pp. 2087-2097, Mar, 2018.
- [7] S. Clegg, and P. Mancarella, "Integrated Modeling and Assessment of the Operational Impact of Power-to-Gas (P2G) on Electrical and Gas Transmission Networks," *IEEE Transactions on Sustainable Energy*, vol. 6(4), no. 4, pp. 1234-1244, May, 2015.
- [8] M. Bao, Y. Ding, C. Shao *et al.*, "Nodal Reliability Evaluation of Interdependent Gas and Power Systems Considering Cascading Effects," *IEEE Transactions on Smart Grid*, vol. 11, no. 5, pp. 4090-4104, Mar, 2020.
- [9] S. Wang, Y. Ding, X. Han *et al.*, "Short-term reliability evaluation of integrated electricity and gas systems considering dynamics of gas flow," *IET Generation, Transmission & Distribution*, vol. 15, no. 20, pp. 2857-2871, 2021.
- [10] M. Bao, Y. Ding, C. Singh *et al.*, "A Multi-State Model for Reliability Assessment of Integrated Gas and Power Systems Utilizing Universal Generating Function Techniques," *IEEE Transactions on Smart Grid*, pp. 1-1, 2019.
- [11] A. Lisnianski, I. Frenkel, and Y. Ding, *Multi-state system reliability analysis and optimization for engineers and industrial managers*, London: Springer Science & Business Media, 2010.

- [12] Y. Ding, L. Cheng, Y. Zhang *et al.*, "Operational reliability evaluation of restructured power systems with wind power penetration utilizing reliability network equivalent and time-sequential simulation approaches," *Journal of Modern Power Systems and Clean Energy*, vol. 2, no. 4, pp. 329-340, 2014.
- [13] M. Chaudry, J. Wu, and N. Jenkins, "A sequential Monte Carlo model of the combined GB gas and electricity network," *Energy Policy*, vol. 62, pp. 473-483, Nov, 2013.
- [14] I. Cameron, "Using an Excel-Based Model For Steady-State And Transient Simulation," in PSIG Annual Meeting, St. Louis, Missouri, 1999, pp. 39.
- [15] C. Unsihuay, J. W. M. Lima, and A. C. Z. d. Souza, "Modeling the Integrated Natural Gas and Electricity Optimal Power Flow," in 2007 IEEE Power Engineering Society General Meeting, 2007, pp. 1-7.
- [16] G. Wacker, and R. Billinton, "Customer cost of electric service interruptions," *Proceedings of the IEEE*, vol. 77, no. 6, pp. 919-930, Jun, 1989.
- [17] A. Alabdulwahab, A. Abusorrah, X. Zhang *et al.*, "Stochastic Security-Constrained Scheduling of Coordinated Electricity and Natural Gas Infrastructures," *IEEE Systems Journal*, vol. 11, no. 3, pp. 1674-1683, Sep, 2017.
- [18] R. D. Zimmerman, C. E. Murillo-Sanchez, and R. J. Thomas, "MATPOWER's extensible optimal power flow architecture." pp. 1-7,26-30 July 2009, 2009.
- [19] C. Grigg, P. Wong, P. Albrecht *et al.*, "The IEEE Reliability Test System-1996. A report prepared by the Reliability Test System Task Force of the Application of Probability Methods Subcommittee," *IEEE Transactions on Power Systems*, vol. 14(3), no. 3, pp. 1010-1020, Aug, 1999.
- [20] D. De Wolf, and Y. Smeers, "The gas transmission problem solved by an extension of the simplex algorithm," *Management Science*, vol. 46, no. 11, pp. 1454-1465, 2000.

4 Risk Evaluation of Integrated Electricity and Gas Systems Considering Cascading Effects

4.1 Introduction

The above chapters mainly focus on the risk evaluation of integrated electricity and gas systems (IEGS) considering the failure propagation from natural gas systems (NGS) to power systems. However, the bidirectional dependence between NGS and power systems can bring about cascading effects in IEGS under special conditions. Due to random failures, the disruptions occurring in one system can have impacts on the operation of the other system, which may further feedback to the original system. Such an iterative process can be defined as cascading effects. When considering the cascading effects between NGS and power systems, small disturbances can be amplified and finally result in widespread damage. The catastrophic outages in the Southwestern United States in February 2011 can be served as a demonstration of the cascading effects in the IEGS [1]. Due to unexpected cold weather, the freezing of water vapor at several gas wellheads significantly reduced the transportation of gas from production areas to demands. Simultaneously, numerous generators were also failed due to weather-related causes, including frozen sensing lines, frozen equipment and etc. Further compounding the problem, the gas load curtailments caused the decrease of gas supplied to GPPs, leading to the massive reduction of the electricity supplies. On the other hand, the electric load curtailments caused the malfunction of electric-driven gas compressors in NGS and more gas loads were curtailed. Finally, more than 4.4 million energy users' power and gas consumption were greatly affected during the long-duration blackout.

The risk evaluation of conventional power systems has been well developed over the past few decades [2-6]. However, these techniques are more focused on the single power system without considering the interactions between NGS and power systems. Currently, several studies have been conducted to analyze the security and risk of IEGS considering the increasing electric and gas interdependence. In reference [7], the long-term risk of IEGS considering the power-to-gas devices and gas storages was evaluated utilizing the Monte Carlo simulation technique. In reference [8], the short-term risk of IEGS is analyzed based on the network equivalent and integrated optimal energy flow techniques. Reference [9] proposes a multi-state model for the risk assessment of IEGS and evaluates the impacts of component failures occurring in NGS on power systems. Reference [10] proposes a risk assessment framework for integrated energy systems and introduces a hierarchical decoupling technique for system optimal dispatch. The risk of IEGS under extreme events is also evaluated in [11] utilizing the Monte Carlo simulation (MCS) method. The risk-based planning for the multiple energy hub of IEGS is proposed in [12] based on a minimal cut-maximal flow algorithm.

Several key issues have not been considered in the prior-art studies for the risk evaluation of IEGS. Firstly, the impacts of interdependence-induced cascading effects on the risk of IEGS are neglected in most studies, which may cause the risk evaluation results more optimistic. Moreover, the previous studies usually adopt a succession of steady-state models to investigate the risk of IEGS supposing that the supply and demand can be balanced at all time in both NGS and power systems [9]. However, these models for risk evaluation cannot practically reflect the dynamic nature of cascading effects in IEGS, since natural gas and electric power flows usually travel through networks via different speeds. Therefore, different dynamic behaviors between power systems and NGS are imperative to be considered in the cascading effects modeling of IEGS. Furthermore, the previous studies usually adopt system-wide indices to represent the risk performances of IEGS without considering the locational difference of risk [7, 10]. Due to the transmission constraints and uneven distributions of energy sources and demands, the effects of random failures on the risk of IEGS can differ at different nodes. Nodal risk, therefore, has been adopted to evaluate the locational risk performances of energy systems [9]. However, the risk indices defined in references [9] are based on the calculation results of steady-state models without considering the temporal cascading effects in IEGS.

The innovative contributions of the chapter are summarized as:

- 1) The framework for the risk evaluation of IEGS considering interdependence-induced cascading effects between power systems and NGS is proposed. Moreover, the MCS technique is utilized to evaluate the impacts of cascading effects on the risk of IEGS.
- 2) The dynamic cascaded analysis model is developed to describe the temporal and spatial process of cascading effects considering the different dynamic behaviors between the power system and NGS. By taking the gas velocity and line pack into consideration, the re-dispatch model of NGS is set up to characterize the dynamic variation of gas pressures and flow rates between two time periods. Moreover, the stopping criterion of cascading effects is defined.
- 3) In order to quantify the regional risk performances of IEGS considering the impacts of cascading effects, nodal risk indices for both the NGS and power system are defined based on the calculation results of dynamic cascaded analysis models.

This chapter includes research related to the risk analysis of IEGS considering cascading failures between NGS and power systems by[13].

4.2 Description of cascading effects in integrated electricity and gas systems

The cascading effects in IEGS can be defined as complicated sequences of dependent events between power systems and NGS under disruptive events [14, 15]. Moreover, the failures propagate between two systems through the coupled com-

ponents. Therefore, the interdependence-induced cascading effects in IEGS are illustrated in Fig. 4.1 with the concentration of the coupled components.

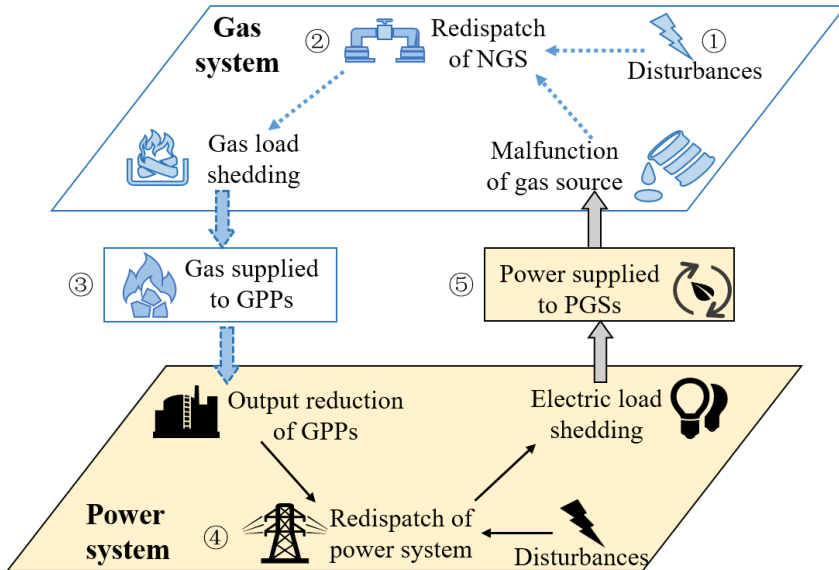


Fig. 4.1 Cascading effects between NGS and power system

Due to the bidirectional interactions between two systems, the disturbances in either NGS or power systems may lead to cascading effects. Taking the initial disturbances in NGS as an example, the cascading effects in IEGS mainly include the following steps:

Step 1) Initial failures in NGS: The initial failures of components can be caused by different disturbances, such as weather conditions or human errors. Due to the initial failures, the NGS will deviate from its normal operating state.

Step 2) Re-dispatch of NGS: Considering the initial failures, the gas system operator needs to adopt measures such as gas production adjustment or gas load shedding for the reliable operation of NGS. Generally, the generation utilities sign interruptible contracts with gas companies. If congestion appears in NGS or gas sources reach their maximum production for contingencies, the gas supplied to GPPs is firstly curtailed according to contractual agreements [16].

Step 3) Impacts of failures in NGS on power systems: The gas load shedding in NGS may lead to the reduction of gas supplied to GPPs. Considering the operation characteristics of GPPs, the GPPs that cannot obtain sufficient gas will correspondingly reduce their power output.

Step 4) Re-dispatch of power systems: Due to the output reduction of GPPs, the power system operator will re-dispatch all the available generation units and loads to eliminate the power imbalance. If the adjustment of generation output cannot

realize the system power balance, electric load shedding will be implemented by system operators.

Step 5) Impacts of re-dispatch of power systems on NGS: The electric load shedding in the power system may lead to the curtailment of power supplied to P2G facilities and EGSs. Hence, the EGSs will stop working if they cannot obtain a sufficient power supply. Likewise, the gas production of P2G facilities may decrease due to the reduction of power supplied to them.

Iterations: If the malfunction of EGSs or the production change of P2G facilities leads to the gas imbalance in NGS, the re-dispatch of NGS will be implemented in Step 2. Under this condition, the NGS and power system will be re-dispatched alternately until the cascading effects in IEGS stop.

The previous analysis of cascading effects in IEGS begins with the disturbances in NGS. Likewise, assuming that the initial disturbances occur in the power system, the cascading effects can be illustrated from Step 4 in Fig. 4.1. Therefore, the cascading effects in IEGS can be viewed as a cycling process.

4.3 Modeling dynamic cascading effects in integrated electricity and gas systems

Based on the illustration in section II, the cascading effects in IEGS can be viewed as an iterative process where the initial failures cause a sequence of coupled component malfunctions, as shown in Fig. 4.2. When considering the dynamic characteristics of IEGS, the cascading effects can spread over time between power systems and NGS. The analysis framework is given in Fig. 4.3 which models the process of temporal and spatial cascading effects under different time periods. For time period t , the re-dispatch model of NGS is conducted to determine the gas load shedding at time $t + \Delta t$ based on the current conditions of NGS and the power supplies of P2G facilities and EGSs obtained in power systems. Similarly, the re-dispatch model of power systems can be conducted to determine the electric load curtailments at time $t + \Delta t$ in continuity to the operating conditions of power systems at time t and the reduction of gas supplied to GPPs obtained in the NGS. The process for the re-dispatch of NGS and power system is then repeated for next time intervals until the stable operation of both systems. Moreover, the dynamic cascaded analysis model is proposed in this section to model the cascading effects in IEGS.

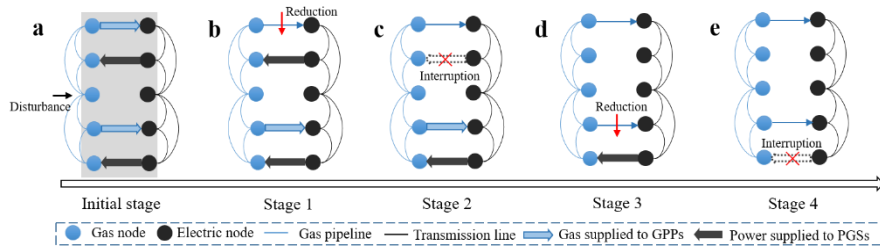


Fig. 4.2 Illustrating an iterative process of cascading effects in IEGS

It should be noted that the steady-state models can be utilized to represent power system operation based on several reasonable assumptions [16]. Since the transients usually fade away and the system reaches steady states again soon, the steady-state models are generally sufficient in the representation of system operation [17]. In this chapter, the optimal power flow (OPF) model is introduced to determine the re-dispatch results of power systems at time $t + \Delta t$. In contrast, gas flows travel at a relatively slower velocity than electricity and the gas networks need to take a longer time to return to stable operating conditions. Besides, a portion of gas can be stored in pipelines in the short term due to the difference of gas pressures at both ends, which is known as line pack [16]. The consideration of gas dynamics (i.e. gas velocity and line pack) is imperative in the re-dispatch of NGS. Therefore, the optimal transient gas flow (OTGF) techniques are introduced to describe the relationship of gas pressures and gas flows between time periods t and $t + \Delta t$.

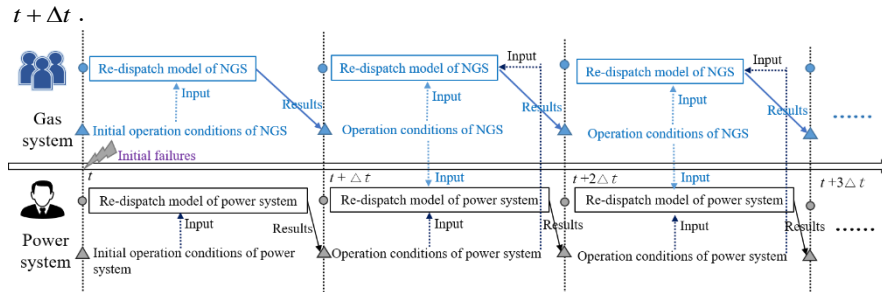


Fig. 4.3 Framework for modeling the dynamic cascading effects in IEGS

4.3.1 Initial failures

The cascading effects in IEGS are often initiated by component failures caused by weather conditions or human errors etc. In this chapter, we consider the potential cascading effects caused by the outages of gas sources, power plants (i.e. CFGs, GPPs, and WTGs), coupled components, gas pipelines and etc. To model the initial states of components in IEGS considering random failures, the availability vector \mathbf{AV} is introduced [18], which can be expressed as:

$$\mathbf{AV} = \left[a_{is}, L, a_{ij}, L, a_{mg}, L, a_{imc} \right]^T \quad (4.1)$$

$$a_{is}, a_{ij}, a_{mg}, a_{imc} \in \{0, 1\}$$

where a_{is} is the state of gas source s at gas node i ; a_{mg} is the state of the generator at electric node m ; a_{ij} is the state of the gas pipeline between nodes i and j ; a_{imc} is the state of coupled component c connected to gas node i and electric node m . It can be noted that the operating state of a component can be either 1 or 0, where 1 corresponds to the normal state and 0 corresponds to the outage state. The initial

states of the components can be determined according to their own failure probabilities utilizing state sampling techniques [18].

During operation, the failure probability of gas pipelines is also closely related to their ambient temperatures. When exposed to abnormal temperatures, the failure probability of gas pipelines can be increased. For example, the increase in ambient temperatures can raise the risk of corrosion, making the pipelines more easily damaged [19]. In this chapter, the failure probability of pipelines under normal and elevated temperatures is set based on the estimation results in reference [19].

4.3.2 Coupled components modeling

The coupled relationship between NGS and power systems can be described by the models of coupled components. According to the conversion direction between gas and power, the coupled components in IEGS can be classified into GPPs, EGSSs, and P2G facilities. During the process of cascading effects, the operating conditions of coupled components depend on both the energy supply and their reliabilities.

1) Gas-fired power plants

As an energy convertor to produce electricity with gas, each GPP is simultaneously connected to the load node i in the NGS and generation node m in power systems. According to the heating rate curve [20], there is a conversion relationship between the power output of GPPs P_{mg}^t and the corresponding nodal gas injection GS_i^t , which can be expressed as:

$$GS_i^t = (\alpha_{mg} + \beta_{mg} \cdot P_{mg}^t + \gamma_{mg} \cdot P_{mg}^{t-2}) / \Gamma \quad (4.2)$$

where α_{mg} , β_{mg} and γ_{mg} represent the heat rate coefficients of GPP g at node m . Γ represents gas gross heating value.

For time t , the power output of GPP g at electric node m can be calculated according to the amount of gas supplied to it:

$$P_{mg}^t = \frac{-\beta_{mg} + [\beta_{mg}^2 - 4 \cdot \gamma_{mg} \cdot (\alpha_{mg} - GS_i^t \cdot \Gamma)]^{1/2}}{2\gamma_{mg}} \quad (4.3)$$

The power output of GPPs also depends on their reliabilities. Based on the operating states of GPPs obtained in (4.1), the power output of GPP g at time t can be expressed as:

$$P_{mg}^t = a_{inc} \cdot \frac{-\beta_{mg} + [\beta_{mg}^2 - 4 \cdot \gamma_{mg} \cdot (\alpha_{mg} - GS_i^t \cdot \Gamma)]^{1/2}}{2\gamma_{mg}} \quad (4.4)$$

2) Electric-driven gas sources

EGSSs need a reliable electricity supply to maintain their proper function. Generally, the power consumption of an EGS D_{mk}^t is related to its gas production W_{ik}^t [21], which can be modeled as:

$$D'_{mk} = \eta_g \cdot W'_{ik} \quad (4.5)$$

where η_g is the conversion factor of EGSs.

During the process of cascading effects, the power supply of EGSs is determined by the load curtailments at the corresponding electric nodes. Generally, in order to guarantee the reliable operation of NGS, the power supply of EGSs is one of the last candidates to be curtailed for contingencies [21]. Therefore, the operating condition of EGS k at node i and time t can be determined by the electric load curtailments:

$$O'_{ik} = \begin{cases} 1, & \text{if } D'_{mk} \leq D'_{mL} - LC'_m \\ 0, & \text{if } D'_{mk} > D'_{mL} - LC'_m \end{cases} \quad (4.6)$$

where O'_{ik} is 0 when the power supply of EGS is interrupted, or 1 when the EGS can obtain enough power supply.

The normal operation of an EGS also depends on its risk. Considering the power supply and risk of an EGS, the operating condition φ'_{ik} of an EGS at node i and time t can be modeled as:

$$\varphi'_{ik} = a_{imc} \cdot O'_{ik} \quad (4.7)$$

3) P2G facilities

P2G facilities convert excessive electricity into synthetic natural gas to satisfy the gas consumption in NGS. The chemical process of P2G technology mainly includes two steps: $2\text{H}_2\text{O} \rightarrow 2\text{H}_2 + \text{O}_2$ and $\text{CO}_2 + 4\text{H}_2 \rightarrow \text{CH}_4 + 2\text{H}_2\text{O}$ [22]. In the first step, the water is split into hydrogen and oxygen through electrolysis. The obtained hydrogen carbon dioxide interacts with carbon dioxide to produce synthetic natural gas through electrolysis in the second step. By combining the two steps of the chemical process, the synthetic natural gas can be produced from electricity with certain energy efficiency.

Considering the power supply and risk of a P2G facility [23], the gas production of a P2G facility at node i and time t can be expressed as:

$$W'_{i,P2G} = a_{imc} \cdot \frac{\eta_{P2G} \cdot (D'_{mL} - LC'_m)}{\Gamma} \quad (4.8)$$

where η_{P2G} refers to the energy conversion factor of P2G facilities from electricity to gas.

4.3.3 Re-dispatch model of gas systems

Both the initial failures and malfunction of EGSs can result in the re-dispatch of NGS. For time t , the operating conditions of EGSs and the power supplied to P2G facilities can be determined according to electric load curtailments using (4.7) and (4.8), respectively. On this basis, the production re-dispatch of gas sources and gas load shedding at time $t + \Delta t$ can be determined using OTGF techniques.

The transient gas flow through one pipeline can be characterized by three equations, namely the equations of state, continuity, and motion (see Appendix A). These equations describe the dynamic characteristics of gas travel with the relationship between gas pressures and flow rates over time [16, 24]. Through the implicit method of finite differences, the continuous equations can be discretized into partial difference equations in time and space (see Appendix A) [25]. On the basis, starting from the pressures and gas flows at time t , the pressures and flows at time $t + \Delta t$ can be determined.

The objective function of the OTGF model is to minimize the total system cost at time $t + \Delta t$, including gas production costs and the interruption costs of gas loads.

$$\text{Min} \sum_{i=1}^N C_{is}(W_{is}^{t+\Delta t}) + C_{ik}(W_{ik}^{t+\Delta t}) + C_{il}(\Delta W_{il}^{t+\Delta t}) \quad (4.9)$$

Subject to the following constraints [16]:

1) *Continuity equation:* Concerning the line pack, the incoming $Q_{D,i}^{t+\Delta t}$ and outgoing flow $Q_{D,j}^{t+\Delta t}$ of pipeline D at time $t + \Delta t$ may differ due to a portion of gas stored in the pipe [16], which can be expressed as:

$$\begin{aligned} f_{S,\text{continuity}} = & \frac{4R \cdot \psi \cdot \rho_n}{\pi d^2} \cdot \frac{\Delta t}{\Delta l} (Q_{D,j}^{t+\Delta t} - Q_{D,i}^{t+\Delta t}) \\ & + \frac{1}{Z_s} \left(\frac{p_{D,i}^{t+\Delta t} + p_{D,j}^{t+\Delta t}}{2} - \frac{p_{D,i}^t + p_{D,j}^t}{2} \right) = 0 \end{aligned} \quad (4.10)$$

where R is the specific gas constant (J/kgK); ψ is the absolute temperature (K); ρ_n is the density (kg/m^3); d is the diameter of the pipeline (m); Δt is time period (s); Δl is the distance of the pipeline (m); Z_s is the compressibility factor.

2) *Motion equation:* The gas flows through pipeline S can be expressed as a function of pressure gradient, travel velocity, and pipeline characteristics. The motion equation is utilized to characterize the change of momentum acting on gas particles, which is shown as:

$$f_{S,\text{motion}} = \frac{(p_{D,j}^{t+\Delta t})^2 - (p_{D,i}^{t+\Delta t})^2}{2 \cdot \Delta l} + \frac{32v^2 \rho_n^2}{F^2 \pi^2 d^5} \cdot \dot{Q}_{D,ij}^{t+\Delta t} \cdot \left| \dot{Q}_{D,ij}^{t+\Delta t} \right| = 0 \quad (4.11)$$

where $\dot{Q}_{D,ij}^{t+\Delta t} = (Q_{D,i}^{t+\Delta t} + Q_{D,j}^{t+\Delta t})/2$ is the average flow; v is the travel velocity of gas flow (m/s); F is the fanning transmission factor.

3) *Nodal balance constraints:* Similar to power systems, the NGS also needs to follow the nodal supply-demand balance. The flows in and out of gas node i can be produced from different sources, including FGS with injection flow $W_{is}^{t+\Delta t}$, EGS with injection flow $W_{ik}^{t+\Delta t}$, P2G facility with injection flow $W_{i,P2G}^{t+\Delta t}$, a compressor station with inlet flow $C_{D,i}^{t+\Delta t}$, a pipeline with incoming flow $Q_{D,i}^{t+\Delta t}$, and gas demand W_{il}^t .

$$a_{is} \cdot W_{is}^{t+\Delta t} + \varphi_{ik}^t \cdot W_{ik}^{t+\Delta t} + W_{i,P2G}^{t+\Delta t} + \sum_{D=1}^{N_D} C_{D,i}^{t+\Delta t} - \sum_{D=1}^{N_D} Q_{D,i}^{t+\Delta t} = W_{iL}^t - \Delta W_{iL}^{t+\Delta t} \quad (4.12)$$

4) *Gas compressor model*: Similar to transformers in power systems, gas compressors are built to modify the suction pressure or discharge pressure to maintain the pressure levels of pipelines [16]. A simplified compressor model is introduced to describe the relationship between the gas pressures at the incoming node i and outgoing node j of pipeline D with a compressor:

$$\underline{\xi}_{cij} \cdot p_{D,j}^{t+\Delta t} \leq p_{D,i}^{t+\Delta t} \leq \overline{\xi}_{cij} \cdot p_{D,j}^{t+\Delta t} \quad (4.13)$$

5) *Nodal pressure constraints*:

$$\underline{p}_{D,i}^{t+\Delta t} \leq p_{D,i}^{t+\Delta t} \leq \overline{p}_{D,i}^{t+\Delta t} \quad (4.14)$$

6) *Pipe flow constraints*:

$$\underline{F}_D^{t+\Delta t} \leq Q_{D,i}^{t+\Delta t} \leq \overline{F}_D^{t+\Delta t} \quad (4.15)$$

7) *Gas production constraints*:

$$0 \leq W_{is}^{t+\Delta t} \leq \overline{W}_{is}^{t+\Delta t} \quad (4.16)$$

$$0 \leq W_{ik}^{t+\Delta t} \leq \overline{W}_{ik}^{t+\Delta t} \quad (4.17)$$

8) *Gas load curtailment constraints*:

$$0 \leq \Delta W_{iL}^{t+\Delta t} \leq W_{iL}^t \quad (4.18)$$

After solving the optimization model in (4.9)-(4.18), the gas load shedding $\Delta W_{iL}^{t+\Delta t}$ at node i and time $t + \Delta t$ can be determined. Accordingly, the gas injection $GS_i^{t+\Delta t}$ supplied to GPP g at node m and time $t + \Delta t$ can be calculated as:

$$GS_i^{t+\Delta t} = W_{iL}^t - \Delta W_{iL}^{t+\Delta t} \quad (4.19)$$

Due to the nonlinearity of the motion equation in (4.11), the feasible region of the re-dispatch model can be nonconvex which will challenge the global optimality. Average flow squared $\bar{Q}_{D,ij}^{t+\Delta t} \cdot |\bar{Q}_{D,ij}^{t+\Delta t}|$ and pressures squared $(p_{D,j}^{t+\Delta t})^2$ are therefore linearized utilizing piecewise linearization techniques (see Appendix B) [16].

4.3.4 Re-dispatch model of power system

Based on the determination of gas injection GS_i^t at node i and time t , the corresponding power output P_{mg}^t of GPP g at electric node m can be calculated using (4.4). Besides modeling the operating characteristics of GPPs, the uncertainty of wind generation should also be considered in the re-dispatch of power systems. Considering that the power output of WTGs is determined by wind speeds, the multi-state model is introduced to characterize the random nature of wind speeds [26], which can be expressed as:

$$\begin{cases} V_{w,h_w}^t = V_{w0}^t + (h_w - 3) \times (5\delta_w^t / 3), & h_w = 1, 2, L, 6 \\ pr_{w,h_w}^t = pr(V_{w,h_w}^t) \end{cases} \quad (4.20)$$

where V_{w0}^t and δ_w^t are the mean value and variance of wind speed distribution of WTG w at time t , respectively. V_{w,h_w}^t and pr_{w,h_w}^t are the wind speed and corresponding probability of WTG w for state h_w at time t , respectively.

The power output P_{mw,h_w}^t of WTG w at node m and time t can be calculated based on wind speeds using (4.21):

$$P_{mw,h_w}^t = \begin{cases} 0 & 0 \leq V_{w,h_w}^t \leq V_{ci} \\ \left[A + B \cdot V_{w,h_w}^t + C \cdot (V_{w,h_w}^t)^2 \right] \cdot P_r & V_{ci} \leq V_{w,h_w}^t \leq V_{rw} \\ P_r & V_{rw} \leq V_{w,h_w}^t \leq V_{co} \\ 0 & V_{co} \leq V_{w,h_w}^t \end{cases} \quad (4.21)$$

where V_{ci} , V_{co} and V_{rw} are the cut-in speed, cut-out speed, and rated speed of WTG w at time t , respectively. A , B and C are functions of operational parameters presented in [26]. P_r is the rated power of WTG w when wind speed is between the rated speed and the cut-out speed.

Due to the power imbalance caused by the output reduction of GPPs or initial failures, the generation re-dispatch of CFGs or load shedding can be determined using OPF techniques [27]. The objective function is to minimize the total system cost at time t , including power generation costs and electric load curtailment costs.

$$\text{Min} \sum_{m=1}^M C_{mf}(P_{mf}^{t+\Delta t}) + C_{mL}(LC_m^{t+\Delta t}) \quad (4.22)$$

Subject to the following constraints:

1) *Power balance constraints:*

$$\begin{aligned} P_{mg}^{t+\Delta t} + a_{mg} \cdot P_{mf}^{t+\Delta t} + P_{mw,h_w}^t - (D_{mL}^t - LC_m^{t+\Delta t}) \\ = \sum_{n=1}^M |V_m^{t+\Delta t}| |V_n^{t+\Delta t}| |Y_{mn}^{t+\Delta t}| \cos(\theta_m^{t+\Delta t} - \theta_n^{t+\Delta t}) \end{aligned} \quad (4.23)$$

$$\begin{aligned} Q_{mg}^{t+\Delta t} + a_{mg} \cdot Q_{mf}^{t+\Delta t} - (Q_{mL}^t - \Delta Q_m^{t+\Delta t}) \\ = \sum_{n=1}^M |V_m^{t+\Delta t}| |V_n^{t+\Delta t}| |Y_{mn}^{t+\Delta t}| \sin(\theta_m^{t+\Delta t} - \theta_n^{t+\Delta t}) \end{aligned} \quad (4.24)$$

2) *Generating unit limits:*

$$\underline{P}_{mf} \leq P_{mf}^{t+\Delta t} \leq \overline{P}_{mf} \quad (4.25)$$

$$\underline{Q}_{mf} \leq Q_{mf}^{t+\Delta t} \leq \overline{Q}_{mf} \quad (4.26)$$

$$\underline{Q}_{mg} \leq Q_{mg}^{t+\Delta t} \leq \overline{Q}_{mg} \quad (4.27)$$

3) *Ramping rate constraints:*

$$P_{mf}^t - RD_{mf} \leq P_{mf}^{t+\Delta t} \leq P_{mf}^t + RU_{mf} \quad (4.28)$$

4) *Load curtailment limits:*

$$0 \leq LC_m^{t+\Delta t} \leq D_{mL}^t \quad (4.29)$$

$$0 \leq \Delta Q_m^{t+\Delta t} \leq Q_{mL}^t \quad (4.30)$$

5) *Line flow constraints:*

$$|S_{mn}^{t+\Delta t}| \leq \overline{S}_{mn} \quad (4.31)$$

6) *Nodal phase and voltage constraints:*

$$\underline{\theta}_m \leq \theta_m^{t+\Delta t} \leq \overline{\theta}_m \quad (4.32)$$

$$\underline{V}_m \leq V_m^{t+\Delta t} \leq \overline{V}_m \quad (4.33)$$

After solving the OPF model in (4.22)-(4.33), the power $D_{mL}^t - LC_m^{t+\Delta t}$ supplied to the EGSs and P2G facilities at time $t+\Delta t$ can be determined. Hence, the operating conditions of EGSs and gas production of P2G facility at node i can be calculated using (4.7) and (4.8), respectively.

4.3.5 Stopping criterion of cascading effects

Due to the interdependence between the two systems, the re-dispatch of the power system and NGS will alternate at different time periods until the stopping criterion is satisfied. The cascading effects in IEGS stop when the operating conditions of NGS and power system at time t are identical to those at time $t + \Delta t$, which can be expressed as:

$$\delta = 1(P_{mg}^t = P_{mg}^{t+\Delta t}) \cdot 1(p_{D,i}^t = p_{D,i}^{t+\Delta t}) \cdot 1(Q_{D,i}^t = Q_{D,i}^{t+\Delta t}) \quad (4.34)$$

where $1(\text{True}) \equiv 1$ and $1(\text{False}) \equiv 0$. Therefore, the cascading effects in IEGS will stop when both the NGS and power system reach stable operation states, which corresponds to $\delta = 1$.

4.4 Risk analysis of IEGS considering cascading effects using MCS techniques

Based on the dynamic cascaded analysis model in the previous section, a framework is proposed for the risk evaluation of IEGS considering cascading effects utilizing MCS techniques. The assessment flowchart is shown in Fig. 4.4. Details of the evaluation framework are presented as follows.

4.4.1 Risk indices

Many indices have been introduced to evaluate the system and load point risk [2]. In this chapter, the expected energy not supplied and the loss of load probability are introduced to evaluate the reliabilities of IEGS.

Supposing the time t for simulating cascading effects is from 0 to T with Δt time step, the expected electricity not supplied ($EENS_m$) and the loss of electric load probability ($LOELP_m$) at node m can be calculated as:

$$EENS_m = \sum_{st=1}^{ST} \sum_{t=0}^T LC_m^t / ST \quad (4.35)$$

$$LOELP_m = \sum_{st=1}^{ST} \left(\sum_{t=0}^T LC_m^t > 0 \right) / ST \quad (4.36)$$

After obtaining the $EENS_m$, the system's $EENS$ can be evaluated based on the following equation:

$$EENS = \sum_{m=1}^M \sum_{st=1}^{ST} \sum_{t=0}^T LC_m^t / ST \quad (4.37)$$

Likewise, the expected gas not supplied ($EGNS_i$) at node i , the loss of gas load probability ($LOGLP_i$) at node i and system $EGNS$ can be defined as:

$$EGNS_i = \sum_{st=1}^{ST} \sum_{t=0}^T \Delta W_{il}^t / ST \quad (4.38)$$

$$LOGLP_i = \sum_{st=1}^{ST} \left(\sum_{t=0}^T \Delta W_{il}^t > 0 \right) / ST \quad (4.39)$$

$$EGNS = \sum_{i=1}^N \sum_{st=1}^{ST} \sum_{t=0}^T \Delta W_{il}^t / ST \quad (4.40)$$

In addition, the occurrence of cascading effects can be judged by determining if additional coupled components are failed during the simulation. If the load curtailments lead to the failures of additional coupled components, the subsequent failure order it will increase correspondingly. Hence, the probability for the occurrence of cascading effects ($POCE$) can be calculated as:

$$POCE = \sum_{st=1}^{ST} \left(it \geq 2 \right) / ST \quad (4.41)$$

Note that $it < 2$ corresponds to no cascading effects, whereas the cascading effects occur in IEGS for $it \geq 2$.

4.4.2 Simulation procedures

As illustrated in Fig. 4.4, the process for the risk evaluation of IEGS can be divided into three steps. The first step is to specify the initial state of the IEGS, where the initial parameters of components in IEGS are set.

The second step is the risk analysis of IEGS using MCS techniques. Based on the risk parameters of components, the initial failures can be obtained by random-

ly sampling the component states according to their failure probabilities. For certain initial failures, the cascading effects between NGS and power systems are simulated utilizing the dynamic cascaded analysis model in section III to determine the load curtailments. Repeat the previous procedures until the stopping criterion for the MCS technique is satisfied.

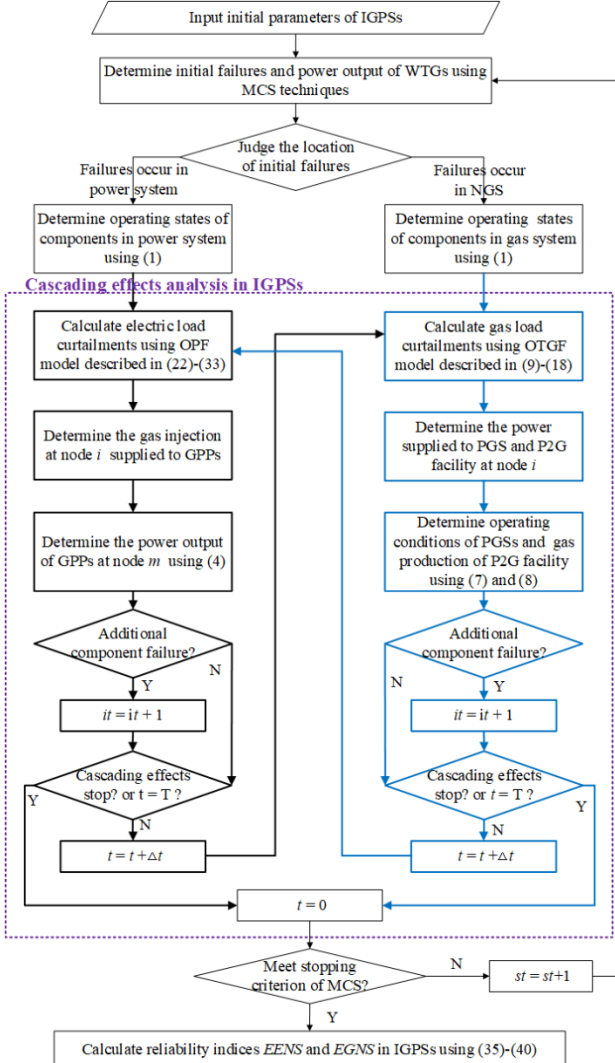


Fig. 4.4 The framework for risk analysis of IEGS considering cascading effects using the MCS technique

The stopping criterion given for the simulation is the minimum value between $EENS$ and $EGNS$ coefficients.

$$\beta = \max\left(\sqrt{V(EENS)}/EENS, \sqrt{V(EGNS)}/EGNS\right) \quad (4.42)$$

where $V(EENS)$ and $V(EGNS)$ are the variances of $EENS$ and $EGNS$, respectively.

Based on the load curtailments for each initial failure, the third step is to calculate risk indices for both NGS and power systems using (4.35)-(4.40).

4.5 System studies

The IEGSs shown in Fig. 4.5 are composed of the IEEE 30-bus power system from [28] and the Belgian 20-node gas system detailed in [29]. The power system is composed of 41 branches, 21 loads, and 6 generating units. There are three GPPs (G1, G4, and G5), three CFGs (G2 and G3), and one WTG (G6) that constitute the generation fleet. The Belgian 20-node gas system has 19 pipelines, 3 compressors, 3 EGSSs, 3 FGSSs, 1 P2G facility, and 9 loads. The GPPs G1, G5, and G4 at electric nodes 1, 13, and 8 are supplied from the gas flow at gas nodes 10, 16, and 6 through connections C1, C2, and C3, respectively. In addition, the EGSSs W3, W4, and W2 at gas nodes 8, 13, and 2 obtain power supply from electric nodes 29, 3, and 20 through connections B1, B2, and B3, respectively. The P2G facility at gas node 5 produces gas with electricity from electric node 23 through connection B4.

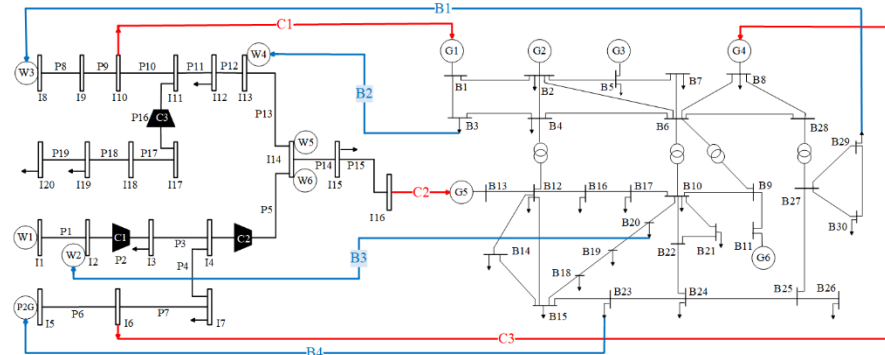


Fig. 4.5 Test system composed of the IEEE 30-bus power system and Belgian 20-node gas system

The physical parameters of pipelines (such as diameter and length) and compressors (such as maximum compressor ratio) can be found in [29]. The ambient temperatures of gas pipelines are assumed as normal. The parameters for modeling transient gas flow are shown in Table 4.1. The detailed parameters for the production capacity of gas sources and gas demand at different nodes are shown in Table 4.8 of Appendix C [29]. The interruption costs of gas are set according to the data in [16]. The energy conversion of P2G facilities is set as $0.09 \text{ m}^3/\text{KW}$ [23]. The conversion factor of EGSSs is assumed to be 0.1 KW/m^3 [30]. Regarding power systems, the detailed parameters for the generation capacity of CFGs and electric demand at different nodes are shown in Table 4.9 of Appendix C. The multi-state

model for the power output of WTGs can be found in [26]. The interruption costs of customers in power systems are set as 2000 \$/MW [31]. The unavailability of gas sources and power generators is set as 0.05 and 0.07, respectively [9]. The stopping criterion for the MCS method is $\beta \leq 0.02$.

Table 4.1 Parameters for modeling transient gas flow

Parameter	Value	Parameter	Value
R (J/kgK)	518.28	Δt (s)	300
ψ (K)	281.15	v (m/s)	348.5
ρ_n (kg/m ³)	0.6106	T (h)	24

The formulation of the cascading effects of IEGS is accomplished by Matlab R2018b. With piecewise linearization techniques, the OTGF model is converted into a linear programming (LP) problem, which can be solved by the Cplex solver. The OPF problem is formulated as a nonlinear optimization problem which is solved by a primal-dual interior-point solver called Matlab Interior Point Solver (MIPS). The study cases are tested by a computer with Intel 1.6 GHz 4-core processor (6 MB L3 cache) and 8 GB memory.

4.5.1 Case 1: impacts of cascading effects on nodal risk

Three scenarios with different interdependence are modeled to evaluate the impacts of cascading effects on the reliabilities of IEGS. All the GPPs G1, G5, and G4 are assumed to obtain gas supply from NGS in three scenarios, whereas different connections from power systems to NGS are considered in these scenarios. **Scenario 1** is the base scenario without considering the cascading effects in IEGS, where all the gas sources are FGSSs that do not get electric supply from power systems. Compared to scenario 1, the gas sources W3 and W4 obtain power supply through connections B1 and B2 in **scenario 2**. In **scenario 3**, the gas sources W3, W4, W2, and P2G need to get electric supply from power systems. Therefore, different levels of interdependence-induced cascading effects are considered in scenarios 2 and 3 through connections from power systems to NGS.

The risk indices $EGNS_i$ (m³), $LOGLP_i$ in NGS and $EENS_m$ (MWh), $LOELP_m$ in power systems at different nodes for different scenarios are shown in Tables 4.2 and 4.3, respectively.

Table 4.2 Risk indices in gas systems for different scenarios

Gas node	SCENARIO A		SCENARIO B		SCENARIO C	
	$LOGLP$	$EGNS$	$LOGLP$	$EGNS$	$LOGLP$	$EGNS$
3	0.001	296.81	0.002	461.87	0.003	1026.06
6	0.004	1272.82	0.006	1724.68	0.010	3386.22
7	0.003	542.43	0.006	790.58	0.009	2102.19
10	0.005	1061.78	0.007	1582.56	0.010	3526.19
12	0.004	724.52	0.006	985.73	0.007	1021.83
15	0.001	466.42	0.002	824.22	0.008	1401.29

16	0.005	3835.86	0.017	5643.32	0.030	10886.1
19	0.006	442.79	0.008	410.85	0.009	499.91
20	0.007	2773.35	0.019	4324.13	0.033	5469.88

Table 4.3 Risk indices in power systems for different scenarios

Electric node	SCENARIO A		SCENARIO B		SCENARIO C	
	LOELP	EENS	LOELP	EENS	LOELP	EENS
2	0.055	2.463	0.063	4.516	0.079	6.594
4	0.058	1.766	0.060	2.267	0.084	3.475
6	0.000	0.000	0.000	0.000	0.000	0.000
8	0.063	2.758	0.065	5.574	0.081	10.402
10	0.060	1.110	0.065	1.514	0.083	2.189
12	0.060	2.068	0.065	2.383	0.083	3.875
14	0.060	1.274	0.065	1.383	0.083	2.270
16	0.060	1.199	0.065	1.517	0.083	2.211
18	0.060	0.741	0.061	0.982	0.083	1.505
20	0.060	0.443	0.065	0.607	0.083	1.054
22	0.000	0.000	0.000	0.000	0.000	0.000
24	0.060	0.864	0.061	1.038	0.083	1.760
26	0.060	0.502	0.061	0.699	0.083	1.226
28	0.000	0.000	0.000	0.000	0.000	0.000
30	0.060	1.001	0.065	1.267	0.083	2.133

Regarding the NGS, both $EGNS$ and $LOGLP$ values increase significantly when considering the cascading effects between power systems and NGS. The system $EGNS$ values in NGS are $1.141 \times 10^4 \text{ m}^3$, $1.675 \times 10^4 \text{ m}^3$, and $2.932 \times 10^4 \text{ m}^3$ for scenarios 1, 2, and 3, respectively. Moreover, it can be noted that there are very large differences between risk indices at different nodes. The $EGNS_i$ at node 16 is the largest among all the gas nodes, whereas the $EGNS_i$ at node 19 is relatively small for all scenarios. This is mainly because the gas loads at nodes 10, 16, and 6 are under interruptible contracts with GPPs and will be firstly curtailed in contingency states.

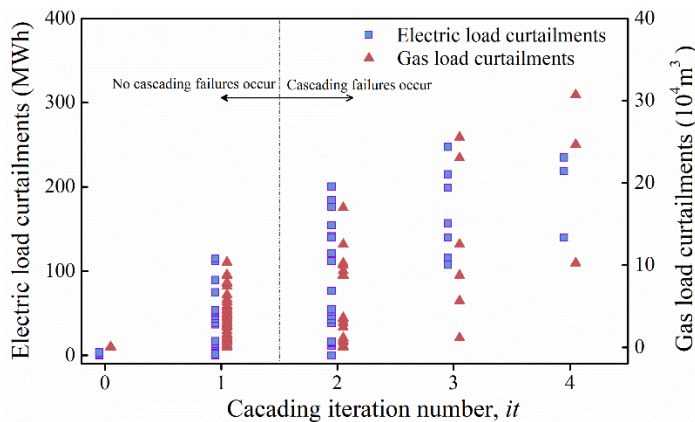
Regarding the power system, it can be seen from Table 4.3 that the $EENS$ and $LOELP$ values increase significantly when considering the cascading effects in IEGS. The system $EENS$ is 29.50 MWh for scenario 1 and increases to 72.49 MWh for scenario 3. In addition, there are also large differences between $EENS_m$ values at different electric nodes. The values of $EENS_m$ at nodes 2 and 8 are relatively large, which are 6.594 MWh and 10.402 MWh for scenario 3, respectively. In contrast, the $EENS_m$ values at nodes 6, 22, and 28 are close to zero for all scenarios. Moreover, the variation trend of $LOELP_m$ values at each node is in accordance with that of $EENS_m$ values.

Table 4.4 Impacts of cascading effects on the risk of IEGS

Indices	SCENARIO 1	SCENARIO 2	SCENARIO 3
System <i>EENS</i> (MWh)	29.50	42.26	72.49
System <i>EGNS</i> (m^3)	11416.7	16747.9	29319.7
<i>POCE</i>	0	0.034	0.072

To investigate the impacts of cascading effects on the reliabilities of IEGS, the *POCE* indices for different scenarios are calculated, as shown in Table 4.4. It can be noted that the increase of interdependence between NGS and power systems can increase the risk of the cascading effects occurring in IEGS. The values of *POCE* in scenarios 1, 2, and 3 are 0, 0.034, and 0.072 respectively. Although the probability for the occurrence of cascading effects is relatively small for scenario 3, their impacts on the reliabilities of IEGS can be significant. It is seen from Table 4.4 that both the system *EENS* and *EGNS* increase sharply from scenario 1 to scenario 3, indicating the reliabilities of IEGS are significantly reduced. Therefore, the cascading effects in IEGS can be regarded as high-impact and low-probability events.

Moreover, the correlations between load curtailments and cascading iteration number it for each simulation time are investigated, as shown in Fig. 4.6. One of the observations is that both the electric and gas load curtailments are positively related to it . Compared to the scenarios where no cascading effects ($it \leq 2$) are considered, the electric and gas load curtailments increase nearly 3 times for $it \geq 3$. Therefore, more load curtailments may be caused during contingencies when considering the cascading effects between two systems, which can significantly reduce the reliabilities of IEGS.

**Fig. 4.6** Correlations between load curtailments and cascading iteration numbers

4.5.2 Case 2: test on the larger scale systems

In order to validate the effectiveness of the proposed technique on larger test systems, two scenarios based on systems with different dimensions are considered

in this case. The power systems used in scenarios A and B are the modified IEEE 118-bus [32] and IEEE 300-bus systems [33], respectively. It is assumed that seven GPPs at electric nodes 19, 46, 59, 70, 87, 103, and 111 in scenario A, at electric nodes 19, 80, 132, 156, 199, 222, and 262 in scenario B are supplied from the gas flow at gas nodes 3, 6, 10, 12, 15, 16 and 20 of NGS, respectively. On the other hand, five EGSSs at gas nodes 1, 2, 5, 8, and 13 obtain power supply from electric nodes 108, 102, 23, 73, and 113 in scenario A, electric nodes 87, 155, 232, 168, and 285 in scenario B, respectively. The generators at electric nodes 8, 36, 56, 91, and 116 in scenario A, at electric nodes 117, 135, 169, 253, and 295 in scenario B are assumed as WTGs, whose power output model can be found in [26]. The detailed parameters of NGS in these two scenarios are the same as those of the previous case. The risk parameters of CFGs and GPPs can be found in [9]. Moreover, the stopping criterion for the MCS method is $\beta \leq 0.02$.

Table 4.5 Risk indices in power system for scenarios A and B

Scenario A (118-bus system)		Scenario B (300-bus system)	
Node	EENS	Node	EENS
4	37.310	4	37.310
12	0.248	12	0.248
20	0.788	20	0.788
28	0.347	28	0.347
39	18.483	39	18.483
47	35.121	47	35.121
51	1.403	51	1.403
57	0.239	57	0.239
67	18.955	67	18.955
76	3.878	76	3.878
86	8.205	86	8.205
97	6.316	97	6.316
103	0.099	103	0.099
112	0.179	112	0.179

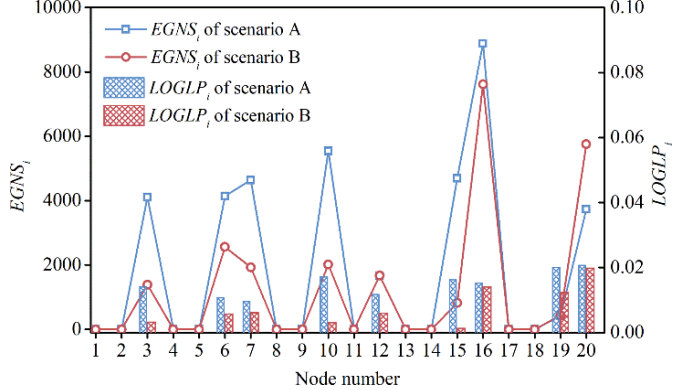


Fig. 4.7 Risk indices of NGS for scenarios A and B

Table 4.6 System risk indices of IEGS in scenarios A and B

Scenarios	System EENS (MWh)	System EGNS (m^3)	POCE
A (118-bus system)	1163.17	37833.84	0.046
B (300-bus system)	1724.78	24199.08	0.011

The risk indices $EENS_m$ (MWh), $LOELP_m$ in power systems and $EGNS_i$ (m^3), $LOGLP_i$ in NGS at different nodes for scenarios A and B are given in Table 4.5 and Fig. 4.7, respectively. Similar to case 1, there also exist significant differences between risk indices at different nodes in both the power system and NGS. Table 4.6 lists the system risk indices of IEGS for scenarios A and B. Although the value of $POCE$ in scenario A increases slightly compared to scenario B, the system $EGNS$ in scenario A can be significantly larger than that in scenario B. The findings imply that the risk of IEGS can be significantly reduced considering cascading effects.

4.5.3 Computation time of risk evaluation

The computation time of the risk evaluation of IEGS for different scenarios in cases 1 and 2 is shown in Table 4.7. It can be noted the computation time of scenario A is smaller than that of scenario C in case 1 since the cascading effects of IEGS are considered in scenario C. Moreover, it can be noted that the computation time of the MCS method for obtaining the results increases a lot with the increase in system size. The computation time in scenarios A and B of case 2 is 2.5 and 3.9 times that in scenario C of case 1, respectively. Since the risk evaluation of IEGS considering cascading effects can be performed offline, the computation time of larger systems is acceptable in real applications [34]. Moreover, the application of modern computers and dedicated machines can also lead to the reduction of computation time for risk evaluation of large-scale systems [2].

Table 4.7 System risk indices of IEGS in scenarios A and B

Cases	Scenarios	Computation time (s)
-------	-----------	----------------------

	Scenario A	6204.68
Case 1	Scenario B	8265.93
	Scenario C	13313.87
Case 2	Scenario A	33543.02
	Scenario B	52659.72

4.6 Conclusion

The interdependence between NGS and power systems entails the need to integrate the cascading effects into the risk analysis of IEGS. This chapter proposes an approach to evaluate the reliabilities of IEGS considering the cascading effects. The dynamic cascaded analysis model is developed to describe the temporal and spatial process of cascading effects considering different dynamic behaviors between power systems and NGS. Moreover, the simulation framework for the risk evaluation of IEGS considering the interdependence-induced cascading effects is proposed by combining the dynamic cascaded analysis model and MCS techniques. Furthermore, the impacts of cascading effects on the nodal reliabilities of IEGS are evaluated in two cases. We find that the reliabilities of IEGS can be significantly reduced when considering dynamic cascading effects between NGS and power systems. The impacts of cascading effects on the risk of IEGS can differ at different nodes. Besides, the results reveal the high-impact and low-probability characteristics of cascading effects.

Appendix A

Generally, the transient gas flow in pipelines can be described by the equations of state (4.43), continuity (4.44), and motion (4.45):

$$\frac{p}{\rho_n} = Z_c R \psi = v^2 \quad (4.43)$$

$$\frac{v^2}{A} \frac{\partial M}{\partial l} + \frac{\partial p}{\partial t} = 0 \quad (4.44)$$

$$\frac{p \partial p}{\partial l} \left(1 - \frac{v^2 M^2}{A^2 p^2} \right) + \frac{2v^2 M |M|}{F^2 dA^2} + \frac{1}{A} \left(p \frac{\partial M}{\partial t} + \frac{v^2}{A} \frac{\partial M^2}{\partial l} \right) = 0 \quad (4.45)$$

where p is gas pressure (Pa); M is the mass flow rate (kg/s); l is the distance of pipelines (m); A is the pipeline's cross-sectional area (m^2).

In real operation conditions, the adoption of some simplification hypotheses in (4.45) can be accepted. The term $\frac{\partial p}{\partial l} \frac{v^2 M^2}{A^2 p}$ represents the force of gravity which can

be simplified for horizontal pipes [16]. The two terms $p \frac{\partial M}{\partial t}$ and $\frac{v^2}{A} \frac{\partial M^2}{\partial l}$ describing the gas inertia and kinetic energy, respectively, can be neglected since they only account for less than 1% of the solution in (4.45) under normal conditions [16]. Instead of using mass flow rate M , the volumetric flow rate Q (m^3/s) is intro-

duced by $Q = M/\rho_n$ [24]. Therefore, the continuity and motion equations of pipelines can be written as:

$$\frac{\rho_n v^2}{A} \frac{\partial Q}{\partial l} + \frac{\partial p}{\partial t} = 0 \quad (4.46)$$

$$\frac{p \cdot \partial p}{\partial l} + \frac{2\rho_n^2 v^2 Q |Q|}{F^2 dA^2} = 0 \quad (4.47)$$

The implicit method of finite differences is utilized to discretize the continuity and motion equations in time and space. As shown in Fig. 4.8, the pipeline with length l is divided into segments with length Δl . Let $Q_{D,i}^t$ and $p_{D,i}^t$ denote the pressure and flow rate at the beginning point i of pipeline D at time t , respectively. Then at time $t + \Delta t$, a finite difference method can be used to resolve the respective values of pressures and flow rates $p_{D,i}^{t+\Delta t}$ and $Q_{D,i}^{t+\Delta t}$. Therefore, the continuity and motion equations of pipelines can be approximated by the difference equations, as shown in (4.10) and (4.11), respectively.

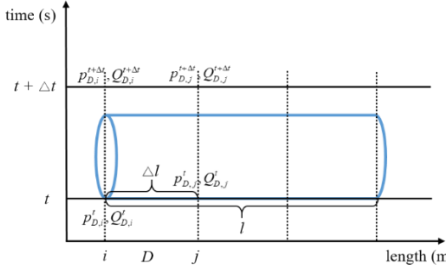


Fig. 4.8 Finite difference method for determination of transient flow equations

The determination of time step Δt used in the finite difference method needs to weigh up many factors, such as the calculation time, the accuracy of the results and etc. [35] Taking into these factors, the time step Δt is usually selected as 300s [16].

Appendix B

Corresponding to the motion equation in (11), the average flow squared $\bar{Q}_{D,ij}^{t+\Delta t} \cdot |\bar{Q}_{D,ij}^{t+\Delta t}|$ and pressures squared $(p_{D,j}^{t+\Delta t})^2$ need to be linearized with piecewise linearization techniques [16]. Taking $\bar{Q}_{D,ij}^{t+\Delta t} \cdot |\bar{Q}_{D,ij}^{t+\Delta t}|$ as an example, it can be regarded as the general form $h(x) = x \cdot |x|$ defined on an interval $L = [L_1, L_2]$, where $x = \bar{Q}_{D,ij}^{t+\Delta t}$. Regarding gas flow rates $\bar{Q}_{D,ij}^{t+\Delta t}$, the operating interval $[L_1, L_2]$ can be determined by the pipeline capacity. By dividing the operating interval at the demarcation points $L_1 = X_1 \leq L \leq X_z \leq L \leq X_Z = L_2$ with corresponding function values

$h(X_z)$, the nonlinear function $h(x) = x \cdot |x|$ can be separated into $Z-1$ linear segments. On this basis, the method to approximate $h(x)$ can be formulated as follows:

$$h(x) \approx h(X_1) + \sum_{z=1}^{Z-1} [h(X_{z+1}) - h(X_z)] \delta_z \quad (4.48)$$

$$x = X_1 + \sum_{z=1}^{Z-1} (X_{z+1} - X_z) \delta_z \quad (4.49)$$

$$\delta_{z+1} \leq \sigma_z \leq \delta_z, \quad z \in \{1, L, Z-2\} \quad (4.50)$$

$$0 \leq \delta_z \leq 1, \quad z \in \{1, L, Z-1\} \quad (4.51)$$

where δ_z denotes continuous variable representing the portion of pipeline flow. σ_z is binary variable to force that if an interval $[X_{z-1}, X_z]$ is chosen, all intervals to its left must be completely used.

Appendix C

Tables 4.8 and 4.9 list the production capacity of gas sources and gas demand at different nodes in NGS [29], the generation capacity of CFGs, and electric demand at different nodes in power systems, respectively.

Table 4.8 Production capacity of gas sources and gas demand at different nodes in NGS

Node	Source capacity/ Gas demand ($10^4 \text{ m}^3/\text{h}$)	Node	Source capacity/ Gas demand ($10^4 \text{ m}^3/\text{h}$)
1	4.329/0	10	0/2.652
2	5.250/0	13	2.833/0
3	0/1.632	14	2.433+2.291/0
5	3.833/0	15	0/2.853
6	0/1.681	16	0/6.507
7	0/2.190	19	0/0.092
8	6.255/0	20	0/0.799

Table 4.9 Generation capacity of CFGs and electric demand at different nodes in power systems

Node	Generation capacity/ Electric demand(MW)	Node	Generation capacity/ Electric demand(MW)
2	140/21.7	16	0/3.5
3	0/2.4	14	0/9.0
4	0/7.6	18	0/3.2
5	100/94.2	19	0/9.5
7	0/22.8	20	0/2.2
8	0/30	21	0/17.5
9	0/0	23	0/3.2
10	0/5.8	24	0/8.7

12	0/11.2	26	0/3.5
14	0/6.2	29	0/2.4
15	0/8.2	30	0/10.6

Reference

- [1] “Severe weather event of February, 2011 and its cascading impacts on utility service. [online].”
- [2] R. Billinton, and N. R. Allan, *Reliability evaluation of power systems*, 2nd ed. New York, NY, USA: Plenum, 1996.
- [3] C. Singh, and R. Billinton, *System reliability, modelling and evaluation*, London: Hutchinson 1977.
- [4] P. Wang, R. Billinton, and L. Goel, “Unreliability cost assessment of an electric power system using reliability network equivalent approaches,” *IEEE Transactions on power systems*, vol. 17, no. 3, pp. 549-556, 2002.
- [5] B. S. Dhillon, and C. Singh, *Engineering reliability: new techniques and applications*.
- [6] Y. Ding, C. Singh, L. Goel *et al.*, “Short-Term and Medium-Term Reliability Evaluation for Power Systems With High Penetration of Wind Power,” *IEEE Transactions on Sustainable Energy*, vol. 5, no. 3, pp. 896-906, Jul, 2014.
- [7] Z. Zeng, T. Ding, Y. Xu *et al.*, “Reliability Evaluation for Integrated Power-Gas Systems with Power-to-Gas and Gas Storages,” *IEEE Transactions on Power Systems*, vol. 35, no. 1, pp. 571-583, 2019.
- [8] W. Sheng, D. Yi, Y. Chengjin *et al.*, “Reliability evaluation of integrated electricity–gas system utilizing network equivalent and integrated optimal power flow techniques,” *Journal of Modern Power Systems and Clean Energy*, pp. 1-13, 2019.
- [9] M. Bao, Y. Ding, C. Singh *et al.*, “A multi-state model for reliability assessment of integrated gas and power systems utilizing universal generating function techniques,” *IEEE Transactions on Smart Grid*, vol. 10, no. 6, pp. 6271-6283, 2019.
- [10] Y. Lei, K. Hou, Y. Wang *et al.*, “A new reliability assessment approach for integrated energy systems: using hierarchical decoupling optimization framework and impact-increment based state enumeration method,” *Applied energy*, vol. 210, pp. 1237-1250, 2018.
- [11] H. Zhang, T. Zhao, P. Wang *et al.*, “Power system resilience assessment considering of integrated natural gas system,” 2017.
- [12] X. Zhang, L. Che, M. Shahidehpour *et al.*, “Reliability-based optimal planning of electricity and natural gas interconnections for multiple energy hubs,” *IEEE Transactions on Smart Grid*, vol. 8, no. 4, pp. 1658-1667, 2015.
- [13] M. Bao, Y. Ding, C. Shao *et al.*, “Nodal Reliability Evaluation of Interdependent Gas and Power Systems Considering Cascading Effects,”

- IEEE Transactions on Smart Grid*, vol. 11, no. 5, pp. 4090-4104, Mar, 2020.
- [14] W. Wang, S. Yang, F. Hu *et al.*, “An approach for cascading effects within critical infrastructure systems,” *Physica A: Statistical Mechanics and its Applications*, vol. 510, pp. 164-177, 2018.
 - [15] G. Pescaroli, and D. Alexander, “Critical infrastructure, panarchies and the vulnerability paths of cascading disasters,” *Natural Hazards*, vol. 82, no. 1, pp. 175-192, 2016.
 - [16] C. M. Correa-Posada, and P. Sánchez-Martín, “Integrated power and natural gas model for energy adequacy in short-term operation,” *IEEE Transactions on Power Systems*, vol. 30, no. 6, pp. 3347-3355, 2015.
 - [17] R. Yao, S. Huang, K. Sun *et al.*, “A multi-timescale quasi-dynamic model for simulation of cascading outages,” *IEEE Transactions on Power Systems*, vol. 31, no. 4, pp. 3189-3201, 2015.
 - [18] A. Mehrtash, P. Wang, and L. Goel, “Reliability evaluation of power systems considering restructuring and renewable generators,” *IEEE Transactions on Power Systems*, vol. 27, no. 1, pp. 243-250, 2012.
 - [19] G. Pettit, and B. Morgan, “A tool to estimate the failure rates of cross-country pipelines,” *Hazards XXI: Process Safety and Environmental Protection in a Changing World. IChemE, London*, vol. 294, pp. 302, 2009.
 - [20] A. Martinez-Mares, and C. R. Fuerte-Esquivel, “A unified gas and power flow analysis in natural gas and electricity coupled networks,” *IEEE Transactions on Power Systems*, vol. 27, no. 4, pp. 2156-2166, 2012.
 - [21] K. A. Pambour, B. Cakir Erdener, R. Bolado-Lavin *et al.*, “Development of a simulation framework for analyzing security of supply in integrated gas and electric power systems,” *Applied Sciences*, vol. 7, no. 1, pp. 47, 2017.
 - [22] J. Yang, N. Zhang, Y. Cheng *et al.*, “Modeling the operation mechanism of combined P2G and gas-fired plant With CO₂ recycling,” *IEEE Transactions on Smart Grid*, vol. 10, no. 1, pp. 1111-1121, 2019.
 - [23] Q. Zeng, J. Fang, J. Li *et al.*, “Steady-state analysis of the integrated natural gas and electric power system with bi-directional energy conversion,” *Applied energy*, vol. 184, pp. 1483-1492, 2016.
 - [24] S. Clegg, and P. Mancarella, “Integrated modeling and assessment of the operational impact of power-to-gas (P2G) on electrical and gas transmission networks,” *IEEE Transactions on Sustainable Energy*, vol. 6, no. 4, pp. 1234-1244, 2015.
 - [25] Y. Zhou, C. Gu, H. Wu *et al.*, “An equivalent model of gas networks for dynamic analysis of gas-electricity systems,” *IEEE Transactions on Power Systems*, vol. 32, no. 6, pp. 4255-4264, 2017.
 - [26] R. Karki, P. Hu, and R. Billinton, “A simplified wind power generation model for reliability evaluation,” *IEEE transactions on Energy conversion*, vol. 21, no. 2, pp. 533-540, 2006.

- [27] C. M. Correa-Posada, and P. Sánchez-Martin, “Security-constrained optimal power and natural-gas flow,” *IEEE Transactions on Power Systems*, vol. 29, no. 4, pp. 1780-1787, 2014.
- [28] C. Shao, Y. Ding, J. Wang *et al.*, “Modeling and integration of flexible demand in heat and electricity integrated energy system,” *IEEE Transactions on Sustainable Energy*, vol. 9, no. 1, pp. 361-370, 2018.
- [29] D. De Wolf, and Y. Smeers, “The gas transmission problem solved by an extension of the simplex algorithm,” *Management Science*, vol. 46, no. 11, pp. 1454-1465, 2000.
- [30] *Energy use in offshore oil and gas production: trends and drivers for efficiency from 1975 to 2025*, Vanner Robin, Policy Studies Institute, 2005.
- [31] A. P. Sanghvi, “Measurement and application of customer interruption costs/value of service for cost-benefit reliability evaluation: some commonly raised issues,” *IEEE Transactions on Power Systems*, vol. 5, no. 4, pp. 1333-1344, 1990.
- [32] Y. Lin, Y. Ding, Y. Song *et al.*, “A Multi-State Model for Exploiting the Reserve Capability of Wind Power,” *IEEE Transactions on Power Systems*, vol. 33, no. 3, pp. 3358-3372, 2018.
- [33] S. Chakrabarti, E. Kyriakides, G. Ledwich *et al.*, “Inclusion of PMU current phasor measurements in a power system state estimator,” *IET generation, transmission & distribution*, vol. 4, no. 10, pp. 1104-1115, 2010.
- [34] K. Morison, L. Wang, and P. Kundur, “Power system security assessment,” *IEEE power and energy magazine*, vol. 2, no. 5, pp. 30-39, 2004.
- [35] E. B. Wylie, M. A. Stoner, and V. L. Streeter, “Network: System transient calculations by implicit method,” *Society of Petroleum Engineers Journal*, vol. 11, no. 04, pp. 356-362, 1971.

5 Definitions and Risk Modeling of Two-Interdependent-Performance Multi-State System and its Application for CHP units

5.1 Introduction

The above three chapters mainly focus on the risk evaluation in the transmission-side of multi-energy systems, i.e. integrated electricity and gas systems. On the distribution side, the risk of integrated electricity and heating systems can also be an important problem, which is closely related to the operation of coupled components, i.e. combined heat and power (CHP) units. To analyze and evaluate the risk of the CHP units, the multi-state system (MSS) models can be adopted in this chapter. Recently, the MSS models have been widely used in the risk evaluation of real-life engineering systems [1-3]. In the MSS theory, a system can perform its intended task with various performance rates. For example, a wind turbine has a single task to perform, i.e., producing electricity, and there could be different performance rates corresponding to the turbine's different available capacities depending on the wind speed. Hence, an MSS can be represented by a finite number of states and the corresponding probabilities, representing different performance rates that can be achieved. The basic concepts and comprehensive presentations of the MSS theory and its applications can be found in [4-6]. Moreover, MSS models are very flexible and can be extended to handle different situations [7]. The MSS modeling in which the surplus performance of a component can be shared with other components was proposed in [8]. The MSS models used in the k -out-of- n system structure have also been proposed and well developed in [9-17]. There are also some studies conducted on developing algorithms for analyzing the risk of the MSS models [18, 19].

In these previous researches, it is usually assumed that the MSS only has one intended task to complete. Therefore, the risk of the MSS can be sufficiently measured by a single performance variable. The risk of a wind turbine, for example, can be measured by a single performance variable, i.e., the capacity of its electric power output. However, there are many systems designed to complete different tasks simultaneously. Therefore, different performance variables are necessary for indicating the risk of such systems. A new multi-state vector- k -out-of- n system model has been proposed in [20], which can describe the stochastic behavior of a wide class of multiple line flow transmission systems, and production and service systems with multiple resource consumption. Authors in [21] have presented the multi-performance multi-state system (MPMSS) model, as another example of the performance vector application. In [21], the performance rate of an MPMSS in each state is represented by a performance vector. Each element in the performance vector corresponds to the capacity of a performance measure in this state. The representation of the performance variables in the vector form allows us to analyze different performances separately and independently. Therefore, the

risk evaluation technique developed in the single-performance MSS can be directly used in the MPMSS models.

However, the performance vector representation cannot take into account the interdependency between different performance variables, and therefore does not apply to the two-interdependent-performance MSS (TIP-mss). The TIP –MSSs are emerging with the development of integrated energy systems (or referred to as multi-carrier systems, energy hubs) [22-25]. The widely used combined heat and power (CHP) units produce both electricity and useful heat for consumers. Hence, the CHP-based systems need to consider two performance variables of electric power and heat power, which are influenced by each other. The operation of such a TIP-MSS is usually constrained by a two-dimension feasible operating region (FOR) specific to the state, which is enclosed by the operating constraints of the two performance variables. For example, the FOR of the CHP unit at its working state could be a quadrilateral area describing the constraints of its electric power capacity and heat power capacity [26, 27]. In other words, we can control the TIP-MSS operation, and correspondingly the system performance vector in each state can be freely chosen within the FOR in response to the load requirements. Moreover, the two performance variables are not always positively related within the FOR. Instead, there is usually a trade-off between one performance and the other. Hence, it is significant to find an object to represent the performance rates of the TIP-MSS in different states, similar to the concept of “capacity” in the single-performance MSS. In this chapter, the performance rate of the TIP-MSS in each state is represented by a performance trade-off curve corresponding to the upper boundary of the FOR. The upper boundary of the FOR is defined as a performance vector set. Given any performance vector within the FOR, a performance vector in the set can be found which is greater than or equal to it.

Concluded from the above discussion, a new modeling method should be developed for risk evaluation of the TIP systems. This chapter develops the TIP-MSS model for risk evaluation of such systems. In the TIP-MSS context, the system performance rate in each state is represented by the performance trade-off curve corresponding to the upper boundary of its FOR specific to this state. Then, the technique for risk evaluation of the TIP-MSS is proposed based on the UGF method. UGF is an effective approach for the system state enumeration and therefore has been widely used in the MSS risk and performance evaluation [28-30]. However, the well-known UGF method is more applicable to one-performance MSS or the MPMSS in which the interdependency between different performance variables is not considered. In this chapter, the classic UGF method is extended to handle the TIP-MSS models, and the concept of TIP-UGF is proposed. Different TIP-UGF composition operators, corresponding to the combination/intersection of the trade-off curves, are defined for analyzing the risk of TIP-MSS with parallel/series structures. Based on the TIP-UGF, the performance distribution of a TIP-MSS consisting of multiple components can be obtained. Moreover, the availability criterion based on the TIP-UGF representation is also proposed. It should be noted that the aleatory and epistemic uncertainties are not considered in

this chapter. However, reference [31] provides a possible solution to generalize the risk model to capture those uncertainties.

This chapter includes research related to definitions and the risk modeling of two-interdependent-performance multi-state systems by [32].

5.2 Definition of Two-Interdependent-Performance Multi-State Components

A two-interdependent-performance multi-state (TIP-MS) component has two intended tasks to complete and therefore is characterized by two performance variables. Moreover, the two performance variables are interdependent on and influenced by each other. In each state, values of the two interdependent performance variables follow a set of constraints, which form the FOR of this state. Following that, the formal definition of a TIP-MS component is given.

Definition 1: TIP-MS component. Component i has two performance variables denoted by $\bar{\mathbf{W}}_i = (\mathbf{W}_i^{(1)}, \mathbf{W}_i^{(2)})$. The component has $M+1$ states, such that $0 \leq j_i \leq M$ where $j_i = 0$ is the complete failure state and $j_i = M$ is the perfect performing state. The two performance variables in state j_i are represented by $\overline{\mathbf{W}}_{i,j_i} = (W_{i,j_i}^{(1)}, W_{i,j_i}^{(2)})$. Moreover, $(W_{i,j_i}^{(1)}, W_{i,j_i}^{(2)})$ is not a deterministic performance vector. Instead, $(W_{i,j_i}^{(1)}, W_{i,j_i}^{(2)})$ can be freely chosen as any performance vector as long as $(W_{i,j_i}^{(1)}, W_{i,j_i}^{(2)}) \in \Gamma_{i,j_i}$. Γ_{i,j_i} denotes the trade-off curve of the two performance variables in state j_i , which corresponds to the upper boundary of the FOR specific to this state. The upper boundary of the FOR is defined as the smallest performance vector set Γ_{i,j_i} . Given any performance vector $(W_{i,j_i}^{(1)}, W_{i,j_i}^{(2)})$ within the FOR, a performance vector in the set $(W_{i,j_i}^{(1)*}, W_{i,j_i}^{(2)*}) \in \Gamma_{i,j_i}$ can be found, satisfying $(W_{i,j_i}^{(1)*} \geq W_{i,j_i}^{(1)}) \& \& (W_{i,j_i}^{(2)*} \geq W_{i,j_i}^{(2)})$.

Definition 1 illustrates that the risk of the TIP-MS component in any state is represented by a performance trade-off curve. It is because only the performance trade-off curve can give a full picture of the availability of the component, as evidenced in Example 1.

Example 1 Here we consider an extraction-condensing CHP unit consisting of two gas turbines of the same. Since CHP is used to produce electricity and useful heat for consumers, the risk of the CHP unit should be measured by two performance variables of available heat power capacity and available electric power capacity. For each turbine, the maximum heat power and electric power capacities are 25MW and 21MW, respectively. Moreover, there are three states of the CHP unit: state 0 where both turbines fail; state 1 where one turbine works and state 2 where both turbines work perfectly.

The FORs of the CHP unit in the three states are shown in Fig. 5.1, which are based on the typical heat-electricity FOR of an extraction condensing CHP unit [33]. In Fig. 5.1, $W_i^{(1)}$ and $W_i^{(2)}$ represent the heat power and electric power capacities, respectively. $W_{i,j_i}^{(1)}$ and $W_{i,j_i}^{(2)}$ represent the heat power and electric power capacities of the unit in state j_i ; $W_{i,j_i}^{(1),\text{Max}}$ and $W_{i,j_i}^{(2),\text{Max}}$ denote the maximum values of heat power and electric power in state j_i , where $j=2,1,0$.

The two performance variables, i.e., heat power and electric power are both zero in state 0. The performance variables in state 1 and state 2 are both constrained by a FOR. The quadrilateral FORs in state 1 and state 2 are enclosed by four boundary curves, corresponding to four operating constraints, including the electric power output constraint, minimum fuel constraint, maximum fuel constraint, and maximum heat extraction constraint. The trade-off curves in state 1 and state 2 are respectively represented by the solid green segment and solid blue segment.

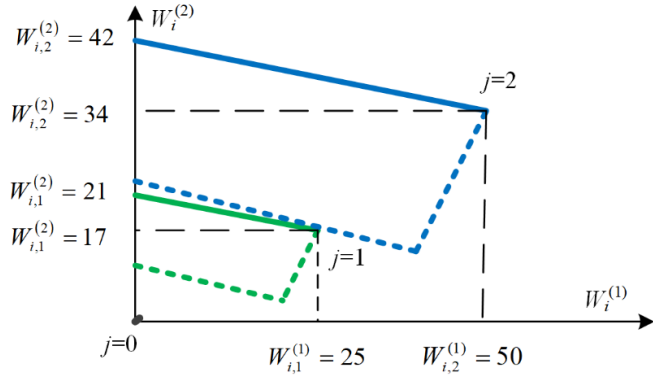


Fig. 5.1 FORs of the extraction-condensing CHP unit in different states [33]

Take state 2 for example. The performance vector in state 2 can be $(0,42)$ if 0MW heat power and 42MW electric power are required. We can also control the CHP unit operation and adjust the performance vector as $(50,34)$ if the load requirements are below $(50,34)$. There are infinite combinations of the available heat power and electric power within the FOR of state 2, corresponding to infinite performance vectors $(W_{i,2}^{(1)}, W_{i,2}^{(2)})$, which can be chosen in this state. Therefore, we need to consider a continuous performance trade-off curve, rather than a certain performance vector, to adequately describe the risk of the CHP unit in a state.

Following **Definition 1**, the state space of the CHP unit in **Example 1** can be expressed as:

$$\left\{ \left(W_{i,0}^{(1)}, W_{i,0}^{(2)} \right) \in \Gamma_{i,0}; \left(W_{i,1}^{(1)}, W_{i,1}^{(2)} \right) \in \Gamma_{i,1}; \left(W_{i,2}^{(1)}, W_{i,2}^{(2)} \right) \in \Gamma_{i,2} \right\}$$

where

$$\begin{aligned} \Gamma_{i,0} &= \left\{ W_{i,0}^{(1)} = 0; W_{i,0}^{(2)} = 0 \right\} \\ \Gamma_{i,1} &= \left\{ \begin{array}{l} 0 \leq W_{i,1}^{(1)} \leq 25 \\ W_{i,1}^{(1)} + 6.25 \cdot W_{i,1}^{(2)} = 131.25 \end{array} \right\} \quad \Gamma_{i,2} = \left\{ \begin{array}{l} 0 \leq W_{i,2}^{(1)} \leq 50 \\ W_{i,2}^{(1)} + 6.25 \cdot W_{i,2}^{(2)} = 262.5 \end{array} \right\} \end{aligned} \quad (5.1)$$

When the two performance variables of the TIP-MSS are positively correlated, there is no trade-off between the two performance variables. Hence, we can use a certain performance vector to replace the performance trade-off curve to represent the performance rates of the TIP-MSS. The elements of the performance vector respectively correspond to the maximum values of the two performance variables. Such systems characterized by two positively correlated performance variables can be viewed as a particular case of the TIP-MSS.

Example 2 Here we consider a back-pressure CHP unit, whose heat power capacity is in proportion to its electric power capacity [34]. In other words, the two performance variables of the back-pressure CHP unit are linearly correlated. Assuming the back-pressure CHP unit has three states: 0, 1, and 2. State 0, state 1, and state 2 have an available heat power capacity of 0MW, 30MW, and 50MW, respectively. The heat-to-electricity coefficients in state 1 and state 2 are assumed to be 1.25 and 1.67, respectively. The FORs of the CHP unit in the three states are shown in Fig. 5.2.

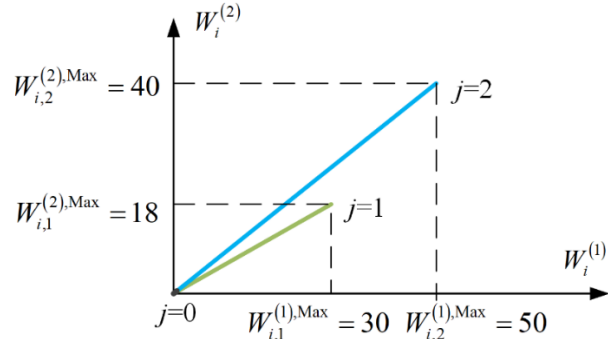


Fig. 5.2 FORs of the back-pressure CHP unit in different states

As shown in Fig. 5.2, the maximum values of the two performance variables in state 1 are $W_{i,1}^{(1),\text{Max}} = 30$ and $W_{i,1}^{(2),\text{Max}} = 18$, respectively. Hence, the performance vector $(W_{i,1}^{(1)}, W_{i,1}^{(2)}) = (30, 18)$ can be viewed as the “capacity” of the component in state 1 and therefore can represent the performance rate of this state. Likewise, $(W_{i,2}^{(1)}, W_{i,2}^{(2)}) = (50, 40)$ can represent the performance rate of the component in state 2.

Follow the general form of expression as (5.1) the state space of the back-pressure CHP unit in Example 2 is expressed as:

$$\left\{ \left(W_{i,0}^{(1)}, W_{i,0}^{(2)} \right) = (0,0); \left(W_{i,1}^{(1)}, W_{i,1}^{(2)} \right) = (30,18); \left(W_{i,2}^{(1)}, W_{i,2}^{(2)} \right) = (50,40) \right\} \quad (5.2)$$

Based on whether conversions between the two performance variables are considered, two models of strong-monotonic-increasing TIP-MSS are defined.

Definition 2 Strong-monotonic-increasing TIP-MSS. For a strong-monotonic-increasing TIP-MSS, the maximum value of each performance variable in state j_s must be not less than those in a lower state. In other words, giving any $\left(W_{s,j_s-1}^{(1)}, W_{s,j_s-1}^{(2)} \right) \in \Gamma_{s,j_s-1}$, there is a $\left(W_{s,j_s}^{(1)}, W_{s,j_s}^{(2)} \right) \in \Gamma_{s,j_s}$ satisfying:

$$\left(W_{s,j_s}^{(1)} \geq W_{s,j_s-1}^{(1)} \right) \& \& \left(W_{s,j_s}^{(2)} \geq W_{s,j_s-1}^{(2)} \right) \quad \forall j_s = 1L M \quad (5.3)$$

Definition 3 Monotonic-increasing TIP-MSS with the weighted-sum conversion. Here we consider the same TIP-MSS as in **Definition 2**. The difference is that the two performance variables can be converted to each other, and therefore can be considered as a whole. The weighting-multipliers of the two performance variables are $c_s^{(1)}$ and $c_s^{(2)}$, which scale their importance. A weighted sum of the two performance variables for the component in state j_s can be evaluated as:

$$W_{i,j_i}^{(\text{sum}),\text{Max}} = \text{Max} \left(c_s^{(1)} \cdot W_{s,j_s}^{(1)} + c_s^{(2)} \cdot W_{s,j_s}^{(2)} \right), \text{ for all } \left(W_{s,j_s}^{(1)}, W_{s,j_s}^{(2)} \right) \in \Gamma_{s,j_s} \quad (5.4)$$

For a monotonic-increasing TIP-MSS with weighted-sum conversion, the maximum value of weighted sum in state j_s must be not less than the value at a lower state, so that:

$$W_{s,j_s}^{(\text{sum}),\text{Max}} \geq W_{s,j_s-1}^{(\text{sum}),\text{Max}} \quad \forall j_s = 1L M \quad (5.5)$$

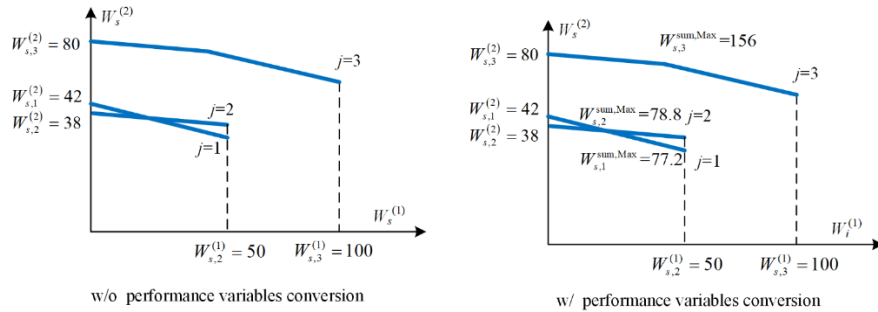


Fig. 5.3. Strong-monotonic-increasing TIP-MSS and monotonic-increasing TIP-MSS with weighted-sum conversion

Example 3 Here we develop a TIP-MSS s consisting of two CHP units. The TIP-MSS has four states, which are state 3, state 2, state 1, and state 0. The performance trade-off curves for the four states are shown in the left part of Fig. 5.3.

As we can see, the TIP-MSS s is not a strong-monotonic-increasing TIP-MSS. The criterion is not satisfied when we compare state 1 and state 2. The performance variables in state 1 can be (0,42) while there is no available performance variable vector in state 2 satisfying:

$$\left(W_{s,2}^{(1)} \geq 0 \right) \& \& \left(W_{s,2}^{(2)} \geq 42 \right) \left(W_{s,2}^{(1)}, W_{s,2}^{(2)} \right) \in \Gamma_{s,2} \quad (5.6)$$

Then, we consider the same TIP-MSS s and equip it with a heat pump (electricity to heat) and a thermoelectric generator (heat to electricity). In this case, the two performance variables (electric power and heat power) can be converted to one another. Assuming the weighting-multipliers of the two performance variables are 1 and 0.8, respectively. Then, we can calculate the maximum weighted sum of the two performance variables for the four states, which are 156, 18.8, 72.2, and 0, respectively. In this case, the TIP-MSS s is considered as a monotonic-increasing TIP-MSS with the weighted-sum conversion.

5.3 The Two-Interdependent-Performance Universal Generating Function Technique

A two-interdependent-performance multi-state system (TIP-MSS) consists of many components. Each component can have different performance levels corresponding to different states. The random process describing the transition of different states of the component can be modeled as a Markov chain (MC) [35]. Assuming that only long-term risk analysis is performed to assess the risk of the TIP-MSS, the component state probabilities can be obtained by solving several algebraic equations in the MC. This part is beyond the scope of the study.

In this chapter, it is assumed that the state probabilities of the components are known. Then, the performance distribution of each component is represented in the UGF form. Based on the proposed UGF combination operators, the performance distribution of the entire TIP-MSS can be obtained based on the UGF of its components.

The UGF technique is used to find the entire performance distribution of the MSS based on the performance distributions of its components. However, the traditional UGF method is more applicable to one-performance MSS or the MSS whose different performance variables are independent of each other. Therefore, the conventional UGF method is extended in this chapter, and the concept of TIP-UGF is proposed.

The traditional UFG representation for a single-performance MS component is generally formed as:

$$u_m(z) = \sum_{j_i=0}^M p_{i,j_i} \cdot z^{Q_{i,j_i}} \quad (5.7)$$

As shown in (5.7), the UGF representation gives the probability (p_{i,j_i}) and performance rate (Q_{i,j_i}) of the component over its $M+1$ states.

Likewise, the general form of the TIP-UGF for the TIP-MS component i is given as:

$$u_i(z) = \sum_{j_i=0}^M p_{i,j_i} \cdot z^{\bar{W}_{i,j_i}} \quad (5.8)$$

The above function is the z -transform of random performance vector. Like the single-performance UGF, the function (5.8) represents the probability mass function of the TIP-MS component, with \bar{W}_{i,j_i} and p_{i,j_i} in the polynomial form corresponding to the performance rate and the corresponding probability for state j_i [36].

The performance rate \bar{W}_{i,j_i} is represented by the performance trade-off curve $(W_{i,j_i}^{(1)}, W_{i,j_i}^{(2)}) \in \Gamma_{i,j_i}$. Hence, (5.8) can be restated as:

$$u_i(z) = \sum_{j_i=0}^M p_{i,j_i} \cdot z^{\bar{W}_{i,j_i}} = \sum_{j_i=0}^M p_{i,j_i} \cdot z^{(W_{i,j_i}^{(1)}, W_{i,j_i}^{(2)}) \in \Gamma_{i,j_i}} \quad (5.9)$$

In the following paragraphs, the TIP-UGF form (5.9) is simplified as:

$$u_i(z) = \sum_{j_i=0}^M p_{i,j_i} \cdot z^{\Gamma_{i,j_i}} \quad (5.10)$$

Then, different composition operators, corresponding to the extension/intersection of the FORs, are defined for analyzing the TIP-MSS with parallel/series structures.

Based on the TIP-UGF technique, the performance distribution of a TIP-MSS containing multiple components can be obtained:

$$\begin{aligned} u_s(z) &= \Omega(u_1(z), L, u_n(z)) \\ &= \Omega\left(\sum_{j_1=0}^M p_{1,j_1} \cdot z^{\Gamma_{1,j_1}}, \dots, \sum_{j_i=0}^M p_{i,j_i} \cdot z^{\Gamma_{i,j_i}}, \dots, \sum_{j_n=0}^M p_{n,j_n} \cdot z^{\Gamma_{n,j_n}}\right) \\ &= \sum_{x=0}^X p_{s,x} \cdot z^{\Gamma_{s,x}} \end{aligned} \quad (5.11)$$

The composition operator Ω includes the parallel operator \otimes_{par} and the series operator \otimes_{ser} . $X+1$ represents the number of the system state, $p_{s,x}$ is the probability of state x , while $\Gamma_{s,x}$ denotes the trade-off curve constraining the performance variables $(W_{s,x}^{(1)}, W_{s,x}^{(2)})$ for this state.

The parallel operator \otimes_{par} and the series operator \otimes_{ser} are introduced in subsections 5.3.1, and 5.3.2, respectively.

5.3.1. Risk modeling of the system with a parallel structure

The parallel composition operator \otimes_{par} is defined to analyze the system with a parallel structure. Similar to that in the well-known single-performance UGF theory [37], \otimes can be illustrated as:

$$\begin{aligned} u_{s(i1,i2)} &= u_{i1}(z) \otimes_{\text{par}} u_{i2}(z) \\ &= \left(\sum_{j_{i1}=0}^{M_1} p_{i1,j_{i1}} \cdot z^{\Gamma_{i1,j_{i1}}} \right) \otimes_{\text{par}} \left(\sum_{j_{i2}=0}^{M_2} p_{i2,j_{i2}} \cdot z^{\Gamma_{i2,j_{i2}}} \right) \\ &= \sum_{j_{i1}=0}^{M_1} \sum_{j_{i2}=0}^{M_2} p_{i1,j_{i1}} p_{i2,j_{i2}} \cdot z^{\text{par}(\Gamma_{i1,j_{i1}}, \Gamma_{i2,j_{i2}})} \end{aligned} \quad (5.12)$$

As shown in (5.12), a special function $\text{par}(\cdot)$ is used to combine the performance trade-off curves of components connected in parallel. The function corresponds to the “addition of two performance variables” in the single-performance UGF. The following paragraphs illustrate the function $\text{par}(\cdot)$. Suppose a TIP-MSS s consists of two components $i1$ and $i2$ connected in parallel. The two components are respectively in state j_{i1} and j_{i2} , and their performance rates in their states are respectively represented as: $(W_{i1,j_{i1}}^{(1)}, W_{i1,j_{i1}}^{(2)}) \in \Gamma_{i1,j_{i1}}$ and $(W_{i2,j_{i2}}^{(1)}, W_{i2,j_{i2}}^{(2)}) \in \Gamma_{i2,j_{i2}}$. Then, the performance rate of the system s in this combination can be expressed as $(W_{s,j_s}^{(1)}, W_{s,j_s}^{(2)}) \in \Gamma_{s,j_s}$ where $\Gamma_{s,j_s} = \text{par}(\Gamma_{i1,j_{i1}}, \Gamma_{i2,j_{i2}})$. The function $\text{par}(\cdot)$ refers to the combination of trade-off curves. Mathematically, $\text{par}(\cdot)$ obtains the expression of the $(W_{i1,j_{i1}}^{(1)} + W_{i2,j_{i2}}^{(1)}, W_{i1,j_{i1}}^{(2)} + W_{i2,j_{i2}}^{(2)})$ given the trade-off curve functions of $(W_{i1,j_{i1}}^{(1)}, W_{i1,j_{i1}}^{(2)})$ and $(W_{i2,j_{i2}}^{(1)}, W_{i2,j_{i2}}^{(2)})$.

Example 4 There are two extraction-condensing CHP units $i1$ and $i2$ at bus i . Each unit has two states, including the best-performing state 1 and complete-failure state 0. Therefore, the TIP-UGF of CHP unit $i1$ can be defined as the following polynomial:

$$u_{i1} = A_{i1} \cdot z^{\Gamma_{i1,1}} + U_{i1} \cdot z^0 \quad (5.13)$$

where A_{i1} and U_{i1} are the availability and unavailability of the CHP unit, respectively. In the best-performing state, its performance is represented by the $\Gamma_{i1,1}$. The trade-off curve in state 0 is simply referred to as ‘0’ here.

Similarly, the TIP-UGF of CHP unit $i2$ is defined as:

$$u_{i2} = A_{i2} \cdot z^{\Gamma_{i2,1}} + U_{i2} \cdot z^0 \quad (5.14)$$

In their TIP-UGF representations, $\Gamma_{i1,1}$ and $\Gamma_{i2,1}$ are mathematically expressed as:

$$\Gamma_{i1,1} = \left\{ \begin{array}{l} a_{i1} \leq W_{i1,1}^{(1)} \leq b_{i1} \\ W_{i1,1}^{(1)} + c_{i1} \cdot W_{i1,1}^{(2)} = d_{i1} \end{array} \right\}; \Gamma_{i2,1} = \left\{ \begin{array}{l} a_{i2} \leq W_{i2,1}^{(1)} \leq b_{i2} \\ W_{i2,1}^{(1)} + c_{i2} \cdot W_{i2,1}^{(2)} = d_{i2} \end{array} \right\} \quad (5.15)$$

Moreover, it is assumed that:

$$c_{i1} \geq c_{i2} \quad (5.16)$$

Under such circumstances, the TIP-UGF of the system s consisting of $i1$ and $i2$ can be obtained as:

$$\begin{aligned} u_s &= u_{i1}(z) \otimes_{\text{par}} u_{i2}(z) \\ &= \left(A_{i1} \cdot z^{\Gamma_{i1,1}} + U_{i1} \cdot z^0 \right) \otimes_{\text{par}} \left(A_{i2} \cdot z^{\Gamma_{i2,1}} + U_{i2} \cdot z^0 \right) \\ &= A_{i1} A_{i2} \cdot z^{\text{par}(\Gamma_{i1,1}, \Gamma_{i2,1})} + A_{i1} U_{i2} \cdot z^{\Gamma_{i1,1}} + A_{i2} U_{i1} \cdot z^{\Gamma_{i2,1}} \\ &= A_{i1} A_{i2} \cdot z^{\Gamma_{s,3}} + A_{i1} U_{i2} \cdot z^{\Gamma_{s,3}} + A_{i2} U_{i1} \cdot z^{\Gamma_{s,3}} + U_{i1} U_{i2} \cdot z^0 \end{aligned} \quad (5.17)$$

In (5.17), $\Gamma_{s,3}$ denotes the performance trade-off curve of the system s when the two CHP units are both at their best-performing state. Moreover, $\Gamma_{s,3}$ can be expressed as:

$$\Gamma_{s,3} = \text{par}(\Gamma_{i1,1}, \Gamma_{i2,1}) = \left\{ \begin{array}{l} a_{i1} + a_{i2} \leq W_{s,3}^{(1)} \leq b_{i1} + b_{i2} \\ W_{s,3}^{(1)} + c_{i2} W_{s,3}^{(2)} = d_{i1} + d_{i2}, \text{ when } a_{i2} \leq W_{s,3}^{(2)} \leq b_{i2} \\ W_{s,3}^{(1)} + c_{i1} W_{s,3}^{(2)} = d_{i1} + d_{i2} - (c_{i1} - c_{i2}) b_{i1}, \text{ when } a_{i1} + b_{i2} \leq W_{s,3}^{(2)} \leq b_{i1} + b_{i2} \end{array} \right\} \quad (5.18)$$

where $W_{s,3}^{(1)} = W_{i1,1}^{(1)} + W_{i2,1}^{(1)}$, $W_{s,3}^{(2)} = W_{i1,1}^{(2)} + W_{i2,1}^{(2)}$.

The function $\text{par}(\cdot)$, in this case, is illustrated in Fig. 5.4. As shown in Fig. 5.4, the trade-off curves of the two CHP units are spliced together to form the trade-off curve of the system s .

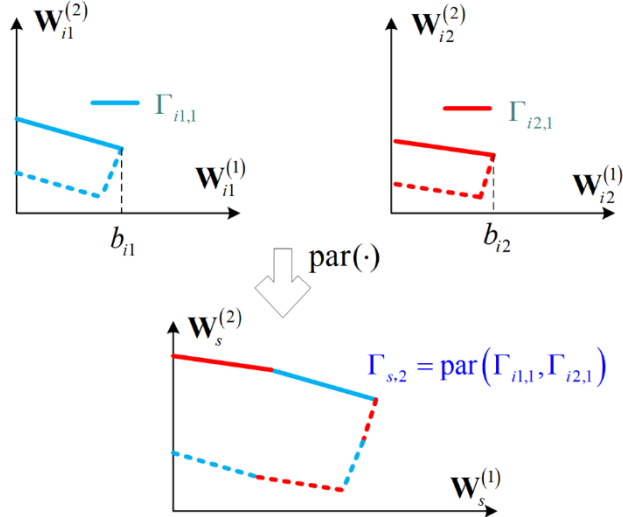


Fig. 5.4. Illustration of combining the states of two CHP units in parallel

5.3.2. Risk modeling of the system with series structure

The series composition operator $\underset{\text{ser}}{\otimes}$ is defined to analyze the system with series structure, which can be illustrated as:

$$\begin{aligned} u_s &= u_{S(i_1, i_2)} = u_{i_1}(z) \underset{\text{ser}}{\otimes} u_{i_2}(z) \\ &= \left(\sum_{j_1=0}^{M_1} p_{i_1, j_1} \cdot z^{\Gamma_{i_1, j_1}} \right) \underset{\text{ser}}{\otimes} \left(\sum_{j_2=0}^{M_2} p_{i_2, j_2} \cdot z^{\Gamma_{i_2, j_2}} \right) \\ &= \sum_{j_1=0}^{M_1} \sum_{j_2=0}^{M_2} p_{i_1, j_1} p_{i_2, j_2} \cdot z^{\text{ser}(\Gamma_{i_1, j_1}, \Gamma_{i_2, j_2})} \end{aligned} \quad (5.19)$$

As shown in (5.19), a special function $\text{ser}(\cdot)$ is used to find the performance trade-off curve of the system when combining the states of two independent components connected in series. Mathematically, the function represents the “intersection of the trade-off curves”. It is assumed that there is a TIP-MSS s consisting of two components i_1 and i_2 connected in series. The two components are respectively in state j_{i_1} and j_{i_2} , and their performance trade-off curves are represented as: $(W_{i_1, j_{i_1}}^{(1)}, W_{i_1, j_{i_1}}^{(2)}) \in \Gamma_{i_1, j_{i_1}}$ and $(W_{i_2, j_{i_2}}^{(1)}, W_{i_2, j_{i_2}}^{(2)}) \in \Gamma_{i_2, j_{i_2}}$. Then, the performance rate of the MSS s in this combination can be expressed as: $(W_{s, j_s}^{(1)}, W_{s, j_s}^{(2)}) \in \Gamma_{s, j_s}$, where $\Gamma_{s, j_s} = \text{ser}(\Gamma_{i_1, j_{i_1}}, \Gamma_{i_2, j_{i_2}})$. The function $\text{ser}(\cdot)$ is used to obtain the intersection of the $\Gamma_{i_1, j_{i_1}}$ and $\Gamma_{i_2, j_{i_2}}$. Assuming that

$\Gamma_{i1,j_1} = \left\{ \mathbf{f}_{i1} \left(W_{i1}^{(1)}, W_{i1}^{(2)} \right) \leq 0 \right\}; \Gamma_{i2,j_2} = \left\{ \mathbf{f}_{i2} \left(W_{i2}^{(1)}, W_{i2}^{(2)} \right) \leq 0 \right\}, \Gamma_{s,j_s}$ can be expressed as: $\Gamma_{s,j_s} = \text{ser} \left(\Gamma_{i1,j_1}, \Gamma_{i2,j_2} \right) = \left\{ \mathbf{f}_{i1} \left(W_{s,j_s}^{(1)}, W_{s,j_s}^{(2)} \right) \leq 0; \mathbf{f}_{i2} \left(W_{s,j_s}^{(1)}, W_{s,j_s}^{(2)} \right) \leq 0 \right\}.$

Example 5 There is a CHP-based energy production system, which consists of a CHP unit and an energy delivery unit in series. The topology of the system is given in Fig. 5.5. It is assumed that the TIP-UGF of the CHP unit is expressed as:

$$u_C = A_C \cdot z^{\Gamma_{c,1}} + U_C \cdot z^0 \quad (5.20)$$

There are four states of the energy delivery unit: state 3, both electric power and heat power can be delivered; state 2, only electric power can be delivered; state 1, only heat power can be delivered; state 0, none of the electric power or heat power can be delivered. Hence, the TIP-UGF of the transmission network is shown as:

$$\begin{aligned} u_T = & A_{ET} A_{HT} \cdot z^{\Gamma_{T,3}} + A_{ET} U_{HT} \cdot z^{\Gamma_{T,2}} + U_{ET} A_{HT} \cdot z^{\Gamma_{T,1}} \\ & + U_{ET} U_{HT} \cdot z^0 \end{aligned} \quad (5.21)$$

where A_{ET} and U_{ET} are the availability and unavailability of the electricity transmission, respectively; A_{HT} and U_{HT} are the availability and unavailability of the heat transmission, respectively.



Fig. 5.5 Topology of the CHP-based energy system

Moreover, the nominal capacities of heat delivery and electricity delivery are 50MW and 40MW, respectively. Therefore, $\Gamma_{T,3}$ can be expressed as:

$$\Gamma_{T,3} = \left\{ W_{T,3}^{(1)} \leq 50; W_{T,3}^{(2)} \leq 40 \right\} \quad (5.22)$$

The TIP-UGF representation of the whole energy system can be expressed as:

$$\begin{aligned} u_{S(C,T)} &= u_C(z) \otimes u_T(z) \\ &= \left(A_C \cdot z^{\Gamma_{c,1}} + U_C \cdot z^0 \right)_{\text{ser}} \otimes \left(A_{ET} A_{HT} \cdot z^{\Gamma_{T,3}} + L + U_{ET} U_{HT} \cdot z^0 \right) \\ &= A_C A_{ET} A_{HT} z^{\text{ser}(\Gamma_{c,1}, \Gamma_{T,3})} + L + A_C U_{ET} A_{HT} \cdot z^{\text{ser}(\Gamma_{c,1}, \Gamma_{T,1})} + L \\ &\quad + (1 - A_C A_{ET} A_{HT} - A_C A_{ET} U_{HT} - A_C U_{ET} A_{HT}) \cdot z^0 \\ &= A A_C A_{ET} A_{HT} z^{\Gamma_{s,3}} + L + A_C U_{ET} A_{HT} \cdot z^{\Gamma_{s,1}} + L \\ &\quad + (1 - A_C A_{ET} A_{HT} - A_C A_{ET} U_{HT} - A_C U_{ET} A_{HT}) \cdot z^0 \end{aligned} \quad (5.23)$$

where $\Gamma_{s,3}$ denotes the performance rate of the energy system when both the CHP unit and the energy delivery unit are at their best state, and so on.

$\Gamma_{s,3}$ can be expressed as:

$$\Gamma_{s,3} = \text{ser}\left(\Gamma_{C,1}, \Gamma_{T,3}\right) = \begin{cases} 0 \leq W_{s,3}^{(1)} \leq 50 \\ W_{s,3}^{(1)} + 6.25 \cdot W_{s,3}^{(2)} = 262.5 \\ W_{s,3}^{(1)} \leq 50; W_{s,3}^{(2)} \leq 40 \end{cases} \quad (5.24)$$

The relationship between $\Gamma_{s,3}$ and Γ_C is shown in Fig. 5.6.

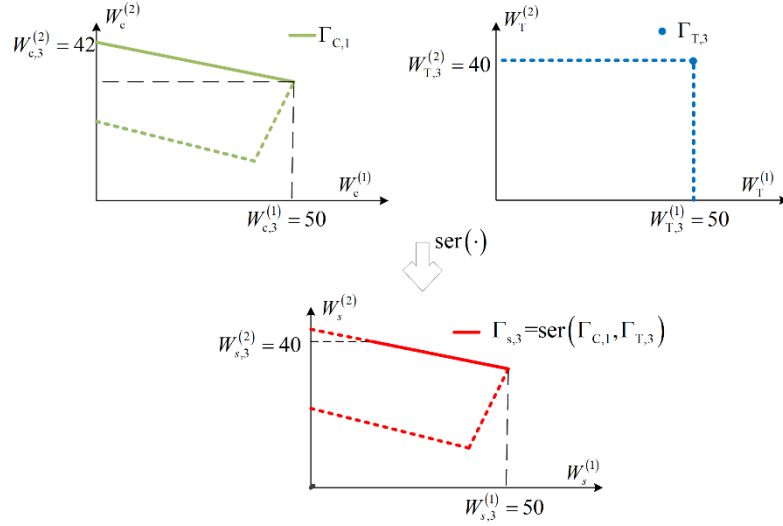


Fig. 5.6. Illustration of combining two components in series

5.4 Risk Evaluation of the TIP-MSS through the TIP-UGF technique

5.4.1. Availability criterion based on the TIP-UGF representation

Once the TIP-UGF of the TIP-MSS is obtained, the system risk for any given demand vector $\bar{k} = (k^1, k^2)$ can be evaluated by:

$$R_s(\bar{k}) = \delta_A(U(z), \bar{k}) = \delta_A\left(\sum_{x=0}^X p_{s,x} \cdot z^{\Gamma_{s,x}}, \bar{k}\right) = \sum_{x=0}^X p_{s,x} \cdot \alpha(\Gamma_{s,x}, (k^1, k^2)) \quad (5.25)$$

The binary value $\alpha(\Gamma_{s,x}, (k^1, k^2))$ in (5.25) takes a value of '1' if there is a performance variable vector $(W_{s,x}^{(1)}, W_{s,x}^{(2)}) \in \Gamma_{s,x}$, satisfying the condition: $(W_{s,x}^{(1)} \geq k^1) \& \& (W_{s,x}^{(2)} \geq k^2)$. As shown in (5.25), the risk is defined as the proba-

bility that the MSS s will be in the states with performance trade-off curves beyond the demand point.

For a TIP-MSS with weighted-sum conversion, the risk can be evaluated as:

$$\begin{aligned} R_s(\bar{k}) &= \delta_A(U(z), k) = \delta_A\left(\sum_{x=0}^X p_{s,x} \cdot z^{\Gamma_{s,x}}, c^1 \cdot k^1 + c^2 k^2\right) \\ &= \sum_{x=0}^X p_{s,x} \cdot \alpha(\Gamma_{s,x}, c^1 \cdot k^1 + c^2 k^2) \end{aligned} \quad (5.26)$$

where $\alpha(\Gamma_{s,x}, c^1 \cdot k^1 + c^2 k^2)$ in (5.26) takes a value of '1' if there is a performance variable vector $(W_{s,x}^{(1)}, W_{s,x}^{(2)}) \in \Gamma_{s,x}$, satisfying the condition: $c^1 \cdot w_{s,x}^1 + c^2 \cdot w_{s,x}^2 \geq c^1 \cdot k^1 + c^2 k^2$.

5.4.2. Illustrative examples

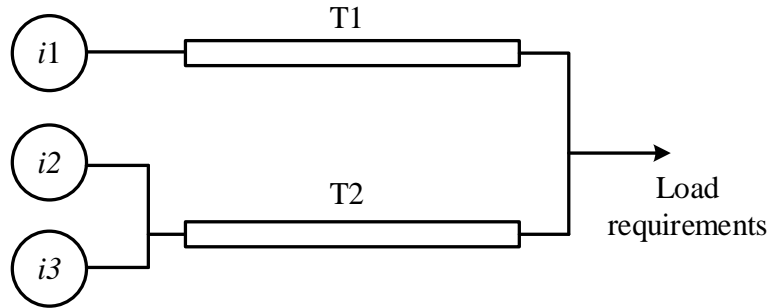


Fig. 5.7 The illustrative test system

Case 1. In this case, an illustrative TIP-MSS is developed as shown in Fig. 5.7. The system has two branches connected in parallel. Branch 1 involves a CHP unit i_1 and an energy delivery unit T_1 which are series-connected. In branch 2, CHP units i_2 and i_3 are connected in parallel, which are then series-connected to T_2 . CHP unit i_1 has a maximum heat power of 50 MW and a maximum electric power of 42 MW in its best-performing state. Both i_2 and i_3 have a maximum capacity of 20 MW heat power and 17 MW electric power. Moreover, every unit has three possible states: 0, 1, and 2 as discussed in Example 1. The nominal heat delivery capacity and electricity delivery capacity of T_1 are 6MW and 50MW, respectively. While the nominal capacities of T_2 are 50MW and 40MW, respectively.

In order to meet the consumers' demands for heat power and electric power, a range of requirements should be met, such that $\bar{k}_1 = (22, 10)$ for the low-level demand and $\bar{k}_2 = (50, 20)$ for high-level demand.

The TIP-UGFs for the three CHP units are defined as:

$$\begin{aligned}
u_{i1}(z) &= p_{i1,2} \cdot z^{\Gamma_{i1,2}} + p_{i1,1} \cdot z^{\Gamma_{i1,1}} + p_{i1,0} \cdot z^0 \\
u_{i2}(z) &= p_{i2,2} \cdot z^{\Gamma_{i2,2}} + p_{i2,1} \cdot z^{\Gamma_{i2,1}} + p_{i2,0} \cdot z^0 \\
u_{i3}(z) &= p_{i3,2} \cdot z^{\Gamma_{i3,2}} + p_{i3,1} \cdot z^{\Gamma_{i3,1}} + p_{i3,0} \cdot z^0
\end{aligned} \tag{5.27}$$

Moreover, it is assumed that $p_{i1,2} = 0.8$, $p_{i1,1} = p_{i1,0} = 0.1$, $p_{i2,2} = p_{i3,2} = 0.9$, $p_{i2,1} = p_{i2,0} = p_{i3,1} = p_{i3,0} = 0.05$.

There are both four states of the energy delivery units T1 and T2. The TIP-UGFs for T1 and T2 are:

$$\begin{aligned}
u_{T1} &= A_{ET1}A_{HT1} \cdot z^{\Gamma_{T1,3}} + A_{ET1}U_{HT1} \cdot z^{\Gamma_{T1,2}} + U_{ET1}A_{HT1} \cdot z^{\Gamma_{T1,1}} \\
&\quad + U_{ET1}U_{HT1} \cdot z^0 \\
u_{T2} &= A_{ET2}A_{HT2} \cdot z^{\Gamma_{T2,3}} + A_{ET2}U_{HT2} \cdot z^{\Gamma_{T2,2}} + U_{ET2}A_{HT2} \cdot z^{\Gamma_{T2,1}} \\
&\quad + U_{ET2}U_{HT2} \cdot z^0
\end{aligned} \tag{5.28}$$

where $A_{ET1} = A_{HT1} = 0.9$; $A_{ET2} = A_{HT2} = 0.9$

The two branches can be regarded as two subsystems $s1$ and $s2$ connected in parallel. The state distributions of the two subsystems can be determined based on the TIP-UGF of their components.

First, the CHP units $i2$ and $i3$ in subsystem $s2$ are combined as pseudo unit $i4$ based on the TIP-UGF equivalent. The TIP-UGF of $i4$ is evaluated as:

$$\begin{aligned}
u_{i4}(z) &= u_{i2}(z) \otimes u_{i3}(z) = p_{i2,2} \cdot p_{i3,2} \cdot z^{\text{par}(\Gamma_{i2,2}, \Gamma_{i3,2})} + (p_{i2,2} \cdot p_{i3,1} + p_{i2,1} \cdot p_{i3,2}) \cdot z^{\text{par}(\Gamma_{i2,2}, \Gamma_{i3,1})} \\
&\quad + (p_{i2,2} \cdot p_{i3,0} + p_{i2,0} \cdot p_{i3,2} + p_{i2,1} \cdot p_{i3,1}) \cdot z^{\Gamma_{i2,2}} + (p_{i2,1} \cdot p_{i3,0} + p_{i2,0} \cdot p_{i3,1}) \cdot z^{\Gamma_{i2,1}} + p_{i2,0} \cdot p_{i3,0} \cdot z^0 \\
&= p_{i4,4} \cdot z^{\Gamma_{i4,4}} + p_{i4,3} \cdot z^{\Gamma_{i4,3}} + p_{i4,2} \cdot z^{\Gamma_{i4,2}} + p_{i4,1} \cdot z^{\Gamma_{i4,1}} + p_{i4,0} \cdot z^0
\end{aligned} \tag{5.29}$$

Then, the state distributions of the two subsystems can be obtained based on the series combination operation.

Finally, the TIP-UGF for the system can be obtained through the parallel combination operator. Subsystems $s1$ and $s2$ have 7 states and 13 states, respectively. Hence, there should be 91 states for the system.

$$\begin{aligned}
u_s(z) &= u_{s1}(z) \otimes_{\text{ser}} u_{s2}(z) \\
&= \left(\sum_{j_{s1}=0}^{M_{s1}} p_{s1,j_{s1}} \cdot z^{\Gamma_{s1,j_{s1}}} \right) \otimes_{\text{ser}} \left(\sum_{j_{s2}=0}^{M_{s2}} p_{s2,j_{s2}} \cdot z^{\Gamma_{s2,j_{s2}}} \right) \\
&= \sum_{j_{s1}=0}^{M_{s1}} \sum_{j_{s2}=0}^{M_{s2}} p_{s1,j_{s1}} p_{s2,j_{s2}} \cdot z^{\text{ser}(\Gamma_{s1,j_{s1}}, \Gamma_{s2,j_{s2}})} \\
&= p_{s,90} \cdot z^{\Gamma_{s,90}} + L + p_{s,40} \cdot z^{\Gamma_{s,40}} + L + p_{s,0} \cdot z^0
\end{aligned} \tag{5.30}$$

Once known the state distribution of the system, the risk can be evaluated based on the criterion (5.25). For example, the trade-off curve of the system state

90 in which all the components are perfectly functional is shown in Fig. 5.8. The system is available for the high-level demand in this state since a performance vector can be found within the performance trade-off curve satisfying the condition: $(W_s^{(1)} \geq 50) \& \& (W_s^{(2)} \geq 20)$.

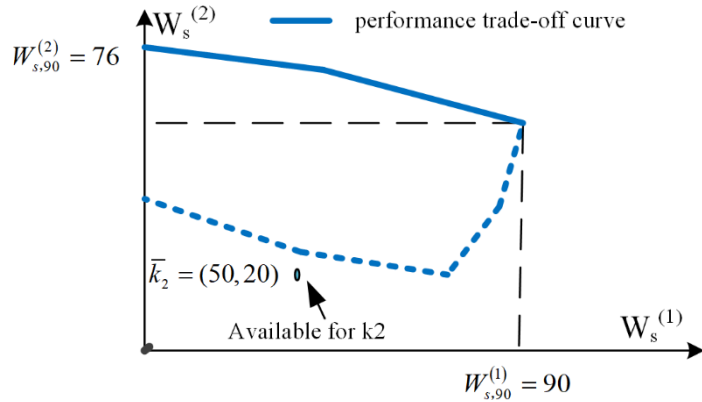


Fig. 5.8 Illustration of the performance trade-off curve $\Gamma_{s,90}$ in case 1

When all the CHP units degrade from state 2 to state 1, the system is degraded to state 76. The performance trade-off curve of this state, denoted by $\Gamma_{s,76}$, is shown in Fig. 5.9.

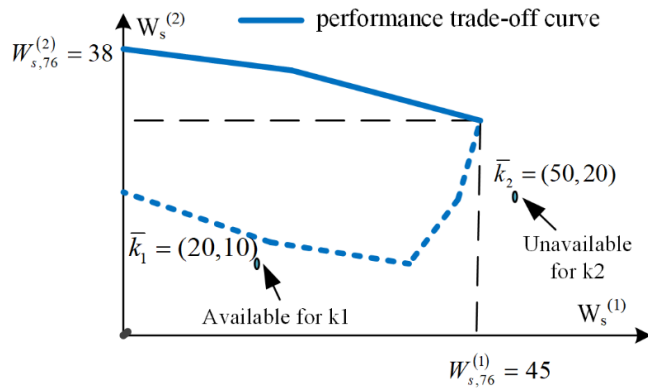


Fig. 5.9 Illustration of the performance trade-off curve $\Gamma_{s,76}$ in case 1

From Fig. 5.9, we can see that the state 76 is unavailable for the high-level demand since we cannot find a performance vector within the trade-off curve satisfying the availability criterion. The other observation is that the system in this state is still available for the low-level demand.

In similar ways, the availability in different system states can be obtained. Then, the probability of the system attaining the high-level requirement can be evaluated as:

$$\begin{aligned} R(\bar{k}_2) &= \delta_A(u_s(z), \bar{k}_2) = \delta_A\left(\sum_{x=0}^{14} p_{s,x} \cdot z^{\Gamma_{s,x}}, \bar{k}_2\right) \\ &= \sum_{x=0}^{90} p_{s,x} \cdot \alpha(\Gamma_{s,x}, (50, 20)) = 0.5839 \end{aligned} \quad (5.31)$$

The probability of the system attaining the low-level requirement is:

$$\begin{aligned} R(\bar{k}_1) &= \delta_A(u_s(z), \bar{k}_1) = \delta_A\left(\sum_{x=0}^{14} p_{s,x} \cdot z^{\Gamma_{s,x}}, \bar{k}_1\right) \\ &= \sum_{x=0}^{90} p_{s,x} \cdot \alpha(\Gamma_{s,x}, (20, 12)) = 0.6495 \end{aligned} \quad (5.32)$$

Case 2 We consider the same TIP-MSS as in Case 1. The difference is that the conversion between the two performances is considered here. Hence, the illustrative system is modeled as a TIP-MSS with the weighted-sum conversion in this case. Moreover, the weighting multipliers of the two performances are set as $c^{(1)}=1$ and $c^{(2)}=0.8$, respectively. In other words, 0.8MW of heat power is equivalent to 1MW of electric power in terms of meeting the consumers' demand. Based on the weighting multipliers, the low-level and high-level demand requirements are converted to $k_1 = 29.6$ and $k_2 = 66$, respectively.

The performance trade-off curves of the TIP-MSS in different states also can be found in (5.30). Based on the criterion (5.26), the availability of TIP-MSS in different states can be evaluated.

In this case, the system performance trade-off curve in state 76 is illustrated in Fig. 5.10.

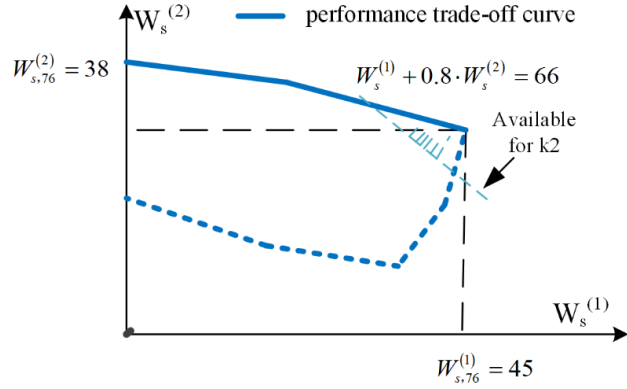


Fig. 5.10 Illustration of performance trade-off curve $\Gamma_{s,76}$ in case 2

As shown in Fig. 5.10, performance vectors $(W_s^{(1)}, W_s^{(2)}) \in \Gamma_{s,76}$ can be found satisfying the condition $W_s^{(1)} + 0.8 \cdot W_s^{(2)} \geq 66$. Hence, the system is still available for high-level demand. It leads to the conclusion that the conversion between the different performances increases the risk of the system.

In similar ways, system availability in different states can be obtained. Then, the probability of the system attaining the high-level requirement can be evaluated as:

$$\begin{aligned} R(\bar{k}_2) &= \delta_A(u_s(z), \bar{k}_2) = \delta_A\left(\sum_{x=0}^{90} p_{s,x} \cdot z^{\Gamma_{s,x}}, \bar{k}_2\right) \\ &= \sum_{x=0}^{90} p_{s,x} \cdot \alpha(\Gamma_{s,x}, 66) = 0.88275 \end{aligned} \quad (5.33)$$

The probability of the system attaining the low-level requirement is:

$$\begin{aligned} R(\bar{k}_1) &= \delta_A(u_s(z), \bar{k}_1) = \delta_A\left(\sum_{x=0}^{90} p_{s,x} \cdot z^{\Gamma_{s,x}}, \bar{k}_1\right) \\ &= \sum_{x=0}^{90} p_{s,x} \cdot \alpha(\Gamma_{s,x}, 29.6) = 0.9198 \end{aligned} \quad (5.34)$$

5.5 Conclusions

This study extends the MSS model to the case where the engineering systems require two interdependent performance variables to measure the risk. The concepts and definitions of the TIP-MSS are introduced in this chapter. The TIP-UGF based risk evaluation technique and the availability criterion are also proposed. Therefore, the risk of the engineering systems, such as CHP based district energy systems, can be evaluated with the consideration of the dependence between different performance variables. The proposed TIP-MSS model also applies to the power generation system when both active power and reactive power are considered. The simulation studies have shown that enabling the conversion between different performance variables is an effective method for improving the risk of the TIP-MSSs.

There are two directions for future work on this research. One is to expand the proposed risk model to MSS which requires more than two dependent performance variables. The other direction is to generalize the proposed risk model to capture the epistemic uncertainties.

References

- [1] B. Sanso, and F. Soumis, “Communication and transportation network reliability using routing models,” *IEEE Transactions on Reliability*, vol. 40, no. 1, pp. 29-38, 1991.
- [2] B. Natvig, *Multistate Systems Reliability Theory with Applications*, 2010.

- [3] Y.-F. Li, and E. Zio, "A multi-state model for the reliability assessment of a distributed generation system via universal generating function," *Reliability Engineering & System Safety*, vol. 106, pp. 28-36, 2012.
- [4] R. E. Barlow, and A. S. Wu, "Coherent Systems with Multi-State Components," *Mathematics of Operations Research*, vol. 3, no. 4, pp. 275-281, 1978.
- [5] E. El-Newehi, "Multistate Coherent Systems," *Journal of Applied Probability*, vol. 15, no. 4, pp. 675-688, 1978.
- [6] A. Lisnianski, and G. Levitin, *Multi-State System Reliability, Assessment, Optimization and Applications*: WORLD SCIENTIFIC, 2003.
- [7] A. Lisnianski, I. Frenkel, and Y. Ding, *Multi-state system reliability analysis and optimization for engineers and industrial managers*, London: Springer Science & Business Media, 2010.
- [8] R. Peng, H. Liu, and M. Xie, "A Study of Reliability of Multi-State Systems with Two Performance Sharing Groups," *Quality & Reliability Engineering International*, vol. 32, no. 7, pp. 2623-2632, 2016.
- [9] W. S. Griffith, "Optimal Reliability Modeling: Principles and Applications," *Technometrics*, vol. 46, no. 1, pp. 112-112, 2002.
- [10] Z. Tian, M. J. Zuo, and R. C. M. Yam, "Multi-state k-out-of-n systems and their performance evaluation," *IIE Transactions*, vol. 41, no. 1, pp. 32-44, 2008/11/07, 2008.
- [11] J. Huang, M. J. Zuo, and Y. Wu, "Generalized multi-state k-out-of-n:G systems," *Reliability IEEE Transactions on*, vol. 49, no. 1, pp. 105-111, 2000.
- [12] J. Huang, M. J. Zuo, and Z. Fang, "Multi-State Consecutive- k -out-of- n Systems," *IIE Transactions*, vol. 35, no. 6, pp. 527-534, 2003/06/01, 2003.
- [13] M. J. Zuo, and Z. Tian, "Performance evaluation of generalized multi-state k-out-of-n systems," *IEEE Transactions on Reliability*, vol. 55, no. 2, pp. 319-327, 2006.
- [14] XianZhao, and LirongCui, "Reliability evaluation of generalised multi-state k-out-of-n systems based on FMCI approach," *International Journal of Systems Science*, vol. 41, no. 12, pp. 1437-1443, 2010.
- [15] W. Li, and M. J. Zuo, "Reliability evaluation of multi-state weighted k-out-of-n systems," *Reliability Engineering & System Safety*, vol. 93, no. 1, pp. 160-167, 2008/01/01/, 2008.
- [16] M. J. Zuo, J. Huang, and W. Kuo, "Multi-state k-out-of-n Systems," *Handbook of Reliability Engineering*, H. Pham, ed., pp. 3-17, London: Springer London, 2003.
- [17] Z. Tian, W. Li, and M. J. Zuo, "Modeling and Reliability Evaluation of Multi-state k-out-of-n Systems," *Recent Advances in Reliability and Quality in Design*, H. Pham, ed., pp. 31-56, London: Springer London, 2008.

- [18] Z. Tian, M. J. Zuo, and H. Z. Huang, “Optimal Redundancy Allocation of Multi-State Systems with Genetic Algorithms,” *Studies in Computational Intelligence*, vol. 39, pp. 191-214, 2007.
- [19] M. Sallak, W. Schön, and F. Aguirre, “Reliability assessment for multi-state systems under uncertainties based on the Dempster–Shafer theory,” *IIE Transactions*, vol. 45, no. 9, pp. 995-1007, 2013.
- [20] G. Levitin, “Multi-State Vector-k-Out-of-n Systems,” *IEEE Transactions on Reliability*, vol. 62, no. 3, pp. 648-657, 2013.
- [21] E. M. Larsen, Y. Ding, Y. F. Li *et al.*, “Definitions of Generalized Multi-Performance Weighted Multi-State K^- -out-of- n System and its Reliability Evaluations,” *Reliability Engineering & System Safety*, 2017.
- [22] J. Wu, J. Yan, H. Jia *et al.*, “Integrated Energy Systems,” *Applied Energy*, vol. 167, pp. 155-157, 2016.
- [23] M. Geidl, and G. Andersson, “Optimal Power Flow of Multiple Energy Carriers,” *IEEE Transactions on Power Systems*, vol. 22, no. 1, pp. 145-155, 2007.
- [24] A. Shabaniour-Haghghi, and A. R. Seifi, “Energy Flow Optimization in Multicarrier Systems,” *IEEE Transactions on Industrial Informatics*, vol. 11, no. 5, pp. 1067-1077, 2015.
- [25] M. Geidl, G. Koeppel, P. Favre-Perrod *et al.*, “Energy hubs for the future,” *Power & Energy Magazine IEEE*, vol. 5, no. 1, pp. 24-30, 2007.
- [26] A. Vasebi, M. Fesanghary, and S. M. T. Bathaei, “Combined heat and power economic dispatch by harmony search algorithm,” *International Journal of Electrical Power & Energy Systems*, vol. 29, no. 10, pp. 713-719, 2007/12/01/, 2007.
- [27] X. Chen, C. Kang, M. O. Malley *et al.*, “Increasing the Flexibility of Combined Heat and Power for Wind Power Integration in China: Modeling and Implications,” *IEEE Transactions on Power Systems*, vol. 30, no. 4, pp. 1848-1857, 2015.
- [28] A. Lisnianski, and G. Levitin, *Multi-state system reliability: assessment, optimization and applications*: World Scientific Publishing Company, 2003.
- [29] Y. Ding, P. Wang, L. Goel *et al.*, “Long-term reserve expansion of power systems with high wind power penetration using universal generating function methods,” *IEEE Transactions on Power Systems*, vol. 26, no. 2, pp. 766-774, 2011.
- [30] G. Levitin, “Universal generating function and its applications,” *Springer, Berlin, Germany*, vol. 159, no. 3, pp. 307-324, 2005.
- [31] Z. Zeng, R. Kang, M. Wen *et al.*, “A model-based reliability metric considering aleatory and epistemic uncertainty,” vol. 5, pp. 15505-15515, 2017.
- [32] C. Shao, and Y. Ding, “Two-interdependent-performance multi-state system: Definitions and reliability evaluation,” *Reliability Engineering & System Safety*, vol. 199, pp. 106883, 2020/07/01/, 2020.

- [33] A. Yazdani, T. Jayabarathi, V. Ramesh *et al.*, "Combined heat and power economic dispatch problem using firefly algorithm," *Frontiers in Energy*, vol. 7, no. 2, pp. 133-139, June 01, 2013.
- [34] C. Lin, W. Wu, B. Zhang *et al.*, "Decentralized solution for combined heat and power dispatch through benders decomposition," vol. 8, no. 4, pp. 1361-1372, 2017.
- [35] A. Lisnianski, D. Laredo, and H. B. Haim, "Multi-state Markov Model for Reliability Analysis of a Combined Cycle Gas Turbine Power Plant." pp. 131-135, 15-18 Feb. 2016, 2016.
- [36] G. Levitin, *The Universal Generating Function in Reliability Analysis and Optimization*: Springer London, 2005.
- [37] I. Ushakov, "A universal generating function," *Soviet Journal of Computer and Systems Sciences*, vol. 24, no. 5, pp. 118-129, 1986.

6 Operational Risk Assessment of Integrated Electricity and Heating Systems with CHP units

6.1 Introduction

As illustrated in the previous chapters, the large-scale deployment of energy-efficient combined heat and power (CHP) has been witnessed in the last few decades. Nowadays, CHP accounts for a significant share of the total electricity generation in countries around the world. For example, CHP accounts for 50%–70% of the generation capacity in the Northern and Northeastern provinces of China [1]. The utilization of CHP has intensified the integration and interdependence between electrical and heating systems. As a consequence, the concept of integrated electricity and heating systems (IEHS) has been proposed [2]. In recent years, IEHS stands as one of the most discussed topics among industry, government, and academic sectors. Many previous studies on IEHS can be found in the literature, where most of them focus on operational flexibility improvement and operation optimization [3-9].

Besides operation optimization issues, the operational risk assessment of the IEHS is also worth investigating. The heating power and electric power of a CHP unit are interdependent, which are constrained by its heat-electricity feasible operation region [10]. Therefore, the risk of the heating system is intertwined with the risk of the electric power system in the IEHS. Considering that, the heating system and electric power system in the IEHS should be viewed as an integrated whole when it comes to the risk assessment.

Recently, many studies were conducted on the risk analysis of the integrated energy system (IES) where different energy vectors are interconnected and integrated. Usually, four steps are involved in the integrated energy system risk evaluation, including 1) building the risk models of the components, 2) selecting the component states and combining them to generate the system state, 3) analyzing the system state based on the optimal energy flow (OEF, the extension of the optimal power flow technique), and 4) calculate the risk indices. Generally speaking, most of the previous studies focus on the state analysis procedure. Previous studies have proposed multiple OEF models for the state analysis, with the consideration of the complementary action of the multiple energy carriers, the dynamic characteristics of the gas and heating power distribution networks, the dynamic behaviors of heating loads, and so on [11]. For example, the authors in [12] addressed the dynamic behavior of loads in the risk evaluation of the IES. Reference [13] proposed a new risk evaluation method considering the impact of the load rebound characteristics on system risk. In [14], the authors proposed a risk evaluation approach for IEHS with electric heat pump (HP) units based on the Monte Carlo simulation. In [15], the system state analysis along with autonomous system reconfiguration was conducted in the risk evaluation. In [16], a general risk assessment method was proposed for energy hubs based on the simulation tech-

nique. The results prove that the multi-energy coupling and coordinated operation can improve the risk of energy hubs. In [17], the optimal self-dispatching demand response model was established by considering multi-energy load reduction and conversion that significantly improve the risk of the IES. In [18], the risk of electricity-gas IES was evaluated considering different dynamic behaviors between power systems and natural gas systems and the cascading effects among them.

In contrast, the risk modeling of the component has not been investigated comprehensively in previous studies. In previous studies, the coupling devices, along with the conventional electrical devices and other devices, are usually modeled as a binary state model or a multi-state model. Moreover, it is assumed that the probability and performance rate of the device over all states are predetermined. However, the aforementioned assumptions may bring errors to the operational risk evaluation of the IEHS. On one hand, each coupling device consists of several elements. Hence, the state probability and performance rate of the coupling device should be obtained based on the analysis of the constitutive elements. On the other hand, different energy carriers are involved in the coupling device operation. Consequently, the performance rates of the coupling devices could be more diverse and complicated to characterize. Considering that, detailed risk modeling of the coupling devices is necessary for the operational risk evaluation of the IEHS. Reference [19] proposed a CHP risk and availability model based on the multi-state system model. However, that study is focused on the CHP unit rather than the whole integrated energy system. As far as we know, no previous research has investigated the operational risk assessment of the IEHS considering both the detailed risk models of the primary devices and operating constraints related to the devices and energy network.

The research gap is filled in this chapter by proposing a framework for the operational risk evaluation of the IEHS. First, the risk of the coupling devices, including CHP units and HP units, is analyzed based on the state space and the Markov process method. It is noteworthy that coupling devices are strikingly different from the conventional generating units regarding risk analysis. Conventional generating units only require a single performance variable of electric power to measure their risk. The coupling units, however, are designed to complete two tasks simultaneously and therefore require two interdependent performance variables of heating power and electric power to measure their risk. Considering that, the performance level of the coupling devices in each state is represented by a performance vector consisting of two interrelated elements.

The operational risk of the IEHS should be measured by the risk indices. The loss of load probability (LOLP) and expected energy not supplied (EENS) are widely used in the risk of the electric power systems [15]. A set of nodal risk indices are defined to measure the LOLP and EENS both in terms of heating power and electric power. The risk indices are calculated through the scenario-based combined heat and power dispatch (CHPD) model in which multiple scenarios are modeled to consider the possible forced outages of the conventional generating units, coupling devices, and energy network devices.

Besides the states of the devices, the other factors that come into play in determining risk indices are the energy loads. Traditionally, the energy load uncertainties are approximated by a multi-state model. However, the number of load states must be large enough to realize an accurate representation of the energy loads. To overcome this problem, the fuzzy multi-state model is developed to characterize the energy load uncertainties. In each load state, the load level is represented by a fuzzy number, which is a connected set of possible values and each possible value has its weight (membership) between 0 and 1. The load states are limited to avoid high computational complexity. Meanwhile, representing load levels by fuzzy numbers enables all possible realizations to be considered.

While calculating the operational risk, it is significant to reduce the scale of the problem and improve the computation efficiency. On one hand, the traditional universal generating function (UGF) that is widely used in single-performance engineering systems, such as power systems [20], is extended to the IEHS context to combine the states of coupling units to reduce the scenarios that need to be considered. On the other hand, the CHPD model is decomposed and linearized to enable it to be solved efficiently.

In the context of the previous research, the innovative contributions of the study can be summarized as:

1. The operational risk of the IEHS is assessed considering the detailed risk models of the coupling devices and the energy network.
2. The performance vectors consisting of two interrelated elements are defined to measure the performance levels of the coupling devices.
3. The fuzzy multi-state system models are proposed to characterize uncertainties related to the energy loads.
4. UGF and decomposition techniques are used to improve the computation efficiency of the risk assessment problem.

This chapter includes research related to the operational risk assessment of IEHSs with CHP units by [21].

6.2 Risk Modeling of the Coupling Devices

6.2.1 Risk model for the HP units

In risk modeling of the HP units, outdoor coil, compressor, expansion device, and indoor coil are the series-connected components that need to be considered [22]. A simple model of the HP unit starting with the outdoor coil and ending with the indoor coil is shown in Fig. 6.1.

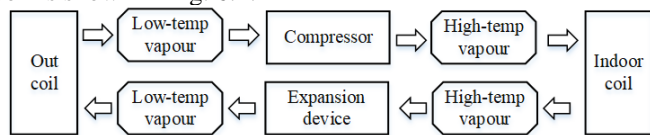


Fig. 6.1 A simple model of the HP unit [22]

Here, we consider the risk of the HP unit as a binary state model. In other words, the HP unit is either in the working state or failure state. Given the failure rate and

repair rate of the components, the equivalent risk indices of the HP unit can be calculated. The state probabilities associated with the HP unit working and failure states are respectively expressed in (6.1) and (6.2). The HP unit equivalent failure rate $\lambda_{j,t}$ can be calculated via (6.3) while the equivalent repair rate $\mu_{j,t}$ would be accordingly found using (6.4) [23].

$$p_{j,t}^1 = \prod_{\phi \in \psi_{C,j}} \left(\frac{\mu_{\phi,t}}{\lambda_{\phi,t} + \mu_{\phi,t}} \right) \quad (6.1)$$

$$p_{j,t}^0 = 1 - \prod_{\phi \in \psi_{C,j}} \left(\frac{\mu_{\phi,t}}{\lambda_{\phi,t} + \mu_{\phi,t}} \right) \quad (6.2)$$

$$\lambda_{j,t} = \sum_{\phi \in \psi_{C,j}} \lambda_{\phi,t} \quad (6.3)$$

$$\mu_{j,t} = \left(\prod_{\phi \in \psi_{C,j}} \frac{\mu_{\phi,t}}{\lambda_{\phi,t} + \mu_{\phi,t}} \right) \cdot \sum_{\phi \in \psi_{C,j}} \lambda_{\phi,t} \cdot \left(1 - \prod_{\phi \in \psi_{C,j}} \left(\frac{\mu_{\phi,t}}{\lambda_{\phi,t} + \mu_{\phi,t}} \right) \right)^{-1} \quad (6.4)$$

In the above equations, ϕ is the index of the constituent components of the HP unit.

Unlike the traditional power system component that only needs a performance variable of electric power, the HP unit needs two performance variables to measure its performance rates. The performance rates of the HP unit in working state (state 1) and failure state (state 0) are expressed as:

$$(QG_j, PG_j) = \begin{cases} (QG_j^{\max}, -PG_j^{\max}), & \text{in state 1} \\ (0, 0), & \text{in state 0} \end{cases} \quad (6.5)$$

In (6.5), QG_j^{\max} is the rated heating power of the HP unit, and PG_j^{\max} is equal to QG_j^{\max}/η_j where η_j is the efficiency of the HP unit. Notably, the HP unit consumes electricity and therefore is considered a negative electricity generation.

6.2.2 Risk model for the CHP units

Based on the analysis of the component functions, a CHP unit is decomposed into three subsystems each of which consists of several components connected in series arrangements [19]. The connection of the three subsystems is shown in Fig. 6.2. Subsystem 1 converts the fuel into thermal energy through the engine or turbine. Hence, the CHP unit is totally out of work if subsystem 1 fails. Subsystem 2 uses hot exhaust gases to produce useful heat energy. Hence, the CHP unit cannot produce heat energy if subsystem 2 fails but still can produce electrical energy if subsystem 1 works. On the contrary, the CHP unit can only produce heat energy if subsystem 3 fails.

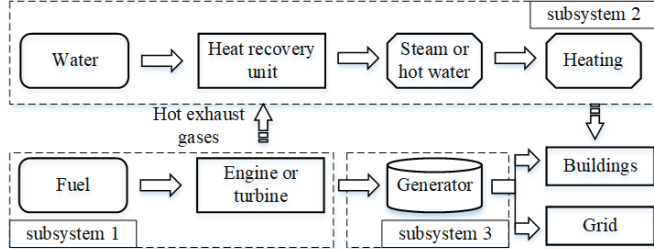


Fig. 6.2 Subsystems in a CHP unit [19]

Hence, a CHP unit has four possible states. State 3 is the perfect working state in which both heat energy and electric energy can be produced. State 2 denotes the situation in that only heat energy can be produced and state 1 denotes the situation where only electric energy can be produced. State 0 is the total failure state.

Then, the Markov process model is used to predict the probabilities of future CHP unit states. The four-state Markov model of the CHP unit is shown in Fig. 6.3. The probabilities of future states are strongly dependent on transition rates between the current state and possible future states [24]. The transition rates can be determined by the risk indices of the subsystems. For example, $\lambda_{s3,t}$ and $\mu_{s3,t}$ are respectively the failure rate and repair rate of subsystem 3, $\lambda_{s2,t}$ and $\mu_{s2,t}$ are respectively the failure rate and repair rate of subsystem 2, $\lambda_{s1,t}$ and $\mu_{s1,t}$ are respectively the failure rate and repair rate of subsystem 1. Notably, the failure rates and repair rates of the subsystems can be calculated in a similar way as (6.3) and (6.4).

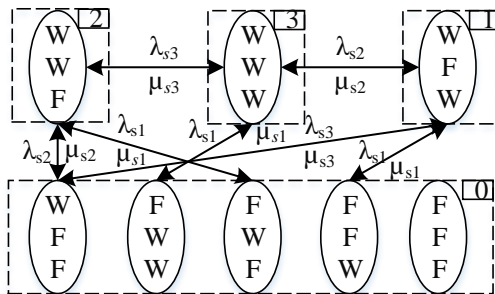


Fig. 6.3 State-space diagram of a CHP unit. “W” and “F” in the ellipse respectively denote the working state and failure state of the subsystems

The transitions among the possible states are expressed as the following differential equations.

$$\begin{aligned}
\frac{dp_{i,t}^3}{dt} &= \mu_{s3,t} \cdot p_{i,t}^2 + \mu_{s2,t} \cdot p_{i,t}^1 + \mu_{s1,t} \cdot p_{i,t}^0 - (\lambda_{s3,t} + \lambda_{s2,t} + \lambda_{s1,t}) \cdot p_{i,t}^3 \\
\frac{dp_{i,t}^2}{dt} &= \lambda_{s3,t} \cdot p_{i,t}^3 + (\mu_{s2,t} + \mu_{s1,t}) \cdot p_{i,t}^0 - (\mu_{s3,t} + \lambda_{s2,t} + \lambda_{s1,t}) \cdot p_{i,t}^2 \\
\frac{dp_{i,t}^1}{dt} &= \lambda_{s2,t} \cdot p_{i,t}^3 + (\mu_{s3,t} + \mu_{s1,t}) \cdot p_{i,t}^0 - (\mu_{s2,t} + \lambda_{s3,t} + \lambda_{s1,t}) \cdot p_{i,t}^1 \\
p_{i,t}^3 + p_{i,t}^2 + p_{i,t}^1 + p_{i,t}^0 &= 0
\end{aligned} \tag{6.6}$$

where $\lambda_{s3,t}$ and $\mu_{s3,t}$ are respectively the failure rate and repair rate of subsystem s3 at time t , and so on.

As we can see from (6), state probabilities are influenced by the transitions among the states. By solving the differential equations (6) under the initial conditions, e.g. $p_{i,t}^3=1, p_{i,t}^2=p_{i,t}^1=p_{i,t}^0=0$, when $t=t_0$, the state probabilities of the CHP unit i over the whole period can be obtained.

In state 1, the performance rate can be represented by $(0, PG_i^{\max})$ where PG_i^{\max} denotes the maximum electric power when the CHP unit. Similarly, the performance rate in state 2 can be represented by $(QG_i^{\max}, 0)$ where QG_i^{\max} denotes the maximum heating power of the CHP unit. Both the heating power and electric power can be adjusted when the CHP unit is in state 3. Moreover, there is usually a trade-off between heating power and electric power. Hence, the performance rate of the CHP unit in state 3 should be represented by a performance vector of two interrelated variables, i.e. $(QG_i^{\text{adj}}, PG_i^{\text{adj}})$. The ranges of QG_i^{adj} and PG_i^{adj} are expressed as:

$$0 \leq QG_i^{\text{adj}} \leq QG_i^{\max}, f^{\min}(QG_i^{\text{adj}}) \leq PG_i^{\text{adj}} \leq f^{\max}(QG_i^{\text{adj}}) \tag{6.7}$$

where $f^{\min}(QG_i^{\text{adj}})$ and $f^{\max}(QG_i^{\text{adj}})$ are the bound functions derived from the CHP unit heat-electricity feasible operating region.

Based on the above discussion, the performance rates of the four states are expressed as:

$$(QG_{i,t}^{s_i}, PG_{i,t}^{s_i}) = \begin{cases} (QG_i^{\text{adj}}, PG_i^{\text{adj}}), s_i=3 \\ (QG_i^{\max}, 0), s_i=2 \\ (0, PG_j^{\max}), s_i=1 \\ (0, 0), s_i=0 \end{cases} \tag{6.8}$$

Note that the time-dependent state probabilities are calculated based on (6).

6.2.4 State combination based on the UGF technique

There could be many CHP units or HP units connected to the same node. The CHP units or HP units on the same node can be aggregated as a typical multi-state CHP group or HP group through the UGF technique. Moreover, the states of the CHP group or HP group with identical performance rates can be emerged to reduce the number of system states.

UGF is a representation of the random variable utilizing moment generating functions and z-transformation for analyzing the risk of the multi-state system (MSS) [25]. The UGF representation as a polynomial gives the probability and performance rates of the component/system over all possible states. Moreover, the UGF technique can find the entire performance distribution of the MSS based on the performance distributions of its components.

Here, we consider three HP units ($j1$, $j2$, and $j3$) with the same nominal capacities. The UGFs of $j1$, $j2$, and $j3$ can be obtained based on their performance distribution:

$$\begin{aligned} u_{j1}(z) &= p_{j1,t}^1 \cdot z^{(QG_{j1}^{\max}, -PG_{j1}^{\max})} + p_{j1,t}^0 \cdot z^0 \\ u_{j2}(z) &= p_{j2,t}^1 \cdot z^{(QG_{j2}^{\max}, -PG_{j2}^{\max})} + p_{j2,t}^0 \cdot z^0 \\ u_{j3}(z) &= p_{j3,t}^1 \cdot z^{(QG_{j3}^{\max}, -PG_{j3}^{\max})} + p_{j3,t}^0 \cdot z^0 \end{aligned} \quad (6.9)$$

where $QG_{j1}^{\max} = QG_{j2}^{\max} = QG_{j3}^{\max}$, $PG_{j1}^{\max} = PG_{j2}^{\max} = PG_{j3}^{\max}$.

Assuming the three HP units are connected in parallel, the equivalent UGF representation of the HP group can be calculated based on the UGF parallel combination operator:

$$\begin{aligned} u_{j1|j2|j3}(z) &= \Omega_{\text{Par}} \left\{ u_{j1,t}(z), u_{j2,t}(z), u_{j3,t}(z) \right\} \\ &= \Omega_{\text{Par}} \left\{ p_{j1,t}^1 \cdot z^{(QG_{j1}^{\max}, -PG_{j1}^{\max})} + p_{j1,t}^0 \cdot z^0, L, L \right\} \\ &= p_{j1,t}^1 p_{j2,t}^1 p_{j3,t}^1 \cdot z^{(3 \cdot QG_{j1}^{\max}, -3 \cdot PG_{j1}^{\max})} + L + p_{j1,t}^0 p_{j2,t}^0 p_{j3,t}^0 \cdot z^{(0,0)} \end{aligned} \quad (6.10)$$

As shown in (6.10), three HP units with each having two states are equivalent to an HP group with four states. In this way, the number of system scenarios that need to be considered is significantly reduced.

Then, the series combination operator is introduced. Assume HP $j1$ and an energy delivery unit κ are connected in series. There are four states of the energy delivery unit: state 3, both heating power and electric power can be delivered; state 2, only heating power can be delivered; state 1, only electric power can be delivered; state 0, none of the electric power or heating power can be delivered. The UGF of the transmission network is shown as:

$$\begin{aligned} u_{\kappa}(z) &= p_{\kappa,t}^3 \cdot z^{(Qr_{\kappa}^{\max}, PT_{\kappa}^{\max})} + p_{\kappa,t}^2 \cdot z^{(Qr_{\kappa}^{\max}, 0)} + p_{\kappa,t}^1 \cdot z^{(0, PT_{\kappa}^{\max})} \\ &\quad + p_{\kappa,t}^0 \cdot z^0 \end{aligned} \quad (6.11)$$

where $p_{\kappa,t}^3$, $p_{\kappa,t}^2$, $p_{\kappa,t}^1$ and $p_{\kappa,t}^0$ are the state probabilities of the energy delivery unit κ . QT_{κ}^{\max} and PT_{κ}^{\max} denote the nominal heating power capacity and electric power capacity of the energy delivery unit, respectively.

Then, the equivalent UGF of the HP $j1$ and energy delivery unit κ can be obtained by the series combination operator:

$$\begin{aligned} u_{j1\&\kappa}(z) &= \Omega_{\text{Ser}} \{u_{j1}(z), u_{\kappa}(z)\} \\ &= \Omega_{\text{Ser}} \left\{ p_{j1,t}^1 \cdot z^{(QG_{j1}^{\max}, -PG_{j1}^{\max})} + p_{j1,t}^0 \cdot z^0, \right. \\ &\quad \left. p_{\kappa,t}^3 \cdot z^{(QT_{\kappa}^{\max}, PT_{\kappa}^{\max})} + p_{\kappa,t}^2 \cdot z^{(QT_{\kappa}^{\max}, 0)} + p_{\kappa,t}^1 \cdot z^{(0, PT_{\kappa}^{\max})} + p_{\kappa,t}^0 \cdot z^0 \right\} \quad (6.12) \\ &= p_{j1,t}^1 p_{\kappa,t}^3 \cdot z^{\left(\min(QG_{j1}^{\max}, QT_{\kappa}^{\max}), -\min(PG_{j1}^{\max}, PT_{\kappa}^{\max})\right)} + L + p_{j1,t}^0 p_{\kappa,t}^0 \cdot z^{(0,0)} \end{aligned}$$

Combining the parallel combination operator and series combination operator, a general combination operator can be defined to obtain the UGF of a system with a more complex structure.

$$\begin{aligned} u_C(z) &= \Omega_{\text{All}}(u_1(z), L, u_N(z)) \\ &= \Omega_{\text{All}} \left(\sum_{s_1=0}^{M_1} p_{1,t}^{s_1} \cdot z^{(Q_1^{s_1}, P_1^{s_1})}, \dots, \sum_{s_N=0}^{M_N} p_{N,t}^{s_N} \cdot z^{(Q_N^{s_N}, P_N^{s_N})} \right) \quad (6.13) \\ &= \sum_{s_C=0}^{M_C} p_{C,t}^{s_C} \cdot z^{(Q_C^{s_C}, P_C^{s_C})} \end{aligned}$$

In (6.13), C denotes a combination of N components/systems indexed by $1, \dots, N$. M_1, \dots , and M_N denote the number of possible states of components $1, \dots, N$, respectively. $p_{N,t}^{s_N}$ is the probability of the component/system N in state s_N , and $(Q_N^{s_N}, P_N^{s_N})$ denotes the performance rate in this state. s_C is the index of the state of the system C and M_C is the number of the total states of the combination C . Ω_{All} represents the general combination operator, which includes the parallel combination operator Ω_{Par} and the series combination operator Ω_{Ser} .

The aforementioned combination operators can deal with the HP units or other units whose performance rates are characterized by a vector of two fixed elements. Under such circumstances, the parallel combination operator sums up the performance rate values of the components while the series combination operator calculates the minimum among the performance rate values of the components. However, as we can see from (6.8), the performance rate of a CHP unit at the perfect working state should be represented by a vector of two variables that satisfy a set of constraints. Hence, the parallel combination operator and series combination operator for dealing with the CHP units are different from the aforementioned operators. The details concerning the combination operators for analyzing the states of CHP units can be found in our previous study [26].

6.3 Risk Evaluation based on the CHPD Model

6.3.1 Modeling of the uncertain energy loads

Usually, it is assumed the heating load and electric load forecast errors are described by Gaussian distributions with standard deviations of $\sigma_{Q,n}$ and $\sigma_{P,n}$, respectively. With the consideration of the forecast errors, the energy loads are approximated by seven-state models [27], as shown in (6.14).

$$\begin{aligned} u_{Q,n}(z) &= \sum_{\alpha=1}^7 p_{n,t}^\alpha \cdot z^{QD_n^\alpha} \\ u_{P,n}(z) &= \sum_{\beta=1}^7 p_{n,t}^\beta \cdot z^{PD_n^\beta} \end{aligned} \quad (6.14)$$

In this chapter, the load level in each state is represented by a fuzzy number to capture the errors due to the modeling inaccuracy (the errors induced by converting the Gaussian distributions to a multi-state model) and parameter uncertainty. The fuzzy load levels are expressed as:

$$\begin{aligned} \tilde{QD}_{n,t}^\alpha &= (QD_{n,t}^{\alpha-}, QD_{n,t}^{\alpha 0}, QD_{n,t}^{\alpha+}) \\ \tilde{PD}_{n,t}^\beta &= (PD_{n,t}^{\beta-}, PD_{n,t}^{\beta 0}, PD_{n,t}^{\beta+}) \end{aligned} \quad (6.15)$$

In (6.15), $PD_{n,t}^{\alpha 0}$ and $QD_{n,t}^{\beta 0}$ denote the average values of the forecasted heating load and electric load. $QD_{n,t}^{\alpha-}$ and $QD_{n,t}^{\alpha+}$ are the lower limit and upper limit of the heating load at state α , respectively. $PD_{n,t}^{\beta-}$ and $PD_{n,t}^{\beta+}$ are the lower limit and upper limit of the electric load at state β , respectively. All the parameters can be determined based on the energy forecasted load values ($QD_{n,t}^*, PD_{n,t}^*$) and forecast errors. $QD_{n,t}^{\alpha-}, QD_{n,t}^{\alpha 0}$ and $QD_{n,t}^{\alpha+}$ are equal to $QD_{n,t}^* + (\alpha - 5) * \sigma_{Q,n}$, $QD_{n,t}^* + (\alpha - 4) * \sigma_{Q,n}$ and $QD_{n,t}^* + (\alpha - 3) * \sigma_{Q,n}$, respectively. $PD_{n,t}^{\beta-}, PD_{n,t}^{\beta 0}$ and $PD_{n,t}^{\beta+}$ are equal to $PD_{n,t}^* + (\beta - 5) * \sigma_{P,n}$, $PD_{n,t}^* + (\beta - 4) * \sigma_{P,n}$ and $PD_{n,t}^* + (\beta - 3) * \sigma_{P,n}$, respectively.

Moreover, the membership functions of the energy loads are non-increasing monotonic linear functions. Take the heating load as an example, the membership function is expressed as (6.16).

$$\chi_{QD_{n,t}^\alpha}(y) = \begin{cases} 1, & y < QD_{n,t}^{\alpha-} \\ 1 - \frac{y - QD_{n,t}^{\alpha-}}{QD_{n,t}^{\alpha+} - QD_{n,t}^{\alpha-}}, & QD_{n,t}^{\alpha-} \leq y \leq QD_{n,t}^{\alpha+} \\ 0, & y > QD_{n,t}^{\alpha+} \end{cases} \quad (6.16)$$

where $\chi_{QD_{n,t}^\alpha}(y)$ denotes the membership assignment to the variable y .

6.3.2 Formulation of the CHPD model

A certain combination of the states of the devices and energy demands produces a corresponding scenario x . In each scenario, the risk indices can be calculated by the CHPD model. The objective of the CHPD model is to minimize the total system load curtailment for specific scenario s :

$$\text{Min } O_x = \sum_{t=1}^{N_T} \sum_{n=1}^{N_B} (w_E \cdot PC_{n,t}^x + w_H \cdot QC_{n,t}^x) \quad (6.17)$$

The model is subject to the following constraints:

The limits of the CPP units and wind power turbines are expressed as:

$$0 \leq PG_{k,t} \leq PG_k^x, 0 \leq PG_{w,t} \leq PG_w^x \quad (6.18)$$

The heating power and electric power of the HP units and CHP units are constrained by (6.5) and (6.8), respectively.

For the sake of simplicity, the superscript s is omitted in the following formulations.

The electric power balance constraints are expressed as:

$$\begin{aligned} & \sum_{i,j,k,w \in \psi_{G,n}} (PG_{i,t} - PG_{j,t} + PG_{k,t} + PG_{w,t}) - \left(\tilde{PD}_{n,t} - PC_{n,t} \right) \\ &= \sum_{m \in \psi_{N,n}} PL_{n-m,t} \end{aligned} \quad (6.19)$$

The operational constraints related to the DHN which consists of symmetric supply and return pipelines are also considered. The DHN model is subject to hydraulic and thermal conditions [28], which are expressed as:

$$\begin{aligned} \sum_{q \in \psi_{T,n}} m_{q,t}^{SU} + m_{n,t}^G &= \sum_{q \in \psi_{F,n}} m_{q,t}^{SU} + m_{n,t}^L \\ \sum_{q \in \psi_{T,n}} m_{q,t}^{RE} + m_{n,t}^L &= \sum_{q \in \psi_{F,n}} m_{q,t}^{RE} + m_{n,t}^G \end{aligned} \quad (6.20)$$

$$\Delta p_{q,t}^{SU} = \gamma_q (m_{q,t}^{SU})^2, \Delta p_{q,t}^{RE} = \gamma_q (m_{q,t}^{RE})^2 \quad (6.21)$$

$$\sum_{q \in \psi_{P,lp}} K_q \Delta p_{q,t}^{SU} = 0, \sum_{q \in \psi_{P,lp}} K_q \Delta p_{q,t}^{RE} = 0 \quad (6.22)$$

$$\sum_{i,j \in \psi_{N,n}} (QG_{i,t} + QG_{j,t}) + Q_{n,t}^{\text{disch}} - Q_{n,t}^{\text{ch}} = c_w m_{n,t}^G * (\tau s_{n,t}^G - \tau r_{n,t}^G) \quad (6.23)$$

$$\tilde{QD}_{n,t}^x + \Delta QD_{n,t} = c_w m_{n,t}^L * (\tau s_{n,t}^L - \tau r_{n,t}^L) \quad (6.24)$$

$$\tau s_{q,t}^O = (\tau s_{q,t}^I - \tau a_{n,t}) e^{-\lambda_q L_q / c_w * m_{q,t}^{SU}} + \tau a_{n,t} \quad (6.25)$$

$$\tau r_{q,t}^O = (\tau r_{q,t}^I - \tau a_{n,t}) e^{-\lambda_q L_q / c_w * m_{q,t}^{RE}} + \tau a_{n,t}$$

$$\sum_{q \in \psi_{F,n}} m_{q,t}^{SU} \cdot \tau s_{q,t}^{OUT} + m_{n,t}^G \cdot \tau s_{n,t}^G = \tau s_{n,t}^{SU} \left(\sum_{q \in \psi_{T,n}} m_{q,t}^{SU} + m_{n,t}^G \right) \quad (6.26)$$

$$\sum_{q \in \psi_{F,n}} m_{q,t}^{RE} \cdot \tau s_{q,t}^{IN} + m_{n,t}^L \cdot \tau s_{n,t}^L = \tau s_{n,t}^{RE} \left(\sum_{q \in \psi_{T,n}} m_{q,t}^{RE} + m_{n,t}^L \right)$$

$$H_{n,t} = \eta_n^{st} \cdot H_{n,t-1} + Q_{n,t}^{disch} / \eta_n^{disch} - Q_{n,t}^{ch} \cdot \eta_n^{ch} \quad (6.27)$$

$$H_{n,t}^{\min} \leq H_{n,t} \leq H_{n,t}^{\max} \quad (6.28)$$

$$Q_{n,t}^{disch,\min} \leq Q_{n,t}^{disch} \leq Q_{n,t}^{disch,\max} \quad (6.29)$$

$$Q_{n,t}^{ch,\min} \leq Q_{n,t}^{ch} \leq Q_{n,t}^{ch,\max} \quad (6.30)$$

Equation (6.20) denotes the continuity of mass flow constraint which guarantees that mass flows entering a node are the same as those leaving the node. Equations (6.21) and (6.22) make sure the fluid pressure drop due to the pipe friction in a closed loop is equal to zero, where $K_q = 1$ indicates that the mass flow direction in pipeline q is consistent with that of loop direction; $K_q = -1$ indicates that the mass flow direction in pipeline q is opposite to that of the loop. Equation (6.23) formulated the relationship between the heat energy provided by heat sources and the mass flow from them. The connection between the heating loads and the mass flow to them is expressed in (6.24). The relation between inlet and outlet pipeline temperatures is established in (6.25). Equation (6.26) calculates the temperature at confluence nodes at which fluids with different temperatures come across. Constraints (6.27)-(6.30) denote the mathematical model of the heat storage device. Equation (6.27) denotes the stored heat energy level of the device. Notably, a small part of the heat would be lost due to energy exchange with the external environment. Thus, this kind of loss should be taken into consideration and is assumed to be proportional to the previously stored heat [29].

Additionally, the heat charging and discharging efficiency are also taken into consideration. Hence, the stored heat energy level at time step t can be expressed as (6.27), where $H_{n,t}$ and $H_{n,t-1}$ are the stored heat level of the accumulator at time step t and $t-1$, respectively, and η_n^{st} , η_n^{ch} and η_n^{disch} are the storage efficiency, heat charging, and discharging efficiency of the thermal storage, respectively. Equation (6.28) restricts the stored heat level of the heat storage device, where $Q_{n,t}^{ch}$ and $Q_{n,t}^{disch}$ are the heat charging and discharging rate of heat accumulator at time step t , respectively. Constraints (6.29)-(6.30) represent the maximum charging and discharging power of the storage device.

The heating load is quite different from the electric load. The thermal inertia of buildings allows a brief period of thermal energy supply interruption or reduction without decreasing the consumers' satisfaction [30]. Considering that, we introduce a slack variable $\Delta QD_{n,t}$ to denote the flexibility of the heating load. $\Delta QD_{n,t}$ can be adjusted as long as the indoor temperature is maintained within the comfort

range. The building temperature $\tau_{b,t}$ is represented as a function of time, which is determined by injected heating power and heat losses [31]:

$$\sum_{b \in \psi_{L,n}} c_b \frac{d\tau_{b,t}}{dt} = \Delta QD_{n,t} \quad (6.31)$$

Equation (6.31) can be discretized as:

$$\sum_{b \in \psi_{L,n}} c_b (\tau_{b,t+1} - \tau_{b,t}) = \Delta QD_{n,t} \quad (6.32)$$

The threshold of the comfortable temperature is expressed as:

$$\tau_{b,t}^{\min} \leq \tau_{b,t} \leq \tau_{b,t}^{\max} \quad (6.33)$$

6.3.3 Algorithm to solving the CHPD model

With the consideration of the fuzzy-number energy loads, the CHPD model is formulated as an optimization problem with fuzzy parameters. Moreover, the CHPD model is linearized in this chapter. Hence, the CHPD model is formulated as (6.34).

$$\begin{aligned} & \min \sum_{g=1}^{N_g} c_g \mu_g \\ \text{s.t. } & g_\varphi(\mu) = \sum_{g=1}^{N_g} a_{\varphi g} \mu_g \leq \tilde{b}_\varphi, \quad \varphi = 1, 2, \dots, N_\varphi \\ & \mu_g \geq 0, \quad g = 1, 2, \dots, N_g \end{aligned} \quad (6.34)$$

where g is the index of variables and N_g is the number of total variables, φ is the index of the constraints, N_φ is the number of the total constraints. $a_{\varphi g}$ and \tilde{b}_φ are the coefficients of the constraints.

Based on the approach proposed by Carlsson and Korhonen [32], the original problem (6.34) is equivalent to the following auxiliary problem:

$$\begin{aligned} & \min \sum_{g=1}^{N_g} c_g \mu_g \\ \text{s.t. } & g_\varphi(\mu) = \sum_{g=1}^{N_g} a_{\varphi g} \mu_g \leq \chi_{\tilde{b}_\varphi}^{-1}(\varepsilon), \quad \varphi = 1, 2, \dots, N_\varphi \\ & \varepsilon \in [0, 1], \mu_g \geq 0, \quad g = 1, 2, \dots, N_g \end{aligned} \quad (6.35)$$

where $\chi_{\tilde{b}_\varphi}^{-1}(\varepsilon)$ is the inverse of the membership function of the energy loads.

Here, ε is defined as the optimism parameter which is adjusted based on the system operator's risk propensity. For each given ε , one can obtain the optimal solution to the problem (6.35), and then the results are presented to the system operator for further decision. A large ε can be chosen if the system operator is more optimistic.

Specific to the energy load, the energy loads can be calculated as (6.36) and (6.37) once the ε is chosen.

$$QD_{n,t}^{\alpha} = (1-\varepsilon) \cdot (QD_{n,t}^{\alpha+} - QD_{n,t}^{\alpha-}) + QD_{n,t}^{\alpha-} \quad (6.36)$$

$$PD_{n,t}^{\beta} = (1-\varepsilon) \cdot (PD_{n,t}^{\beta+} - PD_{n,t}^{\beta-}) + PD_{n,t}^{\beta-} \quad (6.37)$$

In the CHPD model, the operating constraints (6.21), (6.23)-(6.26) are nonconvex and require more computation time and resources. Moreover, it is observed that the DHN operation problem renders the convex optimization problem by fixing the mass flow variables [33]. Thus, a hydraulic-thermal decomposition technique is proposed to decompose the CHPD problem into two linear programming problems that can be solved iteratively. The basic idea of the decomposition technique can be expressed as: 1) calculating the mass flow rate variables $\mathbf{m} = [m_n^G, m_n^L, m_{q,t}^{SU}, m_{q,t}^{RE}]$ when the temperature variables $\boldsymbol{\tau} = [\tau s_{n,t}^G, \tau r_{n,t}^G, \tau s_{n,t}^L, \tau r_{n,t}^L, \tau s_{q,t}^I, \tau r_{q,t}^O]$ are all set as the minimum values. 2) solve the CHPD by fixing \mathbf{m} and update the temperature variables. The two steps are repeated iteratively to obtain the optimal results of the DHN operation problem. The procedure of the hydraulic-thermal decomposition technique is listed as follows.

Algorithm for solving the CHPD model

- Step 1. Set the iteration index $I=1$, and set all the temperatures of pipelines to the lower limits $\boldsymbol{\tau}^{I-1} = \boldsymbol{\tau}^*$.
 - Step 2. Calculate the heat losses during the pipeline. Optimize production plans of heat sources; the total output is equal to the summation of heating loads and pipeline losses. Calculate mass flow rates based on the (6.20)-(6.24).
 - Step 3 Solve the linearized DHN optimization model with fixed \mathbf{m} .
 - Step 4. Calculate the temperatures of pipelines $\boldsymbol{\tau}^I$.
 - Step 5. If $\max |\boldsymbol{\tau}^I - \boldsymbol{\tau}^{I-1}| \leq \varepsilon_1$ or $I \geq \varepsilon_2$ then go to **Step 7**; otherwise, go to **Step 6**.
 - Step 6. Set $I=I+1$, $\boldsymbol{\tau}^I = (\boldsymbol{\tau}^I + \boldsymbol{\tau}^{I-1}) / 2$ and go to **Step 2**.
 - Step 7. **End.**
-

It should be noted that step 5 checks the stopping criteria, where ε_1 represents the convergence threshold that is set as 10^{-3} in this chapter and ε_2 represents the maximum iteration time that is set as 20 in this chapter. The maximum iteration time is a system-dependent parameter and should be determined based on the experimental results. For a larger-scale test system, the maximum iteration time needs to be increased correspondingly.

6.3.4 Risk indices calculation

LOLP and EENS are widely used for risk evaluation in power systems [23]. In this chapter, the LOLP and EENS concepts are extended to evaluate the nodal risk of the IEHS. The calculation of the LOLP and EENS indices follows several steps.

First, establish the system state set, with each system state s corresponding to a certain combination of the component state and load level. Then, calculate the risk-related indices of the IEHS for each system state s . At last, sum up the risk indices of all the possible system states.

The loss of electric load probability $LOLP_{E,n}$, loss of heating load probability $LOLP_{H,n,t}$, and loss of energy load probability $LOLP_{A,n}$ as in (6.41)-(6.43), respectively.

$$LOLP_{E,n} = \left[\sum_{t=1}^{N_T} \sum_{x \in \psi_X} p^x * \text{If}(PC_{n,t}^x > 0) \right] / N_T \quad (6.38)$$

$$LOLP_{H,n} = \left[\sum_{t=1}^{N_T} \sum_{x \in \psi_X} p^x * \text{If}(QC_{n,t}^x > 0) \right] / N_T \quad (6.39)$$

$$LOLP_{A,n} = \left[\sum_{t=1}^{N_T} \sum_{x \in \psi_X} p^x * (\text{If}(PC_{n,t}^x > 0) \parallel \text{If}(QC_{n,t}^x > 0)) \right] / N_T \quad (6.40)$$

where $\text{If}(PC_{n,t}^x > 0)$ and $\text{If}(QC_{n,t}^x > 0)$ are the binary logic variables. When there is the electric load shedding, $\text{If}(PC_{n,t}^x > 0)$ equals 1. Similarly, $\text{If}(QC_{n,t}^x > 0)$ equals 1 when there is heating load shedding.

The expected electricity energy not supplied, expected heat energy not supplied, and expected energy not supplied are expressed as (6.41)-(6.43), respectively.

$$EENS_{E,n} = 8760 \cdot \left(\sum_{t=1}^{N_T} \sum_{x \in \psi_X} p^x * PC_{n,t}^x \right) / N_T \quad (6.41)$$

$$EENS_{H,n} = 8760 \cdot \left(\sum_{t=1}^{N_T} \sum_{x \in \psi_X} p^x * QC_{n,t}^x \right) / N_T \quad (6.42)$$

$$EENS_{A,n} = w_E \times EENS_{E,n} + w_H \times EENS_{H,n} \quad (6.43)$$

6.4 Case Studies

6.4.1 Test system and parameters

A 24-node IEHS is developed to illustrate the risk evaluation technique proposed in this chapter. The topology of the test system is shown in Fig. 6.4.

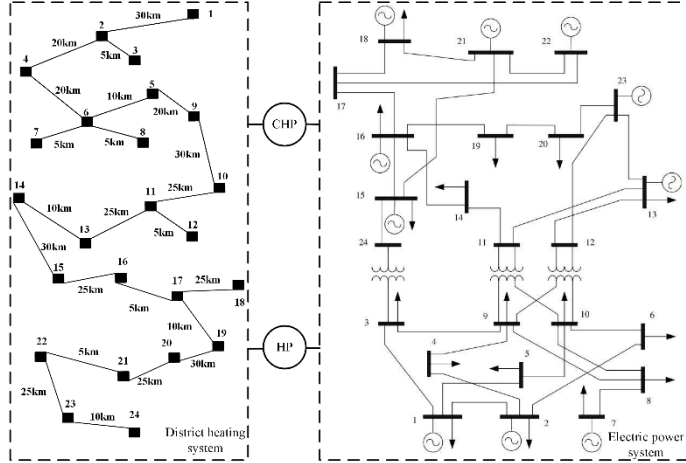


Fig. 6.4 Topology of the 24-node test system

The electric power system is based on the IEEE-RTS system [34]. The district heating system is an extension of the system developed in [35]. There are 20 load-carrying nodes where both heating power and electric power are demanded. Moreover, it is assumed that the heat demand is equal to the electric demand in each node. There are 32 generating units located at ten generating buses in the system, and a part of them are modified to the CHP units. There are also four HP units equipped in the test system.

The data on CHP units and HP units are summarized in Table 6.1.

Table 6.1 Data on CHP and HP units (The unit of the capacity is MW)

CHP units					
Node	Heating capacity	Electric capacity	Node	Heating capacity	Electric capacity
2	253	153	13	400	240
2	253	153	21	500	300
13	400	240	21	500	300
13	500	300	21	500	300
HP units					
Node	Heating capacity	Efficiency	Node	Heating capacity	Efficiency
6	50	0.8	15	80	0.85
6	50	0.8	15	80	0.85

The daily load profiles are shown in Fig. 6.5. The maximum electric demand and heat demand are set as 60% of the installed capacity of electricity generation and heat generation, respectively.

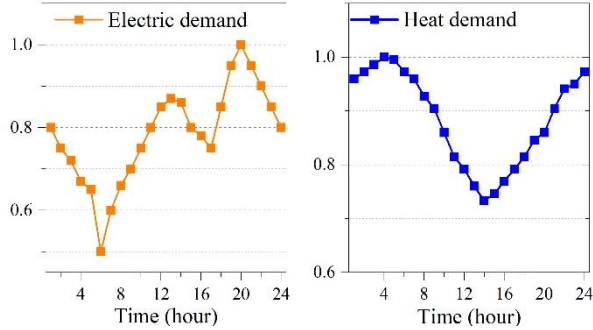


Fig. 6.5 Daily load profiles of the test system

6.4.2 Risk analysis of the test system

First, the risk indices of the test system are calculated based on the proposed risk evaluation technique.

Table 6.2 Nodal LOLP of the test system

Node	LOLP _A	LOLP _E	LOLP _H
2	0.0051	0.0004	0.0051
4	0.0055	0.0008	0.0048
6	0.0051	0.0006	0.0051
8	0.0051	0.0004	0.0051
10	0.0055	0.0008	0.0051
14	0.0040	0.0005	0.0035
16	0.0028	0.0001	0.0028
18	0.0032	0.0004	0.0031
20	0.0012	0.0001	0.0012

The nodal risk indices for part of the load-carrying nodes of the test system are shown in Table 6.2 and Table 6.3. One of the observations from Table 6.2 and Table 6.3 is that the LOLP and EENS of the heating system are larger than those of the electric system. In conclusion, the risk level of the heating-system part is lower than the electric-system part. The main reason behind it is the radiated heat pipeline topology, which has a reduced chance to maintain the heating power supply after a heat pipeline failure.

Table 6.3 Nodal EENS of the test system

Node	EENS _A (MWh)	EENS _E (MWh)	EENS _H (MWh)
2	443.06	77.56	365.50
4	698.09	352.29	345.80
5	364.14	0.00	364.14
6	997.25	485.73	511.52
8	1185.87	547.38	638.50

10	1936.81	1342.85	594.00
14	820.32	319.16	501.16
16	279.61	11.84	267.77
18	11838.36	484.12	654.24
20	276.83	70.86	205.97

The nodal risk indices are evaluated in three cases to test the impact of the capacities of HP units on the risk indices. Case 1 is the basic case. In Case 2, the capacities of the HP units are increased by 50%. In Case 3, the capacities of the HP units are doubled compared with Case 1. The simulation is conducted for over 24 hours. The comparisons between the LOLP_A and EENS_A in different cases are shown in Fig. 6.6 and Fig. 6.7, respectively.

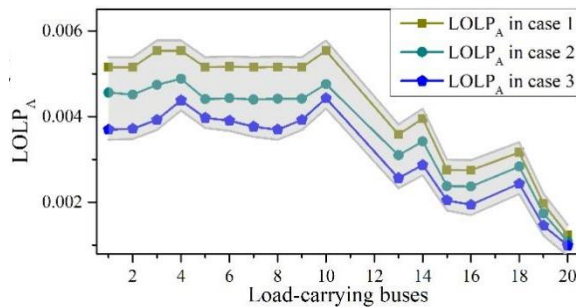


Fig. 6.6 LOLPA of the load-carrying nodes in the three cases

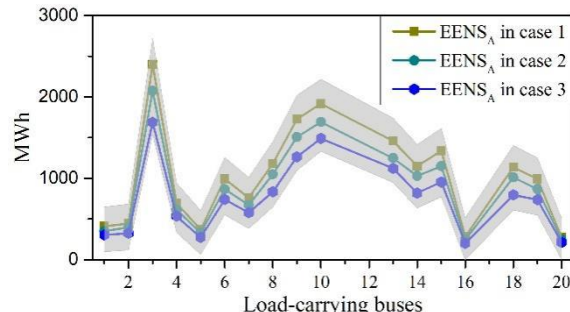


Fig. 6.7 EENS_A of the load-carrying nodes in the three cases

Based on the simulation results, we can conclude that both LOLP_A and EENS_A can be significantly reduced with the increase in capacities of the HP units. Because HP units improve the operational flexibility of the IEHS by converting electric power to heating power and consequently avoid the load curtailment to a cer-

tain extent. The HP units especially contribute to enhancing the risk of the heating power supply since HP units can be considered as heating power sources.

Notably, improving operational risk is not the only value of HP units. HP units also contribute to energy efficiency improvement and wind power integration [36]. Hence, the full cost recovery of the HP units is guaranteed.

6.4.3 Impacts of the optimism parameter on the results

As discussed in Section 6.3, the optimism parameter is introduced to convert the original optimization problem into a deterministic optimization problem. Different optimism parameters would lead to different results for the optimization problem. Then, the results are presented to the system operator for further decision.

The impacts of the optimism parameters on the risk evaluation results are summarized in Fig. 6.8(a) and Fig. 6.8(b), respectively. In conclusion, improving the optimism parameter leads to lower LOLPA and EENS_A. In the risk-neutrality scenario when α is set as 0.5, the average values of LOLPA in three cases are 0.00405, 0.00341 and 0.00300, respectively; the average values of EENS_A are 967.21MWh, 831.12MWh, and 621.25MWh, respectively. In the risk aversion scenario when α is set as 0, the average LOLPA in three cases are 0.00438, 0.00372, and 0.00311, respectively; the average values of EENS_A are 1031.6MWh, 908.64MWh, and 750.12MWh, respectively. In the risk-seeking scenario when α is set as 1, the average values of LOLPA in three cases are 0.00362, 0.00301 and 0.00262, respectively; the average values of EENS_A are 852.30MWh, 723.66MWh, and 600.12MWh, respectively.

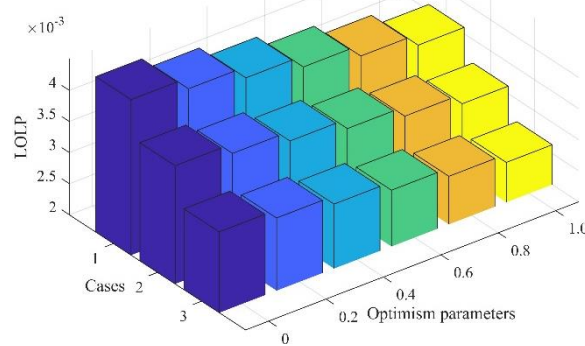


Fig. 6.8(a) Average LOLP_A in three cases with different optimism parameters

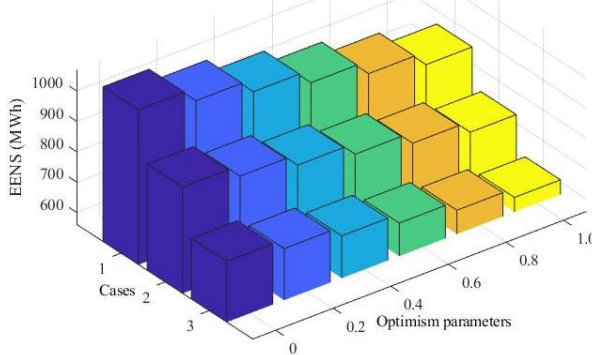


Fig. 6.8(b) Average EENS_A in three cases with different optimism parameters

6.4.4 The computational efficiency of the proposed technique

As far as we know, no previous research has investigated the operational risk of the IEHS considering both risk models of coupling devices and the energy network model. Hence, the MCS method is used as the reference to illustrate the computational efficiency of the proposed risk assessment technique which utilizes the UGF technique. Moreover, the original CHPD model which is formulated as a nonlinear linear programming (NLP) is compared with the proposed LP-based CHPD model in terms of accuracy and computation time for a one-hour-period analysis. All the simulations are on a personal computer with Intel Core i7 2.6 GHz CPU and 16 GB of RAM. Three techniques are compared, including the MCS-NLP technique, UGF-NLP technique, and UGF-LP technique. The comparisons are concluded in Table 6.4.

As shown in Table 6.4, the results of risk indices in different scenarios are very close. The results of the risk indices obtained by MCS are slightly larger than those in the UGF-based methods. In terms of the risk assessment results, the other observation is that the proposed linearization method has a very little bearing on the accuracy of risk assessment results. The relative error between the NLP CHPD model and the LP CHPD model is less than 0.15%.

When it comes to computation time, the benefit of the proposed solution technique is very remarkable. Compared with MCS-NLP and UGF-NLP methods, the computation time of the proposed technique can be reduced by 98.8% and 92.2%, respectively. The high efficiency of the proposed method enables it to be used in the operational risk assessment of the IEHS.

Table 6.4 Comparisons of different techniques

Method	Average LOLP _A	Average EENS _A (MWh)	CPU time (s)
MCS-NLP	0.00452	1112.1	82364.58
UGF-NLP	0.00438	1046.0	12763.47
UGF-LP (proposed)	0.00432	1031.6	1001.21

6.5 Conclusions

In this chapter, the risk models of the coupling devices in the IEHS are first developed. UGF method is used to combine the states of the devices and correspondingly reduce the scenarios that need to be considered. In the risk assessment process, energy loads are represented by fuzzy multi-state models to capture the uncertainties related to the forecast error, model error, and data error. The scenario-based CHPD model is developed to calculate the risk indices. Moreover, the CHPD model is linearized to improve computation efficiency. It is evidenced that the proposed solution technique has distinct advantages over other techniques. Simulation results verify the effectiveness of HP units in increasing the risk of the IEHS.

There are two directions for future studies. On one hand, the condition-dependent failure rates of the devices can be considered to improve the accuracy of the risk analysis results. On the other hand, the risk indices more related to the real-time operation can be established.

References

- [1] X. Chen, C. Kang, M. O'Malley *et al.*, "Increasing the Flexibility of Combined Heat and Power for Wind Power Integration in China: Modeling and Implications," *IEEE Transactions on Power Systems*, vol. 30, no. 4, pp. 1848-1857, 2015.
- [2] G. Streckienė, V. Martinaitis, A. N. Andersen *et al.*, "Feasibility of CHP-plants with thermal stores in the German spot market," *Applied Energy*, vol. 86, no. 11, pp. 2308-2316, 2009/11/01/, 2009.
- [3] Z. Li, W. Wu, M. Shahidehpour *et al.*, "Combined heat and power dispatch considering pipeline energy storage of district heating network." pp. 1-1,16-20 July 2017, 2017.
- [4] C. Lin, W. Wu, B. Zhang *et al.*, "Decentralized Solution for Combined Heat and Power Dispatch Through Benders Decomposition," *IEEE Transactions on Sustainable Energy*, vol. 8, no. 4, pp. 1361-1372, 2017.
- [5] Y. Xue, Z. Li, C. Lin *et al.*, "Coordinated Dispatch of Integrated Electric and District Heating Systems Using Heterogeneous Decomposition," *IEEE Transactions on Sustainable Energy*, pp. 1-1, 2019.
- [6] S. Yao, W. Gu, S. Zhou *et al.*, "Hybrid Timescale Dispatch Hierarchy for Combined Heat and Power System Considering the Thermal Inertia of Heat Sector," *IEEE Access*, vol. 6, pp. 63033-63044, 2018.
- [7] Y. Zhou, W. Hu, Y. Min *et al.*, "Integrated Power and Heat Dispatch Considering Available Reserve of Combined Heat and Power Units," 2018.
- [8] Z. Li, W. Wu, J. Wang *et al.*, "Transmission-Constrained Unit Commitment Considering Combined Electricity and District Heating Networks," *IEEE Transactions on Sustainable Energy*, vol. 7, no. 2, pp. 480-492, 2016.

- [9] Y. Chen, Q. Guo, and H. Sun, "Decentralized Unit Commitment in Integrated Heat and Electricity Systems Using SDM-GS-ALM," *IEEE Transactions on Power Systems*, vol. 34, no. 3, pp. 2322-2333, 2019.
- [10] C. Algie, and K. P. Wong, "A test system for combined heat and power economic dispatch problems." pp. 96-101 Vol.12004.
- [11] J. He, Z. Yuan, X. Yang *et al.*, "Reliability Modeling and Evaluation of Urban Multi-energy Systems: A Review of the State of the Art and Future Challenges," *IEEE Access*, 2020.
- [12] M.-H. Shariatkah, M.-R. Haghifam, M. Parsa-Moghaddam *et al.*, "Modeling the reliability of multi-carrier energy systems considering dynamic behavior of thermal loads," *Energy and Buildings*, vol. 103, pp. 375-383, Sep, 2015.
- [13] G. Li, Y. Huang, and Z. Bie, "Reliability Evaluation of Smart Distribution Systems Considering Load Rebound Characteristics," *IEEE Transactions on Sustainable Energy*, vol. 9, no. 4, pp. 1713-1721, 2018.
- [14] S. Zhang, M. Wen, H. Cheng *et al.*, "Reliability evaluation of electricity-heat integrated energy system with heat pump," *CSEE Journal of Power and Energy Systems*, vol. 4, no. 4, pp. 425-433, 2018.
- [15] G. Li, Z. Bie, Y. Kou *et al.*, "Reliability evaluation of integrated energy systems based on smart agent communication," *Applied Energy*, vol. 167, pp. 397-406, Apr, 2016.
- [16] J. Yu, L. Guo, M. Ma *et al.*, "Risk assessment of integrated electrical, natural gas and district heating systems considering solar thermal CHP plants and electric boilers," *International Journal of Electrical Power & Energy Systems*, vol. 103, pp. 277-287, 2018.
- [17] S. Wang, C. Shao, Y. Ding *et al.*, "Operational reliability of multi-energy customers considering service-based self-scheduling," *Applied Energy*, vol. 254, pp. 113531, Nov, 2019.
- [18] M. Bao, Y. Ding, C. Shao *et al.*, "Nodal Reliability Evaluation of Interdependent Gas and Power Systems Considering Cascading Effects," *IEEE Transactions on Smart Grid*, vol. 11, no. 5, pp. 4090-4104, Mar, 2020.
- [19] M. R. Haghifam, and M. Manbachi, "Reliability and availability modelling of combined heat and power (CHP) systems," *International journal of electrical power & energy systems*, vol. 33, no. 3, pp. 385-393, 2011.
- [20] G. Levitin, "A universal generating function approach for the analysis of multi-state systems with dependent elements," *Reliability Engineering & System Safety*, vol. 84, no. 3, pp. 285-292, 2004/06/01/, 2004.
- [21] Y. Ding, C. Shao, B. Hu *et al.*, "Operational Reliability Assessment of Integrated Heat and Electricity Systems Considering the Load Uncertainties," *IEEE Transactions on Smart Grid*, vol. 12, no. 5, pp. 3928-3939, 2021.

- [22] E. Bilgen, and H. Takahashi, “Exergy analysis and experimental study of heat pump systems,” *Exergy, an international journal*, vol. 2, no. 4, pp. 259-265, 2002.
- [23] H. Sabouhi, A. Abbaspour, M. Fotuhi-Firuzabad *et al.*, “Reliability modeling and availability analysis of combined cycle power plants,” vol. 79, pp. 108-119, 2016.
- [24] Y. Ding, C. Singh, L. Goel *et al.*, “Short-Term and Medium-Term Reliability Evaluation for Power Systems With High Penetration of Wind Power,” *IEEE Transactions on Sustainable Energy*, vol. 5, no. 3, pp. 896-906, Jul, 2014.
- [25] M. Bao, Y. Ding, C. Singh *et al.*, “A Multi-State Model for Reliability Assessment of Integrated Gas and Power Systems Utilizing Universal Generating Function Techniques,” *IEEE Transactions on Smart Grid*, vol. 10, no. 6, pp. 6271-6283, 2019.
- [26] C. Shao, and Y. Ding, “Two-interdependent-performance multi-state system: Definitions and reliability evaluation,” *Reliability Engineering & System Safety*, vol. 199, pp. 106883, 2020/07/01/, 2020.
- [27] M. A. Ortega-Vazquez, and D. S. Kirschen, “Estimating the Spinning Reserve Requirements in Systems With Significant Wind Power Generation Penetration,” *IEEE Transactions on Power Systems*, vol. 24, no. 1, pp. 114-124, 2009.
- [28] Y. Cao, W. Wei, L. Wu *et al.*, “Decentralized Operation of Interdependent Power Distribution Network and District Heating Network: A Market-Driven Approach,” *IEEE Transactions on Smart Grid*, pp. 1-1, 2018.
- [29] H. Wang, W. Yin, E. Abdollahi *et al.*, “Modelling and optimization of CHP based district heating system with renewable energy production and energy storage,” *Applied Energy*, vol. 159, pp. 401-421, 2015/12/01/, 2015.
- [30] D. J. C. U. C. Ryder-Cook, “Thermal modelling of buildings,” 2009.
- [31] H. Hui, Y. Ding, W. Liu *et al.*, “Operating reserve evaluation of aggregated air conditioners,” *Applied Energy*, vol. 196, pp. 218-228, Jun, 2017.
- [32] A. Ebrahimnejad, and J. L. Verdegay, “A new approach for solving fully intuitionistic fuzzy transportation problems,” *Fuzzy Optimization and Decision Making*, vol. 17, no. 4, pp. 447-474, 2018/12/01, 2018.
- [33] P. M. Castro, “Tightening piecewise McCormick relaxations for bilinear problems,” *Computers & Chemical Engineering*, vol. 72, pp. 300-311, 2015/01/02/, 2015.
- [34] T. R. T. S. T. Force, “IEEE Committee Report. IEEE reliability test system,” *IEEE Transactions on Power Apparatus & Systems*, vol. 98, pp. 2047-2054, 1979.
- [35] A. Shabanzour-Haghghi, and A. R. Seifi, “Simultaneous integrated optimal energy flow of electricity, gas, and heat,” *Energy Conversion & Management*, vol. 101, pp. 579-591, 2015.

- [36] I. Vorushylo, P. Keatley, N. Shah *et al.*, “How heat pumps and thermal energy storage can be used to manage wind power: A study of Ireland,” *Energy*, vol. 157, pp. 539-549, 2018/08/15/, 2018.

7 Operational Risk of Multi-Energy Customers Considering Service-Based Self-Scheduling

7.1 Introduction

In the previous six chapters, the risk of integrated electricity and gas systems as well as integrated electricity and heating systems is analyzed. On the demand side of multi-energy systems, the interaction of different energies gives birth to the concept of multi-energy customers. With access to multiple energy supply infrastructures, multi-energy customers are provided with flexible options for satisfying their energy-related service needs. For example, space heating may be provided through electrical air conditions or direct thermal power from district heating networks. The parts of services that can be scheduled by multi-energy customers are referred to as multi-energy flexible services (MEFSs) [1]. Apart from service curtailment and service shifting among different time periods, available options for customers include shifting the MEFSs from one energy type to another in terms of energy substitution. In this manner, customers can self-schedule their energy consumption behaviors to minimize operation costs [2].

The self-scheduling of flexible loads in multi-energy systems has been discussed in previous chapters. In the study [3], a comprehensive model was proposed for self-scheduling an energy hub to supply the cooling, heating, and electrical demands of a building. Real-time demand response in a multi-energy distribution system with its potential and arbitrage was studied in [4]. Optimal day-ahead scheduling of the multi-energy demand in an integrated urban energy system was explored in [5], with specific consideration of using different energy supply and conversion devices to minimize the day-ahead operation cost. The scheduling and interaction between the electricity and heat demands in a smart building were outlined with incentive energy prices in [6]. Additional uncertainties and risks from the renewable generations and the electricity and thermal load were incorporated in the stochastic scheduling framework in [7]. The interactive strategy among a cluster of multi-energy customers was modeled as an ordinal potential game with a unique Nash equilibrium in [8].

On the other hand, the development of information and communication technology also laid the physical foundations to implement self-scheduling for multi-energy customers. In study [9], the residential multi-energy customers were incorporated into automatic decision-making technologies, where the household demand, i.e., water heater and stove, can be optimally controlled in the real-time frame. Similar research was also conducted for the industrial customers in Ontario Clean Water Agency water pumping facility [10]. Transactive energy modeling of a multi-energy demand response business case and its arbitrage opportunities in providing ancillary services were introduced in [11, 12]. Moreover, initiatives such as GridWise and IntelliGrid in the USA and SmartGrids in the EU, have demonstrated progress in providing customers with multiple energy choices to maximize operational efficiency [13]. It has been evidenced both theoretically and

practically that the self-scheduling of multi-energy customers' MEFSSs contributes to reducing the customers' operational costs, as well as maintaining the balance between the system energy supply and demand.

Undoubtedly, securing risk and minimizing service interruption are prerequisites for customers to self-schedule their MEFSSs appropriately. Hence, an effective tool is necessary for monitoring and enhancing the customer-side risk during the operational horizon. Extensive researches have addressed the risk of separated electricity [14], gas [15], and heat systems [16] in the past few decades, while recently, the risk modeling of the multi-energy system (MES) begin to draw great attention. Study [17] laid the foundation for modeling the risk of MES based on the concept of Energy Hub. Study [18] furtherly described the risk of components in MES using a generalized multi-performance weighted multi-state k-out-of-n system. On the other hand, some researches evaluated the risk of MES considering the energy management among the integrated energy distribution networks. A smart agent communication based method was proposed in [19] to improve risk evaluation efficiency. A hierarchical decoupling optimization framework and impact-increment based state enumeration method were put forward in [20] to tackle the non-converge and low-efficiency issues in MES optimal power flow and to enhance the risk efficiency, respectively. However, the behaviours in the customer-side are usually omitted in these researches.

There are a few studies partially addressing the risk issues on the customer side. The adequacy of multi-energy customers was evaluated in [21], and the dynamics of thermal loads were integrated into the operational risk evaluation of MES in [22] using Monte Carlo simulations. Despite that the self-scheduling of energy consumption behaviors and its influence on the risk of power systems have been well developed [23], there still lack studies on the risk of multi-energy customers considering self-scheduling strategies, especially in terms of energy substitution and its chronological characteristics during the operational horizon. It should be noted that the integration of different energy infrastructures will result in significant complexities in the risk evaluation of customers. Firstly, in the case of an energy interruption, customers can shift to another energy type to provide the same service. This indicates that a service interruption is not simply determined by a single energy supply, but associated with the redundancies of other alternative energy supplies. Moreover, possible random failures during service shifting and deployment, as well as the fluctuation in the energy supplies and demands, will have significant impacts on the operational risk of multi-energy customers [24]. Therefore, it is challenging to evaluate the operational risk while considering both the energy substitution and multiple uncertainties during the self-scheduling of MEFSSs. Meanwhile, the interruption of service will bring associated economic loss, which needs to be quantitatively evaluated in the risk analysis. Such economic loss is usually characterized based on customer damage function (CDF) [25]. However, the traditional CDF is formulated with electricity shortages and utilized in power systems. Therefore, it needs to be expanded for measuring the economic loss associated with the interruption of multi-energy services.

In order to address the aforementioned research gaps, this chapter aims to evaluate the operational risk of multi-energy customers, during which the flexibilities and uncertainties brought by self-scheduling with multiple energies are explored. The original contributions of this chapter are illustrated as follows:

(1) A service-based self-scheduling model for multi-energy customers is proposed.

Considering that the consumed energies eventually come down to the energy-related services, the self-scheduling of multi-energy customers in this chapter is implemented from a novel perspective of specific services rather than energy carriers. The chronological characteristics of service curtailment and shifting are also integrated into the self-scheduling model. The service-based point of view is novel and practical in managing the customers' energy consumption and calculating the interruption costs.

(2) Multiple uncertainties, particularly the inherent uncertainties during the service shifting are incorporated into the self-scheduling model.

Both the possible random failures during the service shifting and deployment, and fluctuations in the energy supply and demand are incorporated into the self-scheduling model. Particularly, this chapter is the first to consider the inherent uncertainties during the service shifting among alternative energies, where the possible failure is modeled as an imperfect switching process. The time-sequential Monte Carlo simulation (TSMCS) approach embedded with a scenario reduction technique is developed to cope with the uncertainties [26]. Taking full account of the possible scenarios, the quantitative risk indices of the multi-energy customers can be obtained.

(3) A generalized CDF model is developed for calculating the curtailment and shifting costs of multi-energy services.

In each scenario generated by TSMCS, the optimal self-scheduling of MEFSs is formulated with the objective of minimizing interruption costs during the operational horizon. Considering the electricity can cover most of the services, the CDF of the electricity sector is decoupled into each service, and then used to reconstruct the interruption costs for other energies, and service curtailment and shifting costs.

This chapter includes research related to the operational risk analysis of multi-energy customers by[27].

7.2 General description of multi-energy customers and energy-related services

7.2.1 Introduction to multi-energy customers and energy-related services

Fig. 7.1 depicts the structure of a multi-energy customer and its energy-related services. The general structure involves three sections, namely the multi-energy supply, appliances, and services required by the customer. The multi-energy supply generally includes multiple types of energy input portals, such as those electricity, natural gas, and heat. The services are categorized according to the re-

quirements of customers, including space heating, water heating, cooking, lighting, etc. The appliance section links the energy supplies and services, and each appliance consumes a certain type of energy to provide a specific service.

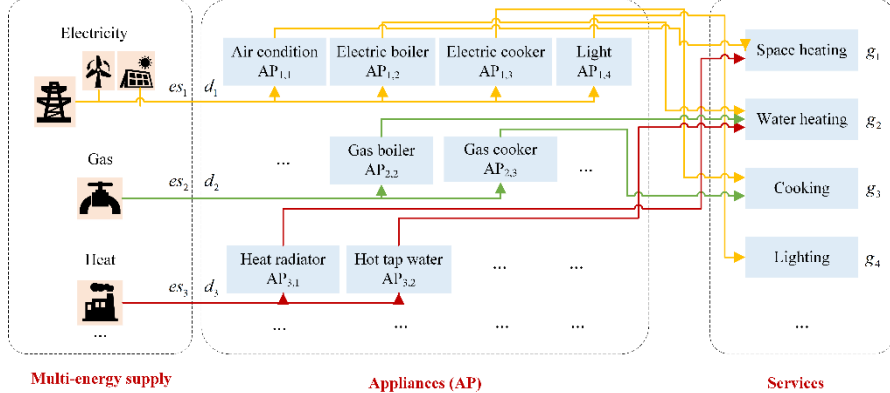


Fig. 7.1. Overview of multi-energy customers and energy-related services

Particularly in the service-based self-scheduling context, each service can be divided into three parts: curtailable service (CS), shiftable service (SS), and fixed service (FS). The CS is defined as the part of the service that is not crucial and can be curtailed by sacrificing the customer's comfort. For example, the temperature setpoint of an air conditioner in the summer can be turned up several degrees in exchange for an electricity demand reduction. The FS is defined as the vital part of a service that cannot be curtailed, or the part of a service that cannot be controlled automatically, such as traditional lights without remote switches. In this chapter, the SS is defined as the part of the service that can be shifted among both time periods and energies. For example, certain cooking services originally depending on natural gas can be rescheduled to another time and satisfied by electromagnetic ovens. Both the CS and SS are defined as MEFSSs. The mathematical description of multi-energy customers can be found in the Appendix.

7.2.2 Chronological multi-state model for multi-energy supply and demand

The service needs are difficult to predict precisely. Therefore, they are usually modeled as stochastic distributions [1]. From the perspective of time, the service needs appear to be sequentially connected in the historical load data [28]. In this chapter, the multi-state model is modified to represent both the uncertainties and chronological characteristics of service needs [28].

The need for service m is modeled as the sum of two parts, the basic service need $g_{0,m}$ and fluctuating part of service need dg_m . The basic service need is provided as a certain value at a time point. The fluctuating part of service need can be clustered into NH levels according to the historical data. The set of all levels

is denoted by $H = \{1, \dots, h, \dots, NH\}$, and the set of the fluctuating part of the need for service m at all levels is denoted by the vector $dG_m^H = \{dg_m^1, \dots, dg_m^h, \dots, dg_m^{NH}\}$. In each time period k , the fluctuating part of the need for service m denoted by $dg_m(k)$ will take a value from the set dG_m^H . In this chapter, the chronological transitions between different levels can be modeled as a Markov process, which has been widely adopted to predict uncertain future states in the operational phase [29]. The duration of each time period T_k is a random value associated with the transition rates among different levels. The probability of $T_k > t$ can be described by a cumulative distribution function $F_k(t)$ following an exponential distribution [29]:

$$F_k(t) = \Pr(T_k > t) = \exp \left\{ - \left(\sum_{p=1}^{NH, p \neq h} \lambda_{h,p} \right) t \right\} \quad (7.1)$$

where h denotes the level of the fluctuating part of the need for service m in time period k , and the transition rate from level h to level p is denoted by $\lambda_{h,p}$.

The modeling of multi-energy supply is identical to the multi-energy demand, which can be divided into the basic part and the fluctuated part. The basic part is determined to follow the multi-energy demand in the normal condition. The fluctuated part is regarded to originate from unpredictable distributed renewable energies, such as wind, and solar [24]. The fluctuation of the multi-energy supply can be predicted by the multi-energy customers in the day ahead based on the historical data [24]. On the other hand, the day ahead prediction of distributed renewable generations was regarded to be shared within the whole multi-energy communities in the previous studies, which means the availability of data is ensured for the multi-energy customers [30, 31].

7.3 Optimal self-scheduling of multi-energy flexible service

Considering the volatilities of the energy supplies and the chronological characteristics of multi-energy services as illustrated in Fig. 7.2, possible scenarios can be generated for the entire study period. In each scenario, the MEFSSs of multi-energy customers will be self-scheduled to minimise the total operational cost (TOC). The self-scheduling strategy involves service curtailment and service shifting. In order to explore the impacts of these self-scheduling behaviors on the multi-energy customers' risk, the chronological characteristics and uncertainties of the MEFSSs during self-scheduling are modeled. Moreover, the costs during self-scheduling of MEFSSs are reconstructed from electricity CDF, and the optimal self-scheduling of MEFSSs is formulated accordingly.

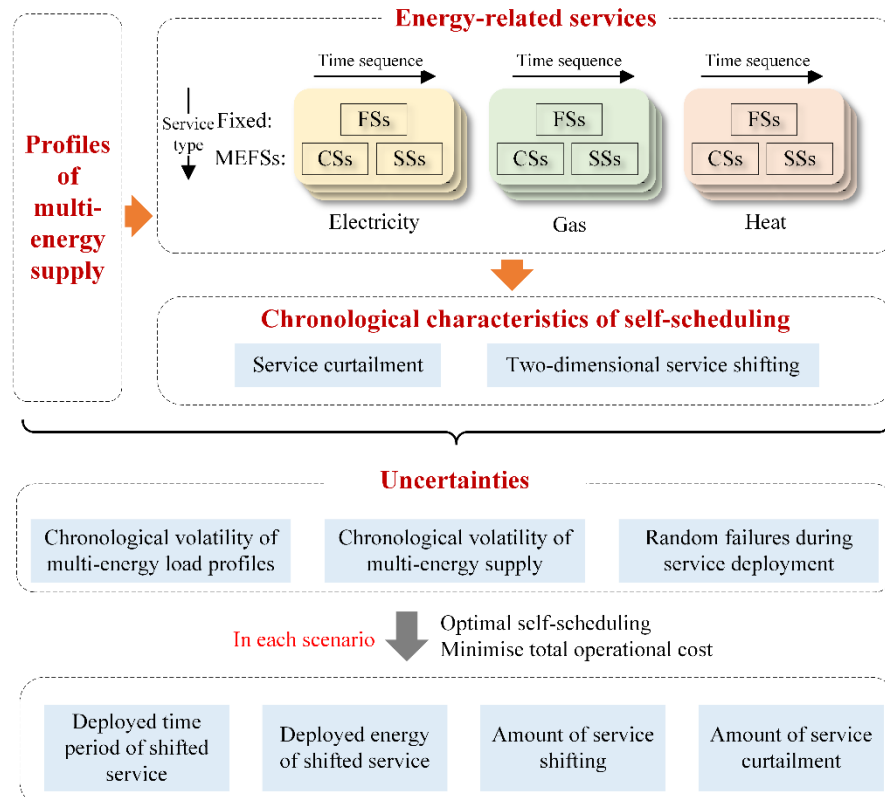


Fig. 7.2. Self-scheduling of MEFSs for multi-energy customers

7.3.1 Chronological characteristics of service curtailment and service shifting

The shifting path of MEFS can be divided into two dimensions, shifting among time periods and shifting among different energy types, as illustrated in Fig. 7.3. The service shifting among time periods is also referred to as energy substitution. In order to replace the same amount of shifted-out service m provided by the original appliance $AP_{l,m}$ for the time length T_k , the new appliance $AP_{l',m}$ should be in operation for time length $T_{k'}$ with a corresponding new efficiency. For example, the efficiency of electric boilers for providing hot water is assumed as 0.5. Electric boilers should be operated at a rated power of 2 MW for 2 h to provide a certain amount of water heating service. If the same service is shifted to use gas boilers with an efficiency of 0.8 and a rated power of 2.5 MW, the deployed time is 1 h. The service shifting process discussed above can be formulated as follows:

$$ss_{l \rightarrow l', k \rightarrow k'}^{out}(m, k) \eta_{l,m} T_k = ss_{l \rightarrow l', k \rightarrow k'}^{in}(m, k) \eta_{l',m} T_{k'}, \forall m, k \quad (7.2)$$

where $ss_{l \rightarrow l', k \rightarrow k'}^{out}(m, k)$ represents the shifted-out amount of the need for service m using energy l in time period k , which is intended to be shifted into time period k' using energy l' . It should be noted that the original energy consumed by service l is given, while the energy shifted into l' is selected by multi-energy customers. The amount of corresponding service deployment in time period k' of energy l' is denoted by $ss_{l \rightarrow l', k \rightarrow k'}^{in}(m, k)$.

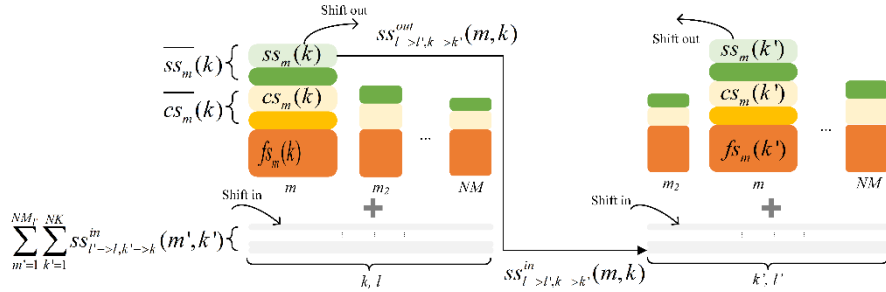


Fig. 7.3. Chronological service curtailment and service shifting

The capacities $\overline{cs}_m(k)$ and $\overline{ss}_m(k)$ set the upper boundaries of the implemented CS and SS of service m in time period k , namely $cs_m(k)$ and $ss_{l \rightarrow l', k \rightarrow k'}^{out}(m, k)$, as in (7.3) and (7.4).

$$0 \leq cs_m(k) \leq \overline{cs}_m(k) \quad (7.3)$$

$$0 \leq ss_{l \rightarrow l', k \rightarrow k'}^{out}(m, k) \leq \overline{ss}_m(k) \quad (7.4)$$

Following the self-scheduling process, the updated energy demand $d_l'(k)$ is:

$$d_l'(k) = d_l(k) - \sum_{m=1}^{NM_l} cs_m(k) - \sum_{m=1}^{NM_l} ss_{l \rightarrow l', k \rightarrow k'}^{out}(m, k) + \sum_{m'=1}^{NM_l} \sum_{k'=1}^{NK} ss_{l' \rightarrow l, k' \rightarrow k}^{in}(m', k') \quad (7.5)$$

where NM_l is the number of services consuming energy l and NK is the number of time periods.

7.3.2 Uncertainties of service deployment among alternative energies

In the service shifting context, a service may be maintained using alternative energies, by switching to another corresponding appliance. This process is defined as service deployment. However, the switching process from one energy type to another is not completely reliable, which may have further significant impacts on the operational risk of multi-energy customers [17, 32].

The imperfect switching model has been widely applied to the risk evaluation of engineering back-up systems [33]. As illustrated in Fig. 7.4, a single switching process can be represented by a three-state model, consisting of the standby state

(state 1), in-service state (state 2), and failure state (state 3). The stochastic transition among different states is modeled as a Markov process, and the necessary corresponding information is presented in the space diagram in Fig. 7.4 [29].

Once the simulation of the study period begins, the potential appliance is in initial state 1. In the following, it is assumed that the supply interruption of energy l occurs in time period k , and hence the appliance $AP_{l,m}$ is forced to be out of service. To satisfy the same service m , the amount of service $ss_{l \rightarrow l', k \rightarrow k'}^{out}(m, k)$ is covered using the remaining capacity of appliance $AP_{l',m}$, where energy l' is consumed to maintain service m . During the deployment of service m , $AP_{l',m}$ may be turned on successfully into state 2, or may fail to be deployed and transit into state 3, where the actual deployment of the shifted-out service $ss_{l \rightarrow l', k \rightarrow k'}^{in}(m, k) = 0$. When time period k is over, the substitutional appliance is assumed to be initialized rapidly and to recover to state 1.

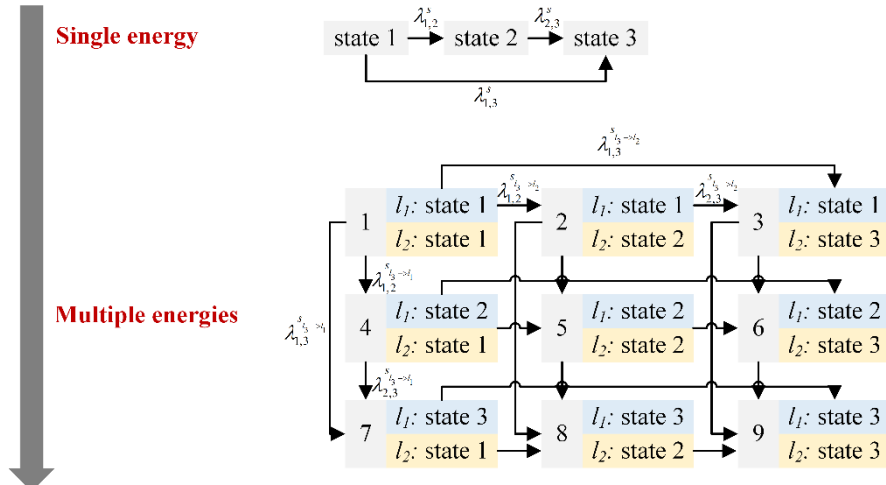


Fig. 7.4. State space diagram of service shifting from a single alternative energy to multiple alternative energies

The transition rates among states are calculated using (7.6) and (7.7), where p_s is the start-up failure probability, and T_s is the mean shut-down time.

$$\lambda_{1,2}^s = (1 - p_s) / T_s \quad (7.6)$$

$$\lambda_{1,3}^s = p_s / T_s \quad (7.7)$$

The risk representation for a single alternative energy has been given above. Under some circumstances, several alternative energies could be available to deploy service m , where the number of alternative energies is $NL_m - 1$. For example, two energies are available to be deployed supposing $NL_m = 3$. The state space

diagram presented in the right half of Fig. 7.4 considers a shift in the service from energy l_3 to l_1 or l_2 .

After integrating random failures of service deployment into self-scheduling, (7.5) should be updated as follows:

$$d_l'(k) = d_l(k) - \sum_{m=1}^{NM_l} cs_m(k) - \sum_{m=1}^{NM_l} ss_{l \rightarrow l', k \rightarrow k'}^{out}(m, k) + \sum_{l'=1}^{NL} \sum_{k'=1}^{NK} \sum_{m=1}^{NM_l} X_{l,m}(k) ss_{l' \rightarrow l, k' \rightarrow k}^{in}(m', k') \quad (7.8)$$

where $X_{l,m}(k)$ represents the state of alternative appliance $AP_{l,m}$:

$$X_{l,m}(k) = \begin{cases} 0, & \text{if } AP_{l,m} \text{ is at state 1 or 3} \\ 1, & \text{if } AP_{l,m} \text{ is at state 2} \end{cases} \quad (7.9)$$

7.3.3 Formulation of optimal self-scheduling of multi-energy flexible service

The optimization objective for the self-scheduling of multi-energy customers is to provide the required services with a minimal TOC, which is related to the unexpected interruption cost (UIC), service curtailment cost (SCC), and service shifting cost (SSC), as in (7.10). In the case when the multi-energy demand exceeds the supply, customers can shift or curtail a part of relatively unimportant services to minimize the unexpected interruption of the important services. It is reasonable since the costs related to the curtailment and shifting of the unimportant services are far below that due to the unexpected interruption of the important service. Besides the data on the supply side, the required data on the customer side, such as the information on the appliance and services, can be easily accessed or analyzed from historical data.

$$\begin{aligned} & \underset{cs_m(k), ss_{l \rightarrow l', k \rightarrow k'}^{out}, (l_m, k), l'(m, k), k'(m, k)}{\text{Minimise}} \quad TOC = UIC + SCC + SSC \\ & = \sum_{k=1}^{NK} \left(\sum_{l=1}^{NL} \left(CDF_l(T_k) \cdot (d_l'(k) - es_l'(k)) \cdot \text{sgn}(d_l'(k) - es_l'(k)) \right) \right. \\ & \quad \left. + CCF_m(T_k) \sum_{m=1}^{NM} cs_m(k) + SCF_m(t_{m,k} - t_{m,k}) \sum_{m=1}^{NM} ss_{l \rightarrow l', k \rightarrow k'}^{out}(m, k) \right) \end{aligned} \quad (7.10)$$

where $\text{sgn}(x) = \begin{cases} 1, & x > 0 \\ 0, & x \leq 0 \end{cases}$. $es_l'(k)$ is set according to

$$es_l'(k) = \begin{cases} es_l(k), & \text{for } \forall k, es_l(k) > 0 \\ \frac{1}{NK} \sum_{k=1}^{NK} es(k), & \text{for } \exists k, es_l(k) = 0 \end{cases} \quad \text{to avoid further demand spikes during}$$

the multi-energy supply interruption. The detailed explanations for other terms in (7.10) are as follows:

The customer damage function (CDF) of energy l (CDF_l) is used to quantify the UIC. When unexpected interruption of energy supplies occurs, the on-going services might be interrupted and consequently, the customers suffer economic losses. Therefore, it is essential to include this kind of loss in risk evaluation. The CDF for electricity in previous studies was associated with the type of the customers, duration of the interruption, and the quantity of the interrupted service. The customer types refer to the industry sector, commercial sector, residential sector, etc.[25]. However, there lacks CDF formulations for other energies, such as gas and heat. Moreover, with multiple energy supplies, the insufficiency of a single energy does not necessarily result in the interruption of services. Considering electricity generally covers all services, therefore it sets the baseline to decouple CDF into each type of service and reconstruct the CDF in terms of other energies.

According to a survey conducted by the Institute for Research in Economics and Business Administration (SNF) and SINTEF Energy Research, the proportions of consumption $X = \{\chi_1, \dots, \chi_{NM}\}$ and interruption costs $\Phi = \{\varphi_1, \dots, \varphi_{NM}\}$ of different end-use categories are presented in [34]. Supposing that l_1 represents electricity, the CDFs for services can be reconstructed from:

$$CDF_m(t) = CDF_{l_1}(t)\varphi_m / \chi_m \quad (7.11)$$

where χ_m and φ_m should satisfy $\sum_{m=1}^{NM} \chi_m = \sum_{m=1}^{NM} \varphi_m = 1$.

The CDFs for other energy $l(l \neq l_1)$ are constructed as a weighted sum of CDFs for services that consume energy l :

$$CDF_l(t) = \sum_{m=1}^{NM} CDF_m(t)c_{l,m}\eta_{l,m} \quad (7.12)$$

Under the framework of self-scheduling in multi-energy customers, service curtailment and service shifting requests should be notified to customers in advance. The curtailment cost function CCF_m is modeled as $CCF_m = \omega_m CDF_m$ where ω_m reflects the lower cost of the initiative service interruption. The shifting cost function SCF_m is calculated as:

$$SCF_m(t) = \Delta t_{m,k} CCF_m(t) / 24 \quad (7.13)$$

where $\Delta t_{m,k}$ is the interval between the shifted-out time $t_{m,k}$ and deployed time $t_{m,k'}$ of the service, $\Delta t_{m,k} = t_{m,k'} - t_{m,k}$. Normally, we assumed that the interval of service shifting is less than 24 h, namely $0 \leq \Delta t_m < 24$.

The control variables of optimal self-scheduling of multi-energy customers include: 1) the amount of curtailment for service m in time period k , $cs_m(k)$; 2) the amount of service shifted out from service m in time period k using energy

l , to energy l' and time period k' , $ss_{l \rightarrow l'; k \rightarrow k'}^{out}(m, k)$; 3) the time period of service deployment, correlating to the original service m and time period k , $k'(m, k)$; 4) the deployed energy for each shifted-out service, correlating to the original service m and period k , $l'(m, k)$. Apart from the limitations for the amount of implemented CSs and SSs as in (7.3) and (7.4), the deployed time periods and energies of service m are limited by the number of time periods NK and set of available energies for service m , L_m , as indicated in (7.14) and (7.15).

$$l'(m, k) \in L_m \quad (7.14)$$

$$0 < k'(m, k) \leq NK, k'(m, k) \in Z \quad (7.15)$$

In summary, the formulation of optimal self-scheduling for multi-energy customers is a mixed-integer non-linear programming (MINLP) problem. The challenges of solving this problem mainly lie in two aspects: 1) it contains both integer variables and nonlinear constraints. 2) there are enormous scenarios simulated by time-sequential Monte Carlo simulation (TSMCS), and each scenario involves an independent MINLP model. Therefore, an effective algorithm is urgently required to apply to the large-scale optimization problem.

Genetic algorithm (GA) has proved its efficiency in extensive previous studies regarding the scheduling of the energy consumption of customers [23, 35]. It has a simple and understandable procedure, including 1) generating an initial population; 2) evaluating the fitness function of each individual, namely, the scores; 3) selecting parents based on the scores and producing children by mutation and crossover. Pass down a certain proportion of elite individuals with high fitness values directly to the next generation; 4) replace the current population with children; 5) continue from step 2) until the stopping criteria are met. Compared with analytical approaches such as branch and bound (BNB), GA is robust to the nonlinearities and non-convexities, and it can balance well between the computation time and the accuracy, which is suitable for simulating the self-scheduling of multi-energy customers practically [23]. Moreover, it can be easily accelerated using parallel computing techniques. Therefore, GA is adopted to solve the self-scheduling problem proposed in this chapter.

7.4 Operational risk evaluation procedures using time-sequential Monte Carlo simulation

For evaluating the operational risk of the self-scheduling of multi-energy customers, the TSMCS approach is used to sample the chronological levels of service needs, fluctuation in the multi-energy supply, and imperfect switching during service deployment. Moreover, the loss of load probability (LOLP) and expected energy not supplied (EENS) used in the power system risk evaluation are expanded to apply to multiple energies [19, 26]. In this manner, we obtain $LOLP(T) = \{LOLP_1(T), \dots, LOLP_{NL}(T)\}$ and

$EENS(T) = \{EENS_1(T), \dots, EENS_{NL}(T)\}$ for evaluating the time-varying reliabil-

ties of all the energies. The l elements of the vectors $LOLP(T)$ and $EENS(T)$ are calculated as follows:

$$LOLP_l(T) = \sum_{k=1}^{\max k(T)} \left(\sum_{is=1}^{NS} T_k \operatorname{sgn}(d_l'(k) - es'_l(k)) \right) / NS \quad (7.16)$$

$$EENS_l(T) = \sum_{k=1}^{\max k(T)} \left(\sum_{is=1}^{NS} T_k (d_l'(k) - es'_l(k)) \left(\operatorname{sgn}(d_l'(k) - es'_l(k)) \right) \right) / NS \quad (7.17)$$

where $\max k(T)$ is the maximal value of k that satisfies $t_{k+1} < T$, and NS represents the simulation times. It should be noted that the TSMCS could be a time-consuming process, as the possible scenarios will grow exponentially with a linear increase in the components. Therefore, a scenario reduction technique is embedded in the TSMCS procedures to reduce the number of scenarios and improve computational efficiency. The steps presented below are the TSMCS procedures for evaluating the operational risk of multi-energy customers considering the self-scheduling of MEFS, and the corresponding flowchart is displayed in Fig. 7.5.

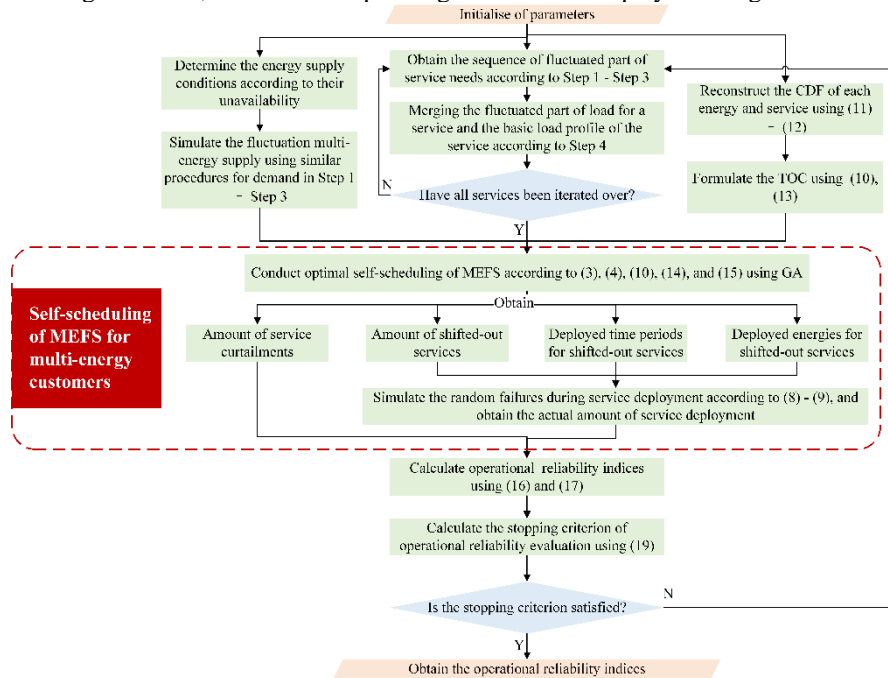


Fig. 7.5. Operational risk evaluation procedure for multi-energy customers

Step1: Calculate the steady probability of the fluctuating part of service need at level h , Pr_h for each service m [36]. Determine the initial level for each service m using the TSMCS sampling technique [37].

Step 2: Determine the duration of the current level and level in the next state for each fluctuating part of need for service m . The duration of the current level h is calculated based on the PDF described in (7.1). The duration is specified as

$$T_k = \ln U / \sum_{p=1}^{NH, p \neq h} \lambda_{h,p}, \text{ where } U \text{ is a uniformly distributed random value over the}$$

interval (0,1) [37]. The probability of state h entering another state h' is

$$\Pr_{h'} = \lambda_{h,h'} / \sum_{h=1}^{NH, h \neq h'} \lambda_{h,h'} . \text{ If } \sum_{h=1}^{h'} \Pr_{h'} < U \leq \sum_{h=1}^{h'+1} \Pr_{h'}, \text{ the level will be } h' \text{ in the next}$$

time period k' .

Step 3: Repeat step 2 until $\sum_{k=1}^{NK} T_k \geq ST$, where ST is the entire study period.

Step 4: Merge the sequence of the fluctuating part of the need for service m , $dg_m(k)$ and basic need for service m , $g_{0,m}(k)$ into a new sequence $g_m(k)$, and reduce the number of scenarios as follows. Suppose that the current time period for the basic need of service $g_{0,m}$ is k . Determine the scenario indices of the fluctuating part of the need for service m , k_s and k_s' satisfying $t_{k_s} \leq t_k < t_{k_s+1}$ and $t_{k_s'} \leq t_{k+1} < t_{k_s'+1}$, respectively, where t_k denotes the beginning time point of period k . Compare k_s and k_s' . Note that $k_s' \geq k_s$. If $k_s' = k_s$, the total need for service m can be calculated as $g_m(k) = g_{0,m}(k) + T_{m,k} dg_m(k)$. Otherwise, calculate the value as follows:

$$g_m(k) = (t_{k_s+1} - t_k) dg_m(k_s) + (t_{k+1} - t_{k_s}) dg_m(k_s') + \sum_{ik=k_s}^k dg_m(ik)(t_{ik+1} - t_{ik}) \quad (7.18)$$

Step 5: Determine the condition of the multi-energy supply based on the unavailability, similar to the process in step 1. In each scenario simulated by TSMCS, GA is applied to solve the optimal self-scheduling of MEFS formed by (7.3), (7.4), (7.10), (7.14), and (7.15) as follows. First, set the boundaries for control variables according to (7.3), (7.4), (7.14), and (7.15); second, calculate the CDF for each energy and service to form the objective function in (7.10). Third, solve the optimal self-scheduling problem using GA [38]. Fourth, simulate the random failures during the service deployment according to (7.8).

Step 6: Calculate the risk indices according to (7.16) and (7.17) based on the actual services that have been deployed. Return to Step 1 until the confidence in-

tervals are satisfied. The stopping criterion provided for the TSMCS is the EENS coefficient of variance ξ_{EENS} , which can be calculated as follows:

$$\zeta_{EENS} = \max(\sqrt{V(EENS_l(T))} / EENS_l(T)) \quad (7.19)$$

where $V(EENS_l(T))$ is the variance of $EENS_l(T)$.

7.5 Case studies and discussions

Case studies are conducted to demonstrate the proposed operational risk evaluation technique. Two cases are presented in this section. Case 1 is organized to validate the effectiveness of the proposed service-based self-scheduling model. It compares the operational reliabilities and costs with those in the scenario without self-scheduling. It should be noted that the uncertainties are not included in Case 1. Case 2 aims to quantitatively analyze the impacts of uncertainties on the operational risk of consumers, and the typical service losses due to random failures during service deployments are considered.

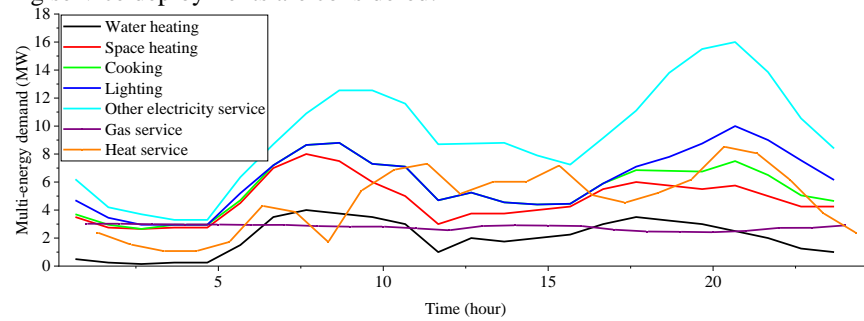


Fig. 7.6. Daily load profile of multi-energy services

Table 7.1. Efficiencies of energies to provide services

	Water heating	Space heating	Cooking	Lighting	Other electricity service	Gas service	Heat service
Electricity	0.5	0.1	0.2	1	1	0.5	0.5
Gas	0.5	0.4	0.8	0	0	1	0.5
Heat	0.5	0.5	0	0	0	0.5	1

In this chapter, the energy supplies provided to multi-energy customers include electricity, gas, and heat, hence there is $NL = 3$. The basic needs for services are illustrated in Fig. 7.6 [21]. The entire study period is set to one day, with each interval for the basic need of services equal to 1 h, hence $NK = 24$. Prior to self-scheduling, the electricity demand is split into five services, and the efficiencies of the energies used to provide the services are listed in Table 7.1 [21]. An efficiency of zero means that the service cannot be provided with this type of energy. The

original gas and heat demand for customers is not split into detailed services. Thus, the number of services adds up to $NM = 7$. The proportions of CS and SS are set as 0.1 and 0.25, respectively. The levels of the fluctuating part of services and their transition rates are derived from a historical load profile during a summer week [39]. The start-up failure probability p_s and the mean shut-down time T_s are set according to [26]. The electricity CDF used in this chapter is presented in Table 7.2 [40]. The unavailability of each energy supply infrastructure is 0.02 [32]. The convergence criterion ξ_{set} is set to 0.05. The numerical simulations are performed on a Lenovo laptop with an Intel® Core™ i5-6200U 2.3 GHz and 8GB of memory.

Table 7.2. Estimated average electric customer interruption costs with different durations

Interruption cost	Interruption duration				
	Momentary	30 minutes	1 hour	4 hours	8 hours
Cost per unserved kWh (\$)	96.5	22.6	15.3	13.0	10.6

7.5.1 Case 1: Chronological characteristics of multi-energy flexible services and the operational risk of multi-energy customers considering self-scheduling

In this case, in order to demonstrate the chronological characteristics during self-scheduling, and compare the operational reliabilities and costs after self-scheduling with their original values without self-scheduling, the failure rate during service deployment is set to zero to exclude uncertainties. That is, the self-scheduling of the MEFSSs could be completed perfectly without unexpected failures. The scale of the optimization problem and the performance of GA is presented in Table 7.3. It can be seen that the average computation time for one optimization and the relative standard deviation of the objective function value are acceptable for the risk evaluation of multi-energy customers.

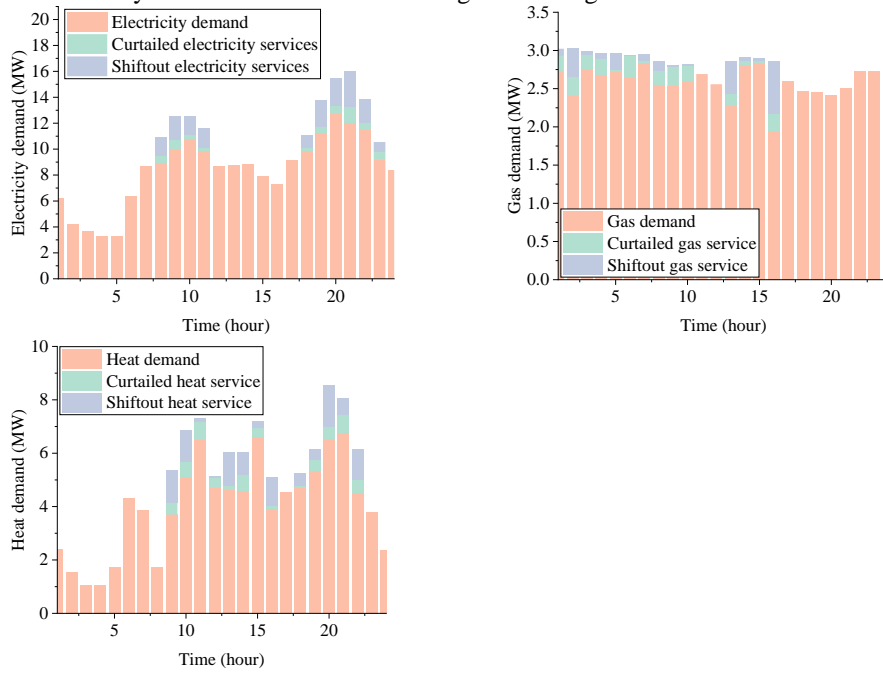
Table 7.3. Scale of the optimization problem and the performance of GA

Problem scale	Number of time period NK	24
	Number of service NM	7
	Number of energy NL	3
	Number of continuous variables	336
Performance	Number of integer variables	336
	Number of constraints	1344
Performance	Average computation time (s)	7.94
	Relative standard deviation of the objective function value	3.69%

For the sake of clarity, the self-scheduling is divided and presented into two stages. The first stage includes service curtailment and service shifting out, as indicated in Fig. 7.7. It can be observed that the self-scheduling of MEFSSs reduces

the peak demands for electricity and heat effectively by 17.96% and 16.18%, respectively. The services shifting out account for the 68.48% of decreasing in energy demand because of relatively lower costs. The service shifting and curtailment are usually implemented during the demand peaks, e.g., 7:00 – 12:00 and 17:00 – 24:00 for the electricity demand. It should be noted that the gas demand continuously maintains a high level from 0:00 to 12:00, and the proportion of the shifted-out gas service is relatively small during that period.

In order to clarify the behavior of specific services during the self-scheduling, Fig. 7.9 and Fig. 7.10 further split the curtailed and shifted-out energy demands into different services. Indicated jointly by the histogram in Fig. 7.9(a) and Fig. 7.10(a) and Fig. 7.10(b) in the time domain, the space heating and water heating are most likely to be curtailed or shifted out, they take 28.42% and 40.05% of the total curtailed services, and 22.33% and 37.94% of the total shifted out services, respectively. Conclusions can be drawn from the first stage that the heating related services are most likely to be curtailed, shifted into another period, or substituted by another type of energy, not only owing to its relatively lower SCC and SSC, but also easy and efficient realization using other energies.



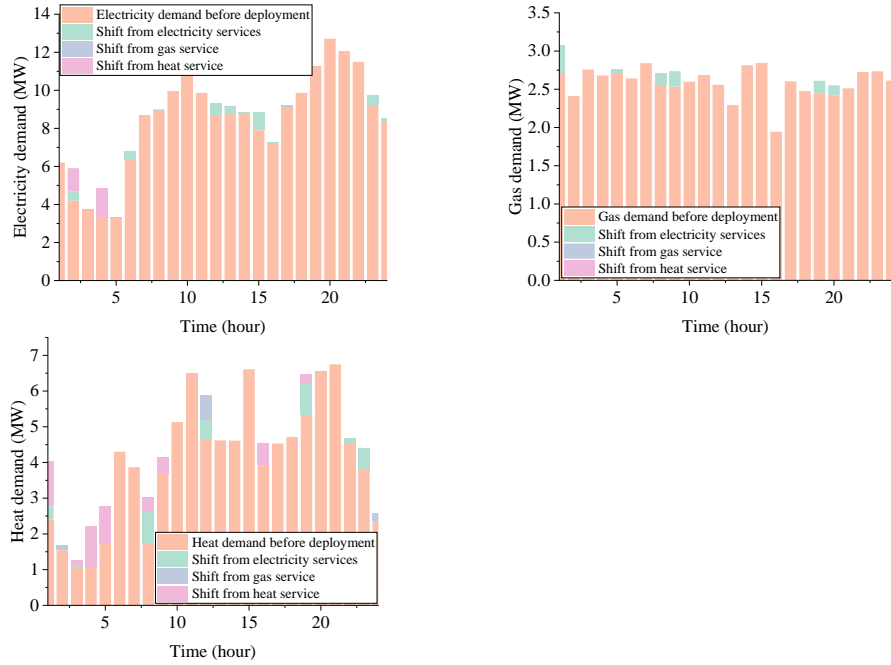


Fig. 7.8. Service deployment from each energy during self-scheduling

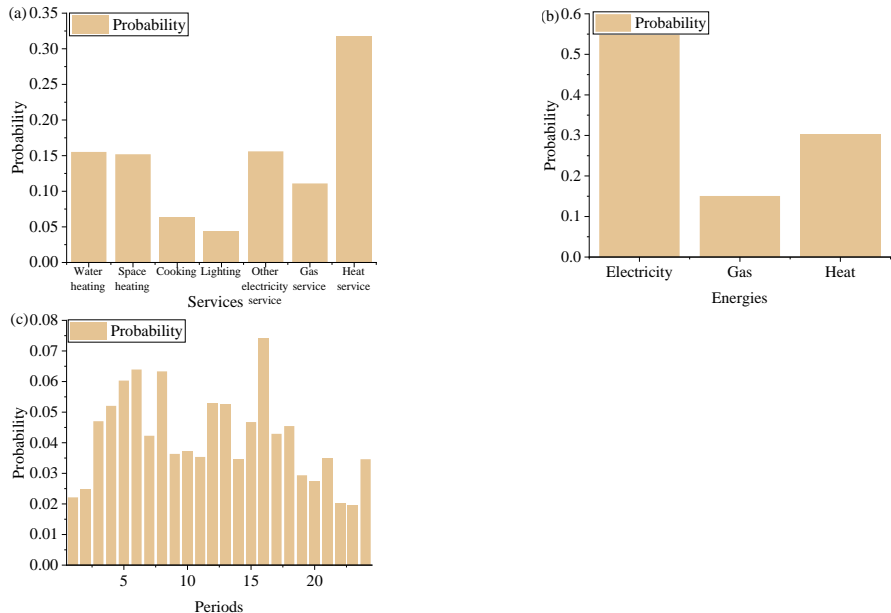


Fig. 7.9. (a) Histogram of services to be curtailed or shifted out; (b) histogram of energies to be deployed; (c) histogram of periods for deployment

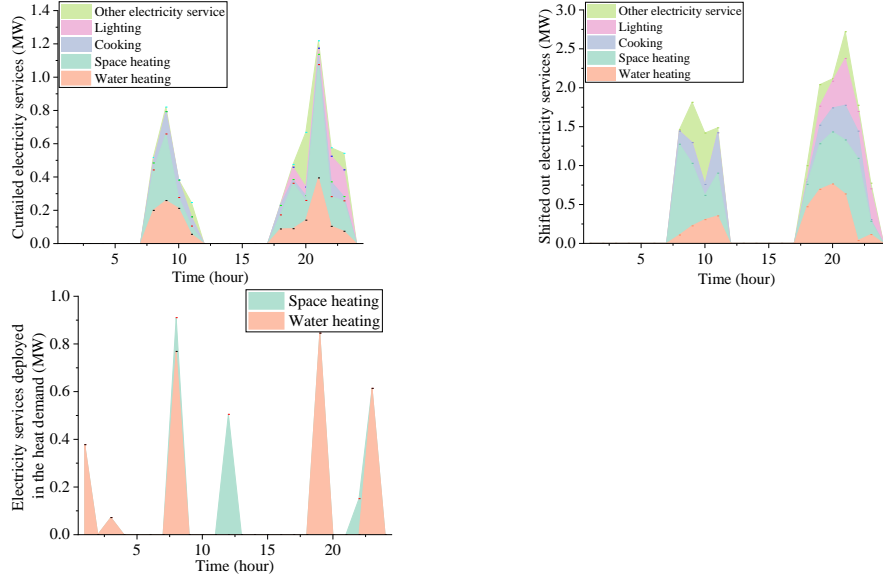


Fig. 7.10. (a) Electricity service curtailment during self-scheduling; (b) Electricity services shifted out during the self-scheduling; (c) Electricity services deployment during self-scheduling

The deployment of shifted-out services for each energy at the second stage is illustrated in Fig. 7.8. The electricity demand is in part substituted with the gas and heat demand, due to its wide utilization in providing services. The shifted-out services are more likely to be deployed to the valley periods of electricity and heat rather than gas. This characteristic is also verified in the histogram in Fig. 7.9(b) and Fig. 7.9(c). Another worth noting point is, from the perspective of all energies, the total amount of service shifting in is less than that of service shifting out. For example, the amount of electricity service shifting out is 16.60 MW over the whole study period, while the amount of electricity demand, gas demand, and heat demand shifted from the electricity services are 3.58, 1.07, and 3.47 MW. This validates that the substitution among energies during self-scheduling can promote the overall efficiency of energy consumption.

Similarly, the deployment of energy demands is further split into detailed services in Fig. 7.10(c). Considering that the deployed electricity demand from heating service and the deployed heat demand from gas service cannot be furtherly split, and the deployed gas demand from electricity service is all cooking service, the deployment process of electricity and gas demand are not furtherly illustrated based on the specific service. However, the deployed heat demand from electricity service can be further split into the water heating and space heating, as presented in Fig. 7.10(c). Observed from Fig. 7.10(b) and Fig. 7.10(c), it is also validated that although the water heating and space heating shifted out are roughly the same,

the proportions of those deployed in the heat demand differ remarkably, owing to their different efficiencies provided by electricity.

We can further compare the operational costs and reliabilities in Fig. 7.11 and Fig. 7.12 to analyze the benefits from self-scheduling. The self-scheduling of MEFS reduces the operational cost by 14.05%, as well as reduces the EENS of multi-energy customers significantly by 56.32%. In Fig. 7.11, the times of the three operational cost peaks are approximately 10:00, 15:00, and 20:00, which are consistent with the times for the electricity and heat demand peaks. During the first peak time at approximately 10:00, the operational cost is mainly composed of the SCC and SSC, because there is enough redundancy in the other energies or time periods for services to be deployed, and therefore unexpected service interruptions can be minimized. During the third peak at approximately 20:00, the UIC becomes enormous because the implemented CSs and SSs are limited by their maximum capacities. The operational risk indices following self-scheduling in Fig. 7.12 appear to exhibit a peak and valley pattern similar to that of the operational cost in Fig. 7.11. It can be concluded that the self-scheduling of MEFSSs is effective in improving the operational risk of multi-energy customers, particularly during peak hours.

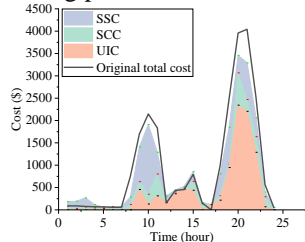


Fig. 7.11. Economic benefits from self-scheduling.

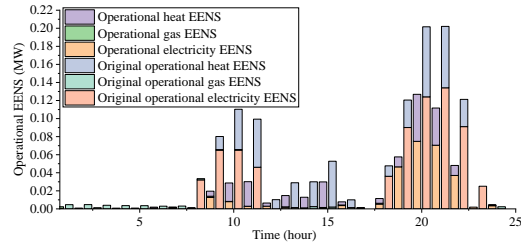


Fig. 7.12. Risk benefits from self-scheduling.

Table 7.4. Reliabilities of the multi-energy customer with different CS and SS proportions

Scenario	Proportion of CS	Proportion of SS	Electricity EENS (MW)	Gas EENS (MW)	Heat EENS (MW)
A	0	0	0.0295	0.0016	0.0189
B	0.1	0.25	0.0127	0.0006	0.0121
C	0.1	0.50	0.0065	0.0015	0.0124
D	0.3	0.50	0.0058	0.0007	0.0070
Scenario	Electricity LOLP (/hour)	Gas LOLP (/hour)	Heat LOLP (/hour)	EENS for multi-energy customers (MW)	LOLP for multi-energy customers (/hour)
A	0.0083	0.0125	0.0110	0.0500	0.0125
B	0.0089	0.0044	0.0107	0.0254	0.0107

C	0.0078	0.0054	0.0109	0.0204	0.0105
D	0.0071	0.0049	0.0093	0.0136	0.0093

In order to quantify the influence of the MEFSS, four scenarios with different CS and SS proportions are studied, and the results are listed in Table 7.4. It can be observed that the EENSs and LOLPs for all energies without MEFSSs in scenario A are larger than those in the other scenarios, where the self-scheduling of MEFSS is taken into account. Moreover, by comparing the last three scenarios, we can conclude that with a greater proportion of MEFSSs, although the EENSs and LOLPs are not monotonic for some energies, generally the EENS and LOLP for multi-energy customers will decrease.

7.5.2 Case 2: Impacts of multiple uncertainties on the operational risk of multi-energy customers

In this case, the uncertainties from random failures during service deployment are studied. The failure rate for service deployment is initialized to $\lambda_{1,3}^s = 0.1$. Fig. 7.13 and Fig. 7.14 demonstrate the impacts of the random failures on the operational risk of multi-energy customers. Fig. 7.13 presents a typical example of service losses due to random failures during service deployments. The orange and purple areas indicate the differences between the scheduled demand and actual demand. It tends to occur at the times of the demand valleys, when service deployments are most likely to take place. It can be observed from Fig. 7.14 that, when random failures during service deployment are considered, the operational risk of multi-energy customers will be slightly inferior. The EENSs for electricity, gas, and heat increase by 4.04%, 7.84%, and 2.16%, respectively.

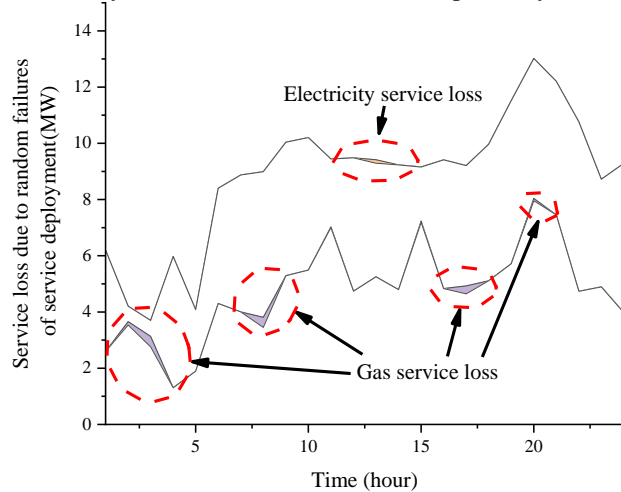
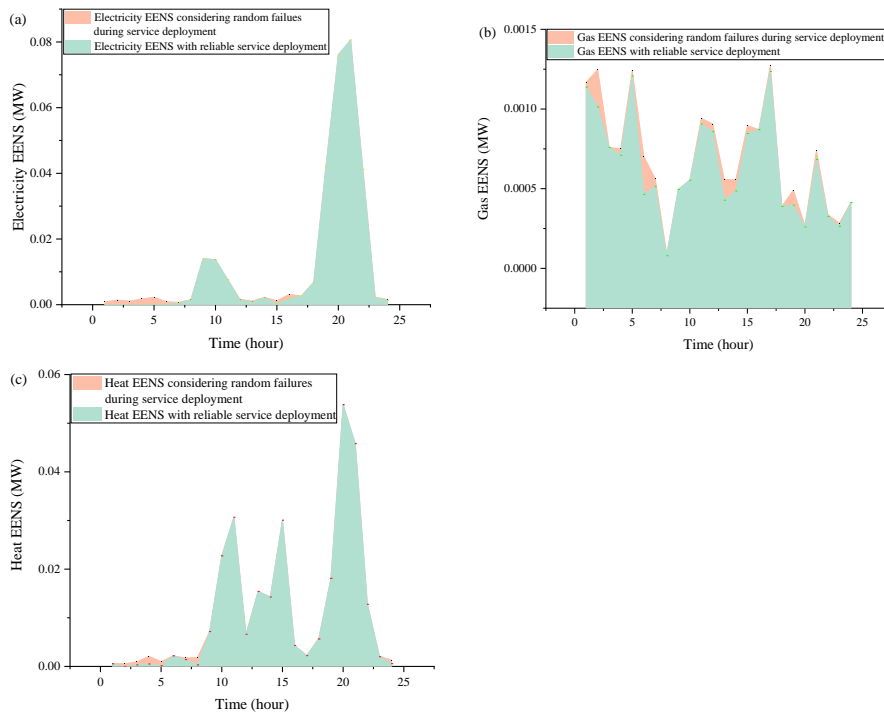


Fig. 7.13. Representative service losses due to random failures during service deployments.

Table 7.5. Risk of multi-energy customers considering different failure rates

Scenario	Failure rate $\lambda_{1,3}^s$ (/hour)	Electricity EENS (MW)	Gas EENS (MW)	Heat EENS (MW)	Electricity (/hour)	LOLP
A	0	0.0121	0.0006	0.0112	0.0083	
B	0.1	0.0128	0.0008	0.0119	0.0089	
C	0.3	0.0139	0.0007	0.0113	0.0083	
D	0.5	0.0154	0.0003	0.0117	0.0117	
Scenario	Failure rate $\lambda_{1,3}^s$ (/hour)	Gas LOLP (/hour)	LOLP	Heat LOLP (/hour)	EENS for multi-energy customers (MW)	LOLP for multi-energy customers (/hour)
A	0	0.0043		0.0107	0.0239	0.0107
B	0.1	0.0054		0.0110	0.0255	0.0110
C	0.3	0.0056		0.0116	0.0259	0.0116
D	0.5	0.0056		0.0136	0.0274	0.0136

**Fig. 7.14.** Impacts of random failures on the operational risk of multi-energy customers.

Furthermore, in order to quantify the impacts of random failures during service deployments, four scenarios with different failure rates are considered. The risk indices are listed in Table 7.5. It can be observed that the failure rate of service deployment will significantly influence the risk of multi-energy customers. The operational risk to customers will be inferior when the failure rate increases. Summarised throughout the two case studies, we can find that even taking the negative impacts from random failures during the service deployment, the operational risk of multi-energy customers can still be improved by implementing self-scheduling.

7.5.3 Case 3: Validation of the proposed technique using a practical case

In order to demonstrate and validate the proposed self-scheduling strategy and corresponding operational risk evaluation technique practically, a new urban district in East China is utilized in this case. This district is involved in a demonstration project on the transformation towards a multi-energy smart district, and therefore its energy demand is metered and kept in the record in high resolution.

Here we take a group of high-rise apartments located in the west of this district as a typical example of a residential multi-energy customer. It occupies a 1.70×10^5 m² land area and owns a 2.54×10^5 m² construction area. The experiment is conducted on a representative winter day, where the peak demands for electricity and heat are 4.74 and 1.89 MW. The massive electricity demand data are available on Electric Energy Data Acquire System of the State grid corporation of China, while the heat demand is derived from the metered mass flow rate and the temperature differential of the supply and return water in the pipelines [41]. The quantity of heating-related services, including water heating and space heating, in electricity demand, is derived by comparing the typical summer electricity demand and the non-seasonable electricity demand in spring or autumn.

Its daily load profile is presented in Fig. 7.15. Only electricity and heat demands are involved in this case, . Corresponding to that, compared with Case 1, the cooking and gas services are no longer available in the self-scheduling context, . Other parameters are set the same as in Case 1.

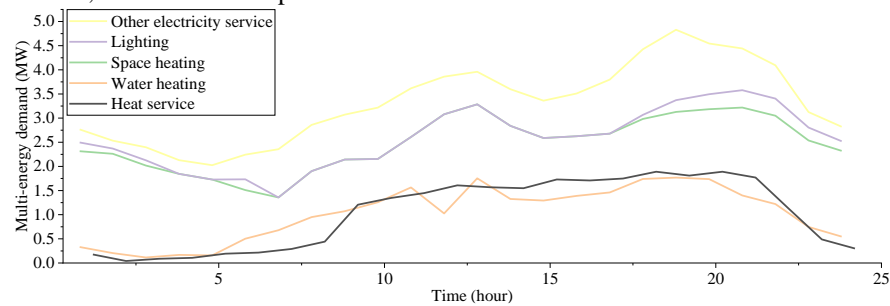


Fig. 7.15. Daily load profile of multi-energy services in a practical case

The two-stage self-scheduling of the multi-energy customer is illustrated in Fig. 7.16–18. It can be observed in Fig. 7.16 that by implementing self-scheduling, the multi-energy customer has reduced its electricity and heat peak demands by 24.35% and 4.27%, respectively. The shifted out services account for 71.79% of the decrease in energy demands. Seen from the perspective of services in Fig. 7.17, heating-related services, including water heating and space heating, are still the major MEFSS for self-scheduling, which takes 45.80% and 41.83% of the total curtailed services, and 42.32% and 54.23% of the shifted out services. It confirms the conclusion in Case 1 that the large proportion of heat-related services will be a prerequisite to promoting the effectiveness of self-scheduling.

As demonstrated in Fig. 7.18, previously shifted out services tend to be deployed at 23:00 – 8:00. From the perspective of all services, the total quantity of deployed services is 3.86 MW, presenting a remarkable reduction of 55.71% compared with 9.13 MW shifted out services. This indicates that the self-scheduling is not only efficient in reallocating the services temporally to improve the operational risk and operational cost, but also in promoting the overall efficiency of energy consumption.

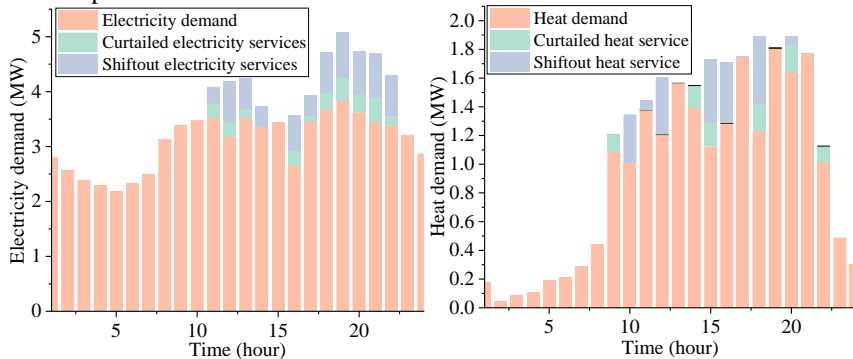


Fig. 7.16. Service curtailment and service shifted out during self-scheduling in the practical case.

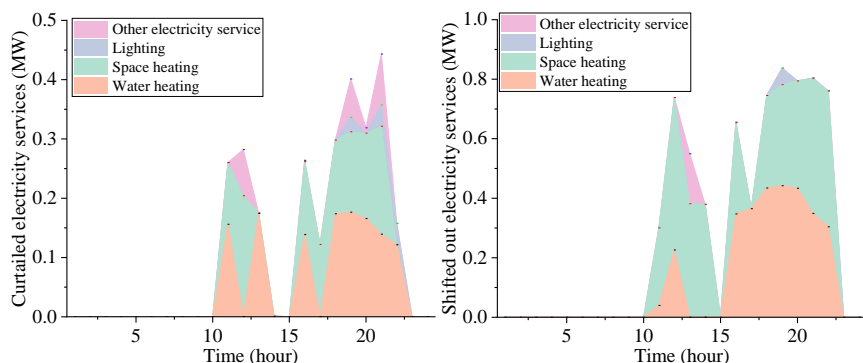


Fig. 7.17. Electricity service curtailment and shifted out during the self-scheduling in the practical case.

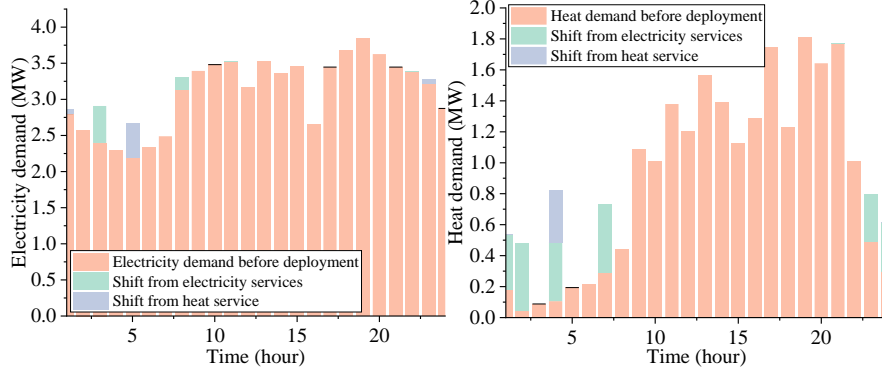


Fig. 7.18. Service deployment from each energy during self-scheduling in the practical case.

Table 7.6. Impacts of self-scheduling and uncertainties on the risk of the multi-energy customer in the practical case

	Scenario A	Scenario B	Scenario C
Electricity LOLP (/hour)	0.0092	0.0059	0.0073
Heat LOLP (/hour)	0.0127	0.0111	0.0120
LOLP for the multi-energy customer (/hour)	0.0136	0.0118	0.0130
Electricity EENS (MW)	0.0074	0.0010	0.0014
Heat EENS (MW)	0.0066	0.0038	0.0042
EENS for the multi-energy customer (MW)	0.0140	0.0049	0.0056

In order to validate the effectiveness of self-scheduling in the practical case, the risk indices of the multi-energy customer are obtained and compared in three scenarios, as presented in Table 7.6. The risk indices in Scenario A are calculated without implementing self-scheduling, and the risk indices in Scenario B are calculated after self-scheduling, but the uncertainties are excluded. In Scenario C, the risk indices are calculated taking full consideration of uncertainties, and the failure rate for service deployment is set to . It can be observed that the reliabilities in terms of all the energies benefit from self-scheduling. The LOLP and EENS of the multi-energy customer reduce by 13.24% and 65.00%, respectively. Moreover, it confirms that even considering the uncertainties such as a relatively high failure rate for service deployment, the risk can still be improved. In this case, the LOLP and EENS of the multi-energy customer are still reduced by 5.83% and 60.00%, respectively.

7.6 Conclusions

This chapter proposes a service-based self-scheduling model for multi-energy customers, and evaluates the operational risk considering the multiple uncertain-

ties. Case studies demonstrate that the expected energy not supplied to the multi-energy customer drops significantly by 56.32% with the self-scheduling strategy. Among various services, the heating related services are most likely to be curtailed or shifted. The operational cost can also be reduced. By increasing the proportion of multi-energy flexible services, the overall operational risk of multi-energy customers can be furtherly improved. On the other hand, the self-scheduling of multi-energy customers is associated with uncertainties. Random failures during the service deployment will have negative impacts on the operational reliabilities. However, even considering this point, the operational risk of multi-energy customers can still be improved by implementing self-scheduling.

With the recent intensified interaction of multi-energy infrastructures, customers become possible and motivated to self-schedule their energy consumption behaviors to maintain more reliable services with lower costs. Therefore, the quantitative operational risk evaluation technique and corresponding conclusions presented in this chapter could provide considerable practical information in the decision-making for customers' energy management.

Appendix: Mathematical descriptions of multi-energy customers

The following definitions are provided for mathematically describing the relationships among the three sections.

1) The multi-energy supply is represented by the vector $ES = \{es_1, \dots, es_l, \dots, es_{NL}\}$, where es_l denotes the amount of energy delivered to the customer, and es_l represents the number of energy types.

2) The energy demands of a multi-energy customer are represented by the vector $D = \{d_1, \dots, d_l, \dots, d_{NL}\}$, where d_l denotes the amount of energy l required by the customer.

3) The service needs are represented by the vector $G = \{g_1, \dots, g_m, \dots, g_{NM}\}$, where g_m denotes the need for service m , and NM denotes the number of services.

The imported energy l can be distributed into different appliances, through which the various services can be provided using different energies:

$$\begin{bmatrix} c_{1,1}\eta_{1,1} & \dots & c_{1,m}\eta_{1,m} & \dots & c_{1,NM}\eta_{1,NM} \\ \dots & \dots & \dots & \dots & \dots \\ c_{l,1}\eta_{l,1} & \dots & c_{l,m}\eta_{l,m} & \dots & c_{l,NM}\eta_{l,NM} \\ \dots & \dots & \dots & \dots & \dots \\ c_{NL,1}\eta_{NL,1} & \dots & c_{NL,m}\eta_{NL,m} & \dots & c_{NL,NM}\eta_{NL,NM} \end{bmatrix}^T \begin{bmatrix} d_1 \\ \dots \\ d_l \\ \dots \\ d_{NL} \end{bmatrix} = \begin{bmatrix} g_1 \\ \dots \\ g_m \\ \dots \\ g_{NM} \end{bmatrix} \quad (7.20)$$

where $c_{l,m}$ is a distribution factor describing the proportion of energy l consumed by appliance $AP_{l,m}$ to provide service m . Obviously, there exists $\sum_{m=1}^{NM} c_{l,m} = 1$. $\eta_{l,m}$ is the efficiency of appliance $AP_{l,m}$.

The capacities of the CS, SS, and FS parts of service m are denoted as \overline{cs}_m , \overline{ss}_m and \overline{fs}_m , respectively.

$$\begin{bmatrix} \overline{cs}_m & \overline{ss}_m & \overline{fs}_m \end{bmatrix} = [\alpha_m \quad \beta_m \quad \gamma_m] g_m \quad (7.21)$$

where α_m , β_m and γ_m denote the proportions of the three parts for service m , and $\alpha_m + \beta_m + \gamma_m = 1$.

References

- [1] P. Mancarella, "Cogeneration systems with electric heat pumps: Energy-shifting properties and equivalent plant modelling," *Energy Conversion and Management*, vol. 50(8), pp. 1991-1999, Aug 2009 Aug.
- [2] Energinet. Environmental Report 2017: Environmental report for Danish electricity and CHP for 2016 status year. [Online]. Available: <https://en.energinet.dk/-/media/C4170984026F4BFD921F6E852446208A.pdf>
- [3] D. Xie, H. Hui, Y. Ding, and Z. Lin, "Operating reserve capacity evaluation of aggregated heterogeneous TCLs with price signals," *Applied Energy*, vol. 216, pp. 338-347, 2018.
- [4] J. Wang, H. Zhong, Z. Ma, Q. Xia, and C. Kang, "Review and prospect of integrated demand response in the multi-energy system," *Applied Energy*, vol. 202, pp. 772-782, 2017/09/15/ 2017.
- [5] I. G. Moghaddam, M. Saniei, and E. Mashhour, "A comprehensive model for self-scheduling an energy hub to supply cooling, heating and electrical demands of a building," *Energy*, vol. 94, pp. 157-170, Jan 2016.
- [6] P. Mancarella and G. Chicco, "Real-Time Demand Response From Energy Shifting in Distributed Multi-Generation," *IEEE Transactions on Smart Grid*, vol. 4, pp. 1928-1938, Dec 2013.
- [7] X. Jin, Y. Mu, H. Jia, J. Wu, X. Xu, and X. Yu, "Optimal day-ahead scheduling of integrated urban energy systems," *Applied energy*, vol. 180, pp. 1-13, 2016.
- [8] C. Shao, Y. Ding, P. Siano, and Z. Lin, "A Framework for Incorporating Demand Response of Smart Buildings Into the Integrated Heat and Electricity Energy System," *IEEE Transactions on Industrial Electronics*, vol. 66(2), pp. 1465-1475, Feb 2019.
- [9] M. H. Shams, M. Shahabi, and M. E. Khodayar, "Stochastic day-ahead scheduling of multiple energy Carrier microgrids with demand response," *Energy*, vol. 155, pp. 326-338, 2018/07/15/ 2018 July.

- [10] S. Bahrami and A. Sheikhi, "From Demand Response in Smart Grid Toward Integrated Demand Response in Smart Energy Hub," *IEEE Transactions on Smart Grid*, vol. 7, pp. 650-658, Aug 2016.
- [11] M. Mohammadi, Y. Noorollahi, B. Mohammadi-ivatloo, M. Hosseinzadeh, H. Yousefi, and S. T. Khorasani, "Optimal management of energy hubs and smart energy hubs – A review," *Renewable and Sustainable Energy Reviews*, vol. 89, pp. 33-50, 2018/06/01/ 2018 June.
- [12] S. Paudyal, C. A. Cañizares, and K. Bhattacharya, "Optimal Operation of Industrial Energy Hubs in Smart Grids," *IEEE Transactions on Smart Grid*, vol. 6, pp. 684-694, 2015.
- [13] N. Good, E. A. Martínez Ceseña, C. Helton, and P. Mancarella, "A transactive energy modelling and assessment framework for demand response business cases in smart distributed multi-energy systems," *Energy*, vol. (In press), 2018/02/20/ 2018.
- [14] E. A. Martínez Ceseña, N. Good, A. L. A. Syrri, and P. Mancarella, "Techno-economic and business case assessment of multi-energy microgrids with co-optimization of energy, reserve and reliability services," *Applied Energy*, vol. 210, pp. 896-913, 2018/01/15/ 2018 Jan.
- [15] G. Strbac, "Demand side management: Benefits and challenges," *Energy Policy*, vol. 36, pp. 4419-4426, 2008/12/01/ 2008.
- [16] R. Billington and R. N. Allan, *Reliability evaluation of power systems*. Canada: Plenum Publishing Corp, 1984.
- [17] W. Yu, K. Wen, Y. Min, L. He, W. Huang, and J. Gong, "A methodology to quantify the gas supply capacity of natural gas transmission pipeline system using reliability theory," *Reliability Engineering & System Safety*, vol. 175, pp. 128-141, 2018/07/01/ 2018 July.
- [18] I. Postnikov, V. Stennikov, E. Mednikova, and A. Penkovskii, "Methodology for optimization of component reliability of heat supply systems," *Applied Energy*, vol. 227, pp. 365-374, 2018/10/01/ 2018 Oct.
- [19] G. Koeppel and G. Andersson, "Reliability modeling of multi-carrier energy systems," *Energy*, vol. 34, pp. 235-244, 2009.
- [20] E. M. Larsen, Y. Ding, Y.-F. Li, and E. Zio, "Definitions of generalized multi-performance weighted multi-state K⁻out-of-n system and its reliability evaluations," *Reliability Engineering & System Safety*, vol. 199, p. 105876, 2020.
- [21] G. Li, Z. Bie, Y. Kou, J. Jiang, and M. Bettinelli, "Reliability evaluation of integrated energy systems based on smart agent communication," *Applied Energy*, vol. 167, pp. 397-406, 2016/04/01/ 2016.
- [22] Y. K. Lei, K. Hou, Y. Wang, H. J. Jia, P. Zhang, Y. F. Mu, *et al.*, "A new reliability assessment approach for integrated energy systems: Using hierarchical decoupling optimization framework and impact-increment based state enumeration method," *Applied Energy*, vol. 210, pp. 1237-1250, Jan 2018.

- [23] M.-H. Shariatkah, M.-R. Haghifam, G. Chicco, and M. Parsa-Moghaddam, "Adequacy modeling and evaluation of multi-carrier energy systems to supply energy services from different infrastructures," *Energy*, vol. 109, pp. 1095-1106, 2016/08/15/ 2016.
- [24] M.-H. Shariatkah, M.-R. Haghifam, M. Parsa-Moghaddam, and P. Siano, "Modeling the reliability of multi-carrier energy systems considering dynamic behavior of thermal loads," *Energy and Buildings*, vol. 103, pp. 375-383, 2015/09/15/ 2015.
- [25] W. Cui, Y. Ding, H. Hui, Z. Lin, P. Du, Y. Song, *et al.*, "Evaluation and Sequential Dispatch of Operating Reserve Provided by Air Conditioners Considering Lead–Lag Rebound Effect," *IEEE Transactions on Power Systems*, vol. 33, pp. 6935-6950, 2018.
- [26] M. Moeini-Aghetaie, H. Farzin, M. Fotuhi-Firuzabad, and R. Amrollahi, "Generalized Analytical Approach to Assess Reliability of Renewable-Based Energy Hubs," *IEEE Transactions on Power Systems*, vol. 32, pp. 368-377, 2017.
- [27] S. Wang, C. Shao, Y. Ding *et al.*, "Operational reliability of multi-energy customers considering service-based self-scheduling," *Applied Energy*, vol. 254, pp. 113531, Nov, 2019.
- [28] Y. Ding, L. Cheng, Y. Zhang, and Y. Xue, "Operational reliability evaluation of restructured power systems with wind power penetration utilizing reliability network equivalent and time-sequential simulation approaches," *Journal of Modern Power Systems and Clean Energy*, vol. 2, pp. 329-340, 2014.
- [29] A. M. L. d. Silva, L. A. D. F. Manso, J. C. D. O. Mello, and R. Billinton, "Pseudo-chronological simulation for composite reliability analysis with time varying loads," *IEEE Transactions on Power Systems*, vol. 15, pp. 73-80, 2000.
- [30] A. Lisnianski, I. Frenkel, and Y. Ding, *Multi-state system reliability analysis and optimization for engineers and industrial managers*. London: Springer Science & Business Media, 2010.
- [31] A. Dolatabadi and B. Mohammadi-Ivatloo, "Stochastic risk-constrained scheduling of smart energy hub in the presence of wind power and demand response," *Applied Thermal Engineering*, vol. 123, pp. 40-49, Aug 2017.
- [32] J. Ramos-Teodoro, F. Rodríguez, M. Berenguel, and J. L. Torres, "Heterogeneous resource management in energy hubs with self-consumption: Contributions and application example," *Applied Energy*, vol. 229, pp. 537-550, Nov 2018.
- [33] M.-H. Shariatkah, M.-R. Haghifam, M. Parsa-Moghaddam, and P. Siano, "Evaluating the reliability of multi-energy source buildings: A new analytical method for considering the dynamic behavior of thermal loads," *Energy and Buildings*, vol. 126, pp. 477-484, Aug 2016.

- [34] M. A. Ortega-Vazquez and D. S. Kirschen, "Optimising the spinning reserve requirements considering failures to synchronise," *IET Generation, Transmission & Distribution*, vol. 2, pp. 655-665, 2008.
- [35] A. Helseth and A. T. Holen, "Impact of Energy End Use and Customer Interruption Cost on Optimal Allocation of Switchgear in Constrained Distribution Networks," *IEEE Transactions on Power Delivery*, vol. 23, pp. 1419-1425, Jun 2008.
- [36] F. Meng and X. Zeng, "A Profit Maximization Approach to Demand Response Management with Customers Behavior Learning in Smart Grid," *IEEE Transactions on Smart Grid*, vol. 7, pp. 1516-1529, 2016.
- [37] J. M. Nahman, "Approximate Expressions for Steady-State Reliability Indexes of Markov Systems," *IEEE Transactions on Reliability*, vol. 35, pp. 338-343, 1986.
- [38] R. Billinton and R. N. Allan, *Reliability evaluation of engineering systems*: Springer, 1992.
- [39] D. E. Goldberg and J. H. Holland, "Genetic Algorithms and Machine Learning," *Machine Learning*, vol. 3, pp. 95-99, October 01 1988.
- [40] H. Jia, Y. Ding, Y. Song, C. Singh, and M. Li, "Operating Reliability Evaluation of Power Systems Considering Flexible Reserve Provider in Demand Side," *IEEE Transactions on Smart Grid*, vol. (Early Access), pp. 1-1, 2018.
- [41] M. J. Sullivan, M. Mercurio, and J. Schellenberg, "Estimated value of service reliability for electric utility customers in the United States," vol. 14, pp. 83-89, 2009.
- [42] C. Ye, Y. Ding, Y. Song, Z. Lin, and L. Wang, "A data driven multi-state model for distribution system flexible planning utilizing hierarchical parallel computing," *Applied Energy*, vol. 232, pp. 9-25, 2018/12/15/ 2018 Dec.

8 Multi-phase Risk Modeling and Evaluation of Multi-energy Systems under Windstorms

8.1 Introduction

The above chapters mainly focus on the risk modeling and analysis of multi-energy systems under normal weather conditions. In the past few decades, climate change has increased the frequency and severity of windstorms and hurricanes [1, 2]. Considering the effects of severe weather, the resilient operation of MESs can be threatened, which may lead to long-duration interruption of energy supplied to consumers [3]. It is reported that the catastrophic outages in Texas on 1st February 2011 resulted from windstorms [4]. Considering the impacts of unexpected windstorms, several electrical components can be out of service, including substations and electric lines. Due to the electric supply interruptions caused by windstorms, several electric-driven components in the gas system could not maintain the normal operation. Under these circumstances, more than 4.4 million energy users' energy consumption (i.e. heat, gas and electricity) was greatly affected during the long-duration blackout [4]. Therefore, considering the dramatic consequences of severe weather, the study on the risk of integrated energy infrastructure systems has drawn more and more attention nowadays.

With respect to energy infrastructure systems, the risk of power systems [10, 13], gas systems [15], and heat systems has been studied independently. Several scholars in electrical engineering concepts focused on the risk modeling and evaluation of power systems using data-based statistical methods [5, 6] and simulation techniques [13, 14]. Based on the historical outage data, reference [5] estimates the effects of tree trimming on power systems risk under hurricanes using statistical methods. In reference [6], the accelerated failure time models are utilized to estimate the risk of power grids in terms of power outage durations during hurricanes. Regarding simulation techniques, a three-stage framework is proposed in [7] to analyze the time-dependent risk of power systems under hurricane hazards. Reference [8] presents a methodology for the spatial and regional risk assessment of power systems affected by severe windstorms. In reference [9], a simulation framework is proposed to assess the risk of power transmission grids subject to cascading failures under high winds and lightning. At the same time, many scholars focused on the risk assessment of gas systems. Reference [10] presents a performance assessment methodology to evaluate the risk of natural gas systems considering the impacts of the earthquake. It can be concluded that the previous studies are more focused on the risk assessment of a single energy system without considering the energy interactions. Actually, the dependent and coupling relationship between different energy carriers in the MESs would definitely influence the risk of the energy systems, which could not be captured and characterized by the technique in previous studies. Hence, a comprehensive framework needs to be developed to evaluate the risk of MESs with the consideration of the interactions among different energy subsystems.

In order to quantify the risk performance of energy systems, various indices have been proposed in previous studies. For example, the risk is quantified using the area between the real and target performance curves in [10], [11], and [12]. In reference [8], power system risk is measured by the expected energy losses compared to the pre-event states, while reference [11] measures the system risk using the recovery speeds from post-event degraded states to pre-event states. In references [13] and [14], system risk is quantified by the area between the real and target performance curves. However, the previous studies usually adopt system-wide indices to represent the risk performances of MESs without considering the locational difference of risk. Due to the limited transmission capacity and the uneven distributions of energy sources and demands, the impacts of severe weather on the risk of MESs can differ at various nodes [15]. Therefore, new evaluation metrics need to be proposed to quantify the nodal risk performance in different energy subsystems of MESs.

For calculating the risk indices, the primary issue is to assess the energy losses of MESs at different time steps following the extreme event. The optimal power flow model that aims to minimize the load curtailment costs is utilized in [8], [16], and [1] to evaluate the electric losses during hurricanes. Reference [17] proposes an optimal gas and power flow model to calculate the energy losses based on the minimization of gas and electric curtailment costs. For the optimal energy flow models in the previous studies, the total curtailment costs of energy carriers usually serve as the objection function without subdividing the specific services of different energy. Actually, the energy consumers in MESs are more focused on the energy-related service instead of different energy carriers. For example, the consumers are more concerned with the availability of space heating rather than where the heat comes from, e.g. produced through electrical heat pumps or directly from district heating networks. Under this circumstance, the energy-based optimal analysis model cannot characterize the identical service for different energy carriers, which may lead to impractical simulation results. Therefore, a service-based optimal energy flow model is necessary for practically evaluating the energy losses of MESs under windstorms.

In order to address the aforementioned research gaps, this chapter aims to evaluate the nodal risk of MESs considering the interactions between different energy carriers, where the impacts of high winds on component and system operation are modeled during windstorms. The whole process of windstorms is divided into four phases: (i) pre-disturbance phase, (ii) disturbance progress phase, (iii) post-event degradation phase, and (iv) system restoration phase. The innovative contributions of the study are summarized as:

- (1) A comprehensive framework is proposed to evaluate the impacts of windstorms on the risk of MESs considering the interactions among different energy carriers. To model the time-dependent performance levels of MESs at different phases, the multi-phase performance response curve is utilized. Besides, the Monte-Carlo simulation (MCS) method is introduced to model the

chaotic failures and restoration of components according to the weather extent.

- (2) Nodal risk metrics for different energy subsystems are defined to quantitatively evaluate the risk of MESs. The proposed metrics include the expected energy losses, collapse ratio, and recovery ratio, which can describe the expected level and instantaneous characteristics of risk in MESs.
- (3) A modified optimal energy flow model is proposed to practically assess the energy losses of MESs considering the energy-related services of different consumers. The proposed model aims to minimize the total costs of energy services rather than energy carriers under windstorms by coordinating the energy production adjustment among different energy subsystems.

The chapter includes research related to multi-phase risk analysis of multi-energy systems under windstorms by [18].

8.2 Risk of multi-energy systems under windstorms

8.2.1 Illustration of multi-phase risk in multi-energy systems

In order to illustrate the multi-phase risk of the MESs, the performance response curve is utilized to quantify the risk level of MESs [7, 11], as shown in Fig. 8.1. The performance response curve denotes the performance level change of MESs with time following the disturbance events. The performance levels of MESs $\text{Per}(t)$ can be measured by different metrics, such as the number of functional components or the amount of energy supplied in the disasters.

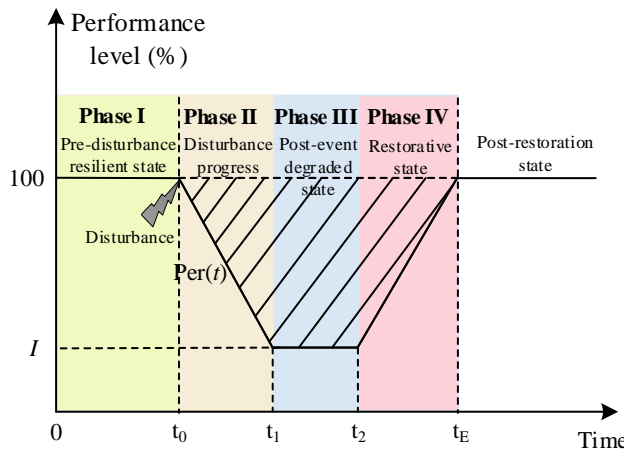


Fig. 8.1. Illustration of the multi-phase performance response curve of MESs.

Four phases can be seen in the multi-phase performance response curve of MESs of Fig. 8.1, namely [19]:

1) *Phase I*, the pre-disturbance phase ($t \in [0, t_0]$) represents the disaster prevention of MESs from normal operation to the onset of random failures. In this phase, the initial performance level of MESs $\text{Per}(t)$ is 100% before the disturbance events occur at t_0 .

2) *Phase II*: disturbance progress phase ($t \in [t_0, t_1]$) reflects the absorptive capacity of MESs to resist the impacts of initial failures. During this phase, the system operator will re-dispatch all the available resources (e.g. generation units, gas sources, and energy loads) for the reliable operation of MESs. Under this circumstance, the performance level of MESs $\text{Per}(t)$ can decrease from 100% to I when time t changes from t_0 to t_1 .

3) *Phase III*: post-event degraded phase ($t \in [t_1, t_2]$) represents the time duration for designing the disaster recovery plan. In this phase, the performance level $\text{Per}(t)$ resides at the post-disturbance degraded state I for some time before the restoration is initiated at t_2 .

4) *Phase IV*: restoration phase ($t \in [t_2, t_E]$) represents the recovery process of MESs during which the repair crews are dispatched to implement disaster recovery plans. With the restoration of damaged components, the performance level $\text{Per}(t)$ of MESs will recover from I to the normal operation level 100%.

Based on the illustration of the multi-phase performance response curve, the expected performance loss (EPL) is defined to represent the risk of MESs with the trapezoid area marked in a shadow of Fig. 8.1 [12], which can be expressed as:

$$EPL = \frac{\int_{t=0}^{t_E} [1 - \text{Per}(t)] dt}{\int_{t=0}^{t_E} dt} \quad (8.1)$$

The risk indicator EPL describes the average performance losses of MESs considering both the intensity and duration of windstorms. Larger EPL values indicate lower risk whereas smaller EPL values imply higher risk [20]. Moreover, in order to describe the instantaneous variation of performance levels in MESs, the collapse ratio CR in phase II and the recovery ratio RR in phase IV are defined in this chapter.

The collapse ratio CR in the disturbance progress phase reflects how fast the performance levels of MESs drop, which can be calculated as:

$$CR = \frac{d[\text{Per}(t)]}{dt} \quad t \in [t_0, t_1] \quad (8.2)$$

The recovery ratio RR in the restorative phase reflects how promptly the MESs can restore to their initial performance level, which can be calculated as:

$$RR = \frac{d[\text{Per}(t)]}{dt} \quad t \in [t_2, t_E] \quad (8.3)$$

8.2.2 The outline to evaluate the multi-phase risk of multi-energy systems

Based on the multi-phase performance response curve in Fig. 8.1, the outline to evaluate the risk of MMESs is illustrated in Fig. 8.2. During all the phases of an event, the impacts of weather extent (i.e. wind speeds) on the component failures and the re-dispatch of MESs are modeled. In the pre-disturbance phase (i.e. phase I), the failure models of components are introduced to characterize their failure probability related to wind speeds. Due to the component failures caused by windstorms, a service-based optimal energy flow model is developed in the disturbance progress phase (i.e. phase II) to assess the performance losses of MESs. The duration of the post-event degraded phase (i.e. phase III) is determined according to the intensity of component damage caused by windstorms. In the restoration phase (i.e. phase IV), the weather-related restoration model is applied to determine the repair time of components based on the damage intensity.

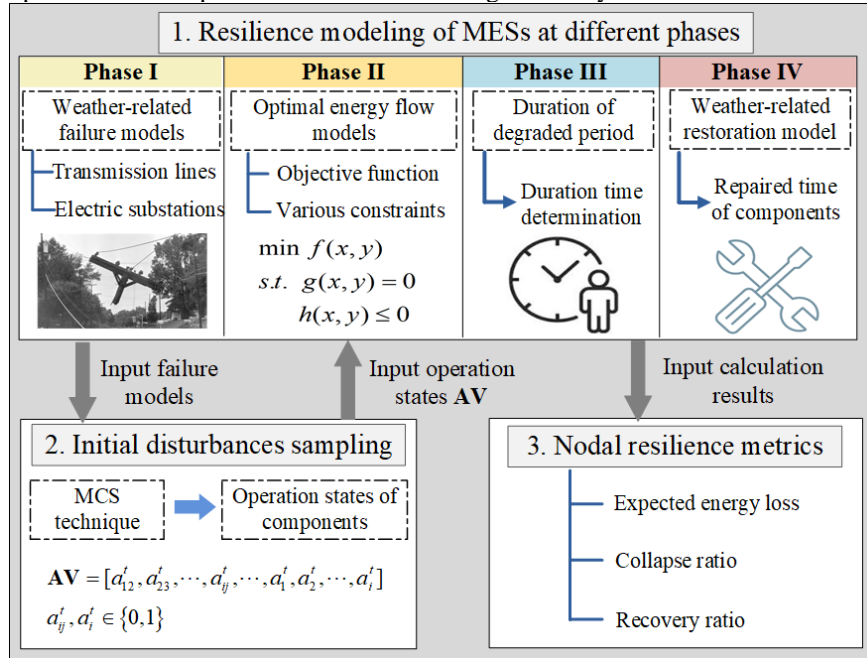


Fig. 8.2. The schematic diagram for illustrating the risk evaluation of MESs.

In order to model the chaotic failures influenced by severe weather, the MCS method is then introduced in this chapter. For different initial disturbances sampled by the MCS method, the time-dependent performance levels of MESs at different phases can be determined using the previous risk analysis model. On this basis, nodal risk metrics for different energy subsystems can be calculated to quantify the regional risk of MESs considering the impacts of windstorms, including the expected energy losses, collapse ratio, and recovery ratio. The proposed

metrics can describe the expected level and instantaneous characteristics of risk in MESs. On the one hand, the expected energy losses are used as quantitative indicators to evaluate the average risk performance of MESs under windstorms. On the other hand, the collapse and recovery ratios can capture the degradation and restoration features of risk in MESs, i.e. how fast the system performance drops when the weather event hits MESs and how long the system recovers to its initial state, respectively.

8.3 Risk modeling of MESs under windstorms

Due to the interactions between different energy carriers, the component failures caused by high winds in electric systems can also lead to gas or heat interruptions in the other energy subsystems. Based on the previous illustration of the multi-phase performance response curve of Fig. 8.1, the risk of MESs is studied in this section.

8.3.1 Phase I: pre-disturbance phase

During phase I, the MESs continue the normal operation until the disturbance events (i.e. windstorms) occur at t_0 . Under windstorms, the components in the electric network can suffer different extents of damage due to their different working characteristics. Generally, the components in an electric network can be classified as transmission lines (i.e. overhead lines, underground cables) and electrical substations. In this section, the failure models of different components considering the impacts of windstorms are illustrated.

(1) Risk model of overhead lines

In order to model the fragility of overhead lines to high winds, the fragility curve is introduced here, which characterizes the relationship between the failure probability of overhead lines and their surrounding weather extent (e.g. wind speeds) [11]. On this basis, the weather-dependent and time-dependent failure probability of overhead lines can be determined by mapping the profile of wind speed to the fragility curve. As illustrated in [1], a generic fragility curve can be expressed as:

$$p_{ij}^{over}(v) = \begin{cases} p_{ij}^0, & \text{if } v \leq v_{cri} \\ p_{ij_v}(v), & \text{if } v_{cri} < v \leq v_{col} \\ 1, & \text{if } v > v_{col} \end{cases} \quad (8.4)$$

where $p_{ij}^{over}(v)$ denotes the failure probability of overhead lines as the function of wind speed v ; p_{ij}^0 denotes the failure probability of lines under good weather conditions; $p_{ij_v}(v)$ denotes the relation between failure probability and wind speed v from v_{cri} to v_{col} .

(2) Risk model of underground cables

In contrast to overload lines, the electric cables are usually buried underground, which are more resilient to windstorms. Therefore, the failure probability of underground cables has no relation to wind speeds, which can be calculated as:

$$p_{ij}^{cab}(v) = p_{ij}^{cab,0} \quad (8.5)$$

where $p_{ij}^{cab,0}$ denotes the failure probability of cable ij under normal conditions.

(3) Risk model of electrical substations

To characterize the vulnerability of electrical substations to high winds, the fragility functions are introduced in this chapter, which model the relationship between the failure probability of substations and the weather extent. According to [21], the failure probability of substation i under the given wind speed can be evaluated using the following function:

$$p_i^{subs}(v) = \phi\left(\frac{\ln(v) - \mu}{\sigma}\right) \quad (8.6)$$

where μ and σ are the logarithmic mean and the standard deviation, respectively. The set of parameters μ and σ is related to the structural characteristics and layout of a substation. The estimation results of μ and σ for different layouts of substations (open, suburban, light urban and etc.) are provided in [21]. Taking the suburban substation as an example, the values of μ and σ in the fragility functions are 5.419 and 0.419, respectively. On this basis, the failure probability of a suburban substation for wind speed v can be determined using the fragility functions in (8.6).

(4) The availability of electrical components

To model the operation states of electrical components (i.e. lines and substations) considering the impacts of high winds at different time, the availability vector \mathbf{AV} is introduced here, which can be expressed as:

$$\mathbf{AV} = [a'_{12}, a'_{23}, L, a'_{ij}, L, a'_1, a'_2, L, a'_i] \quad (8.7)$$

$$a'_{ij}, a'_i \in \{0, 1\}$$

where a'_{ij} denotes the operation state of overhead line ij or cable ij at time t ; a'_i denotes the operation state of substation i at time t .

The operation states of electrical components can be either 0 or 1, where 1 corresponds to component connection and 0 corresponds to the component outage. Besides, it should be noted that the operation states of components at time t are dependent on the operation states at the previous time steps. In specific, the component tripped at time t will stay failed in the following time steps since no repair crews are dispatched during windstorms for safety reasons [11]. Taking overhead line ij as an example, its operation state a'_{ij} at time t can be determined based on the current failure probability and the previous operation states utilizing state sampling techniques [22].

$$a'_{ij} = \begin{cases} a'^{-1}_{ij} \cdot 1, & \text{if } p'^{\text{over}}_{ij}(v) \leq r \\ a'^{-1}_{ij} \cdot 0, & \text{if } p'^{\text{over}}_{ij}(v) > r \end{cases}$$

where r is the random number sampled from the uniform distribution in the interval $(0,1)$, which can be represented as $r: U(0,1)$. The variable r is generated to determine the operation state of line ij , which is not dependent on wind speed v . The impacts of weather conditions on the operation state of line ij can be embodied in the failure probability $p'^{\text{over}}_{ij}(v)$.

8.3.2 Phase II: disturbance progress phase

Due to the chaotic component failures caused by windstorms from t_0 to t_1 , the MESs will deviate from its normal operation state. Under this circumstance, the re-dispatch of power generation and gas sources or load shedding will be adopted by system operators for the reliable operation of MESs [15]. In order to minimize the consequences caused by windstorms, the modified optimal energy flow techniques in (8.8)-(8.28) are proposed in this chapter to determine the re-dispatch results of MESs at different time t . In this chapter, the performance levels of MESs $\text{Per}(t)$ are measured by the percentage of electric loads, gas loads, and heat loads connected to systems.

Considering the difference in energy services among consumers in different sectors, we categorize the consumers into residential, commercial, and industrial ones. Table 8.1 shows the primary services of different energy for different energy customer sectors based on the statistical data in [23, 24]. Taking electricity as an example, the primary services of electricity for residential consumers are electronic appliances (e.g. TV) and lighting. Regarding commercial consumers, their electricity services mainly consist of heating and lighting. Industrial consumers mainly use electricity for product processing and heating.

Generally, the priority of energy demands can be converted into the corresponding interruption cost to shed loads. For example, the interruption costs of lighting can be larger than TV since the lighting is more important. Therefore, the objective function is to minimize the total costs of energy load curtailments at time t .

$$\text{Min} \left\{ \sum_{i=1}^N \sum_{s=1}^S \sum_{z=1}^Z \left[C'_{isz} (\Delta P'_{isz}) + C'_{isz} (\Delta L'_{isz}) \right] + \sum_{m=1}^M \sum_{s=1}^S \sum_{z=1}^Z \left[C'_{msz} (\psi \cdot \Delta W'_{msz}) \right] \right\}$$

$$\text{where } \Delta P'_{il} = \sum_{s=1}^S \sum_{z=1}^Z \Delta P'_{isz}, \quad \Delta L'_{ie} = \sum_{s=1}^S \sum_{z=1}^Z \Delta L'_{isz} \\ \Delta W'_{ml} = \sum_{s=1}^S \sum_{z=1}^Z \Delta W'_{msz}, \quad \Delta L'_{ih} = \sum_{s=1}^S \sum_{z=1}^Z \Delta h'_{isz} \quad (8.8)$$

where $\Delta P'_{isz}$ and C'_{isz} denote the electric load curtailment and the corresponding compensation cost (\$/MW) of consumer z in sector s at electric node i and

time t , respectively. ΔL_{isz}^t denotes the electric load curtailment of consumer z in sector s for the EH connected to electric node i . ΔW_{msz}^t and C_{msz}^t denotes the gas load curtailment and the corresponding compensation cost (\$/m³) of consumer z in sector s at gas node m and time t , respectively. Δh_{is}^t and C_{is}^t denotes the heat load curtailment and the corresponding compensation cost (\$/MW) of consumers in sector s for the EH connected to electric node i . ψ denotes the gas gross heating value (MW/m³). ΔP_{il}^t denotes the total electric load curtailment at electric node i and time t . ΔW_{ml}^t denotes the total gas load curtailment at electric node i and time t . ΔL_{ie}^t and ΔL_{ih}^t denote the electric and gas load curtailments of the EH connected to electric node i at time t , respectively.

Table 8.1 Illustration of the primary services of different energy for different energy customer sectors

Consumer sector	Electricity	Gas	Heat
Residential	Lighting, electronic appliances	Heating, cooking	Heating
Commercial	Heating, lighting	Heating, equipment driving	Heating
Industrial	Product processing, heating	Product processing, heating	Heating

The optimal energy flow also needs to satisfy the following constraints:

(1) *Constraints of coupled components*

The coupled relationship between different energy carriers in MESs can be described by coupled components. Generally, the coupled components in MESs can be classified into EH and electric-driven gas sources (EGSs). In this section, the operation models of coupled components are illustrated.

a) *Energy hub*

The coupling relationship between inputs and outputs of EH is illustrated in Fig. 8.3, which can be expressed as [25]:

$$\begin{bmatrix} L_{ie}^0 - \Delta L_{ie}^t \\ L_{ih}^0 - \Delta L_{ih}^t \end{bmatrix} = \begin{bmatrix} \alpha_i^t & v_i^t \cdot \eta_e \cdot \psi \\ (1 - \alpha_i^t) \cdot \varphi & v_i^t \cdot \eta_h \cdot \psi + (1 - v_i^t) \cdot \vartheta_g \end{bmatrix} \cdot \begin{bmatrix} P_{i,EH}^t \\ F_{m,EH}^t \end{bmatrix} \quad (8.9)$$

where α_i^t represents the dispatch factor of electricity flow. v_i^t represents the dispatch factor of gas flow. η_e and η_h represent the electrical efficiency and thermal efficiency of CHP, respectively. φ and ϑ_g represent the efficiency of the heat pump and gas boiler, respectively. L_{ie}^0 and L_{ih}^0 represent the electricity demand and heat demand of EH connected to electric node i in normal conditions, respectively. $P_{i,EH}^t$ and $F_{m,EH}^t$ represent the input electricity flow and gas flow to EH at time t , respectively.

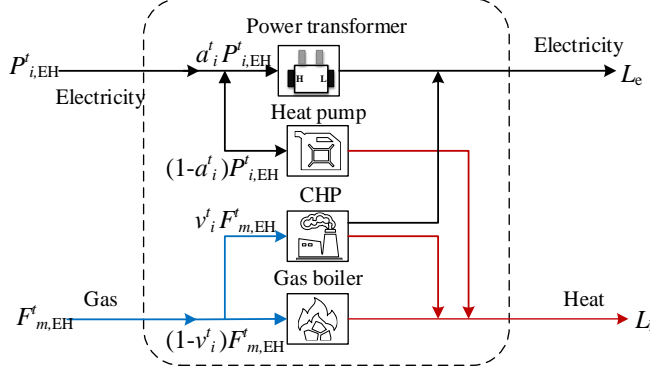


Fig. 8.3. The coupling relationship between inputs and outputs of the energy hub
The dispatch factor of EH is bounded by:

$$0 \leq \alpha'_i \leq 1, 0 \leq v'_i \leq 1 \quad (8.10)$$

The energy load curtailments of EH are bounded by:

$$0 \leq \Delta L'_{ie} \leq L^0_{ie} \quad (8.11)$$

$$0 \leq \Delta L'_{ih} \leq L^0_{ih} \quad (8.12)$$

b) Electric-driven gas sources

The EGSs in the natural gas network need to get an electric power supply from the power system to maintain proper operation. Generally, the power consumption D'_{ik} of EGS k is related to its gas production W'_{mk} , which can be described as [15]:

$$D'_{ik} = \eta_g \cdot W'_{mk} \quad (8.13)$$

where η_g represents the conversion factor of EGSs (MW/m³).

Considering the impacts of windstorms, the power supply of EGS k at time t can be determined by the electric load curtailments at the corresponding nodes. In order to guarantee the reliable operation of EGSs, the power supplied to EGSs needs to be satisfied firstly during contingencies [8]. Therefore, the operation state ψ'_{mk} of EGS k at gas node m and time t can be determined as:

$$\psi'_{mk} = \begin{cases} 0, & \text{if } D'_{ik} > D^0_{il} - \Delta P'_{il} \\ 1, & \text{if } D'_{ik} \leq D^0_{il} - \Delta P'_{il} \end{cases} \quad (8.14)$$

where D^0_{il} denotes the initial electric load at electric node i in normal conditions. It can be noted that EGS k will be interrupted when the power $D^0_{il} - \Delta P'_{il}$ supplied to EGS is smaller than its power requirement D'_{ik} for proper operation.

(2) Natural gas network constraints

A typical natural gas system consists of gas sources, pipelines, and compressors from gas production to consumption [26]. In addition to EGSs, there are fuel-

driven gas sources (FGSs) that can supply gas to consumers in natural gas systems. During operation, these components need to satisfy the following constraints:

a) Pipeline flow constraints

The gas flow f_{mn}^t through pipeline mn at time t can be calculated using the Weymouth equation [26], which can be expressed as:

$$|f_{mn}^t| \cdot f_{mn}^t = M_{mn} \cdot \left[(\pi_m^t)^2 - (\pi_n^t)^2 \right] \quad (8.15)$$

where π_m^t and π_n^t represent the gas pressures of node m and node n at time t , respectively. M_{mn} denotes constant pipeline flow coefficient, which is related to the diameter and length of the pipeline, pressure, and temperature of the gas.

The gas flow through pipeline mn is also restricted by its pipeline capacity:

$$\underline{f}_{mn}^t \leq f_{mn}^t \leq \overline{f}_{mn}^t \quad (8.16)$$

where \overline{f}_{mn}^t and \underline{f}_{mn}^t represent the maximum and minimum gas flow of pipeline mn at time t , respectively.

b) Gas flow balance at each node

Similar to power systems, the natural gas system needs to satisfy the constraint that the gas injected into a node must also flow out of the node, which can be expressed as:

$$\psi_{mk}^t \cdot W_{mk}^t + W_{ms}^t - (D_{mL}^0 - \Delta W_{mL}^t) - F_{m,EH}^t - \sum_{n=1}^M f_{mn}^t - \sum_{c=1}^{CO} f_c^t = 0 \quad (8.17)$$

where W_{mk}^t denotes the gas production of EGS k at node m and time t ; W_{ms}^t denotes the gas production of FGS s at node m and time t ; f_c^t denotes the gas flow through compressor c at time t ; CO refers to the total number of compressors.

c) Compressor model

For compressor stations, the pressure π_m^t at the incoming node m can be proportional to the pressure π_n^t at out-coming node n , which is expressed as:

$$\pi_n^t = \tau_c^t \cdot \pi_m^t \quad (8.18)$$

$$\underline{\tau}_c^t \leq \tau_c^t \leq \overline{\tau}_c^t \quad (8.19)$$

where τ_c^t denotes the compression ratio of compressor c at time t ; $\overline{\tau}_c^t$ and $\underline{\tau}_c^t$ represent the maximum and minimum compression ratios of compressor c , respectively.

d) Gas pressure constraints

The pressure levels at each node are bounded by:

$$\underline{\pi}_m^t \leq \pi_m^t \leq \overline{\pi}_m^t \quad (8.20)$$

where $\overline{\pi_m^t}$ and $\underline{\pi_m^t}$ represent the maximum and minimum gas pressures at node m and time t , respectively.

e) *Gas source production constraints*

The gas production of EGSs and FGSs is constrained by minimum and maximum levels, which can be expressed as:

$$\underline{W_{ms}^t} \leq W_{ms}^t \leq \overline{W_{ms}^t} \quad (8.21)$$

$$\underline{W_{mk}^t} \leq W_{mk}^t \leq \overline{W_{mk}^t} \quad (8.22)$$

where $\overline{W_{ms}^t}$ and $\underline{W_{ms}^t}$ represent the maximum and minimum production of FGS s at node m and time t , respectively; $\overline{W_{mk}^t}$ and $\underline{W_{mk}^t}$ represent the maximum and minimum production of EGS k at node m and time t , respectively.

f) *Gas load curtailment constraints*

The gas load curtailment at each node is bounded by:

$$0 \leq \Delta W_{mL}^t \leq D_{mL}^0 \quad (8.23)$$

(3) *Electric network constraints*

Due to the impacts of component damages caused by windstorms, the power flow through electric systems will be re-dispatched. Therefore, similar to natural gas systems, the *operation* of electric systems needs to satisfy the following constraints [27]:

a) *Power flow balance at each node*

$$P_{ig}^t - (D_{iL}^0 - \Delta P_{iL}^t) - P_{i,EH}^t = \sum_{j=1}^N \frac{\theta_i^t - \theta_j^t}{x_{ij}^t} \quad (8.24)$$

b) *Generating unit limits*

$$\underline{P_{ig}^t} \leq P_{ig}^t \leq \overline{P_{ig}^t} \quad (8.25)$$

c) *Line flow constraints*

$$\left| \frac{\theta_i^t - \theta_j^t}{x_{ij}^t} \right| \leq a_{ij}^t \cdot \overline{S_{ij}^t} \quad (8.26)$$

d) *Bus phase constraints*

$$\underline{\theta_i^t} \leq \theta_i^t \leq \overline{\theta_i^t} \quad (8.27)$$

e) *Electric load curtailment constraints*

$$0 \leq \Delta P_{iL}^t \leq D_{iL}^0 \quad (8.28)$$

where P_{ig}^t represents the power output of generator g at node i and time t ; θ_i^t represents the phase angle of node i at time t ; x_{ij}^t represents the reactance of line between node i and node j ; $\overline{P_{ig}^t}$ and $\underline{P_{ig}^t}$ represents the maximum and mini-

mum output of generators; $\overline{S_{ij}^t}$ represents the power flow limits of line i, j ; $\overline{\theta_i^t}$ and $\underline{\theta_i^t}$ represent the maximum and minimum of phase angle at node i .

The modified optimal energy flow model under windstorms can be formulated as the non-linear optimization problem in (8.8)-(8.28). However, due to the non-linearity of the pipeline equation in (8.15), the feasible region of the optimal energy flow model can be nonconvex which will challenge the global optimality. Therefore, the piecewise linearization techniques are introduced in this chapter to linearize the pipeline equation [28]. Then, the proposed model is converted into a linear programming (LP) problem, which can be solved by the Cplex solver.

8.3.3 Phase III: post-event degraded phase

After the windstorm is ended at t_1 , the system operator will start to make recovery measures about how the MESs are restored. Besides, the restoration resources need to be allocated, including repair crews, vehicles, equipment, and some replacement components [7]. In this phase, the performance level of MESs resides at the post-disturbance degraded state I until the restoration is initiated at t_2 . Generally, the duration of the post-event degraded period is related to the extent of component damages caused by windstorms [11]. If the windstorms affect wider areas or lead to larger losses in MESs, the time needed for the implementation of recovery measures can be relatively longer.

In order to characterize the impacts of component damage on the measure-making, the duration of post-event degraded period $t_2 - t_1$ can be assumed as the function of wind speed v [11], which is expressed as:

$$t_2 - t_1 = \phi(v) \cdot T_d^{normal} \quad (8.29)$$

where T_d^{normal} refers to the mean time needed for measure-making under normal weather, which is assumed to be 3h. $\phi(v)$ is multiplying operator to model the positive relationship between period duration and wind speeds.

8.3.4 Phase IV: restoration phase

Based on the predetermined recovery measures in phase III, the restoration of MESs is initiated at t_2 . It should be illustrated that no restoration is implemented during windstorms due to safety reasons, so the repair crews are dispatched only in the restoration phase [11]. Moreover, it will take more time for repair crews to restore the damaged components for higher wind speeds [9]. Therefore, a weather-related restoration model is introduced to calculate the repair time of damaged components TTR :

$$TTR = \varphi(v) \cdot MTTR^{normal} \quad (8.30)$$

where $MTTR^{normal}$ denotes the mean time to repair damaged components under normal weather, which is assumed to be 2h for lines and 8h for substations. $\varphi(v)$

represents the multiplying operator to model the increasing repair time for higher component damage caused by larger wind speeds.

During the restorative phase from t_2 to t_E , this chapter adopts a random restoration strategy, where the damaged lines and substations are randomly selected to repair. For time t in phase III, the damaged component for repair and its corresponding repair time TTR will be determined utilizing state sampling techniques. Therefore, the performance levels of MESs at time t can then be evaluated.

8.4 Framework for risk evaluation of MESs utilizing Monte Carlo simulation

8.4.1 Nodal risk metrics

According to the illustration of the multi-phase performance response curve in section 2.2, different metrics are defined to quantify the nodal risk of MESs under windstorms, including the expected energy load curtailments, the collapse ratio, and the recovery ratio of energy supply level [11]. After the simulation, the expected electric load curtailments ($EELC_i$) at electric node i , expected gas load curtailments ($EGLC_m$) at gas node m and expected heat load curtailments ($EHLC_i$) at electric node i in MESs for $t \in [0, t_E]$ can be calculated as:

$$EELC_i = \sum_{st=1}^{ST} \left[\sum_{b=0}^{t_E/\Delta t} \left(\frac{\Delta P_{il}^{b,\Delta t} + \Delta L_{ie}^{b,\Delta t}}{D_{il}^0 + L_{ie}^0} \right) \cdot \Delta t \Big/ t_E \right] \Big/ ST \quad (8.31)$$

$$EGLC_m = \sum_{st=1}^{ST} \left[\sum_{b=0}^{t_E/\Delta t} \frac{\Delta W_{ml}^{b,\Delta t}}{D_{ml}^0} \cdot \Delta t \Big/ t_E \right] \Big/ ST \quad (8.32)$$

$$EHLC_i = \sum_{st=1}^{ST} \left[\sum_{b=0}^{t_E/\Delta t} \frac{\Delta L_{ih}^{b,\Delta t}}{L_{ih}^0} \cdot \Delta t \Big/ t_E \right] \Big/ ST \quad (8.33)$$

where Δt denotes the time interval for the risk re-evaluation of MESs, which is assumed as 1h. b denotes the total number of re-evaluations, which equals to $t_E/\Delta t$. ST represents the total simulation times of MCS.

After obtaining the expected energy load curtailments at different nodes, the system's $EELC$, $EGLC$ and $EHLC$ can be calculated based on the following equations:

$$EELC = \sum_{st=1}^{ST} \left[\sum_{b=0}^{t_E/\Delta t} \sum_{i=1}^N \left(\frac{\Delta P_{il}^{b,\Delta t} + \Delta L_{ie}^{b,\Delta t}}{D_{il}^0 + L_{ie}^0} \right) \cdot \Delta t \Big/ t_E \right] \Big/ ST \quad (8.34)$$

$$EGLC = \sum_{st=1}^{ST} \left[\sum_{b=0}^{t_E/\Delta t} \sum_{m=1}^M \frac{\Delta W_{ml}^{b,\Delta t}}{D_{ml}^0} \cdot \Delta t \Big/ t_E \right] \Big/ ST \quad (8.35)$$

$$EHLC = \sum_{st=1}^{ST} \left[\sum_{b=0}^{t_E/\Delta t} \sum_{i=1}^N \frac{\Delta L_{ih}^{b,\Delta t}}{L_{ih}^0} \cdot \Delta t \Big/ t_E \right] \Big/ ST \quad (8.36)$$

To quantify the overall risk of MESs, the synthetic energy loss (*SEL*) is proposed by incorporating the load curtailments in different energy subsystems. After unifying the units of electricity, gas, and heat, the *SEL* of MESs can be calculated using the following equation:

$$SEL = \frac{EELC \cdot \sum_{i=1}^N (D_{iL}^0 + L_{ie}^0) + \psi \cdot EGLC \cdot \sum_{m=1}^M D_{mL}^0 + EHLC \cdot \sum_{i=1}^N L_{ih}^0}{\sum_{i=1}^N (D_{iL}^0 + L_{ie}^0) + \psi \cdot \sum_{m=1}^M D_{mL}^0 + \sum_{i=1}^N L_{ih}^0} \quad (8.37)$$

where ψ denotes gas gross heating value.

Regarding the instantaneous variation of system energy supply level, the collapse ratios and recovery ratios in MESs are defined. During disturbance progress for $t \in [t_0, t_1]$, the collapse ratio of electricity (*CRE*), gas (*CRG*), and heat (*CRH*) supply level can be calculated using the different methods [29], which can be expressed as:

$$CRE = \sum_{st=1}^{ST} \left[\sum_{b=1}^{\frac{(t_1-t_0)/\Delta t}{\Delta t}} \frac{\sum_{i=1}^N (\Delta P_{iL}^{t_0+(b-1)\Delta t} + \Delta L_{ie}^{t_0+(b-1)\Delta t} - \Delta P_{iL}^{t_0+b\Delta t} - \Delta L_{ie}^{t_0+b\Delta t}) / \Delta t}{(t_1 - t_0) / \Delta t} \right] / ST \quad (8.38)$$

$$CRG = \sum_{st=1}^{ST} \left[\sum_{b=1}^{\frac{(t_1-t_0)/\Delta t}{\Delta t}} \frac{\sum_{m=1}^M (\Delta W_{mL}^{t_0+(b-1)\Delta t} - \Delta W_{mL}^{t_0+b\Delta t}) / \Delta t}{(t_1 - t_0) / \Delta t} \right] / ST \quad (8.39)$$

$$CRH = \sum_{st=1}^{ST} \left[\sum_{b=1}^{\frac{(t_1-t_0)/\Delta t}{\Delta t}} \frac{\sum_{i=1}^N (\Delta L_{ih}^{t_0+(b-1)\Delta t} - \Delta L_{ih}^{t_0+b\Delta t}) / \Delta t}{(t_1 - t_0) / \Delta t} \right] / ST \quad (8.40)$$

Similarly, the recovery ratio of electricity (*RRE*), gas (*RRG*), and heat (*RRH*) supply level for $t \in [t_2, t_E]$ can be calculated as:

$$RRE = \sum_{st=1}^{ST} \left[\sum_{b=1}^{\frac{(t_E-t_2)/\Delta t}{\Delta t}} \frac{\sum_{i=1}^N (\Delta P_{iL}^{t_2+b\Delta t} + \Delta L_{ie}^{t_2+b\Delta t} - \Delta P_{iL}^{t_2+(b-1)\Delta t} - \Delta L_{ie}^{t_2+(b-1)\Delta t}) / \Delta t}{(t_E - t_2) / \Delta t} \right] / ST \quad (8.41)$$

$$RRG = \sum_{st=1}^{ST} \left[\sum_{b=1}^{\frac{(t_E-t_2)/\Delta t}{\Delta t}} \frac{\sum_{m=1}^M (\Delta W_{mL}^{t_2+b\Delta t} - \Delta W_{mL}^{t_2+(b-1)\Delta t}) / \Delta t}{(t_E - t_2) / \Delta t} \right] / ST \quad (8.42)$$

$$RRH = \sum_{st=1}^{ST} \left[\sum_{b=1}^{(t_E-t_2)/\Delta t} \frac{\sum_{i=1}^N (\Delta L_{ih}^{t_2+b\cdot\Delta t} - \Delta L_{ih}^{t_2+(b-1)\cdot\Delta t}) / \Delta t}{(t_E - t_2) / \Delta t} \right] / ST \quad (8.43)$$

8.4.2 Simulation procedures

As illustrated in Fig. 8.4, the procedures for risk evaluation of MESs can be divided into four steps. The first step is the initialization of MESs, where the initial parameters are set. On this basis, the initial operation states of MESs can be obtained.

The second step is the risk simulation of MESs considering the impacts of windstorms with Δt temporal resolution from 0 to t_E . As illustrated in section 2.2, the process for the risk evaluation of MESs consists of four phases. During phase I for $t \in [0, t_0]$, the MESs continue normal operation until the windstorms occur at t_0 . The failure probability of overhead lines, underground cables, and electrical substations can be determined according to wind speeds using (8.4), (8.5) and (8.6), respectively. During phase II for $t \in [t_0, t_1]$, the operation states of electrical components \mathbf{AV} can be obtained using MCS techniques. For certain component failures, the energy supply levels of MESs can be calculated using the optimal energy flow model in (8.8)-(8.28). During phase III for $t \in [t_1, t_2]$, the MESs will reside at the post-disturbance degraded state until the recovery measure is initiated at t_2 . The time duration $t_2 - t_1$ of phase III can be determined using (8.29) according to wind speeds. During phase IV for $t \in [t_2, t_E]$, the damaged component for repair and its corresponding repair time TTR can be determined using (8.30). Considering the implementation of recovery measures, the energy supply restoration of MESs can be calculated using the optimal energy flow model in (8.8)-(8.28). On this basis, the energy supply levels of MESs under windstorms can be characterized as the function of time t .

The third step is to repeat the previous procedures until the stopping criterion of the MCS technique is satisfied. The stopping criterion provided for the MCS technique is the variation coefficient of risk metrics, which can be calculated as:

$$\xi = \max \left(\sqrt{V(EELC)} / EELC, \sqrt{V(EGLC)} / EGLC, \sqrt{V(EHLC)} / EHLC \right) \quad (8.44)$$

where $V(EELC)$, $V(EGLC)$ and $V(EHLC)$ are the variances of $EELC$, $EGLC$ and $EHLC$, respectively.

Based on the energy load curtailments for each simulation time, the fourth step is to calculate the risk metrics of MESs using (8.31)-(8.43).

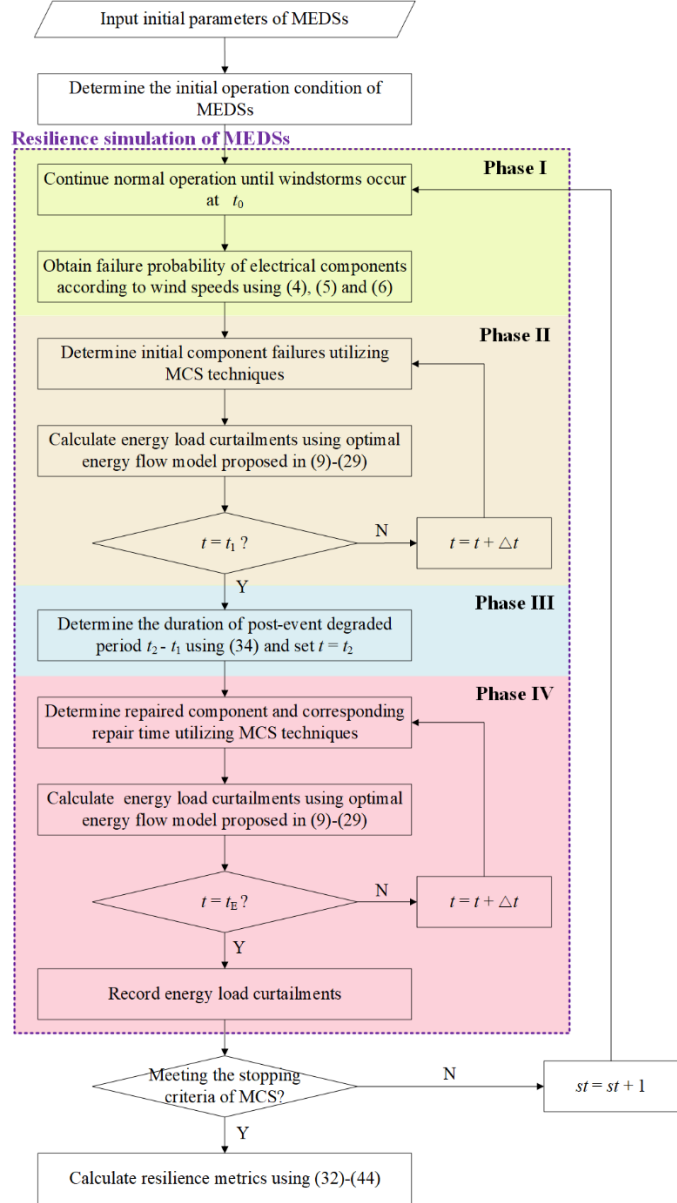


Fig. 8.4. Simulation procedures for risk evaluation of MESs utilizing the MCS technique

8.5 Case studies and discussions

8.5.1 Descriptions of test systems and simulation data

The proposed techniques and models are applied to evaluate the risk of MESS composed of IEEE 33-bus system from [30] and 20-node gas system detailed in [31], as shown in Fig. 8.5. The IEEE 33-bus electric system is composed of 7 generating nodes, 32 load nodes, 37 lines, and 6 DERs. The lines 23-24, 24-25, 14-15, 16-17, 4-5, and 8-9 are assumed as underground cables. On the other hand, the 20-node gas system has two EGSSs, one FGS, three gas compressors, and 19 pipelines. The EGSSs W1 and W2 at gas nodes 8 and 5 are supplied from power flow at electric nodes 18 and 19. In addition, 7 EHs are plugged into electric nodes 24, 25, 7, 8, 30, 14, and 33 in the electric network and gas nodes 6, 7, 15, 16, 12, 19, and 20 in the gas network.

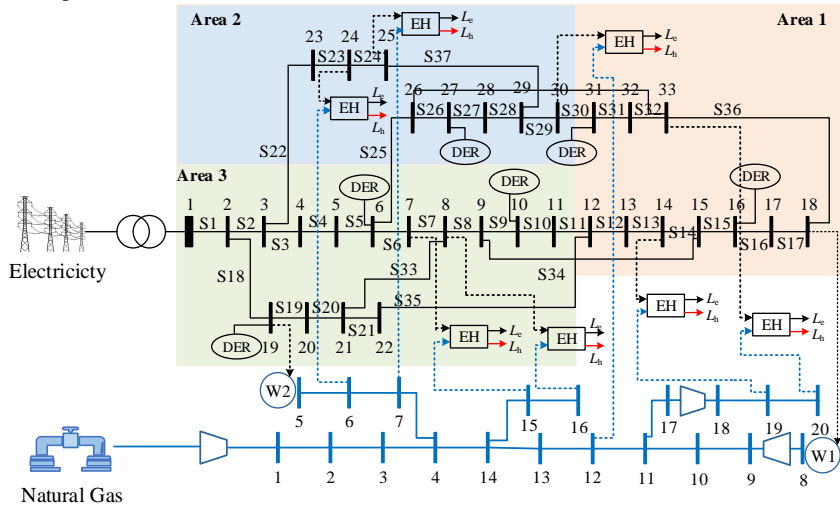


Fig. 8.5. Test system composed of IEEE 33-bus system and 20-node gas system

The physical parameters of gas compressors (such as maximum and minimum compression ratio), pipelines (such as diameter and length), and gas sources (such as production capacity) can be found in [31]. The generating capacity of DERs in the electric network is set as 1MW. Regarding EH, the electrical efficiency η_e and thermal efficiency η_h of CHP are 0.4 and 0.45, respectively [32]. The heat pump efficiency φ is assumed to be 3 [32]. The efficiency of gas boiler ϑ_g is assumed as 0.85. The heat demand L_{ih}^0 of EH at node i is assumed to be 0.9 times the corresponding electricity demand L_{ie}^0 . The gas gross heating value ψ is set as 8.4 KW/m³ [15].

Based on the categories of energy services in Table 8.1, it is assumed that the proportions of residential, commercial, and industrial consumers at each node are

35%, 35%, and 30%, respectively. The proportions of electricity and gas services are set as 50% in the respective customer sectors. The interruption costs of the energy services for different customer sectors are shown in Table 8.2, which are assumed according to the analysis results in [15]. It should be noted that the compensation costs are identical for electricity, gas, and heat with the same services. For instance, since electricity and heat can both be used for heating in the commercial sectors, their compensation costs are identical. Besides, the units of gas interruption costs are converted into $\$/10^3\text{m}^3$ using gas gross heating value ψ .

Table 8.2 The interruption costs of energy services for different energy customer sectors

Consumer sector	Electricity (\$/MW)	Gas(\$/ 10^3m^3)	Heat(\$/MW)
Residential	Lighting (5000), electronic appliances (4000)	Heating (4000/8.4), cooking (5000/8.4)	Heating (4000)
Commercial	Heating (8000), lighting (10000)	Heating (8000/8.4), equipment driving (10000/8.4)	Heating (8000)
Industrial	Product processing (5000), heating (4000)	Product processing (5000/8.4), heating (4000/8.4)	Heating (8000)

Regarding the risk evaluation of MESs, the wind fragility curves of overhead lines can be found in [11]. The overhead line failure probability can be determined with the fragility curves for higher wind speeds ($v > 20\text{m/s}$) whereas the line normal failure probability 0.005 is used for normal weather conditions ($v \leq 20\text{m/s}$) [8]. The failure probability of underground cables is assumed to be 0.005. It is assumed that all the components are online at the beginning of the simulation until the windstorms hit MESs at 10h. The duration $t_1 - t_0$ of windstorms is assumed to be 12h, with an hourly time Δt risk re-evaluation of MESs. During phase III, the mean time T_d^{normal} needed for measure-making under normal weather is assumed as 3h. During phase IV, the mean time to repair damaged lines and substations under normal weather $MTTR^{\text{normal}}$ is assumed as 2h and 8h.

The hourly time scale Δt is selected to make a balance between simulation accuracy and computation time [1]. In specific, the time scales for assessing the risk of MESs are closely related to the different characteristics of electricity and gas networks as well as the EH [33]. Generally, the time scale for assessing the risk of the electric network can become much smaller than that for a CHP unit of EH. Nevertheless, the computation burden can also increase significantly with the decrease in time scales. Therefore, the time scales to evaluate the risk of MESs are set as one hour by weighing up accuracy and efficiency. Moreover, it should be noted that a smaller time scale can be adopted in the proposed framework if required.

8.5.2 Case studies

Case 1: Risk evaluation of MESSs under the impacts of grid-scale windstorms

In this case, the wind speeds in three areas are the same and three scenarios with different weather extents v are analyzed, including 31m/s, 36m/s, and 41m/s wind speeds. The wind speeds in the three scenarios are selected according to the classification of storms, which can be found in [8]. In practical application, the wind speeds of storms can be preset by readers as required. According to the fragility curves in [8], the failure probability of overhead lines is 0.05, 0.10, and 0.20 corresponding to 31m/s, 36m/s, and 41m/s wind speeds, respectively.

In order to model the increasing repair time due to wind speeds, the multiplying operator $\varphi(v)$ is determined by uniformly sampling within a pre-determined range (i.e. $\varphi(v) : [h_1, h_2]$). In this application, the range $[h_1, h_2]$ is $[2,3]$ for $30 \leq v \leq 40$ and $[3,4]$ for higher wind speeds. Similarly, the multiplying operator $\phi(v)$ in (8.29) can be determined by utilizing uniform sampling techniques to model the impacts of wind speeds on the duration of phase III $t_2 - t_1$.

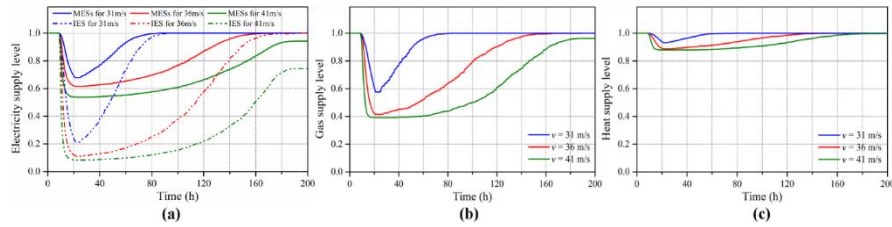


Fig. 8.6. Energy supply level of MESSs as a function of time for different wind speeds. a) Electricity supply level. b) Gas supply level. c) Heat supply level.

The electricity, gas, and heat supply level considering the impacts of windstorms for different wind speeds (i.e. 31m/s, 36m/s, and 41m/s) are given in Fig. 8.6. It can be noted that the shapes of the energy supply level curves recall the response curve of Fig. 8.1, where the four phases of risk evaluation can be distinguished: pre-disturbance phase, disturbance progress, post-event degraded phase, and restoration phase. Based on the variation of energy supply levels with time in Fig. 8.6, the nodal risk indices ($EELC_i$, $EGLC_m$ and $EHLC_i$) for different wind speeds are presented in Fig. 8.7. It should be noted that only the risk values associated with the energy nodes can be obtained via the simulation. With respect to the remaining points, their risk values are estimated based on the obtained values at different energy nodes using interpolation methods. From subpictures (a)-(c) of Fig. 8.7, it can be noted that there are huge differences between nodal risk indices at different nodes. Taking the electric system as an example, the values of $EELC_i$ at electric node 21 are the largest among all nodes, which are 0.344, 0.599, and 0.796 for 31m/s, 36m/s, and 41m/s wind speeds, respectively. In contrast, the val-

ues of $EELC_i$ at electric nodes 30, 8, and 9 are relatively small for all scenarios. This is mainly because the demands at electric nodes 30, 8, and 9 can obtain electricity supply from EH under severe weather.

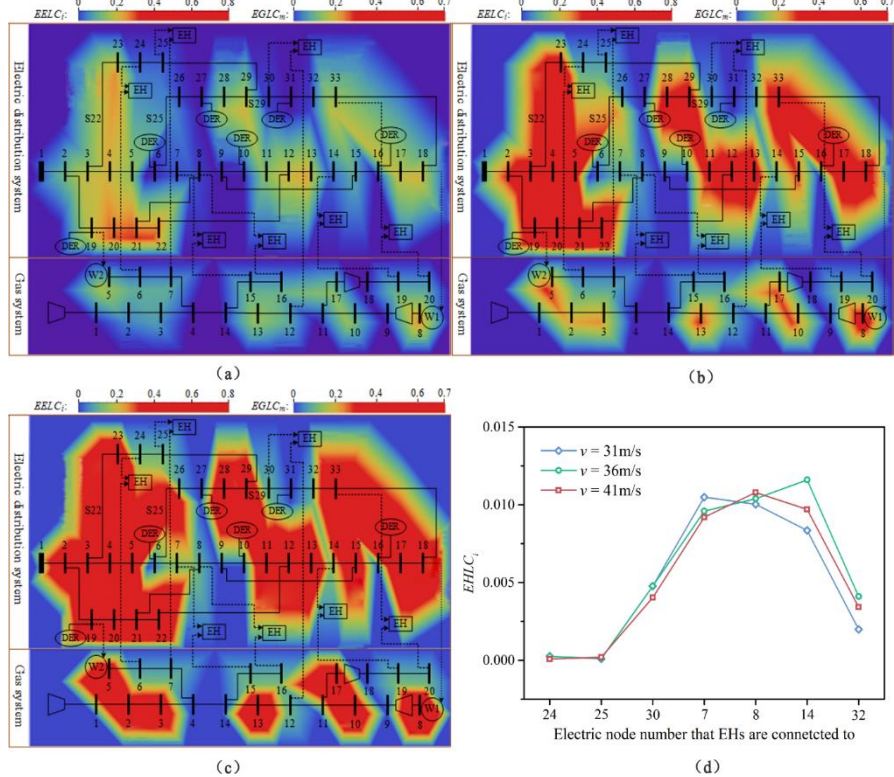


Fig. 8.7. Expected energy load curtailments at different nodes for different wind speeds. a-c) Heat maps of MESs showing the distribution of nodal $EELC_i$ and $EGLC_m$ for 31m/s, 36m/s and 41m/s wind speeds, respectively d) Nodal $EHLC_i$ for different wind speeds

Besides, we also sort the nodal risk indices $EELC_i$ and $EGLC_m$ from the biggest to the smallest, as shown in Fig. 8.8. The electric nodes with the top 50% of $EELC_i$ and the gas nodes with the top 30% of $EGLC_m$ are marked with node numbers. This is mainly because these nodes with larger demands are relatively far away from energy resources. Under this circumstance, the power is more difficult to be transported from generators to consumers under windstorms, considering the operating constraints of power systems. It can be noted that the increase in wind speeds has a relatively small impact on the ranking of nodal risk indices in both gas and power systems. For example, the electric nodes with the top three nodal $EELC_i$ in power systems are all nodes 21, 22, and 20. The findings can

help us improve the risk of MESs by hardening the electrical components at nodes with larger risk indices.

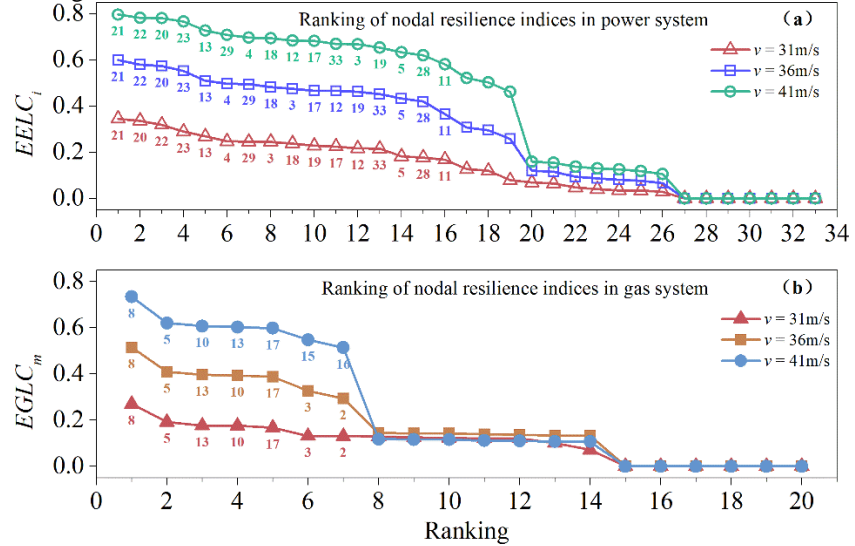


Fig. 8.8. Ranking of nodal risk indices for different wind speeds. a) Ranking of nodal $EELC_i$ b) Ranking of nodal $EGLC_m$

The system risk metrics of different energy carriers for different wind speeds are presented in Fig. 8.9. It can be clearly seen that the increase in wind speeds can significantly reduce the system risk of MESs. For storms with larger wind speeds, the expected energy load curtailments and the collapse ratios both increase significantly, whereas the recovery ratios tend to decrease. The values of $EGLC$ are 0.099, 0.234, and 0.368 for 31m/s, 36m/s, and 41m/s wind speeds, respectively, indicating that more gas loads will be interrupted for larger weather extent. When wind speeds v change from 31m/s to 41m/s, the values of CRG increase from 0.038 to 0.061, whereas the values of RRG decrease from 0.006 to 0.003. This means that the MESs will break down more rapidly in phase II and recover to normal operation more slowly in phase IV for higher wind speeds.

Regarding the comparison of system risk between different energy carriers, we can find that the losses of heat supply caused by windstorms are smaller than those of power supply and gas supply, indicating the heat system is relatively more resilient to windstorms than the other two systems. As shown in Fig. 8.9, there is 88.1% of heat loads supplied by MESs after the attacks of storms with 41m/s wind speed, whereas there are only 53.8% electricity loads and 39.2% gas loads connected after windstorms. Moreover, the values of CRH are much smaller than those of CRE and CRG for different wind speeds. This is mainly because the heat demands of MESs are simultaneously supplied by electricity and gas through EH. When the power system cannot supply sufficient electricity to the heat pump of EH for con-

tingency states, the gas system can increase gas injection to CHP units and the gas boiler of EH to satisfy heat demands.

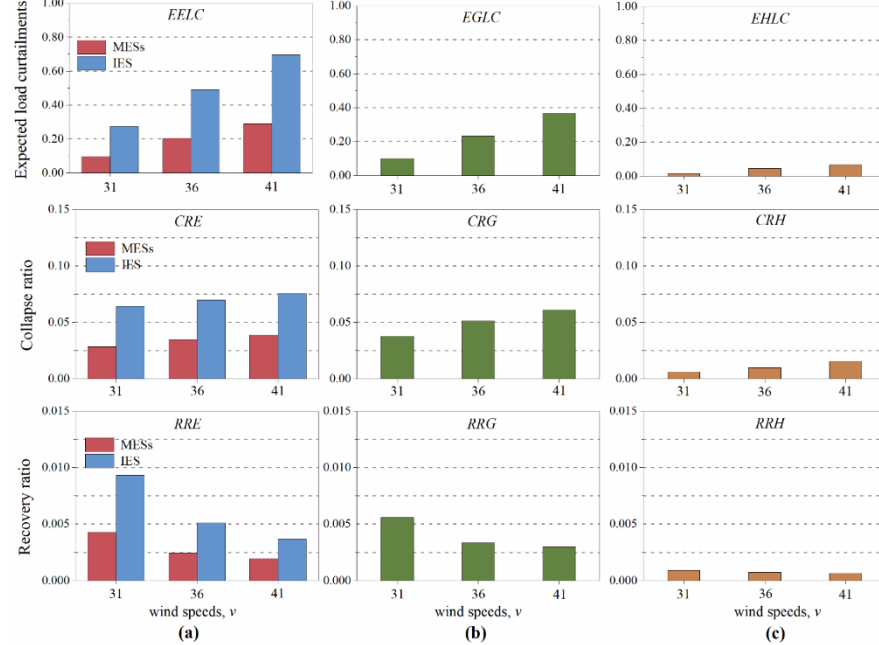


Fig. 8.9. Risk metrics of MESs for different wind speeds. a) Electric risk metrics. b) Gas risk metrics. c) Heat risk metrics

In this case, the system risks of MESs and isolated electric systems (IES) under different wind events are also compared. As seen in the subpicture (a) of Fig. 8.6, the power system in MESs is more resilient than IES under the same windstorms, which is shown in the expected energy losses, collapse ratios, and recovery ratios. The subpicture (a) of Fig. 8.9 illustrates the comparison of risk metrics between MESs and IES for different wind speeds. Firstly, windstorms can cause more electricity load losses in IES than those in MESs. For storms with 41m/s wind speed, the *EELC* in IES can reach 0.696, which is over two times that in MESs with the value of 0.289. Moreover, the MESs can better resist disruptive events in phase II and more quickly recover from a degraded state in phase IV compared to IES. For instance, the values of *CRE* in IES are nearly two times those in MESs for 31m/s, 36m/s, and 41m/s wind speeds. The main reason to account for this phenomenon is that the gas system can increase gas injection to CHP units of EH to satisfy the electric demands in MESs for contingency states.

To further show the impacts of energy interaction on the overall risk of MESs, the synthetic energy loss (*SEL*) of MESs is compared with that of isolated energy subsystems (IESS) for different wind speeds, as shown in Table 8.3. It can be noted that the energy interaction can improve the risk of MESs for smaller wind

speeds, since the *SEL* values of MESs and IESS are 0.0795 and 0.0934 for $v = 31$ m/s, respectively. In contrast, the risk of MESs can be reduced compared to IESS for larger wind speeds due to the interaction between different energy carriers. This is mainly because the EGSSs can obtain sufficient power supply in most time of phase I when MESs are hit by storms with small wind speeds. Under this circumstance, the gas system can provide adequate gas for EH to produce electricity and heat for MESs. Instead, for storms with larger wind speeds, the EGSSs may stop working due to inadequate power supply at the beginning of phase I. Due to the reduction of gas supply, the EH will correspondingly reduce the energy production for MESs.

Table 8.3 Comparison of *SEL* between MESs and IESS for different wind speeds

Test systems	$v = 31$ m/s	$v = 36$ m/s	$v = 41$ m/s
MESs	0.0795	0.1750	0.2781
IESS	0.0934	0.1667	0.2369

The computation time for the risk evaluation of MESs for different wind speeds is shown in Table 8.4 to show the efficiency of the proposed method. It can be noted that the average computation time of the optimal energy flow model ranges from 4s to 5s for all wind speeds. Nevertheless, the total computation time for obtaining the results increases a lot with the increase in wind speeds. This is mainly because the MESs can recover quickly to the normal operation level in phase III for smaller wind speeds. Under this circumstance, the average number to calculate the optimal power flow per sample is relatively small for 31m/s wind speeds.

Table 8.4 The computation time of risk evaluation for different wind speeds

Wind speeds	Average computation time of optimal energy flow model (s)	Average computation time per sample (s)	Total calculation time (s)
$v = 31$ m/s	4.61	35.40	43152.60
$v = 36$ m/s	4.67	49.33	66348.85
$v = 41$ m/s	4.58	66.78	80336.34

Case 2: Risk analysis of MESs under the impacts of region-scale windstorms

In order to model the region-scale windstorms, the windstorms are assumed to only hit one area of the test system in Fig. 8.5. On this basis, the initialization of wind speeds in different areas is given in Table 8.5. Firstly, it should be noted that $v = 20$ m/s corresponds to normal weather conditions with a 0.005 line failure probability. Therefore, the windstorms are assumed to only hit areas 1, 2, and 3 of MESs corresponding to scenarios A, B, and C, respectively. Moreover, there also exist region-scale windstorms whose wind speeds in different areas can differ. As shown in scenario D, the wind speeds of storms are therefore assumed as 41m/s, 31m/s, and 20m/s for areas 1, 2, and 3, respectively. Besides, the techniques to de-

termine the repair time TTR of damaged components and the duration of phase III are in accordance with those in case 1.

Table 8.5 Illustration of four scenarios with different regional wind speeds

Wind speeds (m/s)	Scenario A	Scenario B	Scenario C	Scenario D
v_1	41 m/s	20 m/s	20 m/s	41 m/s
v_2	20 m/s	41 m/s	20 m/s	31 m/s
v_3	20 m/s	20 m/s	41 m/s	20 m/s

The electricity, gas and heat supply levels considering the impacts of windstorms for different scenarios are given in Fig. 8.10. Similar to case 1, the shapes of the energy supply level curves recall the response curve of Fig. 8.1. On this basis, the risk metrics for different scenarios are given in Table. 8.6. Regarding electric systems, it can be noted that more electric losses are caused when windstorms hit area 3. The values of $EELC$ in MESs are 0.0391, 0.0402, 0.1163, and 0.0819 for scenarios A, B, C, and D, respectively. This is mainly because the DERs in area 3 account for nearly 50% of total generation capacity. Regarding natural gas systems, the simulation results of scenario A show that the windstorms can lead to more gas losses when windstorms hit area 1. The value of $EGNS$ is only 0.0543 for scenario C and increases to 0.1731 for scenario A. This is mainly because the electric-driven gas source W2 at node 8 accounts for over 50% production capacity in natural gas systems. The windstorms in area 3 can lead to the interruption of power supplied to W2. In accordance with case 1, there is only a small fraction of heat loss caused by windstorms for all scenarios in case 2.

Based on the simulation results in Table. 8.6, we can draw the conclusion that the risk in area 3 of MESs is the lowest considering the impacts of region-scale windstorms. Therefore, it is an effective measure to harden electrical components in area 3 for improving the risk of MESs.

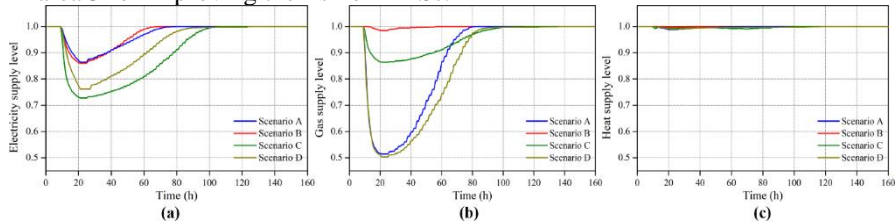


Fig. 8.10. Energy supply level of MESs as a function of time for different scenarios. a) Electricity supply level. b) Gas supply level. c) Heat supply level

Table 8.6 System risk metrics of MESs for different scenarios in case 2

Energy carriers	Risk metrics	Scenario A	Scenario B	Scenario C	Scenario D
Electricity	$EELC$	0.0391	0.0402	0.1163	0.0819
	CRE	0.0114	0.0115	0.0208	0.0202
	RRE	0.0018	0.0022	0.0027	0.0021
Gas	$EGLC$	0.1731	0.0024	0.0543	0.2009
	CRG	0.0369	0.0014	0.0109	0.0362

	<i>RRG</i>	0.0072	0.0002	0.0014	0.0046
Heat	<i>EHLC</i>	0.0023	0.0003	0.0036	0.0045
	<i>CRH</i>	0.0011	0.0002	0.0010	0.0010
	<i>RRH</i>	0.0002	0.0001	0.0002	0.0001

Case 3: Correlation analysis between risk and economy

In the previous cases, the risk of heat subsystems is improved at the cost of increased investment, since gas boilers, heat pumps, and CHPs are introduced to supply heat. In order to show the correlation between risk and cost, two scenarios are introduced with different components contained in EH. Scenario A is the base case with the largest cost, where the EH contains gas boilers, heat pumps, and CHP. In scenario B, only the CHP is introduced in EH to supply heat. In accordance with case 1, the risk of MESs in these two scenarios is evaluated under grid-scale windstorms with 31m/s, 36m/s, and 41m/s wind speeds. The techniques to determine the failure probability of components, the repair time *TTR* of damaged components, and the duration of phase III are identical to those in case 1.

The risk metrics of MESs are compared between two scenarios for different wind speeds, as shown in Table 8.7. It can be noted that the values of *EHLC* in scenario B are much larger than those in scenario A, indicating that the removal of gas boilers and heat pumps in EH can significantly reduce the risk of heat subsystems. The *EHLC* values in scenario B are 2.69, 5.76, and 6.01 times than those in scenario A for 31m/s, 35m/s, and 41m/s wind speeds, respectively. The findings reveal the inverse correlation between system risk and cost. Moreover, the removal of elements in EH has little effect on the risk of electric and gas systems, since the change of *EELC* and *EGLC* values are small from scenarios A to B. Furthermore, the values of *EELC* in scenario B are smaller than those of IES, whose risk metrics are given in Fig. 8.8. The results show that the CHP units can significantly improve the risk of power systems compared to gas boilers and heat pumps.

Table 8.7 System risk metrics of MESs for different scenarios and wind speeds

Risk metrics	$v = 31\text{m/s}$		$v = 35\text{m/s}$		$v = 41\text{m/s}$	
	Scenario	Scenario	Scenario	Scenario	Scenario	Scenario
		A		B		B
<i>EELC</i>	0.0960	0.0992	0.2040	0.2017	0.2895	0.2783
<i>EGLC</i>	0.0998	0.0933	0.2340	0.2342	0.3677	0.3420
<i>EHLC</i>	0.0061	0.0164	0.0102	0.0588	0.0159	0.0956

8.6 Conclusions

The growing frequency and extent of windstorm events entail the need to analyze the risk of multi-energy systems (MESs). This chapter proposes a comprehensive framework to evaluate the impacts of windstorms on the nodal risk of MESs. The multi-phase performance response curve is utilized to characterize the time-dependent performance levels of MESs at different phases, where the impacts of weather extent on component and system operation are modeled. Moreover, a service-based optimal energy flow model is proposed to assess the perfor-

mance losses of MESs under windstorms through coordination among different energy subsystems. Furthermore, nodal risk metrics for different energy subsystems are defined to quantitatively evaluate the risk of MESs.

Case studies demonstrate that the increase in weather extent can dramatically decrease the system risk indicators of MESs. Regarding the risk of energy subsystems, the heat system can be more resilient than the electric system and gas system since the heat demands are simultaneously supplied by electricity and gas through the energy hub (EH). Besides, due to the support of power supply from combined heat and power units of EH, the risk of the electric system in MESs can be highly improved compared to isolated electric systems. Under the impacts of region-scale windstorms, the values of risk indicators of area 3 in MESs are the smallest among all areas. Therefore, it is an effective measure to harden electrical components in area 3 for improving the risk of MESs. Moreover, the removal of gas boilers and heat pumps in EH can significantly reduce the risk of heat subsystems, revealing the inverse correlation between system risk and cost. The proposed model and method can provide system operators with a useful tool to analyze the risk of MESs under windstorms. Furthermore, the previous findings can effectively guide system operators to constitute targeted measures to enhance the risk of MESs.

In this study, it is assumed that the storms have constant wind speeds in one region without considering the varying weather conditions over time. When considering the temporal wind speeds, the failure probability of components can change with time, which is not considered in this study. Nevertheless, the multi-phase simulation framework in this chapter can be applied to the risk of MESs under varying weather conditions, if the time series of wind speeds are determined. In specific, the failure probability of electric components at different time steps can be calculated according to the time series of wind speeds using the failure models in (4)-(6). By sampling component failures using the Monte-Carlo simulation technique, the risk of MESs under windstorms can be evaluated using the proposed multi-phase framework. Concerning the determination of the time series of weather conditions, several methods can be utilized, including statistical analysis methods [34] and projection models [16]. In future work, the analysis framework in this chapter can be expanded to evaluate the risk of MESs under various weather conditions.

References

- [1] X. Jin, Y. Mu, H. Jia, J. Wu, X. Xu, and X. Yu, "Optimal day-ahead scheduling of integrated urban energy systems," *Applied energy*, vol. 180, pp. 1-13, 2016.
- [2] P. Gabrielli, M. Gazzani, E. Martelli, and M. Mazzotti, "Optimal design of multi-energy systems with seasonal storage," *Applied Energy*, vol. 219, pp. 408-424, 2018.

- [3] T. Ma, J. Wu, L. Hao, W.-J. Lee, H. Yan, and D. Li, "The optimal structure planning and energy management strategies of smart multi energy systems," *Energy*, vol. 160, pp. 122-141, 2018.
- [4] M. Panteli and P. Mancarella, "Modeling and evaluating the resilience of critical electrical power infrastructure to extreme weather events," *IEEE Systems Journal*, vol. 11, pp. 1733-1742, 2015.
- [5] I. Abdin, Y.-P. Fang, and E. Zio, "A modeling and optimization framework for power systems design with operational flexibility and resilience against extreme heat waves and drought events," *Renewable and Sustainable Energy Reviews*, vol. 112, pp. 706-719, 2019.
- [6] Y. Lin and Z. Bie, "Study on the resilience of the integrated energy system," *Energy Procedia*, vol. 103, pp. 171-176, 2016.
- [7] *The Natural Gas Grid Needs Better Monitoring. [online]*. Available: <https://issues.org/the-natural-gas-grid-needs-better-monitoring/>
- [8] H. Liu, R. A. Davidson, and T. V. Apanasovich, "Statistical forecasting of electric power restoration times in hurricanes and ice storms," *IEEE Transactions on Power Systems*, vol. 22, pp. 2270-2279, 2007.
- [9] R. Nateghi, S. D. Guikema, and S. M. Quiring, "Comparison and validation of statistical methods for predicting power outage durations in the event of hurricanes," *Risk Analysis: An International Journal*, vol. 31, pp. 1897-1906, 2011.
- [10] M. Ouyang, L. Dueñas-Osorio, and X. Min, "A three-stage resilience analysis framework for urban infrastructure systems," *Structural safety*, vol. 36, pp. 23-31, 2012.
- [11] M. Panteli, C. Pickering, S. Wilkinson, R. Dawson, and P. Mancarella, "Power system resilience to extreme weather: fragility modeling, probabilistic impact assessment, and adaptation measures," *IEEE Transactions on Power Systems*, vol. 32, pp. 3747-3757, 2016.
- [12] F. Cadini, G. L. Agliardi, and E. Zio, "A modeling and simulation framework for the reliability/availability assessment of a power transmission grid subject to cascading failures under extreme weather conditions," *Applied energy*, vol. 185, pp. 267-279, 2017.
- [13] G. P. Cimellaro, O. Villa, and M. Bruneau, "Resilience-based design of natural gas distribution networks," *Journal of Infrastructure systems*, vol. 21, p. 05014005, 2014.
- [14] M. Panteli, P. Mancarella, D. N. Trakas, E. Kyriakides, and N. D. Hatziargyriou, "Metrics and quantification of operational and infrastructure resilience in power systems," *IEEE Transactions on Power Systems*, vol. 32, pp. 4732-4742, 2017.
- [15] M. Ouyang and L. Dueñas-Osorio, "Time-dependent resilience assessment and improvement of urban infrastructure systems," *Chaos: An Interdisciplinary Journal of Nonlinear Science*, vol. 22, p. 033122, 2012.

- [16] M. Ouyang and L. Duenas-Osorio, "Multi-dimensional hurricane resilience assessment of electric power systems," *Structural Safety*, vol. 48, pp. 15-24, 2014.
- [17] R. Francis and B. Bekera, "A metric and frameworks for resilience analysis of engineered and infrastructure systems," *Reliability Engineering & System Safety*, vol. 121, pp. 90-103, 2014.
- [18] M. Bao, Y. Ding, C. Singh, and C. Shao, "A multi-state model for reliability assessment of integrated gas and power systems utilizing universal generating function techniques," *IEEE Transactions on Smart Grid*, vol. 10, pp. 6271-6283, 2019.
- [19] H. Zhang, L. Cheng, S. Yao, T. Zhao, and P. Wang, "Spatial-temporal Reliability and Damage Assessment of Transmission Networks under Hurricanes," *IEEE Transactions on Smart Grid*, 2019.
- [20] W. Sheng, D. Yi, Y. Chengjin, W. Can, and M. Yuchang, "Reliability evaluation of integrated electricity–gas system utilizing network equivalent and integrated optimal power flow techniques," *Journal of Modern Power Systems and Clean Energy*, vol. 7, pp. 1523-1535, 2019.
- [21] J. Lu, J. Guo, Z. Jian, Y. Yang, and W. Tang, "Resilience Assessment and Its Enhancement in Tackling Adverse Impact of Ice Disasters for Power Transmission Systems," *Energies*, vol. 11, p. 2272, 2018.
- [22] S. Hosseini, K. Barker, and J. E. Ramirez-Marquez, "A review of definitions and measures of system resilience," *Reliability Engineering & System Safety*, vol. 145, pp. 47-61, 2016.
- [23] A. F. Mensah, "Resilience assessment of electric grids and distributed wind generation under hurricane hazards," 2015.
- [24] A. Mehrtash, P. Wang, and L. Goel, "Reliability evaluation of power systems considering restructuring and renewable generators," *IEEE Transactions on Power Systems*, vol. 27, pp. 243-250, 2012.
- [25] *Natural gas generators make up the largest share of overall U.S. generation capacity*. [online]. Available: <https://www.eia.gov/todayinenergy/detail.php?id=30872>
- [26] *Gas power*. [online]. Available: https://www.statkraft.com/globalassets/old-contains-the-old-folder-structure/documents/gas-09-eng_tcm9-4573.pdf
- [27] B. Morvaj, R. Evins, and J. Carmeliet, "Optimization framework for distributed energy systems with integrated electrical grid constraints," *Applied energy*, vol. 171, pp. 296-313, 2016.
- [28] A. Martinez-Mares and C. R. Fuerte-Esquivel, "A unified gas and power flow analysis in natural gas and electricity coupled networks," *IEEE Transactions on Power Systems*, vol. 27, pp. 2156-2166, 2012.
- [29] H. Jia, Y. Ding, Y. Song, C. Singh, and M. Li, "Operating reliability evaluation of power systems considering flexible reserve provider in demand side," *IEEE Transactions on Smart Grid*, vol. 10, pp. 3452-3464, 2018.

- [30] C. M. Correa-Posada and P. Sanchez-Martin, "Integrated power and natural gas model for energy adequacy in short-term operation," *IEEE Transactions on Power Systems*, vol. 30, pp. 3347-3355, 2014.
- [31] Y. Zhou, C. Gu, H. Wu, and Y. Song, "An equivalent model of gas networks for dynamic analysis of gas-electricity systems," *IEEE Transactions on Power Systems*, vol. 32, pp. 4255-4264, 2017.
- [32] D. De Wolf and Y. Smeers, "The gas transmission problem solved by an extension of the simplex algorithm," *Management Science*, vol. 46, pp. 1454-1465, 2000.
- [33] G. Chicco and P. Mancarella, "Matrix modelling of small-scale trigeneration systems and application to operational optimization," *Energy*, vol. 34, pp. 261-273, 2009.
- [34] M. Bao, Y. Ding, C. Shao, Y. Yang, and P. Wang, "Nodal Reliability Evaluation of Interdependent Gas and Power Systems Considering Cascading Effects," *IEEE Transactions on Smart Grid*, 2020.
- [35] A. Perera, V. M. Nik, D. Chen, J.-L. Scartezzini, and T. Hong, "Quantifying the impacts of climate change and extreme climate events on energy systems," *Nature Energy*, pp. 1-10, 2020.

9 Long-term Reserve Expansion of Integrated Electricity and Gas Systems for Risk Mitigation

9.1 Introduction

The previous chapters have analyzed the short-term risk evaluation and operational risk assessment for multi-energy systems. This chapter proposes a long-term reserve expansion scheme for the MES's risk mitigation. As discussed, the ever-increasing utilization of GPPs strengthens the coupling relationship between natural gas systems (NGS) and electric power systems (EPS), bringing new reliability problems to integrated electricity-gas systems (IEGSs) [1]. In specific, different from coal-fired power plants whose fuel supply is traditionally considered sufficient, the power output of GPPs relies on gas supply from NGS. Random failures occurring in NGS may cause the interruption of gas supplied to GPPs, leading to the shortage of generating capacity and finally jeopardizing power system security [2]. Such failure amplification process from NGS to EPS through coupled components can be defined as cross-sectorial failure propagation [3]. When considering the failure propagation from NGS to EPS, small disturbances may propagate to the whole system and further engender widespread damage. The catastrophic outages in Texas, America on 15th February 2021 can be served as a demonstration of cross-sectorial failure propagation [4].

In recent years, the failure propagation issues have gained increasing attention in both industry and academic sectors. In [5] and [6], an integrated simulation framework is proposed to simulate the bi-directional cascading failure propagation in IEGSs. Reference [7] evaluates the vulnerability of IEGSs by combining the cascading failure simulation and a machine learning method. A graph theory-based method is proposed in [8] to assess the impacts of failure propagation on network robustness. In [9], a non-sequential Monte Carlo simulation framework is proposed to analyze the reliability of IEGSs considering failure propagation. The previous works mainly focus on failure propagation simulation [5, 6] and reliability/ robustness analysis [7-9]. However, the countermeasures to guarantee the reliability level of IEGSs under failure propagation are seldom investigated.

As an effective measure to improve the reliability of IEGSs, the long-term reserve expansion aims to determine the deployment of different energy production components, such as power plants, to fulfill the energy consumption of consumers [10]. Reasonable reserve planning results can provide system operators with sufficient standby resources to deal with demand growth or component failures. Considering that, several studies have been carried out on the reserve expansion of IEGSs by allocating new components. A bi-level multi-stage programming model is proposed in [11] considering the bi-directional energy conversion between the power system and NGS. In [12], a two-stage stochastic optimization model is developed to realize the trade-offs between constructing gas pipelines, GPPs, and other units. Reference [13] proposes a dynamic stochastic joint expansion planning of IEGSs considering long-term uncertainties of gas prices. The authors in

[14] propose a bi-level model to allocate the gas storage and uncertain wind farms considering the temporal correlation of wind power. A multi-period framework is proposed in [15] to determine the optimal generation, transmission and gas network expansions. However, the system reliability issues, especially the impacts of component failures on system operation, are seldom considered in the system expansion of the previous studies.

Motivated by the catastrophic outages in Texas attributed to insufficient reserve capacity, the security and reliability issues are essential in the reserve planning of IEGSs for reliable energy delivery. To model the random component failures, the N-1 criterion is widely used in combined energy system planning as a deterministic approach [16, 17]. Nevertheless, the N-1 standard can only ensure the reliable operation of IEGSs under a single component outage, whereas neglecting the simultaneous failures of multiple components. Alternatively, the probabilistic reliability indices, e.g. loss of load probability (LOLP) and expected energy not supplied are considered in [2] and [18]. The existing reliability indices of different energy subsystems are individually formulated considering their autogenic uncertainties, such as gas/electric load variation and electric component failure [18-20]. However, the gas component failures and the corresponding failure propagation, on reliability indices of power systems are seldom considered, which may make the long-term reserve expansion results unreasonable. To address this, the multifactor-influenced reliability indices are proposed in this chapter considering the synthetic effects of autogenic and external uncertainties, including cross-sectorial failure propagation, and uncertainties of components and loads. On this basis, a synthetic reserve expansion model is developed to coordinate the planning of energy production components in IEGSs, while guaranteeing the reliability of both subsystems.

Considering the superposed influence of multiple uncertainties, the system contingency states for the calculation of reliability indices can be enormous which requires high computation resources [21]. Under this circumstance, the traditional planning model that considers all system states may not be applicable due to high computation complexity. In order to address that, clustering methods are required to aggregate adjacent system states of IEGSs to decrease the computation burden. As a typical clustering method, the fuzzy set theory can effectively characterize the performance behavior of system states in one cluster (set) instead of using a single crisp number. The degree of different system states that belong to the same set is measured by a membership function, based on which the features of the clustered set can be described in detail [22]. The fuzzy set theory proved as an effective measure for the reliability analysis [23] and operation optimization [24] of energy systems.

Due to its effectiveness and advantage in dealing with data clustering, the fuzzy set theory is introduced and combined with traditional methods, e.g. Monte-Carlo simulation (MCS) technique, to achieve great computational improvement [16]. In specific, based on the component failure states sampled by the MCS technique, the fuzzy theory is applied to aggregate adjacent states into one cluster. In each cluster,

the system failure degree is represented by a fuzzy parameter, which is a set of possible values and each value has its own membership. Similarly, the 8760-hour load curve can also be combined with fuzzy set theory to represent a set of aggregate load values using fuzzy representation. On this basis, the number of system contingency states can be significantly reduced. Accordingly, the reserve expansion model is formulated as a fuzzy optimization problem.

In this chapter, a multifactor-influenced reliability-constrained reserve expansion is proposed to reduce the adverse effects of failure propagation on IEGSs. Compared with previous studies, the innovative contributions are summarized as:

(1) By analytically expressing the contribution of failure propagation on system reliability, the novel multifactor-influenced reliability indices are defined considering the autogenic and external uncertainties. The reliability-constrained expansion model is then developed to guarantee the long-term adequacy of IEGSs.

(2) This chapter firstly combines the fuzzy set theory and MCS technique to decrease system states for computation efficiency improvement. Based on the defined measurement of system failure degree, the fuzzy method is utilized to aggregate the discrete generation failure states into one cluster.

(3) This chapter proposes an efficient algorithm to solve the developed fuzzy reserve expansion model. Optimism parameters are introduced to deal with fuzzy numbers considering the risk propensity of system planners. The decomposition technique is applied to decompose the proposed decision problem into a master problem and two correlated reliability subproblems, where the multifactor-influenced reliability indices can be effectively calculated considering failure propagation.

This chapter includes research related to the long-term reserve expansion of IEGSs for risk mitigation by [25].

9.2 The relationship between long-term reserve planning and failure propagation

9.2.1 Impacts of cross-sectorial failure propagation on long-term reserve planning of IEGSs

Cross-sectorial failure propagation can be defined as the complicated sequences of dependent events triggered by disruptive events. Due to the coupling relationship between two systems, the random failures occurring in NGS may propagate to EPS through coupled components, i.e. GPPs. The detailed cross-sectorial failure propagation mainly includes the following steps [26].

Step 1) Initial disturbance in NGS: The initial component failures triggered by various disturbances may make the NGS change its operation state.

Step 2) Gas load curtailments: Due to the initial disturbance, several measures may be adopted for the reliable operation of NGS, such as gas production adjustment or gas load curtailments. Due to the interruptible contracts signed between generation units and gas companies, the gas supply of GPPs will be firstly curtailed if the gas production cannot satisfy gas loads [27].

Step 3) Power output reduction GPPs: The gas load curtailments may result in the interruption of the gas supply of GPPs. Considering that, the GPPs have to reduce their output due to insufficient gas supply.

Step 4) Electric load curtailments: Due to the reduction of power output, all the available power plants and loads will be re-dispatched to eliminate the power imbalance. If the adjusting of generating output cannot realize power balance, the electric load shedding will be utilized.

Based on the failure propagation process, we can conclude that the random failures occurring in NGS can simultaneously affect the reliability of NGS and EPS, leading to the increasing requirement for power capacity. Accordingly, it is essential to develop an integrated framework for the synergetic planning of gas and power production capacity.

Note that failure propagation is a result of the adjustment/dispatch decisions after the failure occurs, which can be naturally embedded in the optimization model. However, in the previous studies about system planning, the components in gas systems are assumed completely available and the gas-fired power plants can obtain sufficient fuel supply [2, 18]. Hence, the gas component failures and the corresponding failure propagation from gas system to power system are seldom modeled in the previous planning models.

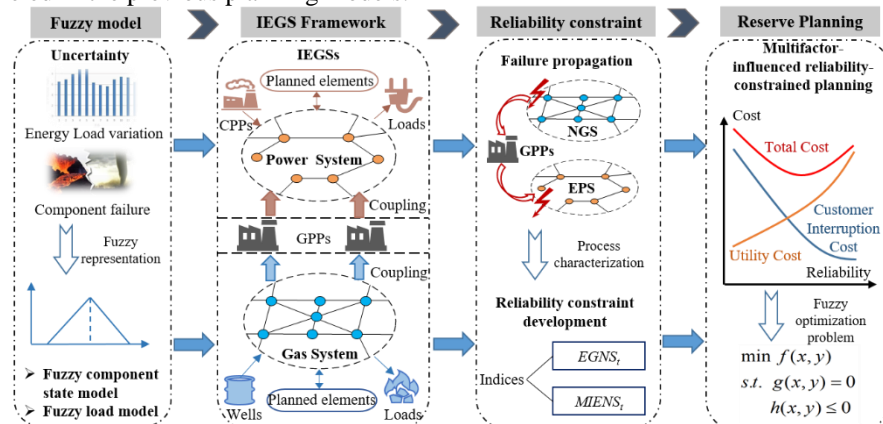


Fig. 9.1. The outline of this chapter to determine long-term reserve expansion

9.2.2 The outline of this chapter to determine long-term reserve

The outline to determine the long-term reserve of IEGSs is illustrated in Fig. 9.1. Firstly, the MCS technique and fuzzy set theory are combined to aggregate adjacent system states into one cluster represented by a fuzzy number. Similarly, the fuzzy set theory is combined with the LDC model to achieve load representation with fewer load states. According to the fuzzy models of energy loads and component failures, multifactor-influenced reliability indices are formulated, where the cross-sectorial failure propagation is considered. Moreover, the reliability-constrained reserve expansion model is developed to determine the construction of power units, gas suppliers, and power-to-gas (P2G) units. In specific, the proposed

model is to minimize the total system costs, including investment costs, operation costs, and load interruption costs. Finally, an efficient algorithm to solve the proposed fuzzy models by introducing optimism parameters and benders decomposition.

9.3 Fuzzy models to characterize load and generation uncertainties

9.3.1 Fuzzy component operation state curve to characterize generation uncertainties

Considering the failures and maintenance of components in IEGSSs, the component operation states in each year can be numerous. Taking EPS as an example, the sequential operation curves of units in one year can be obtained according to their failure and repair rates utilizing the MCS technique [28]. However, the discrete generation operation states, i.e. 1 and 0, cannot be directly clustered using fuzzy set theory since the quantification of failure degree is missing. Considering that, the measurement, i.e. available generating capacity is proposed to quantify the failure degree of power systems in different states. By aggregating the sampled unit operation states in Fig. 9.2, the 8760-hour generating capacity curve of EPS can be determined.

$$\mathbf{GC}_t^0 = [GC_{t1}^0, L, GC_{ts}^0, L, GC_{t8760}^0] \quad (9.1)$$

where GC_{ts}^0 represents the system available generating capacity at hour s and year t .

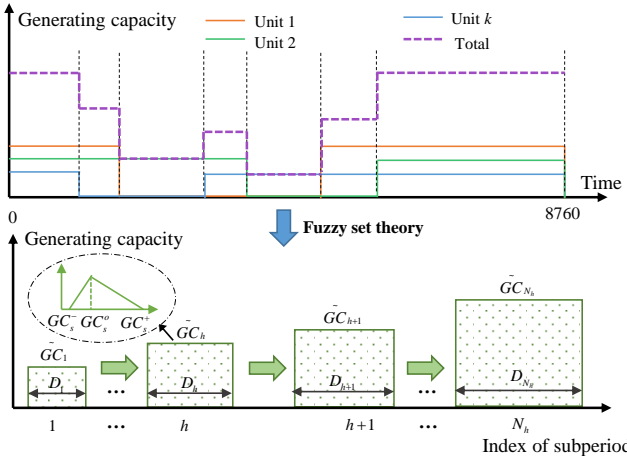


Fig. 9.2. Description of fuzzy component state curve model

The corresponding 8760-hour operation state curve of different units O_t^0 can be expressed as:

$$\mathbf{O}_t^0 = [O_{t1}^0, L, O_{ts}^0, L, O_{t8760}^0], \text{ where } \mathbf{O}_{ts}^0 = [O_{ts}^0, L, O_{kts}^0] \quad (9.2)$$

Through the clustering technique, the 8760 hourly generating capacity curve \mathbf{GC}_t^0 can be divided into N_s clusters. The N_s clusters can be expressed as (9.3), where each cluster \mathbf{GC}_{ts} represents multiple hourly generating capacities.

$$\mathbf{GC}_t = [\mathbf{GC}_{tL}, \mathbf{GC}_{ts}, \mathbf{GC}_{tN_s}] \quad (9.3)$$

In the clustering process, the within-cluster sum of squares (WCSS) is minimized [29]. The WCSS can be expressed as:

$$\Omega = \arg \min_{\mathbf{GC}_t} \sum_{s=1}^{N_s} \sum_{\mathbf{GC}_{ts}^0 \in \mathbf{GC}_s} \|\mathbf{GC}_{ts}^0 - \kappa_s\| \quad (9.4)$$

where κ_s is the mean value of hourly generating capacity in cluster s . Then the clustered unit operation state curve can be expressed as:

$$\mathbf{O}_t = [\mathbf{O}_{tL}, \mathbf{O}_{ts}, \mathbf{O}_{tN_s}] \quad (9.5)$$

As shown in Fig. 9.2, the annual generating capacity curve is divided into N_s subperiods, where each subperiod can represent a generating capacity cluster. The duration of subperiod s can be represented as:

$$\mathbf{D}^{FE} = [D_1^{FE}, L, D_s^{FE}, L, D_{N_s}^{FE}] \quad (9.6)$$

For conventional probability theory, the performance rate of cluster s is usually represented by a certain value, e.g. the mean value of load levels in this cluster. However, a single crisp value may not effectively describe the detailed features of the load cluster. Considering that, the fuzzy set theory is then introduced to represent each generating capacity cluster using a triangular membership function, as illustrated in Fig. 9.2. The fuzzy representation of the performance rate of cluster s is $\mathbf{GC}_{ts} \in \dot{\mathbf{GC}}_{ts} = (GC_{ts}^-, GC_{ts}^0, GC_{ts}^+)$, where the most possible membership GC_{ts}^0 corresponds to the mean value of generating capacity in cluster s , i.e. κ_s . GC_{ts}^- and GC_{ts}^+ denote the smallest and the largest values of possible generating capacity in cluster s , respectively. Accordingly, the fuzzy operating state of unit k in cluster s can be expressed as $O_{kts} \in \dot{O}_{kts} = (O_{kts}^-, O_{kts}^0, O_{kts}^+)$, where O_{kts}^- , O_{kts}^0 and O_{kts}^+ represent the unit operating states when generating capacities are GC_{ts}^- , GC_{ts}^0 and GC_{ts}^+ , respectively. The triangular membership function can be represented as:

$$\Psi(GC_{ts}) = \begin{cases} 0, & GC_{ts} \leq GC_{ts}^- \\ \left(GC_{ts} - GC_{ts}^- \right) / \left(GC_{ts}^0 - GC_{ts}^- \right), & GC_{ts}^- < GC_{ts} \leq GC_{ts}^0 \\ \left(GC_{ts}^+ - GC_{ts} \right) / \left(GC_{ts}^+ - GC_{ts}^0 \right), & GC_{ts}^0 < GC_{ts} \leq GC_{ts}^+ \\ 0, & GC_{ts} \geq GC_{ts}^+ \end{cases} \quad (9.7)$$

The values of membership $\Psi(GC_{ts})$ are between 0 and 1, which can represent the weight of GC_{ts} in cluster s . By representing the cluster s as a fuzzy value

\dot{GC}_{ts} , the degree of different generation capacity states GC_{ts} that belong to cluster s can be determined by the membership function, based on which the features of generation capacity can be described in detail. Besides, the probability of cluster s can be determined by the duration of this cluster, which can be calculated as $\Pr\left(\dot{GC}_{ts}\right) = D_s^{FE} / \sum_{s=1}^{N_s} D_s^{FE}$. Note that in accordance with the conventional probability theory, the performance characteristics of load cluster s can also be described using the probabilities $\Pr\left(\dot{GC}_{ts}\right)$ and performance rates \dot{GC}_{ts} of this cluster. Due to the advantage in state aggregation and cluster representation, the fuzzy set theory has proven an effective method in the reliability analysis of energy systems [22].

Likewise, the fuzzy operation state curves of gas wells in NGS can be determined by the combination of MCS and fuzzy set theory. In specific, the fuzzy representation of production capacity in subperiod s is $\dot{PC}_{ts} = (PC_{ts}^-, PC_{ts}^0, PC_{ts}^+)$. The corresponding fuzzy operating states of gas well w in subperiod s is $\dot{O}_{wts} = (O_{wts}^-, O_{wts}^0, O_{wts}^+)$ with duration time D_s^{FG} .

9.3.2 Fuzzy load duration curve model to characterize load uncertainties

Considering the stochastic fluctuation of energy demands, the 8760-hour load curve is transformed into the fuzzy load duration curve (FLDC) model in this chapter. The procedures to determine the fuzzy models of energy loads are in accordance with those of component state aggregation. Taking electric load as an example, the annual load curve before clustering is represented as:

$$\dot{PD}_t^0 = [PD_{t1}^0, L, PD_{t\zeta}^0, L, PD_{t8760}^0] \quad (9.8)$$

where $PD_{t\zeta}^0$ represents the electric load at hour ζ and year t .

Similarly, the clustering technique is introduced to divide 8760 hourly loads \dot{PD}_t^0 into N_h clusters, as expressed in (9.9).

$$\dot{PD}_t = [\dot{PD}_{th}, L, \dot{PD}_{th}, L, \dot{PD}_{tN_h}] \quad (9.9)$$

The corresponding duration of cluster h determined by the size of the corresponding cluster, as shown in (9.10).

$$\dot{D}^E = [D_1^E, L, D_h^E, L, D_{N_h}^E] \quad (9.10)$$

By means of fuzzy set theory, the fuzzy representation of cluster h is $\dot{PD}_{th} = (PD_{th}^-, PD_{th}^0, PD_{th}^+)$, where PD_{th}^0 , PD_{th}^- and PD_{th}^+ denote the mean, the smallest, and the largest values of hourly loads in cluster h , respectively.

Likewise, the annual gas loads in NGS can be transformed into the FLDC model. The fuzzy representation of gas load cluster h is

$\dot{GD}_{th} = (GD_{th}^-, GD_{th}^0, GD_{th}^+)$ with duration time D_h^G . Compared to the annual load duration curve model which is usually approximated as a limited number of states, the FLDC model can make load presentation more accurate [30].

9.4 Reserve expansion model considering multifactor-influenced reliability constraints

9.4.1 Objective function

The proposed long-term reserve expansion model is to minimize the total costs of IEGSs on the planning horizon. The objective function (9.11) includes energy asset investments IC , the operation costs OC of IEGSs, and the costs of unserved energy. Equation (9.12) calculates the investment costs of new power plants and Gas suppliers. Equation (9.13) represents the operation costs of non-gas thermal units and new power plants in EPS, gas wells, and new Gas suppliers in NGS. The costs of unserved energy are determined by multiplying the energy load curtailments and load shedding costs. The $1/(1+d)^{t-1}$ denotes the present-worth value, where d is the discount rate and t is the planning year. The system state b can be obtained by combining the load uncertainties and component failures.

$$\min TC = IC + OC + \sum_t \frac{MIENS_t \cdot C_t^E + EGNS_t \cdot C_t^G}{(1+d)^{t-1}} \quad (9.11)$$

$$IC = \sum_t \sum_{e \in CS} \frac{C_{et}}{(1+d)^{t-1}} P_{et}^{\max} (z_{et} - z_{e(t-1)}) \quad (9.12)$$

$$+ \sum_t \sum_{g \in CG} \frac{C_{gt}}{(1+d)^{t-1}} W_{gt}^{\max} (z_{gt} - z_{g(t-1)})$$

$$+ \sum_t \sum_{\chi \in PG} \frac{C_{\chi t}}{(1+d)^{t-1}} W_{\chi t}^{\max} (z_{\chi t} - z_{\chi(t-1)})$$

$$OC = \sum_t \sum_b \frac{1}{(1+d)^{t-1}} \cdot \left(\sum_{k \in EG} C_k \cdot P_{kitb} + \sum_{e \in CS} C_e \cdot P_{etb} \right) \cdot D_{tb}^E \quad (9.13)$$

$$+ \sum_t \sum_b \frac{1}{(1+d)^{t-1}} \cdot \left(\sum_{w \in EW} C_w \cdot W_{w tb} + \sum_{g \in CG} C_g \cdot W_{gtb} \right) \cdot D_{tb}^G$$

where $MIENS_t$ and $EGNS_t$ represent the expected electric and gas load curtailments at year t , respectively. C_t^E and C_t^G are the shedding costs for power loads and gas loads. P_{et}^{\max} and C_{et} are the generating capacity of candidate unit e and the investment costs, respectively. W_{gt}^{\max} and C_{gt} are the production capacity of candidate gas suppliers g and the investment costs, respectively. $W_{\chi t}^{\max}$ and $C_{\chi t}$ are the

capacity of P2G facility χ and the investment costs, respectively. $z_{\chi t}$, z_{et} , and z_{gt} denote the construction state of candidate P2G facility χ , power unit e , and gas supplier g , respectively. P_{gtb} and P_{etb} denote the output of power unit g and candidate unit e for system state b at year t . W_{wbt} and W_{ktb} denote the gas production of gas well w and candidate gas supplier k for system state b at year t . C_g and C_e represent generation costs of power unit g and candidate unit e , respectively. C_w and C_k are gas production costs of gas well w and candidate gas supplier k , respectively.

Note that the basic planning thing of the proposed model is power unit e , gas supplier g , and P2G facility χ , whose construction states are represented as z_{et} , z_{gt} , and $z_{\chi t}$, and sizes are represented as P_{et}^{\max} , W_{gt}^{\max} , and $W_{\chi t}^{\max}$.

9.4.2 Multifactor-influenced reliability constraints considering failure propagation

1) Comparison between multifactor-influenced reliability indices and traditional indices

In the previous studies, the reliability indices of different energy subsystems are individually formulated considering their autogenic uncertainties, such as load variation and component failure [31]. For example, the electric not supplied (*EENS*) is a traditional reliability index that can be calculated by the probability-weighted sum of electric load curtailments for different contingency states b .

$$EENS = \sum_b \Pr_b(x^e, y^e) \cdot LC_b(x^e, y^e) \cdot 8760 \quad (9.14)$$

where $\Pr_b(x^e, y^e)$ and $LC_b(x^e, y^e)$ represent the probability and electric load curtailments of state b . x^e and y^e denote the electric load variation factor and electric component failure factor in power systems.

In this chapter, besides autogenic uncertainties, the effects of failure propagation on system reliability indices are quantified. Following the formulation process of traditional reliability indices, the multifactor-influenced expected electric not supplied (*MENS*) is proposed considering the synthetic effects of failure propagation, load uncertainties, and component failures.

$$MENS = \sum_b \Pr_b(x^e, y^e | z^g) \cdot \Pr_b(z^g) \cdot \\ [LC_b(x^e, y^e) + LC_b(z^g)] \cdot 8760 \quad (9.15)$$

where $\Pr_b(x^e, y^e | z^g)$ represents the conditional probability of electric load variation x^e and electric component failures y^e for certain conditions that failures propagate from the gas system z^g . $\Pr_b(z^g)$ is the probability of failure propagation.

tion from the gas system to the power system. $LC_b(z^s)$ denotes the electric load curtailments caused by the failure propagation factor z^s .

Compared to the traditional reliability index $EENS$, the proposed reliability index $MIENS$ can more accurately quantify the reliability levels of IEGSs and further guide reasonable planning results.

2) Reliability index formulation in IEGSs

Considering the failure propagation process, the reliability indices of NGS and power systems are developed in sequence. Since the reliability level of NGS is mainly affected by gas load variation and gas well failures, the reliability index is formulated according to the formulation process in (9.14). Hence, the expected gas not supplied ($EGNS$) can be calculated based on gas load curtailments in state b .

$$EGNS_t = \sum_m \sum_b \Pr\left(\dot{GD}_{th}, \dot{O}_{wts}\right) \cdot GLC_{mtb}\left(\dot{GD}_{th}, \dot{O}_{wts}\right) \cdot 8760 \quad (9.16)$$

where $\Pr\left(\dot{GD}_{th}, \dot{O}_{wts}\right)$ represents the probability of gas load curtailment $GLC_{mtb}\left(\dot{GD}_{th}, \dot{O}_{wts}\right)$ at node m in state b and year t , which can be calculated by aggregating the fuzzy load states \dot{GD}_{th} and gas well states \dot{O}_{wts} . Hence, $EGNS_t$ can be represented as:

$$EGNS_t = \sum_m \sum_b \frac{D_s^{FG}}{\sum_{s=1}^{N_s} D_s^{FG}} \cdot \frac{D_h^G}{\sum_{h=1}^{N_h} D_h^G} \cdot GLC_{mtb}\left(\dot{GD}_{th}, \dot{O}_{wts}\right) \cdot 8760 \quad (9.17)$$

The reliability of EPS is simultaneously influenced by electric load variation, unit outages, and failure propagation from gas systems. According to (9.15), the reliability index of power systems at year t can be represented as:

$$\begin{aligned} MIENS_t = & \sum_m \sum_b \Pr_b\left(\dot{PD}_{th}, \dot{O}_{kts} | GLC_{mtb}\right) \cdot \Pr_b(GLC_{mtb}) \cdot \\ & \left[ELC_b\left(\dot{PD}_{th}, \dot{O}_{kts}\right) + ELC_b(GLC_{mtb}) \right] \cdot 8760 \end{aligned} \quad (9.18)$$

It should be noted that the failure probabilities of uncertainties in power systems and gas load curtailments are independent. Therefore, the failure probability of electric load curtailments in (9.18) can be represented as the product of $\Pr_b\left(\dot{PD}_{th}, \dot{O}_{kts}\right)$ and $\Pr_b(GLC_{mtb})$.

By aggregating the fuzzy representations of load variation, unit failures, and gas load curtailment states, the $MIENS_t$ can be represented as:

$$MIENS_t = \sum_i \sum_b \frac{D_s^{FG} \cdot D_h^G}{\sum_{s=1}^{N_s} D_s^{FG} \cdot \sum_{h=1}^{N_h} D_h^G} \cdot \frac{D_s^{FE} \cdot D_h^E}{\sum_{s=1}^{N_s} D_s^{FE} \cdot \sum_{h=1}^{N_h} D_h^E} \cdot \left[ELC_b \left(\begin{array}{c} \vdots \\ PD_{tb}, O_{kts} \end{array} \right) + ELC_b \left(GLC_{mtb} \right) \right] \cdot 8760 \quad (9.19)$$

Compared to the general reliability indices in (9.15), it can be found that the load and generation uncertainties in (9.19) are represented as fuzzy numbers.

On this basis, the annual reliability indices are limited as:

$$EGNS_t \leq EGNS^{\text{limit}} \quad (9.20)$$

$$MIENS_t \leq MIENS^{\text{limit}} \quad (9.21)$$

where $EGNS^{\text{limit}}$ and $MIENS^{\text{limit}}$ represent the limits of reliability indices in NGS and EPS, respectively.

9.4.3 State and construction constraints

If the candidate device is installed in IEGSs, its construction state will be set as 1 in the following years. Hence, the construction states of candidate power unit k , gas supplier g , and P2G facility χ are restricted by:

$$z_{e(t-1)} \leq z_{et} \quad (9.22)$$

$$z_{g(t-1)} \leq z_{gt} \quad (9.23)$$

$$z_{\chi(t-1)} \leq z_{\chi t} \quad (9.24)$$

The total gas and electricity production capacity in the IEGSs must supply the forecasted energy loads and reserve requirements, which can be expressed as:

$$\sum_i \sum_{e \in CS} P_{iet}^{\max} \cdot z_{et} + \sum_i \sum_{k \in EG} P_{ik}^{\max} \geq PD_{tb} + PR_{tb} + W_{\chi t}^{\max} / \eta_{p2g} \quad (9.25)$$

$$\sum_m \left(\sum_{g \in CG} W_{mgt}^{\max} \cdot z_{gt} + \sum_{\chi \in PG} W_{m\chi t}^{\max} \cdot z_{\chi t} \right) + \sum_{w \in EW} W_{mw}^{\max} \geq GD_{tb} + GR_{tb} \quad (9.26)$$

where P_{ik}^{\max} represents the maximum output of power unit k at node i . W_{mw}^{\max} represents the maximum gas production of gas well w at node m . ER_{tb} and GR_{tb} denote the gas reserve and power reserve requirements of power system and NGS for system state b at year t . η_{p2g} denotes the conversion efficiency of P2G facilities.

9.4.4 system operation constraints

1) Natural gas system

Gas system operation constraints in (9.27)-(9.39) describe the operating condi-

tions of gas wells, pipelines, and gas suppliers. The gas nodal balance equation is given in (9.27). The Nonlinear Weymouth equation (9.28) shows that the pipeline flow is a function of the squared gas pressures [32]. Constraints (9.29)-(9.31) restrict the gas flow direction through pipelines. Nodal squared pressures and pipeline flows are limited in (9.32) and (9.33), respectively. Constraints (9.34) and (9.35) describes the operating characteristics of gas compressors. Production limits of candidate gas suppliers and gas wells are given in (9.36) and (9.38), respectively. Constraint (9.39) limits gas load curtailments at each node.

$$\begin{aligned} & \sum_{w \in EW} W_{mwtb} + \sum_{g \in CG} W_{mgth} + \sum_{\chi \in PG} W_{m\chi tb} \\ & = GD_{mtb} - GLC_{mtb} + \sum_{p \in GL} \tau_{ptb} + \sum_{c \in GC} \tau_{ctb} \end{aligned} \quad (9.27)$$

$$(\sigma_{ptb}^+ - \sigma_{ptb}^-) \cdot (\pi_{mtb} - \pi_{ntb}) = \tau_{ptb}^2 / M_p \quad (9.28)$$

$$-(1 - \sigma_{ptb}^+) \cdot \tau_p^{\max} \leq \tau_{ptb} \leq (1 - \sigma_{ptb}^-) \cdot \tau_p^{\max} \quad (9.29)$$

$$-(1 - \sigma_{ptb}^+) \cdot \tau_p^{\max} \leq \pi_{mtb} - \pi_{ntb} \leq (1 - \sigma_{ptb}^-) \cdot \tau_p^{\max} \quad (9.30)$$

$$\sigma_{ptb}^+ + \sigma_{ptb}^- = 1 \quad (9.31)$$

$$\pi_m^{\min} \leq \pi_{mtb} \leq \pi_m^{\max} \quad (9.32)$$

$$-\tau_c^{\max} \leq \tau_{ctb} \leq \tau_c^{\max} \quad (9.33)$$

$$\Gamma_{ctb} = \pi_{cmtb} / \pi_{cntb} \quad (9.34)$$

$$\Gamma_c^{\min} \leq \Gamma_{ctb} \leq \Gamma_c^{\max} \quad (9.35)$$

$$0 \leq W_{mgth} \leq W_{mg}^{\max} \cdot z_{gt} \quad (9.36)$$

$$0 \leq W_{m\chi tb} \leq W_{m\chi}^{\max} \cdot z_{\chi t} \quad (9.37)$$

$$0 \leq W_{mwtb} \leq W_{mw}^{\max} \cdot \theta_{wtb} \quad (9.38)$$

$$GLC_{mtb} \leq GD_{mtb} \quad (9.39)$$

where W_{mwtb} , W_{mktb} and $W_{m\chi tb}$ represent the production of gas well w , candidate gas supplier k , and P2G facility χ at node m , respectively. GD_{mtb} denotes the fuzzy gas load for system state b at node m and year t . τ_{ptb} denotes gas flow through pipeline p for system state b at year t . π_{mtb} represents the squared pressure at node m for system state b and year t . M_p is the transmission coefficient of pipeline p . σ_{ptb}^+ and σ_{ptb}^- are binary variables indicating gas flow direction of pipeline p . τ_p^{\max} is the maximum gas flows through pipeline p . τ_{ctb} and τ_c^{\max} represent the gas flow and the transmission capacity of compressor C , respectively. π_m^{\min} and π_m^{\max} are the minimum and maximum squared gas pressures at node

m , respectively. Γ_{ctb} denotes the squared compressor ratio of compressor C for system state b at year t . Γ_c^{\min} and Γ_c^{\max} are the minimum and maximum squared compressor ratios of compressor C , respectively.

2) Electric power system

The model in (9.40)-(9.47) describes the operating features of EPS. Equation (9.40) represents nodal power balance. Equation (9.41) calculates network power flow using the DC model. Line flow limits and nodal phase angles are limited by (9.42) and (9.43), respectively. Constraints (9.44) and (9.45) limit the power output of candidate units and coal-fired power plants, respectively. The power output of GPPs is calculated by the corresponding gas supplied to them, as shown in (9.46). Constraint (9.47) limits power load curtailments at each node.

$$\begin{aligned} \sum_{e \in CS} P_{ietb} + \sum_{k \in EG} (P_{iktb}^{GG} + P_{iktb}^{CG}) - \sum_{l \in EL} f_{ltb} \\ = PD_{itb} - PLC_{itb} - W_{m\chi tb} / \eta_{p2g} \end{aligned} \quad (9.40)$$

$$f_{ltb} = (\theta_{itb} - \theta_{jtb}) / x_l \quad (9.41)$$

$$-f_l^{\max} \leq f_{ltb} \leq f_l^{\max} \quad (9.42)$$

$$-\theta_i^{\max} \leq \theta_{itb} \leq \theta_i^{\max} \quad (9.43)$$

$$-P_{ie}^{\max} \cdot z_{et} \leq P_{ietb} \leq P_{ie}^{\max} \cdot z_{et} \quad (9.44)$$

$$0 \leq P_{iktb}^{CG} \leq P_{ik}^{\max} \cdot \theta_{ktb} \quad (9.45)$$

$$P_{iktb}^{GG} = (GD_{mtb} - GLC_{mtb}) \cdot g \cdot \theta_{ktb} \quad (9.46)$$

$$PLC_{itb} \leq PD_{itb} \quad (9.47)$$

where P_{iktb}^{CG} and P_{iktb}^{GG} represent the power outputs of GPPs and coal-fired power plants for system state b at node i . P_{ietb} represents the output of candidate unit e for system state b at node i . PD_{itb} denotes the fuzzy electric load for system state b at node i . f_{ltb} denotes the electricity flow through power line l for system state b at year t . θ_{itb} and x_l represent the angle of node i for system state b and the reactance of line l , respectively. f_l^{\max} denotes the transmission capacity of line l .

9.5 Solution methodology

9.5.1 The treatment of fuzzy parameters

As discussed in chapter 10.2, both the energy loads and component states are expressed as fuzzy numbers. The reserve planning model is formulated as a

mixed-integer non-linear optimization problem with fuzzy parameters (MNOFP). Considering that, one effective method is to convert the fuzzy parameters into a crisp parameter using an optimism value [33]. In specific, the fuzzy electric loads $\dot{PD}_{tb} = (PD_{tb}^-, PD_{tb}^0, PD_{tb}^+)$ can be replaced by (9.48) which allows the MNOFP to be solved with a compromise approach.

$$\dot{PD}_{tb} = \left(\frac{\omega_d PD_{tb}^-}{2} + \frac{PD_{tb}^0}{2} + \frac{(1-\omega_d) PD_{tb}^+}{2} \right) \quad (9.48)$$

where the optimism value $0 \leq \omega_d \leq 1$ can be adjusted based on the risk propensity of system planners.

To deal with the fuzzy unit states, the corresponding fuzzy system generating capacity \dot{GC}_{tb} is firstly converted into a crisp parameter using optimism value ω_c in (9.49). Based on the calculated \dot{GC}_{tb} , the operating states θ_{kib} for different units in subperiod b can be determined.

$$\dot{GC}_{tb} = \left(\frac{(1-\omega_c) GC_{tb}^-}{2} + \frac{GC_{tb}^0}{2} + \frac{\omega_c GC_{tb}^+}{2} \right) \quad (9.49)$$

Similarly, the fuzzy gas loads and gas well state can be replaced by crisp parameters using optimism values. On this basis, the proposed MNOFP can be converted into a mixed-integer non-linear programming (MINLP) problem.

It can be should that the robustness of planning results can be guaranteed by setting a smaller optimism value. Taking electric load \dot{PD}_{tb} as an example, the system electric load level can increase with the decrease of optimism values ω_d . Under this circumstance, more energy production components need to be constructed to satisfy the requirements of energy loads.

9.5.2 The solution of the reliability-constrained reserve expansion model

This proposed reserve planning model cannot be efficiently solved due to the reliability constraints in (14) and (17). Benders decomposition is therefore applied to decompose the original optimization problem into a master problem to optimize the base-case investment decisions, and two subproblems to check the reliability constraints of EPS and NGS [34].

In the steady-state analysis of gas systems, the gas flow models can be divided into two categories [35]. The first one is the controllable-flow model where the pipeline flows are fully controllable and are modeled as control variables limited by pipeline limits [2]. The second one is the noncontrollable-flow model, i.e. Weymouth function where the pipeline flows are modeled as state variables restricted by nodal pressures [36]. In the gas reliability subproblem, the controllable-flow model is utilized to guarantee the convergence and optimality of Benders

cuts. The simplification of the gas flow model has proved to be acceptable for investment problems over a long time horizon and has been widely used in system planning [2, 37]. The measures in [36] to deal with the nonlinear and nonconvex gas flow model in the subproblems will be introduced for future studies about the optimal operation of IEGSs.

1) Master investment problem

The master investment problem is presented in (9.50), where the dual cuts generated from the gas system and power system reliability subproblems are iteratively added. The master problem mainly determines the optimal investment and operation decisions in the base case considering load variations. The stochastic failures of components are considered in the two subproblems to check the reliability requirements of IEGSs. Hence, the operating states of gas wells $\delta_{w_{tb}}$ and generating units $\delta_{k_{tb}}$ are set as 1 in the master problem. Optimal solutions $\underline{\lambda}_{et}$, $\underline{\lambda}_{gt}$ and $\underline{\lambda}_{xt}$ are sent to the two subproblems.

$$\begin{aligned} & \min TC \\ & \text{S.t. } TC \geq IC + OC \\ & \quad \text{Constraints (22)-(38), (40)-(46)} \\ & \quad \text{Dual reliability cuts generated} \\ & \quad \text{Optimality cuts generated} \end{aligned} \tag{9.50}$$

It should be noted that the master problem is an MINLP problem due to gas flow equations (9.28). The auxiliary variables λ_{ptb} are firstly defined to replace $(\sigma_{ptb}^+ - \sigma_{ptb}^-) \cdot (\pi_{mtb} - \pi_{ntb})$. Based on the second-order cone relaxation technique, the gas flow equation (9.28) can then be relaxed as [18]:

$$\lambda_{ptb} \cdot M_p \geq \tau_{ptb}^2 \tag{9.51}$$

$$\lambda_{ptb} = (\sigma_{ptb}^+ - \sigma_{ptb}^-) \cdot (\pi_{mtb} - \pi_{ntb}) \tag{9.52}$$

The non-linear function (9.52) can then be linearized by a standard McCormick relaxation [38], which can be represented as:

$$\lambda_{ptb} \geq \pi_{ntb} - \pi_{mtb} + (\sigma_{ptb}^+ - \sigma_{ptb}^- + 1)(\pi_m^{\min} - \pi_n^{\max}) \tag{9.53}$$

$$\lambda_{ptb} \geq \pi_{mtb} - \pi_{ntb} + (\sigma_{ptb}^+ - \sigma_{ptb}^- - 1)(\pi_m^{\max} - \pi_n^{\min}) \tag{9.54}$$

$$\lambda_{ptb} \leq \pi_{ntb} - \pi_{mtb} + (\sigma_{ptb}^+ - \sigma_{ptb}^- + 1)(\pi_m^{\max} - \pi_n^{\min}) \tag{9.55}$$

$$\lambda_{ptb} \leq \pi_{mtb} - \pi_{ntb} + (\sigma_{ptb}^+ - \sigma_{ptb}^- - 1)(\pi_m^{\min} - \pi_n^{\max}) \tag{9.56}$$

Hence, the original MINLP model can be transformed into a mixed-integer second-order cone program (MISOCP) problem.

2) Gas system reliability subproblem

Once the construction states of gas suppliers and P2G facilities are identified by the master problem, the NGS reliability subproblem is to determine whether

the planning decisions satisfy the reliability requirements. The problem objective (9.57) is to minimize the total gas load curtailments for each system state. The proposed reliability subproblem needs to follow the constraints (9.58).

$$\begin{aligned} \min & \sum_m \sum_t \sum_b \sigma_m \cdot GLC_{mtb} \cdot D_{tb} \\ \text{s.t. } & z_{gt} = \$_{gt} (\mu_{gt}) \\ & z_{\chi t} = \$_{\chi t} (\mu_{\chi t}) \end{aligned} \quad (9.57)$$

Constraints (9.27), (9.32) – (9.39)

where σ_m represents the weights of gas loads at node m that distinguish the shedding sequence of loads supplied to GPPs and remainders, e.g. heaters. Considering the prior curtailment of gas supplied to GPPs, the corresponding values of σ_m can be slightly smaller than those for remaining loads.

Based on the gas load curtailments solved by the subproblem, the annual $EGNS_t$ can be calculated using (9.17). When the annual $EGNS_t$ reliability constraint (9.20) is not satisfied, the dual cut (9.59) will be added to the master investment problem for the solution in the next iteration.

$$\begin{aligned} & \sum_m \sum_b GLC_{mtb} \cdot D_{tb} + \sum_{g \in CG} \mu_{gt} (z_{gt} - \$_{gt}) \\ & + \sum_{\chi \in PG} \mu_{\chi t} (z_{\chi t} - \$_{\chi t}) \leq EGNS_t^{\text{limit}} \end{aligned} \quad (9.59)$$

where μ_{gt} and $\mu_{\chi t}$ is the dual values of the constraints associated with the construction states of gas suppliers and P2G facilities.

3) Power system reliability subproblem

Based on the planning decisions of power units from the master problem, the reliability requirements of EPS are evaluated in this subproblem. The problem objective (9.60) is to minimize the total electric load curtailments subject to the constraints (9.61). To simplify the calculation, the power outputs of GPPs can be determined according to the expected gas load curtailments $EGNS_{mt}$ at the corresponding nodes.

$$\begin{aligned} \min & \sum_i \sum_t \sum_b PLC_{itb} \cdot D_{tb} \\ \text{s.t. } & z_{et} = \$_{et} (\mu_{et}) \\ & P_{iktb}^{GG} = (GD_{mtb} - EGNS_{mt}) \cdot 9 \cdot 80_{kib} \end{aligned} \quad (9.60)$$

Constraints (9.40) – (9.45), (9.47)

Likewise, the annual $MIENS_t$ can be calculated using (9.19) to identify whether the reliability constraint (9.21) can be satisfied. If violated, the corresponding dual cut will be generated:

$$\sum_i \sum_b PLC_{ib} \cdot D_{tb} + \sum_{e \in CS} \mu_{et} \left(z_{et} - \$_{et} \right) \leq MIENS^{\text{limit}} \quad (9.62)$$

When the reliability constraints (9.20) and (9.21) are satisfied, The optimal reliability subproblem (9.63) for IEGSs is modeled subjected to (9.64). Then the reliability cost obtained in this subproblem will be added to the investment and operation costs to calculate the total planning cost. If it is not equal to the total planning costs TC , the optimality cut (9.65) will be added to the master problem.

$$\min lc = \sum_m \sum_t \sum_b \frac{\sigma_m GLC_{mtb} D_{tb} C_t^G}{(1+d)^{t-1}} + \sum_i \sum_t \sum_b \frac{PLC_{ib} D_{tb} C_t^E}{(1+d)^{t-1}} \quad (9.63)$$

$$\begin{aligned} \text{s.t. } z_{gt} &= \$_{gt} (\mu'_{gt}) \\ z_{et} &= \$_{et} (\mu'_{et}) \\ z_{\chi t} &= \$_{\chi t} (\mu'_{\chi t}) \end{aligned} \quad (9.64)$$

Constraints (27), (32)–(47)

$$TC \geq ic + oc + lc + \sum_{e \in CS} \sum_t \mu'_{et} \left(z_{et} - \$_{et} \right) + \sum_{g \in CG} \sum_t \mu'_{gt} \left(z_{gt} - \$_{gt} \right) \quad (9.65)$$

where ic , oc and lc denotes the variables of investment costs, operation costs, and load curtailments for the certain component construction states determined in the master problem. Hence, the values of ic , oc and lc can change for each iteration.

9.5.3 Solution procedures of the proposed model

Fig. 9.3 shows the solution procedures for the long-term reserve expansion problem.

Step 1. Determine the fuzzy models of energy loads and component failures using the fuzzy set theory.

Step 2. Introduce optimism values to convert fuzzy parameters into a crisp value using (9.48) and (9.49). Set iteration number $v = 1$.

Step 3. Solve the master investment problem (9.50)–(9.56) and send the optimal results $\$_{gt}$, $\$_{et}$ and $\$_{\chi t}$ to steps 4 and 5. The calculated total results of the master problem at iteration v is $TC^{\min(v)}$, which is the lower bound for the optimal value of the original problem.

Step 4. Solve the gas system reliability subproblem (9.57)–(9.58) with respect to $\$_{gt}$ and $\$_{\chi t}$. Calculate the annual reliability index and send $EGNS_{mt}$ to step 5. If the reliability constraint (9.20) is violated, add the dual cut (9.59) to the master problem and go to Step 3.

Step 5. Solve the power system reliability subproblem (9.60)–(9.61) for certain values of $\$_{et}$ and $MIENS_t$, and calculate the reliability index. If the reliability

constraint (9.21) is violated, add the dual cut (9.62) to the master problem and go to Step 3.

Step 6. If all the reliability constraints in both NGS and EPS are satisfied, solve the optimal *reliability* subproblem in (9.63)-(9.65). Calculate the lower bound for the optimal value of the original problem by adding up the investment, operation, and reliability costs, which can be represented as $TC^{\max,(v)} = IC^{(v)} + OC^{(v)} + LC^{(v)}$.

Step 7. Determine if the convergence criterion of the Benders decomposition is satisfied. If the convergence criterion is violated, add the dual cut (9.65) to the master problem. Let $v=v+1$ and go to Step 3. If the convergence criterion is satisfied, Terminate.

$$\frac{2|TC^{\max,(v)} - TC^{\min,(v)}|}{TC^{\max,(v)} + TC^{\min,(v)}} \leq \varepsilon \quad (9.66)$$

where ε is the tolerance of convergence.

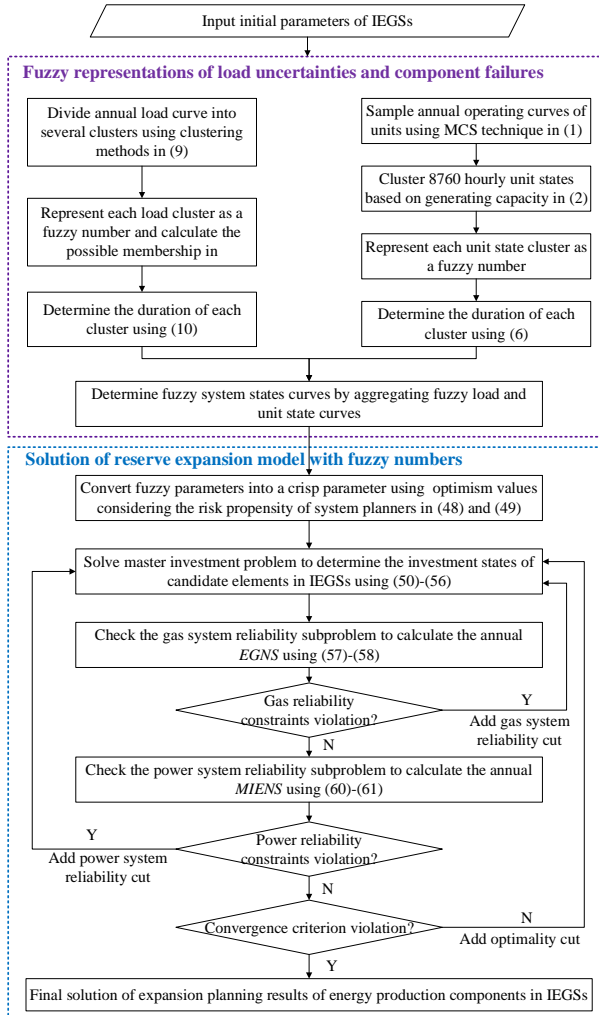


Fig. 9.3 The flow chart of the solution procedures

Here, the convergence of the solution method is demonstrated. Fig. 9.4 shows the relation between the master problem and two reliability subproblems, whose solution can be divided into two phases. In the first phase (①+②), the master investment problem calculates the construction states of gas suppliers based on the feasibility cuts from the gas reliability subproblem. The two problems are calculated iteratively until the reliability constraint of the gas subsystem is satisfied. After the solution process is ended, the construction states of gas suppliers and P2G facilities, as well as gas load shedding results can be determined.

For certain gas load shedding results in the first phase, the generation losses of gas-fired power plants (GPPs) can then be determined, which remain unchanged in the second phase (①+③). Considering that, the interaction process between the

master problem and power reliability subproblem is similar to that in the first phase. The construction states of power units can be determined until the reliability constraints of the power subsystem can be satisfied. After both the feasibility of the two subproblems is satisfied, the optimality cuts will be fed back to the master problem for the next iteration. Note that the developed optimality cut combines the gas and power load curtailment costs of two subproblems, which are equivalent to two optimality cuts respectively formulated in two phases. Therefore, the optimization models in the two phases follow the specific structure that is particularly amenable to the Benders decomposition. The detailed proof of the convergence of the solution method in each phase can be seen in [39].

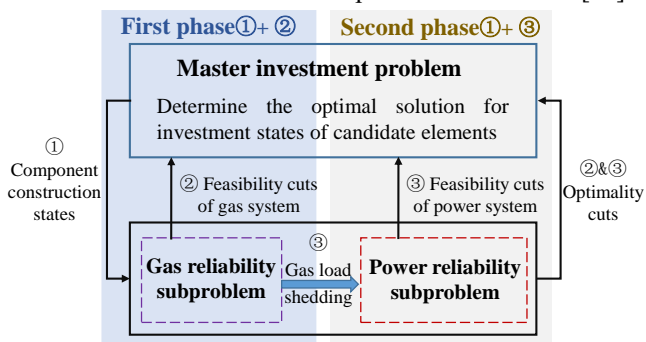


Fig. 9.4 The relation between the master problem and two reliability subproblems

9.6 Case study

The IEGSs composed of the modified IEEE 30-bus power system [40] and Belgian 20-node gas system [32] are introduced to show the effectiveness of the proposed model. The modified EPS is composed of six power units, where three GPPs at electric nodes 5, 8, and 13 obtain fuels from gas nodes 3, 7, and 20. The electric load data are derived from [41]. The modified gas system consists of 19 pipelines, three compressors, and six gas wells. The physical parameters of pipelines, compressors, and wells can be found in [32]. The hourly gas load levels in NGS are estimated according to the data in [42]. Both the electric loads and non-power gas loads have an average load growth rate of 3%. The discount rate α is set at 5% and the planning horizon is set at 10 years.

Table 9.1 and Table 9.2 respectively show the data of six candidate power units and five candidate gas suppliers. The listed data of power plants and gas suppliers include location, capacity, investment cost, and operating cost. Note that the investment of P2G facilities is only considered in Case study D. The failure rates of power units and gas wells are both set as 0.001, while their repair rates are 0.02 and 0.01, respectively [26]. The reserve requirement is 5% of energy loads at each state. The shedding costs for electric loads and gas loads are set as 1000\$/MWh [43] and 0.64\$/m³, respectively. The optimism values of system planners are as-

sumed as 0.5. The pre-determined tolerance ϵ is set as 0.01.

Table 9.1 Candidate power units data

Power units	Bus	Capacity (MW)	Investment cost (10^3 \$/MW)	Operating cost (\$/MWh)
ES1	30	80	250	50
ES2	26	60	210	45
ES3	17	50	190	55
ES4	15	60	230	45
ES5	10	50	220	40
ES6	4	30	180	40

Table 9.2 Candidate gas supplier and P2G data

Gas suppliers	Node	Capacity (10^4 m ³)	Investment cost (\$/m ³)	Operating cost (\$/m ³ h)
GS1	7	4	6000	0.020
GS2	17	3.5	6300	0.015
GS3	16	2.8	6200	0.025
GS4	20	2.8	6200	0.025
GS5	4	3.2	6300	0.015

9.6.1 Effectiveness analysis of the proposed model compared to conventional existing models

In this case, the effectiveness of the proposed model with multifactor-influenced reliability indices is demonstrated compared to other conventional existing models. In the previous studies, the gas components are assumed completely available and the failure propagation from gas systems to power systems is not considered [18]. The traditional reliability indices, e.g. *EENS* are usually utilized to characterize the reliability levels of power systems [17]. In the proposed model, component failures in gas systems and the corresponding failure propagation are considered. The *MIENS* index and *ENGS* index are utilized to quantify the reliabilities of power systems and gas systems, respectively. In this case, the limits of *EENS* and *MIENS* indices are identical, which are set as 10000 MWh. The limit of the *EGNS* index is set as 1.5×10^7 m³.

Table 9.3 shows the comparison of planning results between the proposed model and the existing planning models. Firstly, it can be found that more gas suppliers and power plants are deployed in the proposed model. Secondly, both the installation of power plants and gas suppliers are brought forward in the proposed model. This is mainly because gas system uncertainties and failure propagation are not considered in the conventional models and deployment of candidate elements only needs to meet the forecasted loads.

Table 9.3 Installation year of candidate elements for different models

Candidate units	Proposed model	Existing model	Candidate gas suppliers	Proposed model	Existing model
ES1	-	-	GS1	1	-
ES2	-	-	GS2	-	-
ES3	3	2	GS3	7	-
ES4	-	-	GS4	-	-
ES5	5	7	GS5	3	7
ES6	1	6	-	-	-

Based on the determined candidate element installation in Table 9.3, the reliabilities of IEGSs at different years are evaluated considering gas component failures and failure propagation. Fig. 9.5 shows the reliability evaluation results of the proposed model and the existing planning model. Firstly, it can be found that the neglect of gas component failures in the existing model may lead to over-optimistic planning results, which cannot guarantee the reliable operation of NGS. It can be found that the maximum value of *ENGs* of the existing model is $4.25 \times 10^7 \text{ m}^3$, which is over 4 times than *ENGs* requirements. In contrast, the *ENGs* values in the proposed model are all smaller than *ENGs* requirements. The analysis results indicate that the reliability requirements of NGS cannot be achieved in the existing model when considering component failures.

Considering the cross-sectorial failure propagation, unreasonable gas supplier plans in the existing model also make the deployment of power plants cannot satisfy reliability requirements. As illustrated in Fig. 9.5, the *EENS* values calculated in the existing model increase rapidly from year 2 to year 10, which are all larger than reliability requirements. On the contrary, the maximum value of *MIENS* in the proposed model is only 9290.23 MWh, which is smaller than the reliability requirements. The reliability analysis results further demonstrate that the proposed model can plan reasonable reserve to guarantee the reliability levels of IEGSs.

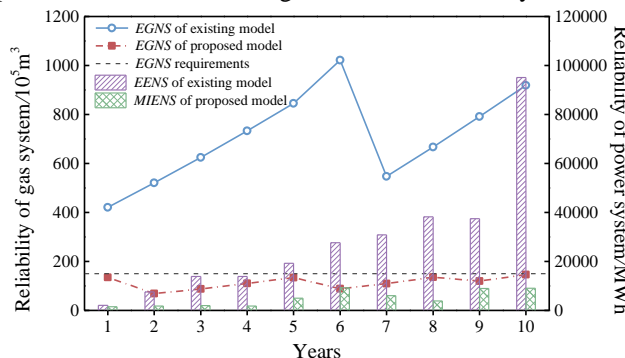


Fig. 9.5 Comparisons of reliability indices in different models considering cross-sectorial failure propagation

The total planning costs of different models are also compared in Table 9.4. At

the end of the planning horizon, the investment costs of the proposed model can be 5.76×10^8 \$ (much higher than that in the existing model) since more gas suppliers are deployed. Nevertheless, the operation costs in the proposed model are relatively smaller due to the lower operation costs of new power plants and gas suppliers. In specific, the operation costs of the proposed model are 1.617×10^8 \$, which is 0.90 times those of the existing model. Despite the investment cost saving in the previous model with fewer gas supplier constructions, the neglect of gas contingencies can lead to more energy curtailment costs. The unserved energy costs of the previous model are nearly 5 times those of the proposed model. Synthesizing the investment costs, operation costs, and unserved energy costs, the total planning costs of the proposed model can save 2.23×10^8 \$ costs. The analysis results demonstrate that the proposed model can realize the coordination between economy and reliability.

Table 9.4 Operation scheduling results of different models

Cost ($\times 10^8$ \$)		Existing model	Proposed model
Investment costs	Gas suppliers	1.504	5.524
	Power plants	0.236	0.231
Operation costs		1.783	1.617
Unserved energy costs		6.805	0.734
Total co-optimization costs of IEGSs		10.33	8.105

In order to demonstrate the effectiveness of the second-order cone relaxation technique for convexifying the gas flow model, another widely-used linearization technique, i.e. piecewise linearization method is introduced in this chapter as a comparative method to solve the proposed model. The total optimal objective calculated by the piecewise linearization method is 8.112×10^8 \$, with only a 0.08% difference from the objective value obtained by the second-order cone relaxation method. The difference in pipeline flows between these two methods at different states of year 10 is calculated, as illustrated in Fig. 9.6, whose largest value is smaller than 2%. With regard to computation efficiency, the computation time of the MCE method is 1101.89 s, which is 0.48 times that of the piecewise linearization technique.

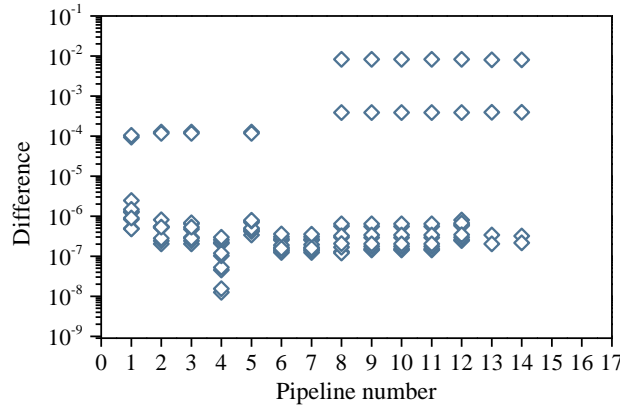


Fig. 9.6 Difference of pipeline flows at different states of year 10 between second-order cone relaxation and piecewise linearization methods

Moreover, the second-order cone relaxation technique has been widely used in the expansion and optimization of gas systems [18, 38, 44], whose optimality gap and efficiency have also been explained in [38]. By potentially modifying the gas components in Belgium gas network topology, different test systems are developed in [38] to compare the optimal objective value, optimality gap, and the efficiency between different methods. The analysis results in reference [38] show that the second-order cone relaxation technique can derive high-quality solutions compared to other methods. Besides, the optimality gaps of the second-order cone relaxation technique are provably tight, which can also lead to global optimal solutions in some cases. Furthermore, the computation efficiency of the second-order cone relaxation technique is much higher than other methods.

9.7.2 Sensitivity analysis of reliability requirements on planning results

In this case, the impacts of reliability requirements $EGNS^{\text{limit}}$ and $MIENS^{\text{limit}}$ on the reserve planning results of IEGSs are analyzed. When $EGNS^{\text{limit}}$ changes from $0.6 \times 10^7 \text{ m}^3$ to $2.7 \times 10^7 \text{ m}^3$ and $MIENS^{\text{limit}}$ changes from 4000 MWh to 12000 MWh, the variation of deployed energy reserve and the corresponding planning costs are analyzed.

With the change of reliability requirements in both NGS and EPS, the total gas reserve and electric reserve at the end of the planning horizon are given in Fig. 9.7 and Fig. 9.8, respectively. With regard to NGS, we can find that the deployed gas reserve increases with the decrease of $EGNS^{\text{limit}}$ values. As shown in Fig. 9.7, the deployed gas reserve decreases from $1.35 \times 10^7 \text{ m}^3$ to $0.95 \times 10^7 \text{ m}^3$ when $EGNS^{\text{limit}}$ changes from $0.9 \times 10^7 \text{ m}^3$ to $2.1 \times 10^7 \text{ m}^3$. In contrast, the variation of reliability requirements in the power system has no impact on the gas reserve planning results. Hence, the expansion planning of gas reserve mainly depends on $EGNS$ requirements due to the unidirectional energy interaction between NGS and EPS through

GPPs.

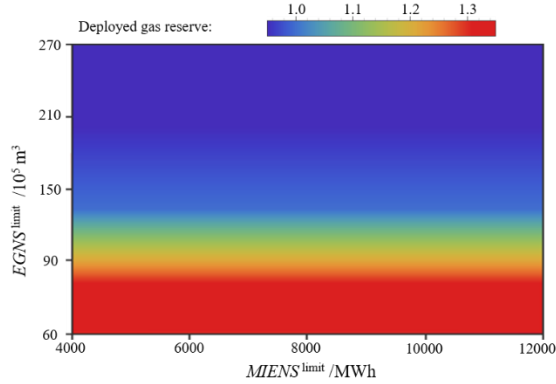


Fig. 9.7 Total deployed gas reserve with varying MIENS and EGNS limits

Regarding EPS, the planning results of the electric reserve are simultaneously affected by the change in reliability requirements in NGS and EPS. Firstly, it can be noted that the reduction of $MIENS^{limit}$ can increase the deployment of electric reserve in EPS. Moreover, we can find that the increase in reliability requirements in NGS can reduce the deployment of power units in EPS. This is mainly because the decrease in $EGNS^{limit}$ can reduce the probability of gas interruption to GPPs in contingency states. Due to the adequacy of gas fuels, the GPPs need not reduce their power output during contingencies. Considering that, less electric reserve is required to guarantee the reliability level of EPS. The simulation results also indicate that we can improve the reliability of EPS by simultaneously optimizing the energy resources in both systems.

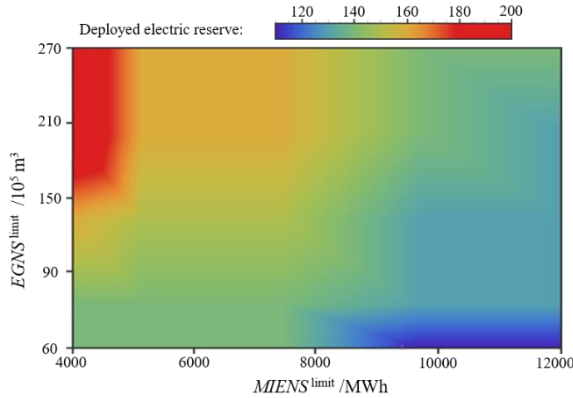


Fig. 9.8 Total deployed electric reserve with varying MIENS and EGNS limits

9.7.3 The impacts of optimism values on planning results

The impacts of optimism values on investment decisions of IEGSs are shown in Table 9.5 and Table 9.6. Three scenarios are considered: S1 is the based case

where the optimism values are set as 0.5 in accordance with the previous studies. The optimism values of S2 and S3 are set as 0.2 and 0.8, respectively.

Table 9.5 Installation year of candidate units for different optimism values

Candidate power units	S1: 0.5	S2: 0.2	S3: 0.8
ES1	-	-	-
ES2	-	-	-
ES3	3	1	4
ES4	-	6	-
ES5	5	9	9
ES6	1	1	1

Table 9.6 Installation year of candidate gas suppliers for different optimism values

Candidate gas suppliers	S1: 0.5	S2: 0.2	S3: 0.8
GS1	1	1	-
GS2	-	1	3
GS3	7	6	6
GS4	-	9	-
GS5	3	0	-

In conclusion, the increase in optimism values can decrease the allocation of energy production components by system planners. For example, the system planners tend to allocate the candidate components more conservatively if they are not very optimistic (with small optimism values in S2). The installation of power units and gas suppliers will be brought forward and more energy reserves will be allocated. Under this circumstance, more costs will be required to ensure the higher reliability of IEGSs. In contrast, the system planners will be more likely to postpone and reduce the allocation of production components if they are more optimistic (with small optimism values in S3). Accordingly, the costs of reserve expansion will be smaller and the system reliability level is relatively lower. The simulation results further demonstrate that the intermediate optimism values can realize the coordination between costs and reliability.

9.7.4 Coordination analysis between P2G facilities and gas suppliers

In this case, the allocation of P2G facilities and gas suppliers are coordinated for the reserve expansion of IEGSs. Four candidate P2G facilities are planned together with gas suppliers, whose data are shown in Table 9.7 [45]. The conversion coefficient of P2G facilities is set as $50 \text{ m}^3/\text{MW}$ [46]. Considering different costs of power generation in EPS, two scenarios are introduced. Scenario I is the base scenario where the operating and investment costs of power units are identical to those in Case A. In scenario II, the corresponding costs are set as 80% of those in scenario I.

Table 9.7 Data of candidate P2G facilities

Gas suppliers	Gas Node	Electric node	Capacity (10^4m^3)	Investment cost (\$/ m^3)
P2G-1	4	4	0.1	10000
P2G-2	4	9	0.08	9500
P2G-3	4	14	0.08	10500
P2G-4	4	20	0.1	10000

Table 9.8 shows the planning results of candidate components for different scenarios. Firstly, it can be found that the installation of gas suppliers is appreciated in scenario I. With the decrease in power generation costs in scenario II, P2G facilities will be installed to satisfy the gas demand in IEGSs. Besides, more power units are planned in scenario II due to the installation of P2G facilities. The study results show that the P2G facilities tend to be installed for scenarios where the average power generation costs are relatively lower, e.g. power systems with a high proportion of renewable energy. On the contrary, the investment in P2G facilities will increase the installation of high-cost power units, which can be more expensive than the investment of gas suppliers.

Table 9.8 Installation year of candidate elements for different scenarios

Candidate units	Scenario I	Scenario II	Candidate gas elements	Scenario I	Scenario II
ES1	-	10	GS1	1	7
ES2	-	-	GS2	-	1
ES3	3	2	GS3	7	3
ES4	-	1	GS4	-	-
ES5	5	6	GS5	3	-
ES6	1	3	P2G-1	-	2
-	-	-	P2G-2	-	2
-	-	-	P2G-3	-	-
-	-	-	P2G-4	-	-

9.7 Conclusion

Considering the impacts of cross-sectorial failure propagation, a multifactor-influenced reliability-constrained reserve expansion is proposed to determine the allocation of energy production components. In the proposed model, the novel multifactor-influenced reliability indices are defined considering the synthetic effects of multiple uncertainties, including failure propagation, load uncertainties, and component failures. The fuzzy set theory is combined with conventional methods to reduce the number of system contingency states for computation efficiency improvement. Case studies demonstrate that the proposed model can realize the coordination between economy and reliability compared to the previous studies. Moreover, the simulation results indicate that we can improve the reliability of EPS by simultaneously optimizing the energy resources in both systems.

Furthermore, the robustness of the proposed model can be guaranteed by setting a smaller optimism value. Hence, the proposed model in this chapter can provide useful references for system planners to constitute reasonable reserve expansion plans to guarantee the reliability levels of IEGSs.

References

- [1] M. Bao, Y. Ding, C. Singh, and C. Shao, "A multi-state model for reliability assessment of integrated gas and power systems utilizing universal generating function techniques," *IEEE Transactions on Smart Grid*, vol. 10, pp. 6271-6283, 2019.
- [2] X. Zhang, M. Shahidehpour, A. S. Alabdulwahab, and A. Abusorrah, "Security-constrained co-optimization planning of electricity and natural gas transportation infrastructures," *IEEE Transactions on Power Systems*, vol. 30, pp. 2984-2993, 2014.
- [3] G. Stergiopoulos, P. Kotzanikolaou, M. Theocharidou, G. Lykou, and D. Gritzalis, "Time-based critical infrastructure dependency analysis for large-scale and cross-sectoral failures," *International Journal of Critical Infrastructure Protection*, vol. 12, pp. 46-60, 2016.
- [4] ERCOT. *Review of February 2021 Extreme Cold Weather Event-ERCOT Presentation*. [online]. Available: http://www.ercot.com/content/wcm/key_documents_lists/225373/Urgent_Board_of_Directors_Meeting_2-24-2021.pdf
- [5] Z. Bao, Z. Jiang, and L. Wu, "Evaluation of bi-directional cascading failure propagation in integrated electricity-natural gas system," *International Journal of Electrical Power & Energy Systems*, vol. 121, p. 106045, 2020.
- [6] Z. Bao, Q. Zhang, L. Wu, and D. Chen, "Cascading failure propagation simulation in integrated electricity and natural gas systems," *Journal of Modern Power Systems and Clean Energy*, vol. 8, pp. 961-970, 2020.
- [7] S. Li, T. Ding, W. Jia, C. Huang, J. P. Catalao, and F. F. Li, "A Machine Learning-based Vulnerability Analysis for Cascading Failures of Integrated Power-Gas Systems," *IEEE Transactions on Power Systems*, 2021.
- [8] J. Beyza and J. M. Yusta, "Robustness assessment of the expansion of coupled electric power and natural gas networks under cascading failures," *IET Generation, Transmission & Distribution*, vol. 12, pp. 5753-5760, 2018.
- [9] O. A. Ansari, C. Chung, and E. Zio, "A Novel Framework for the Operational Reliability Evaluation of Integrated Electric Power-Gas Networks," *IEEE Transactions on Smart Grid*, 2021.
- [10] M. Farrokhifar, Y. Nie, and D. Pozo, "Energy systems planning: A survey on models for integrated power and natural gas networks coordination," *Applied Energy*, vol. 262, p. 114567, 2020.
- [11] Q. Zeng, B. Zhang, J. Fang, and Z. Chen, "A bi-level programming for multi-stage co-expansion planning of the integrated gas and electricity system," *Applied energy*, vol. 200, pp. 192-203, 2017.

- [12] B. Zhao, A. J. Conejo, and R. Sioshansi, "Coordinated expansion planning of natural gas and electric power systems," *IEEE Transactions on Power Systems*, vol. 33, pp. 3064-3075, 2017.
- [13] A. Gholami, H. Nafisi, H. Askarian Abyaneh, and A. Jahanbani Ardakani, "Dynamic stochastic joint expansion planning of power systems, natural gas networks, and electrical and natural gas storage," *IET Generation, Transmission & Distribution*, 2021.
- [14] X. Wang, Z. Bie, F. Liu, Y. Kou, and L. Jiang, "Bi-level planning for integrated electricity and natural gas systems with wind power and natural gas storage," *International Journal of Electrical Power & Energy Systems*, vol. 118, p. 105738, 2020.
- [15] F. Barati, H. Seifi, M. S. Sepasian, A. Nateghi, M. Shafie-khah, and J. P. Catalão, "Multi-period integrated framework of generation, transmission, and natural gas grid expansion planning for large-scale systems," *IEEE Transactions on Power Systems*, vol. 30, pp. 2527-2537, 2014.
- [16] J. Qiu, H. Yang, Z. Y. Dong, J. H. Zhao, K. Meng, F. J. Luo, *et al.*, "A linear programming approach to expansion co-planning in gas and electricity markets," *IEEE Transactions on Power Systems*, vol. 31, pp. 3594-3606, 2015.
- [17] Y. Zhang, Y. Hu, J. Ma, and Z. Bie, "A mixed-integer linear programming approach to security-constrained co-optimization expansion planning of natural gas and electricity transmission systems," *IEEE Transactions on Power Systems*, vol. 33, pp. 6368-6378, 2018.
- [18] C. He, L. Wu, T. Liu, and Z. Bie, "Robust co-optimization planning of interdependent electricity and natural gas systems with a joint N-1 and probabilistic reliability criterion," *IEEE Transactions on Power Systems*, vol. 33, pp. 2140-2154, 2017.
- [19] X. Zhang, L. Che, M. Shahidehpour, A. S. Alabdulwahab, and A. Abusorrah, "Reliability-based optimal planning of electricity and natural gas interconnections for multiple energy hubs," *IEEE Transactions on Smart Grid*, vol. 8, pp. 1658-1667, 2015.
- [20] B. Odetayo, J. MacCormack, W. Rosehart, H. Zareipour, and A. R. Seifi, "Integrated planning of natural gas and electric power systems," *International Journal of Electrical Power & Energy Systems*, vol. 103, pp. 593-602, 2018.
- [21] Q. Shi, F. Li, T. Kuruganti, M. Olama, J. Dong, X. Wang, *et al.*, "Resilience-Oriented DG Siting and Sizing considering Stochastic Scenario Reduction," *IEEE Transactions on Power Systems*, 2020.
- [22] Y. Ding and A. Lisnianski, "Fuzzy universal generating functions for multi-state system reliability assessment," *Fuzzy Sets and Systems*, vol. 159, pp. 307-324, 2008.
- [23] Y.-F. Li, H.-Z. Huang, J. Mi, W. Peng, and X. Han, "Reliability analysis of multi-state systems with common cause failures based on Bayesian network and fuzzy probability," *Annals of Operations Research*, pp. 1-15, 2019.
- [24] M. Mohammadi, Y. Noorollahi, and B. Mohammadi-ivatloo, "Fuzzy-based scheduling of wind integrated multi-energy systems under multiple uncertain-

- ties," *Sustainable Energy Technologies and Assessments*, vol. 37, p. 100602, 2020.
- [25] M Bao, X Sun, Y Ding, C Ye, C Shao, S Wang and Y Song. Multifactor-influenced reliability-constrained reserve expansion of integrated electricity-gas systems considering failure propagation[J]. *CSEE Journal of Power and Energy Systems*, 2022.
 - [26] C. Liu, M. Shahidehpour, and J. Wang, "Coordinated scheduling of electricity and natural gas infrastructures with a transient model for natural gas flow," *Chaos: An Interdisciplinary Journal of Nonlinear Science*, vol. 21, p. 025102, 2011.
 - [27] L. Goel, S. Ren, and P. Wang, "Modelling station-originated outages in composite system using state duration sampling simulation approach," *Computers & Electrical Engineering*, vol. 27, pp. 119-132, 2001.
 - [28] T. Kanungo, D. M. Mount, N. S. Netanyahu, C. D. Piatko, R. Silverman, and A. Y. Wu, "An efficient k-means clustering algorithm: Analysis and implementation," *IEEE transactions on pattern analysis and machine intelligence*, vol. 24, pp. 881-892, 2002.
 - [29] C. Shao, M. Shahidehpour, and Y. Ding, "Market-based integrated generation expansion planning of electric power system and district heating systems," *IEEE Transactions on Sustainable Energy*, vol. 11, pp. 2483-2493, 2019.
 - [30] M. Bao, Y. Ding, X. Yin, C. Shao, and C. Ye, "Definitions and reliability evaluation of multi-state systems considering state transition process and its application for gas systems," *Reliability Engineering & System Safety*, vol. 207, p. 107387, 2021.
 - [31] D. De Wolf and Y. Smeers, "The gas transmission problem solved by an extension of the simplex algorithm," *Management Science*, vol. 46, pp. 1454-1465, 2000.
 - [32] M. Verma and K. K. Shukla, "Application of fuzzy optimization to the orienteering problem," *Advances in Fuzzy Systems*, vol. 2015, pp. 1-12, 2015.
 - [33] M. Shahidehpour and Y. Fu, "Benders decomposition: applying Benders decomposition to power systems," *IEEE Power and Energy Magazine*, vol. 3, pp. 20-21, 2005.
 - [34] C. Wang, W. Wei, J. Wang, F. Liu, and S. Mei, "Strategic offering and equilibrium in coupled gas and electricity markets," *IEEE Transactions on Power Systems*, vol. 33, pp. 290-306, 2017.
 - [35] X. Zheng, Y. Xu, Z. Li, and H. Chen, "Co-optimisation and settlement of power-gas coupled system in day-ahead market under multiple uncertainties," *IET Renewable Power Generation*, vol. 15, pp. 1632-1647, 2021.
 - [36] W. Wei and J. Wang, *Modeling and optimization of interdependent energy infrastructures*: Springer, 2020.
 - [37] C. Borraz-Sánchez, R. Bent, S. Backhaus, H. Hijazi, and P. V. Hentenryck, "Convex relaxations for gas expansion planning," *INFORMS Journal on Computing*, vol. 28, pp. 645-656, 2016.

- [38] N. Sahinidis and I. E. Grossmann, "Convergence properties of generalized Benders decomposition," *Computers & Chemical Engineering*, vol. 15, pp. 481-491, 1991.
- [39] C. Shao, Y. Ding, J. Wang, and Y. Song, "Modeling and integration of flexible demand in heat and electricity integrated energy system," *IEEE Transactions on Sustainable Energy*, vol. 9, pp. 361-370, 2018.
- [40] R. D. Zimmerman, C. E. Murillo-Sánchez, and R. J. Thomas, "MATPOWER: Steady-state operations, planning, and analysis tools for power systems research and education," *IEEE Transactions on power systems*, vol. 26, pp. 12-19, 2010.
- [41] H. Su, E. Zio, J. Zhang, M. Xu, X. Li, and Z. Zhang, "A hybrid hourly natural gas demand forecasting method based on the integration of wavelet transform and enhanced Deep-RNN model," *Energy*, vol. 178, pp. 585-597, 2019.
- [42] M. Chaudry, N. Jenkins, and G. Strbac, "Multi-time period combined gas and electricity network optimisation," *Electric power systems Research*, vol. 78, pp. 1265-1279, 2008.
- [43] A. Gholami, H. Nafisi, H. Askarian-Abyaneh, A. Jahanbani Ardakani, and Z. Shad, "Second-order cone programming for linepack in multistage stochastic co-expansion planning power and natural gas systems with natural gas storage," *AUT J. Electr. Eng.*, 2021.
- [44] H. Zhou, J. Zheng, Z. Li, Q. Wu, and X. Zhou, "Multi-stage contingency-constrained co-planning for electricity-gas systems interconnected with gas-fired units and power-to-gas plants using iterative benders decomposition," *Energy*, vol. 180, pp. 689-701, 2019.
- [45] C. Baumann, R. Schuster, and A. Moser, "Economic potential of power-to-gas energy storages," in *2013 10th International Conference on the European Energy Market (EEM)*, 2013, pp. 1-6.

10 Outlook of Incorporating Integrated Demand Response in Risk Control of Multi-energy systems

10.1 Introduction

Multi-energy vectors are closely coordinated in the entire process from energy production to consumption. On the demand side, distributed multi-energy systems (DMS) can integrate the local multi-energy generation, conversion, and utilization [3]. Generally, the DMS consists of two sections, including district energy supply systems (DESS) and terminal multi-energy loads. The DESS refers to the aggregation of local energy producers and converters, e.g. combined heat and power (CHP) units which can provide multi-energy supply for terminal loads. In terms of terminal loads, the industrial loads require multiple varieties of energy and occupy a considerable share of final energy consumption. Compared with residential and commercial consumers, the energy consumption of industrial facilities accounts for nearly 54% of the global end-use energy consumption in 2020 [4]. Especially in areas with extremely dense industries, local DESSs are always constructed to satisfy the enormous multi-energy requirements of terminal industrial loads (IL). Therefore, the typical DMS composed of the DESS and the IL, named as a distributed multi-energy system with industrial loads (DMSI) is becoming a dominant form for energy system terminals.

With the widespread implementation of renewable energy, the conventional flexible resources provided by the energy supply side may no longer be able to envelop renewable energy fluctuation in MESs. Meanwhile, the demand side system can unlock substantial flexibility for system operation with the development of advanced technologies such as demand response (DR) and distributed energy conversion [5]. As for the DMSI, both the energy conversion in the DESS and the adjustable production plan in the IL can provide flexibility. On the one hand, the energy converters and storages in the DESS can not only shift energy inputs among different times but realize energy conversion among various energy carriers. On the other hand, the factories have intermediate material storage and redundant equipment, and the industrial process does not need to work at full load all the time. Considering that, they can adjust their production plans and shift energy demands. Therefore, a DMSI that combines the above two adjustable sections has tremendous potential for increasing the flexibility of MESs.

The awareness and excavation of the flexibility in DMSIs can bring enormous benefits for both the utility system and the end-users. For the utility system, system operators can better allocate flexible resources between the supply and demand sides [6] to reduce price spikes in the energy market [7]. Besides, the pressure of high investment in traditional flexible fossil-fired units can be significantly alleviated [8]. For the demand system, local aggregators can optimize the operation of DMSIs in the energy market environment and further adjust their participa-

tion in various energy markets, thereby reducing the energy purchase cost [9]. The previous results have shown that the flexibility of the demand-side resources can contribute to the economic and environmental benefits for the whole society [10]. Therefore, it is urgent to explore the flexibility of the DMSI to provide flexible resources for the optimal operation of MESs.

There have been several researches to explore the integrated flexibility of MESs. Reference [11] models and evaluates the flexible demand in heat and electricity integrated systems. Reference [12] proposes a scheme to evaluate the flexible natural gas load in natural gas systems. Reference [13] characterizes the allowable range of active and reactive power outputs of a virtual power plant to incorporate the operation of the virtual power plant in utility system operation and market clearing. These references mainly evaluate the flexibility of the DMS for a single energy sector such as electric flexibility. Due to the multi-energy integration in the MES, the flexibility of different energy vectors can be interrelated and the evaluation method for a single energy sector may not be applicable. A flexible region could be adopted to describe the flexibility of the demand side for different energy sectors. References [14,15] introduce a feasible region to evaluate the integrated flexibility of the DESS. In general, these studies construct different ways to explore the flexible resources mainly from the DESS and make great contributions to the improvement of the integrated flexibility of MESs. Nevertheless, the integrated flexibility of the terminal loads should be further explored and mathematically described, especially that of the IL. As a large share of the terminal load, the absence of the IL cannot comprehensively excavate the flexibility of the DMSI, resulting in a waste of flexible resources. In this context, this study proposes a method to construct a feasible region to evaluate the integrated flexibility of the DMSI which consists of the DESS and the IL.

On the demand side, there are many studies dedicated to exploring the flexibility of the terminal load. References [16–18] excavate, model, and quantify the flexibility of smart appliances such as washing machines, dishwashers, and tumble dryers. Reference [19] evaluates the flexibility provided by the aggregated air conditions for power system operation. Reference [20] utilizes thermal energy storage in the form of hot water storage and storage in building material to optimize the operation of the residential electro-thermal equipment for the provision of electric flexibility. These references mainly focus on the flexibility of the residential loads. Compared with the residential loads, the IL has multiple manufacturing processes and the flexibility of these manufacturing processes is coupled. In other words, if a process keeps reducing production for decreasing energy consumption, its subsequent processes cannot maintain production since the raw materials for the subsequent processes could run out [21]. Besides, since the IL has a variety of energy demands, the flexibility of different energy vectors may be coupled and simultaneous. Considering that, this study mainly focuses on the integrated flexibility of the industrial loads.

In terms of the industrial loads, there are also many researches studying the flexibility of the industrial processes. Reference [22] summarizes the challenges

and opportunities of building a flexible industry that could produce different products according to customers' requirements. References [23,24] propose the flexible production planning to arrange and execute different production orders within limited time and limited machinery resources. In the area of industry research, the flexibility is mainly concerned with the adjustment of products or materials. Besides the material adjustment, the flexibility of the terminal load in this chapter focuses more on the adjustment of multi-energy consumption provided by the energy converters or the adjustable manufacturing processes. In this context, the flexibility definitions and modeling methods of the aforementioned references may not be applicable to describe the integrated flexibility of the IL in this chapter.

On the other hand, several studies have been conducted to manage the optimal operation of the IL from the view of energy consumption. Reference [25] identifies the flexibility options in the manufacturing processes to accommodate renewable energy and achieve the net-zero target for factories. Reference [26] sizes energy storage systems and production buffer stocks as the flexibility options to maximize the matching between renewable energy generation and flexible demand in factories for the net-zero target. Reference [27] divides the processing tasks in industrial facilities into non-schedulable tasks and schedulable tasks to facilitate their participation in the electric DR. Reference [28] utilizes a multi-state model to describe the operation of each workstation and constructs possible penalties in case the production target is not met. Reference [29] proposes a DR scheme for steel powder manufacturing based on the real-time electric price. Reference [30] models the refinery process and proposes an electric DR scheme to shift the demand from peak to non-peak periods. Reference [31] divides the tasks into non-schedulable tasks, schedulable tasks, and storage tasks and proposes a coupling model for the production process and the DESS. These researches mainly focus on the optimal adjustment of the IL considering energy prices and economic incentives. Besides, most of them model the energy consumption and the production of the IL by several operating points, which limits the flexibility in practice. Therefore, the integrated flexibility that the DMS can provide for multiple energy sectors is not elaborately characterized.

In order to facilitate the excavation and utilization of more flexible resources by system operators, it is essential to develop an effective methodology to evaluate the flexibility of the DMSI considering multi-energy conversion and adjustable production plans. Due to the interaction between the DESS and the IL, the flexibility evaluation of the DMSI can be more complicated. At first, enforced by the physical limits of energy converters in the DESS, the energy conversions between electricity, gas, and heat are closely correlated and interdependent. Utilizing or restricting the flexibility of one type of energy could inevitably affect that of the others. Moreover, the reduction of the IL may affect the production process due to the positive correlation between its energy consumption and production. Considering the huge default losses and credit losses caused by unfulfilled production targets, the DMSI can only adjust the IL's production plan to provide flexibility un-

der the premise of ensuring the production target. Furthermore, the operation of various energy converters in the DESS can be represented by their input and output energy flows, while the processing of the IL should be modeled by the input energy flows, input material flows, and output material flows of different manufacturing processes. Considering that, a unified form should be proposed to model the energy converters and the adjustable manufacturing processes together, which could facilitate the complex coupling of energy flows and material flows in the DMSI. Furthermore, the energy-material integrated model should be able to generate various constraints and coupling matrices for different energy converters and manufacturing processes in a unified and compact form. In this context, the energy-material relationship of different manufacturing processes and the multi-energy relationship of different converters can be modeled with similar steps and into a unified form. On this basis, the integrated flexible region can be further excavated considering both the energy conversion constraints and the production limits.

In order to address the aforementioned research gaps, this chapter aims to excavate and characterize the integrated flexibility of the DMSI. The main contributions of this chapter can be summarized as follows:

(1) This chapter innovatively proposes a method to explore the integrated flexibility of the DMSI considering the joint adjustment between the DESS and the IL. Both the physical limits of multi-energy converters in the DESS and the production targets of the production process in the IL are considered in the flexibility excavation of the DMSI.

(2) An energy-material integrated model based on the energy hub (EH) abstraction is proposed to describe the operating characteristics of the DESS and the IL in a unified manner. First, the IL is divided into four subtasks considering the characteristics of the production process and energy consumption. In accordance with the energy flow modeling between different components in the DESS, the material flows between different subtasks of the IL are then modeled. By combining the IL and the DESS models, an energy-material integrated model of the DMSI can be obtained to describe the interaction between energy and material flows. With the proposed method, the modeling of the energy converters and industrial subtasks is in a unified form and compactly automated, which is applicable to a wide variety of DMSIs.

(3) The integrated flexibility is mathematically characterized by an integrated flexible region (IFR) based on the polytopic projection. In this context, a calculation method based on vertex enumeration is proposed to find the feasible region of the DMSI. By projecting the feasible region into the space of input energy vectors, the IFR of the DMSI is explored, in which the multi-energy inputs of the DMSI can be simultaneously adjusted.

This chapter includes research related to the integrated demand response provided by industrial loads by [32].

10.2 Flexibility illustration of integrated demand response provided by industrial loads

10.2.1 The structure of distributed multi-energy systems with industrial loads

As illustrated in Fig. 10.1, the DMSI usually contains the DESS and the IL that are located on the demand side of the entire energy supply chain. The DESS obtains the energy directly from the utility side and then adjusts the multi-energy proportion with its energy conversion devices to supply the IL. The IL is the terminal load served by its coupled DESS. As mentioned before, the IL has a variety of energy requirements, including electricity, natural gas, thermal energy, etc. Natural gas is an important energy resource in the industry. It can be used as raw material for producing chemical products and fuel for cutting and welding [33]. Thermal energy also has a wide variety of applications in industry, including bleaching in textile industries, drying in painting processes, and much more [34].

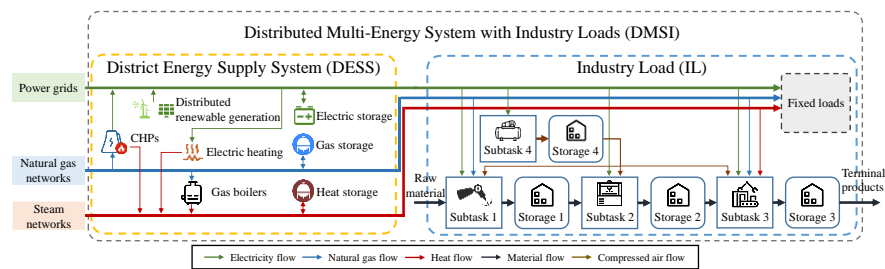


Fig. 10.1. The framework of the district energy supply system and industrial loads

1) District energy supply system

The DESS consists of renewable energy sources, energy converters, and energy storages. As shown in Fig. 10.1, the DESS has multi-energy inputs from the power grid, the natural gas network, and the steam network on the utility side. Renewable energy sources such as solar photovoltaic and wind power could also provide power for the local electric system [35]. The energy converters are devices that realize energy conversion among different energy carriers. For example, the CHP consumes natural gas to generate electricity and heat. The electric heating equipment and the gas boiler generate heat through the consumption of electricity and natural gas, respectively. The storage equipment for different energy sources can store and release energy.

By means of energy conversion devices and energy storage devices, the multi-energy inputs of the DESS can be alternative and flexible. For instance, the DESS can reduce its electricity input without limiting the terminal electricity load by generating more electricity from its CHP. Moreover, when the pressure in gas pipelines drops, the DESS can cut off the CHP and acquire more energy from the power grid. In conclusion, the DESS can provide flexibility for the operation of the MES.

2) Industrial loads

Generally, the IL consists of two different load categories during the industrial process, including fixed loads and schedulable loads from production equipment. Since fixed loads are not adjustable, such as lighting and security loads, this chapter mainly focuses on the adjustable equipment considering the production process. In specific, the processing of materials by a device is called a step. In the entire industrial process, many steps are forced by strict sequence restrictions and time restrictions. Certain steps must be carried out in order, and the output material of the previous step has to enter the next step immediately. These specific steps with strict time and sequence constraints can be integrated into aggregated subtasks. As long as a subtask has its own raw material, the subtask can carry out its production process independently, and the intermediate material produced by the subtask can be stored. Fig. 10.2(a) illustrates a typical subtask in industry, namely the sheet metal fabrication. This subtask consists of steps such as shearing, punching, welding, and surface treatment. Since the devices in each step of the assembly line are different, the production adjustment of this subtask should consider the coordination and interdependence of these steps.

Therefore, it is obvious that adjusting the operation of a device in the IL independently is inappropriate. Assembly lines at the subtask level rather than devices at the device level should be modeled and scheduled to study the flexibility of the IL. In other words, in the example of Fig 10.2(a), what needs to be concerned is the production and energy consumption of the sheet metal fabrication rather than those of a step.

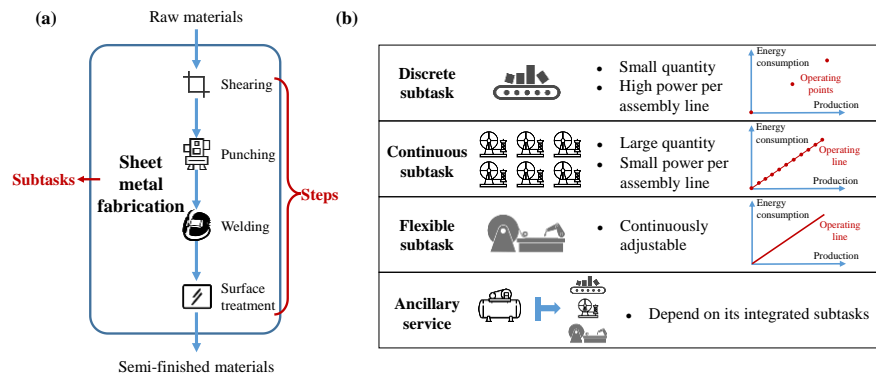


Fig. 10.2. The framework of subtasks in industry: (a) the difference between steps and subtasks; (b) the difference between different types of subtasks

With adjustable subtasks and redundant production capacity, the IL can reschedule its production plan to transfer part production from the peak-load period to the valley-load period. Consequently, the multi-energy demands can be regulated in a certain range according to the production plan. For instance, the IL in Fig. 10.1 has fixed loads, three productive subtasks, an ancillary subtask, and material

storages. Subtask 1 consumes electricity, natural gas, and ancillary materials to produce its intermediate products. The DMSI can reduce the production of Subtask 1 to limit electricity and gas consumption. Meanwhile, Subtask 2 can maintain production without interference as long as there is sufficient inventory for intermediate products of Subtask 1.

In order to explore the adjustability of subtasks comprehensively and precisely, the subtasks are further divided into four categories according to their load characteristics to better describe the relationship between production and energy consumption as shown in Fig. 10.2(b).

(1) Discrete subtasks

The energy consumption and production of discrete subtasks only switch between a few fixed operating points. The assembly lines of discrete subtasks have the characteristics of high power, small quantity, and non-adjustment. The typical case is the coiling process and the traditional final assembly line. When the production needs adjusting, such subtasks can only shut down or start part of their assembly lines, resulting in that they can only be switched between a few operating points.

(2) Continuous subtasks

The energy consumption and production of continuous subtasks can be adjusted approximately continuously. The assembly lines of continuous subtasks have the characteristics of small power, large quantity, and non-adjustment. The typical case is the weaving process and the injection modeling process. This type of subtask also adjusts the production by shutting down or starting their assembly lines. However, due to the small power of a single unit and the large overall quantity, the relationship between energy consumption and production can be considered continuous. For countable materials, there could be a small error in using continuous numbers to describe countable materials. However, for continuous subtasks with large quantities of countable materials, the small error is acceptable.

(3) Flexible subtasks

The energy consumption and production of assembly lines in flexible subtasks can be continuously adjusted. The typical case is the surface mounted technology (SMT) process. Therefore, the relationship between energy consumption and the production of flexible subtasks is continuous.

(4) Ancillary services

Ancillary service is a special subtask whose function is to provide ancillary materials for other subtasks. For instance, the ancillary service of the compressed air can provide compressed air to the final assembly line and the injection modeling process. Therefore, the operation and energy consumption of the ancillary service depend on those of its integrated subtasks.

In Fig. 10.1 Subtask 4 is an ancillary subtask and Subtasks 1-3 are productive subtasks which could be discrete subtasks, continuous subtasks, or flexible subtasks. To avoid confusion, it should be pointed out that not every industrial plant has exactly these four subtasks, i.e. a discrete subtask, a continuous subtask, a flexible subtask, and an ancillary subtask. The composition and connection of sub-

tasks in different industrial plants are not the same. The four categories are proposed to classify the existing subtasks, facilitating the modeling and the IFR excavation of the IL.

10.2.2 The basic concept of integrated flexibility

Generally, the integrated flexibility can be defined as the multi-energy adjustment ability of the distributed energy supply system and its terminal multi-energy loads to adjust their multi-energy demands without violating the internal security constraints and production targets. The alterable combination of multiple energy demands of the DMSI constitutes an integrated flexible region (IFR) as shown in Fig. 10.3. Taking the DMSI in Fig. 10.1 as an example, it contains three kinds of energy inputs, i.e. electricity, heat, and natural gas. The input energy demand is the red point in the three-dimensional space as shown in Fig. 10.3(a). When considering the flexibility provided by the IL, the input energy demand can move within a certain range, which is marked as the blue sphere. If the DESS and the IL are simultaneously adjusted, the IFR is further expanded to the green sphere. Regarding the flexibility of single energy at different times, e.g. electricity, its IFR can transform from the red line to the blue area considering the adjustment of the IL as shown in Fig. 10.3(b). After considering the flexibility of the DESS, its IFR can further expand to green areas.

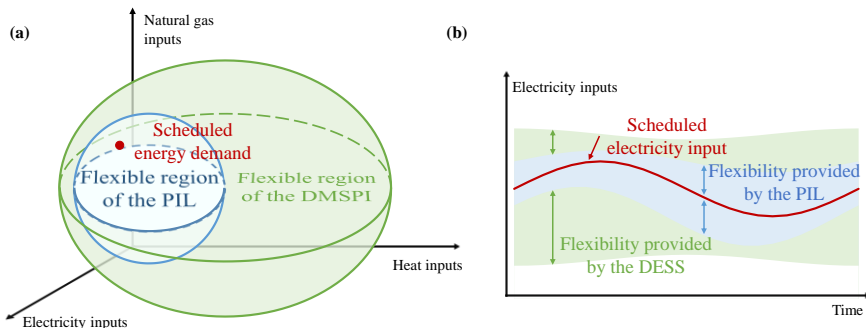


Fig. 10.3. The integrated flexibility of the DESS and IL: (a) integrated flexibility at a certain time; (b) electricity flexibility over a period of time

In general, in the interaction between the DMSI and the utility system, the DMSI only provides the utility operators with the IFR. The utility operators do not need to attain the internal information of the IL but receive the IFR from the DMSI to dispatch the flexible resources on the demand side. With the application of the IFR, the utility system operators can easily confirm the adjustable capacity at the demand side without acquiring privacy information from the local systems. For the demand-side systems, the IFR can help them interact with the operation of the utility system and participate in the energy market for more benefits, which further promotes the development of distributed renewable energy.

10.3 Operation modeling of industrial loads considering energy conversion and production tasks

In this section, the modeling of the DESS based on the EH is first presented. A new element, i.e. the bus, is proposed to simplify the conventional EH model. Then, operating constraints and production target constraints are constructed for the modeling of the IL and an energy-material integrated model is proposed to characterize the operation and connection of the DESS and the IL.

10.3.1 Modeling of the DESS

According to reference [36], the operating characteristic of the DESS can be modeled based on the standardized matrix modeling method. The introduced model develops the characteristics of equipment in DESS based on the graph theory as shown in Fig. 10.4. There are three key elements in the DESS topology constructed by the method, i.e., node, port, and branch. A node represents an energy converter. A port is an abstract place for the energy input and energy output of a node. Each node has a fixed number of input ports and output ports. When a node outputs the same kind of energy to other nodes, these energy flows are output from one port. Similarly, when the same kind of energy inputs to a node, these energy flows are input to one port of the node. A branch represents an energy flow from or to a node.

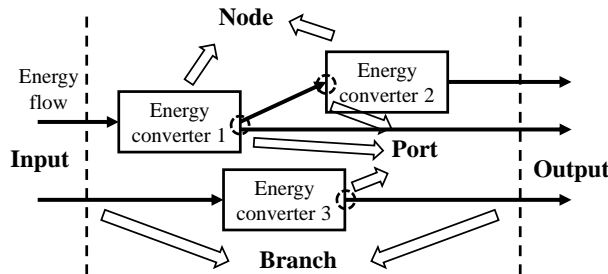


Fig. 10.4. The framework of standardized EH models for the DESS

However, when the system structure is complex, the standardized matrix model introduces a lot of branches, making the model redundant. Since some nodes have no direct physical connection with other nodes, the non-existent branches can make the introduced matrix contain many unnecessary elements. In this context, a new element, i.e. a bus, is proposed. A bus is the abstraction of a distributed energy network. Taking the system in Fig. 10.5 as an example, the system structure changes from Fig. 10.5(a) to Fig. 10.5(b) after introducing the bus. Buses can be regarded as special nodes, however, they have the following differences: 1) Nodes convert different types of energy, so the input and output energy types are usually different; while buses integrate the same type of energy, so the input and output energy types are the same. 2) Nodes may have multiple input or output ports for

their input or output may have multiple types of energy, while buses only have one input port and one output port. 3) The physical carrier of a node is an energy converter, while that of a bus is a distributed energy network.

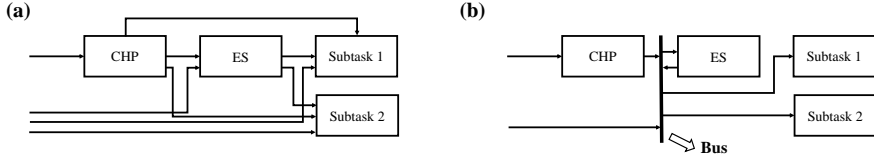


Fig. 10.5. The structure of a system modeled by (a) the conventional standardized matrix model and (b) the improved model

With the introduction of the bus, the number of ports of the original nodes in the system does not change, whereas the number of branches in the system can be reduced. For instance, the number of branches is reduced from 8 in Fig. 10.5(a) to 6 in Fig. 10.5(b). When a system has a large variety of equipment and complex energy flows, the improved method can make better use of its advantages to reduce redundant branches.

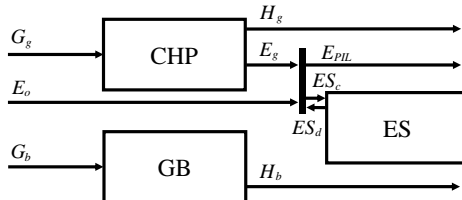


Fig. 10.6. The structure of a DESS

Based on the concept of the EH, energy conversion equations, operating constraints, energy storage constraints, and energy balance equations are sequentially formulated to model the DESS. Taking the DESS in Fig. 10.6 as an example, it has three nodes, one bus, and nine branches. The nodes consist of a combined heat and power (CHP) unit, a gas boiler (GB), and an electricity storage (ES). The set of branches (energy flows) can be expressed as:

$$\mathbf{F}_{DESS} = [G_g, E_g, H_g, E_o, ES_c, ES_d, G_b, H_b, E_{PIL}]^T \quad (10.1)$$

where G_g and G_b are natural gas consumption flows of the CHP and the GB, respectively. H_g and H_b represent the heating generation flows of the CHP and the GB, respectively. E_g is the electricity generation flows of the CHP. ES_c and ES_d represent the charging and discharging energy flows of the ES. E_o refers to the input electricity flow from the power grid. E_{PIL} represents the output electricity flow to the terminal IL.

(1) Energy conversion equations

Energy conversion equations define the relationship between the input and output of energy flows in each energy conversion node. They represent that the sum of the energy output is equal to the sum of the energy input multiplied by the conversion efficiency. The specific steps to formulate energy conversion equations are shown as follows:

First, a port-branch incidence matrix is formulated to define the connections between the ports of a node and branches. Taking the CHP as an example, the connections between the ports and the branches can be written as:

$$\mathbf{J}_{CHP} = \begin{bmatrix} 1 & 0 & 0 & | & \\ 0 & -1 & 0 & | & \mathbf{0}_{3 \times 6} \\ 0 & 0 & -1 & | & \end{bmatrix} \quad (10.2)$$

where the element $J_{p,b}$ of \mathbf{J}_{CHP} equals 1 if the p th port of the CHP is the sink of branch b , equals -1 if the p th port is the source of branch b , and equals 0 otherwise.

Second, a converter characteristic matrix is formulated to describe the energy conversion efficiency. The energy conversion of the CHP can be expressed as:

$$\mathbf{K}_{CHP} = \begin{bmatrix} \eta_G^e \lambda_{gas} & 1 & 0 \\ \eta_G^h (1 - \eta_G^e) \lambda_{gas} & 0 & 1 \end{bmatrix} \quad (10.3)$$

where the rows reflect the numbers of energy conversion processes and the columns represent the numbers of ports. For instance, the CHP has two energy conversion processes, i.e. gas to electricity and gas to heat, and three ports. Therefore, the \mathbf{K}_{CHP} has two rows and three columns. The element $K_{pr,p}$ equals the energy efficiency if the p th port is the input of process pr , equals 1 if the p th port is the output of process pr , and equals 0 otherwise. η_G^e and η_G^h represent the electric generation ratio and heating generation ratio. λ_{gas} is the calorific value of natural gas.

Third, the nodal energy conversion matrix of the CHP node can be expressed as:

$$\mathbf{C}_{CHP} = \mathbf{K}_{CHP} \mathbf{J}_{CHP} \quad (10.4)$$

To sum up, the energy conversion equation of the CHP node can be expressed as:

$$\mathbf{C}_{CHP} \mathbf{F}_{DESS} = \mathbf{0} \quad (10.5)$$

(2) Operating constraints

In the operation, the energy flow is constrained by the capability of the energy converters:

$$\bar{\mathbf{F}}_{DESS,\min} \leq \mathbf{F}_{DESS} \leq \bar{\mathbf{F}}_{DESS,\max} \quad (10.6)$$

where $\bar{\mathbf{F}}_{DESS,\min}$ and $\bar{\mathbf{F}}_{DESS,\max}$ represent the minimum and maximum limits of energy flows enforced by the converter capability.

(3) Energy storage constraints

Different from ordinary energy conversion nodes, the input energy and output energy of an energy storage node are not the same in quantity. In order to describe the increment of the energy, a virtual port, and a virtual branch are introduced to construct an augmented port-branch incidence matrix. Taking the electric storage in Fig. 10.6 as an example, the set of branches with the virtual branch is written as:

$$\mathbf{F}'_{DESS} = [\Delta S_{ES}, \mathbf{F}_{DESS}^T]^T \quad (10.7)$$

If the virtual port, the input port, and the output port are respectively numbered as port 1, port 2, and port 3, the augmented port-branch incidence matrix of the electric storage can be expressed as:

$$\mathbf{J}_{ES} = \left[\begin{array}{c|ccccc|c} -1 & 0 & 0 & 0 & 0 & 0 & \rightarrow \text{virtual port} \\ 0 & 0 & 0 & 0 & 1 & 0 & \rightarrow \text{input port} \\ 0 & 0 & 0 & 0 & 0 & -1 & \rightarrow \text{output port} \\ \hline \Delta S_{ES} & \underbrace{0 \ 0 \ 0 \ 0}_{\mathbf{F}} & & & & & \end{array} \right] \quad (10.8)$$

where the element J_{ES} equals -1 in the virtual port row and the virtual branch column, and 0 otherwise.

The converter characteristic matrix of the energy storage node has only one row, since the energy storage charges and discharges the same variety of energy, which is equivalent to an energy conversion process. Considering the virtual branch, the converter characteristic matrix is augmented to:

$$\mathbf{K}_{ES} = \begin{bmatrix} 1 & \eta_c & \frac{1}{\eta_d} \end{bmatrix} \quad (10.9)$$

where the element K_{ES} in the virtual port column equals 1. η_c and η_d refer to the charging and discharging ratio, respectively.

With the port-branch incidence matrix and the converter characteristic matrix, the nodal energy conversion matrix and the energy conversion equation of the electric storage node are presented in (10.10) and (10.11), respectively.

$$\mathbf{C}_{ES} = \mathbf{K}_{ES} \mathbf{J}_{ES} \quad (10.10)$$

$$\mathbf{C}_{ES} \mathbf{F}'_{DESS} = \mathbf{0} \quad (10.11)$$

Furthermore, the charging constraint, the discharging constraint, and capacity constraints of the electric storage node are presented:

$$\begin{cases} -\Delta \bar{S}_{ES,\min} \leq \Delta S_{ES} \leq \Delta \bar{S}_{ES,\max} \\ \bar{S}_{ES,\min} \leq \Delta S_{ES} + S_{ES,t-1} \leq \bar{S}_{ES,\max} \end{cases} \quad (10.12)$$

where $\Delta\bar{S}_{ES,\max}$ and $\Delta\bar{S}_{ES,\min}$ refer to the maximum charging and discharging rate, respectively. $\bar{S}_{ES,\max}$ and $\bar{S}_{ES,\min}$ are the maximum and minimum storage, respectively. $S_{ES,t-1}$ represents the state of charge (SOC) of the electric storage.

(4) Energy balance equations

For the proposed element bus, the energy balance equations can be formulated using the same method for energy conversion equations. Taking the electric bus in Fig. 10.6 as an example, the port-branch incidence matrix can be written as:

$$\mathbf{J}_{EB} = \begin{bmatrix} 0 & 1 & 0 & 1 & 0 & 1 & 0 & 0 & 0 \\ 0 & 0 & 0 & 0 & -1 & 0 & 0 & 0 & -1 \end{bmatrix} \quad (10.13)$$

The first row represents the connection between the input port and the branches. The second row represents the connection between the output port and the branches. The converter characteristic matrix of the bus has one row and two columns. The elements in the matrix all equal 1.

$$\mathbf{K}_{EB} = [1 \ 1] \quad (10.14)$$

The nodal energy conversion matrix and the energy balance equation for the electricity bus are given in (10.15) and (10.16), respectively.

$$\mathbf{C}_{EB} = \mathbf{K}_{EB} \mathbf{J}_{EB} \quad (10.15)$$

$$\mathbf{C}_{EB} \mathbf{F}_{DESS} = \mathbf{0} \quad (10.16)$$

10.3.2 Modeling of the IL

According to the concept of the IL's subtasks and the EH models, an energy-material integrated model considering industrial loads is established as illustrated in Fig. 10.7. In the proposed model, a node can not only represent an energy converter, but also a subtask of the IL. A port can simultaneously represent the abstraction of the energy conversion and the material conversion. A branch can not only represent an energy flow, but also a material flow. A bus still represents a distributed energy network.

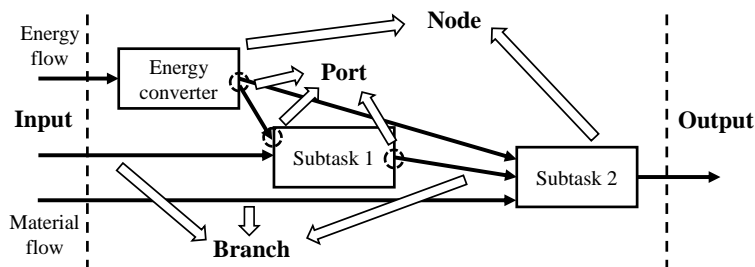


Fig. 10.7. The framework of proposed energy-material integrated models for the DMSI

In this context, energy and material conversion equations, operating constraints, material storage constraints, energy balance equations, and subtask production target constraints are sequentially formulated to model the IL. Taking the IL in Fig. 10.8 as an example, it has five nodes and eleven branches. The nodes consist of three subtasks and two material storages. The set of integrated branches (energy flows and material flows) can be expressed as:

$$\mathbf{F}_{PIL} = [H_1, E_1, E_2, E_3, RM_1, RM_2, IM_1, IM_2, IM_{13}, IM_{23}, IM_3]^T \quad (10.17)$$

where E_1 , E_2 , and E_3 are electricity consumption flows of Subtask 1, Subtask 2, and Subtask 3, respectively. H_1 is the heat consumption flow of Subtask 1. RM_1 and RM_2 are input material flows of Subtask 1 and Subtask 2, respectively. IM_1 , IM_2 , and IM_3 represent production flows of Subtask 1, Subtask 2, and Subtask 3, respectively. IM_{13} and IM_{23} are input material flows of Subtask 3.

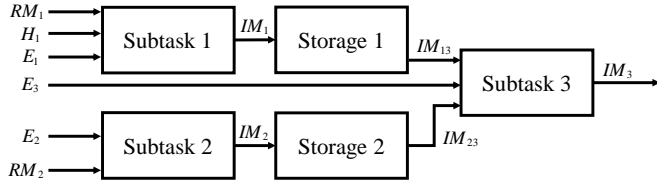


Fig. 10.8. The structure of an IL

(1) Energy and Material Conversion Equations

Energy and material conversion equations define the relationship between the input and output of energy flows and material flows in each energy conversion node and subtask node. They model the relationship between the input (including energy input and raw material input) and the material production. Different materials are imported or exported in a certain proportion which is presented by several correlation parameters in the energy and material conversion equations. Moreover, the energy consumption and the raw material consumption are modeled as linear or piecewise linear relationships with the production. Taking Subtask 1 as an example, the energy and material conversion equation in (10.21) is composed of the port-branch incidence matrix in (10.18), the converter characteristic matrix in (10.19), and the nodal conversion matrix in (10.20).

$$\mathbf{J}_{T1} = \left[\begin{array}{cc|cc|cc} 1 & 0 & 0 & 0 & 0 \\ 0 & 1 & \mathbf{0}_{4 \times 2} & 0 & 0 & 0 \\ 0 & 0 & & 1 & 0 & 0 \\ 0 & 0 & & 0 & 0 & -1 \\ \hline H_1 & E_1 & & RM_1 & & IM_1 \\ \end{array} \right] \quad (10.18)$$

$$\mathbf{K}_{T1} = \begin{bmatrix} \kappa_T^h & 0 & 0 & 1 \\ 0 & \kappa_T^e & 0 & 1 \\ 0 & 0 & \kappa_T^{rm} & 1 \end{bmatrix} \quad (10.19)$$

$$\mathbf{C}_{T1} = \mathbf{K}_{T1} \mathbf{J}_{T1} \quad (10.20)$$

$$\mathbf{C}_{T1} \mathbf{F}_{PIL} - \mathbf{A} = \mathbf{0} \quad (10.21)$$

where κ_T^h , κ_T^e , and κ_T^{rm} represent the heating consumption rate, the electricity consumption rate, and the raw material consumption rate of Subtask 1. \mathbf{A} is a given $_{1 \times 11}$ matrix. The element $A_{l,f}$ is a constant term in the linear relationship between energy consumption and production.

(2) Operating constraints

The operating constraints of different subtasks are related to their production characteristics. According to the classification of subtasks in chapter 10.2.1, Subtask1, Subtask 2, and Subtask 3 in Fig. 10.8 are set as a discrete subtask, a continuous subtask, and a flexible subtask, respectively.

For Subtask 1 (discreet subtasks), the adjustment of production is through shutting down or starting part of assembly lines. Therefore, the total production volume is an integer multiple of a unit production volume:

$$IM_1 = c \cdot \overline{IM}_1 \quad \overline{IM}_1 = 0, 1, 2, \dots, n \quad (10.22)$$

where \overline{IM}_1 represents the unit production volume of an assembly line. n is the total number of assembly lines in Subtask 1.

For Subtask 2 (continuous subtasks), the adjustment of production is also through shutting down or starting part of assembly lines. However, the power and production of an assembly line are small and the number of assembly lines is large in a continuous subtask. Therefore, the production can be adjusted approximately continuously and is subject to the maximum production and the minimum production:

$$\overline{IM}_{2,\min} \leq IM_2 \leq \overline{IM}_{2,\max} \quad (10.23)$$

For Subtask 3 (flexible subtasks), the production can be flexibly adjusted, therefore it is also limited by the maximum production and the minimum production:

$$\overline{IM}_{3,\min} \leq IM_3 \leq \overline{IM}_{3,\max} \quad (10.24)$$

Moreover, ancillary services provide ancillary materials for other subtasks. Their operating constraints are modeled using the same methods for other categories of subtasks.

(3) Material storage constraints

Like the energy storage in the DESS, the material storage also brings virtual branches and virtual ports to the original model. The set of branches is augmented to:

$$\mathbf{F}'_{PIL} = [\Delta S_{TS1}, \Delta S_{TS2}, \mathbf{F}_{PIL}^T]^T \quad (10.25)$$

Taking Material Storage 1 as an example, the port-branch incidence matrix and the converter characteristic matrix are formulated in (10.26) and (10.27), respectively. In this context, the nodal energy conversion matrix and the energy conversion equation of Material Storage 1 node are presented in (10.28) and (10.29), respectively.

$$\mathbf{J}_{TS1} = \left[\begin{array}{cc|ccc|c} -1 & 0 & 0 & 0 & 0 & \\ 0 & 0 & \mathbf{0}_{3 \times 6} & 1 & 0 & 0 & \xrightarrow{\text{virtual port}} \\ 0 & 0 & & 0 & 0 & -1 & \xrightarrow{\text{input port}} \\ \hline \Delta S_{TS1} & \Delta S_{TS2} & & IM_1 & & IM_{13} & \xrightarrow{\text{output port}} \end{array} \right] \quad (10.26)$$

$$\mathbf{K}_{TS1} = [1 \ 1 \ 1] \quad (10.27)$$

$$\mathbf{C}_{TS1} = \mathbf{K}_{TS1} \mathbf{J}_{TS1} \quad (10.28)$$

$$\mathbf{C}_{TS1} \mathbf{F}'_{PIL} = \mathbf{0} \quad (10.29)$$

The production storing constraint, the production releasing constraint (which may be limited by the transportation capacity to the linked subtask), and the capacity constraint of material storage nodes are presented:

$$\begin{cases} -\Delta \bar{S}_{TS1,\min} \leq \Delta S_{TS1} \leq \Delta \bar{S}_{TS1,\max} \\ \bar{S}_{TS1,\min} \leq \Delta S_{TS1} + S_{TS1,t-1} \leq \bar{S}_{TS1,\max} \end{cases} \quad (10.30)$$

where $\Delta \bar{S}_{TS1,\max}$ and $\Delta \bar{S}_{TS1,\min}$ refer to the maximum storing and releasing rate, respectively. $\bar{S}_{TS1,\max}$ and $\bar{S}_{TS1,\min}$ are the maximum and minimum storage capacity, respectively. $S_{TS1,t-1}$ represents the material inventory.

(4) Energy balance equations

The energy balance equations can be formulated using the same method in the DESS. In the example of Fig. 10.8, the energy balance equations for the electricity bus are expressed by Eq. (10.13) - (10.16).

(5) Subtask production target constraints

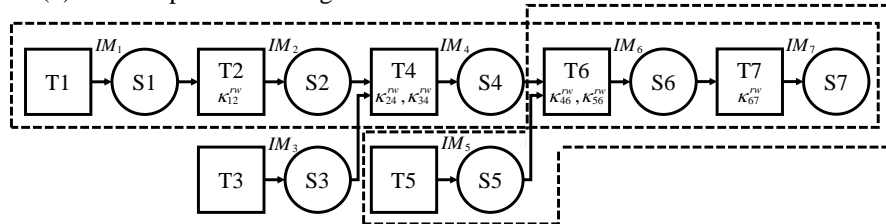


Fig. 10.9. The structure of an IL

The IL provides the system with flexibility for a period of time by shifting part of the production. However, within an entire production cycle, the scheduled total production volume must be met. Therefore, for Subtask i , if the production IM_i

is reduced at time t , the existing inventory ($\Delta S_i + S_{i,t-1}$) plus the maximum production in subsequent periods ($\sum_{t+1}^T \overline{IM}_{i,\max}$) should be greater than the scheduled production volume (TA_i) plus the consuming production by subsequent subtasks in subsequent periods.

The consuming production by subsequent subtasks is formulated based on the unidirectional material flow from node i to the output node. Taking a complex IL in Fig. 10.9 as an example, the consuming production IM_1 of Subtask 1 is determined by the production of Subtask 2, Subtask 4, Subtask 6, and Subtask 7. The consuming production IM_5 of Subtask 5 is only determined by the production of Subtask 6 and Subtask 7. Therefore, the schedule constraint of Subtask 1 is written as:

$$\begin{aligned} \Delta S_1 + S_{1,t-1} + \sum_{t+1}^T \overline{IM}_{1,\max} &\geq TA_1 + \frac{1}{\kappa_{12}^{rm}} (TA_2 - \Delta S_2 - S_{2,t-1}) + \frac{1}{\kappa_{12}^{rm} \kappa_{24}^{rm}} (TA_4 - \Delta S_4 - S_{4,t-1}) \\ &+ \frac{1}{\kappa_{12}^{rm} \kappa_{24}^{rm} \kappa_{46}^{rm}} (TA_6 - \Delta S_6 - S_{6,t-1}) + \frac{1}{\kappa_{12}^{rm} \kappa_{24}^{rm} \kappa_{46}^{rm} \kappa_{67}^{rm}} (TA_7 - \Delta S_7 - S_{7,t-1}) \end{aligned} \quad (10.31)$$

where κ_{ij}^{rm} represents the material conversion ratio from IM_i to IM_j .

Returning to the IL in Fig. 10.8, subtask schedule constraints of the IL can be expressed as:

$$\Delta S_{PIL} + S_{PIL,t-1} + \sum_{t+1}^T \overline{IM}_{\max} - H_{PIL} (\mathbf{TA} - \Delta S_{PIL} - S_{PIL,t-1}) \geq \mathbf{TA} \quad (10.32)$$

where T is the total time of the production cycle. \mathbf{TA} refers to the set of scheduled production volumes of different subtasks. H_{PIL} is an incidence matrix calculated by:

$$H_{i,j} = \begin{cases} 1 / \prod_{i \rightarrow j} \kappa^{rm} & \text{if node } j \text{ is on the unidirectional flow from node } i \text{ to the output node} \\ 0 & \text{otherwise} \end{cases} \quad (10.33)$$

where $\prod_{i \rightarrow j} \kappa^{rm}$ represents the product of all material conversion ratios from node i to node j .

10.3.3 Modeling of the DMSI by combining the DESS and the IL

Integrating the DESS in Fig. 10.6 and the IL in Fig. 10.8, the DMSI is given in Fig. 10.10. The DMSI has eight nodes, three buses, and twenty-one branches. The nodes consist of a CHP, a GB, an ES, three subtasks, and two material storages.

The buses consist of an electric bus, a natural gas bus, and a heating bus. The set of integrated branches (energy flows and material flows) can be expressed as:

$$\mathbf{F} = \left[\mathbf{F}_{DESS}^T, \mathbf{F}_{PIL}^T \right]^T \quad (10.34)$$

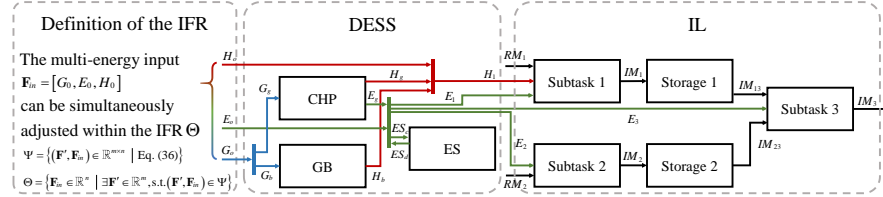


Fig. 10.10. The structure of a DMSI composed of a DESS and an IL

In general, with nodal energy conversion matrices of all energy converters and buses in the DESS and all subtasks in the IL, the system energy conversion matrix of the DMSI can be expressed as:

$$\mathbf{C} = \left[\mathbf{C}_{CHP}^T, \mathbf{C}_{GB}^T, \mathbf{C}_{ES}^T, \mathbf{C}_{EB}^T, \mathbf{C}_{T1}^T, \mathbf{C}_{T2}^T, \mathbf{C}_{T3}^T, \mathbf{C}_{TS1}^T, \mathbf{C}_{TS2}^T \right]^T \quad (10.35)$$

Consequently, comprehensively considering energy and material conversion equations, operating constraints, storage constraints, energy balance equations, and subtask production target constraints in the DESS and the IL, the system operating equations and constraints of the DMSI can be summarized as:

$$\begin{cases} \mathbf{CF}' - \mathbf{A}' = \mathbf{0} \\ \bar{\mathbf{F}}_{DESS,\min} \leq \mathbf{F}_{DESS} \leq \bar{\mathbf{F}}_{DESS,\max} \\ \mathbf{IM}_{ds} = \mathbf{C}_{ds} \cdot \bar{\mathbf{IM}}_{ds} \quad \bar{\mathbf{IM}}_{ds} = 0, 1, 2, \dots, n \\ \bar{\mathbf{IM}}_{cs,\min} \leq \mathbf{IM}_{cs} \leq \bar{\mathbf{IM}}_{cs,\max} \\ \bar{\mathbf{IM}}_{fs,\min} \leq \mathbf{IM}_{fs} \leq \bar{\mathbf{IM}}_{fs,\max} \\ \Delta \bar{\mathbf{S}}_{\min} \leq \Delta \mathbf{S} \leq \Delta \bar{\mathbf{S}}_{\max} \\ \bar{\mathbf{S}}_{\min} \leq \Delta \mathbf{S} + \mathbf{S}_{t-1} \leq \bar{\mathbf{S}}_{\max} \\ \Delta \mathbf{S}_{PIL} + \mathbf{S}_{PIL,t-1} + \sum_{t+1}^T \bar{\mathbf{IM}}_{\max} - \mathbf{H}_{PIL} (\mathbf{TA} - \Delta \mathbf{S}_{PIL} - \mathbf{S}_{PIL,t-1}) \geq \mathbf{TA} \end{cases} \quad (10.36)$$

where \mathbf{C}'_{node} and \mathbf{F}' represent the augmented nodal energy conversion matrix and the augmented branch vector considering virtual branches brought by energy storage and material storage, respectively. \mathbf{IM}_{ds} , \mathbf{IM}_{cs} , and \mathbf{IM}_{fs} refer to the set of the output material flows of discrete subtasks, continuous subtasks, and flexible subtasks, respectively. $\Delta \mathbf{S}$ represents the set of energy storage increments and material storage increments.

10.4 The method to determine the flexible region of industrial loads

10.4.1 Modeling of the integrated flexible region

As shown in Fig. 10.10, the energy conversion and the production plan adjustment can constitute an IFR of multi-energy inputs. The multi-energy input of the DMSI \mathbf{F}_{in} can be simultaneously adjusted within a feasible region represented by Θ . Based on the integrated model of the DESS and the IL, the input of the DMSI can be described as:

$$\mathbf{F}_{in} = \mathbf{H}_{in}\mathbf{F}' \quad (10.37)$$

where \mathbf{H}_{in} represents the incidence matrix to extract the input element from the set of branches. In the example of Fig. 10.10, $\mathbf{F}_{in} = [G_0, E_0, H_0, RM_1, RM_2]$. Considering only the energy input, the input of the DMSI is $\mathbf{F}_{in} = [G_0, E_0, H_0]$.

In general, based on the DMSI operating equations and constraints, the feasible region of $(\mathbf{F}', \mathbf{F}_{in})$ can be formulated as:

$$\Psi = \{(\mathbf{F}', \mathbf{F}_{in}) \in \mathbb{R}^{m \times n} \mid \text{Eq. (10.36)}\} \quad (10.38)$$

where „ m “ and „ n “ represent the number of all branches in the DMSI and the number of input branches, respectively.

The operating constraints equations and constraints in Eq. (10.36) are linear and the state variable \mathbf{F}' is bounded. Therefore, Ψ is a bounded polyhedron, which is termed a polytope. The IFR can be mathematically defined as the projection of Ψ onto to subspace of \mathbf{F}_{in} :

$$\Theta = \{\mathbf{F}_{in} \in \mathbb{R}^n \mid \exists \mathbf{F}' \in \mathbb{R}^m, \text{s.t. } (\mathbf{F}', \mathbf{F}_{in}) \in \Psi\} \quad (10.39)$$

It should be noted that since Ψ is a polytope, the projected region Θ of Ψ is also a polytope which has been proved in reference [37]. The IFR maps all the feasible operating states of the DMSI to the energy input vector. On this basis, the operation of the energy delivery and generation can be scheduled more optimally and flexibly without interfering with the independent operation of the local systems.

10.4.2 The calculation method

In order to calculate the projection of the polytope, a method based on vertex enumeration is proposed. First, we select free variables from all branch variables. Free variables are defined as any two branch variables that are linear independent. Then, all vertices of the polytope in the space of free variables are enumerated and projected to the subspace of the input variables. Finally, compare these projection points in the subspace and retain vertices. The flow chart of the calculation procedures is shown in Algorithm 10.1.

(1) Selecting free variables

Considering some variables in the set of branches are linearly correlated, all variables should be divided into two categories, i.e. bound variables and free variables. Bound variables are defined as variables that can be described by a linear combination of one or more free variables. Free variables are linearly independent with other free variables. Taking the branches connected to the CHP node as an example, the input gas flow, the output electricity flow, and the output heating flow are linearly correlated. Therefore, any one of them can be selected as a free variable, and the others are bound variables that can be represented by the linear function of the free variable. Enumerating vertices of the feasible region in the space of free variables can save computing time and resources compared with doing that in the space of all variables. Specific steps are listed as follows:

Step 1. Reform the system energy and material conversion matrix of the DESS and the IL into a row echelon form. Taking the conversion matrix of Subtask 1 in Fig. 10.8 as an example, the row echelon form of Eq. (10.20) is presented as:

$$\mathbf{C}_{T1} = \left[\begin{array}{ccc|ccc|c} \kappa_T^h & 0 & & 0 & 0 & -1 & \\ 0 & \kappa_T^e & \mathbf{0}_{4 \times 2} & 0 & 0 & -1 & \mathbf{0}_{5 \times 4} \\ 0 & 0 & & \kappa_T^{rm} & 0 & -1 & \\ \hline H_1 & E_1 & & RM_1 & & IM_1 & \end{array} \right] \quad (10.40)$$

Step 2. Select the variables corresponding to the leading coefficients of nonzero rows as bound variables and the others are free variables. In Eq. (10.40), H_1 , E_1 , and RM_1 are variables corresponding to the leading coefficients of nonzero rows. Therefore, for Subtask 1, IM_1 can be selected as a free variable.

In general, for the DMSI, reform the system energy and material conversion matrix, i.e. Eq. (10.35), into a row echelon form, and free variables can be selected. Moreover, all variables in the system can be represented by these free variables using an incidence matrix \mathbf{H}_f . Let \mathbf{F}_f and f represent the set of free variables and the number of free variables, respectively. Each constraint in Eq. (10.36) can also be transformed into a constraint on free variables.

$$\mathbf{F}' = \mathbf{H}_f \mathbf{F}_f \quad (10.41)$$

Consequently, the feasible region of $(\mathbf{F}_f, \mathbf{F}_{in})$ is presented in Eq. (10.42) and the IFR reformulated into the projection of Ω is presented in Eq. (10.43).

$$\Omega = \{(\mathbf{F}_f, \mathbf{F}_{in}) \in \mathbb{R}^{f \times n} \mid \text{Eq. (10.36)}\} \quad (10.42)$$

$$\Theta = \{\mathbf{F}_{in} \in \mathbb{R}^n \mid \exists \mathbf{F}_f \in \mathbb{R}^f, \text{s.t. } (\mathbf{F}_f, \mathbf{F}_{in}) \in \Omega\} \quad (10.43)$$

(2) Enumerating vertices and forming the IFR

If an IL has discrete subtasks, there are integer variables in Eq.(10.35), which could make the problem non-convex. To solve this problem, these integer variables are fixed first and the IFR is calculated based on a fixed set of integer variables. Then, combine different IFRs. Specific steps are listed as follows:

Step 1. Fix a set of integer variables.

Step 2. Enumerate vertices of the feasible region Ω . Select f constraints in Eq. (10.36) arbitrarily to form a judgment matrix \mathbf{C}_i . If \mathbf{C}_i is not full of rank, there are linearly correlated constraints among the f constraints, and the next constraint selection continues. If \mathbf{C}_i is full of rank, a unique solution can be obtained, and the solution is a vertex $\mathbf{F}_{f,i}^v$ of polytope Ω . After all the constraint combinations are traversed, all the vertices of polytope Ω can be obtained.

Step 3. Project the vertices of polytope Ω onto the subspace of input energy vector \mathbf{F}_{in} .

Step 4. In the subspace of the input energy vector, calculate the vertices of the convex hulls composed of the projection points, i.e. $\mathbf{F}_{in}^{v \in \Omega}$. The vertices of polytope Θ are represented by $\mathbf{F}_{in}^{v \in \Theta}$. In three-dimensional space, the incremental method [38] can be used to find the vertices of the convex hull.

Algorithm 10.1: Vertex enumeration.

#1 Selecting free variables

- 1: reform \mathbf{C} into a row echelon form.
- 2: select free variables \mathbf{F}_f .

#2 Enumerating vertices and forming the IFR

- 3: for $\overline{IM}_{ds} = 0, 1, 2, \dots, n$
 - 4: for arbitrary f constraints in Eq. (34): \mathbf{C}_i
 - 5: if $rank(\mathbf{C}_i) = f$
 - 6: $\mathbf{F}_{f,i}^v = \mathbf{C}_i^{-1} \mathbf{A}_i$
 - 7: end if
 - 8: end for
 - 9: $\mathbf{B}_f^{v \in \Omega}$ represents the set of the $\mathbf{F}_{f,i}^v$
 - 10: $\mathbf{F}_{in}^{v \in \Omega} = \mathbf{H}_{in} \mathbf{H}_f \mathbf{F}_f^v$
 - 11: the incremental method: $\mathbf{F}_{in}^{v \in \Omega} \rightarrow \mathbf{F}_{in}^{v \in \Theta}$
 - 12: end for
-

10.4.3 Case studies and discussions

1) Illustration of the test system

Based on the integrated EH model, the topological diagram of the DMSI is shown in Fig. 10.11. There are three input energy sources for this system, namely electricity power, natural gas, and heating energy. The equipment in the DESS includes a CHP, an electric heating equipment (EH), a GB, a ES, and a gas storage

(GS). The parameters of the equipment are shown in Table 10.1. The IL in the test system is a real air conditioning equipment manufacturing plant in China. The manufacturing process in the industrial plant can be divided into six subtasks, including the coiling and shearing processing, the sheet metal fabrication, the inner component processing, the electronic components processing, the final assembly processing, and the compressed air production. The first five subtasks are represented as Subtasks 1-5 in turn and the last subtask is represented as Subtask a. The final products of the plant are air conditionings and the specific role of each subtask is presented in Table 10.2.

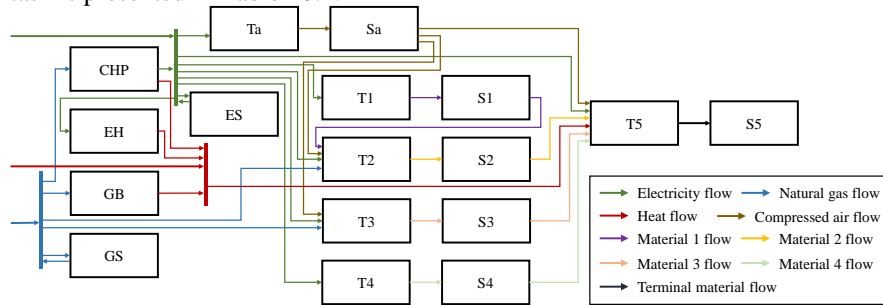


Fig. 10.11. The diagram of the test system

Table 10.1. The parameters of the equipment in the DESS.

Equipment	Power	Capacity	Efficiency
CHP	15-250 m^3/h	-	0.33(η_G^C)/0.64(η_G^h)
EH	0-1000 kW	-	0.9
GB	0-1000 kW	-	0.9
ES	170 kW	96-864 kWh	0.95(η_c)/0.95(η_d)
GS	90 m^3/h	40-500 m^3	0.9(η_c)/0.9(η_d)

Table 10.2. The role of each subtask in the entire manufacturing process.

Subtask	Steps	Energy input	Material input	Material output
Coiling and shearing processing (T1)	Cutting and bending	Power	Raw sheet steel	Steel work cells (IM_1)
Sheet metal fabrication (T2)	Punching	Power and compressed air		
	Welding	Natural gas	IM_1	Shaped encasement parts (IM_2)
	Surface treatment	Power		
Inner component processing (T3)	Injection modeling	Power and compressed air	Raw injection molding material	Plastic parts
	Condenser and evaporator processing	Power and natural gas	Raw metal parts and pumps	Condensers and evaporators

	Inner component assembly	Power	Plastic parts, condensers, and evaporators	Complete inner components (IM_3)
Electronic components processing (T4)	Welding and assembling	Power	Raw electronic parts	Useful electronic components (IM_4)
Final assembly processing (T5)	Assembling Drying	Power Heat	IM_2 , IM_3 , and IM_4	Finished air conditionings (IM_5)
Compressed air production (Ta)	-	Power	Air	Compressed air (IM_a)

Table 10.3. The parameters of different subtasks in the IL.

Sub-task	Type	Unit electricity consumption (kW)	Unit natural gas consumption (m^3/h)	Unit heating consumption (kW)	Unit compressed air consumption (m^3/h)	Equipped storage capacity	Production target
T1	DS	0.93	-	-	-	2100	825
T2	CS	0.71	0.057	-	0.57	1900	1176
T3	CS	7.6	0.4	-	5	150	141
T4	FS	7.14	-	-	-	30	21
T5	FS	7.14	-	1.4	0.71	3600	3359
Ta	AS	1	-	-	-1.1	1240-1760	-
						m^3	

* DS is discreet subtask, CS is continuous subtask, FS is flexible subtask, and AS is ancillary subtask

Utilizing the proposed classification method, T1 is a discrete subtask, T2 and T3 are continuous subtasks, T4 and T5 are flexible subtasks, and Ta is an ancillary subtask. The parameters of these subtasks are shown in Table 10.3. The production of subtasks can be adjusted in hour time scales and the production planning cycle of the IL is one day. The industrial plant carries out the hourly production plan for each subtask one day before the scheduled day. Therefore, the DMSI composed of the DESS and the IL can provide the hourly integrated flexibility for the MES. Moreover, when providing the integrated flexibility, it is required to meet the production targets at the end of each day. The production of T5 represents the terminal materials of the IL, while the production requirements of T1-T4 are to reserve some intermediate materials for the next day's production to ensure continuity between the production cycles. T1 has three assembly lines and the unit production of each is set as 70, which can be formulated by $IM_1 = c \cdot \overline{IM}_1$, $\overline{IM}_1 = 0, 1, 2, 3$, and $c = 70$. The maximum production of other subtasks at differ-

ent times and the day-ahead production schedule of these subtasks are given in Fig. 10.12.

In order to validate the proposed method to explore the IFR of the DMSI, three cases are conducted. Case 1 compares the proposed method with a benchmark to verify the accuracy of the proposed method. Case 2 respectively analyzes IFRs of the DESS and the IL. Besides, their IFRs are compared with that of the DMSI considering the integration of the DESS and the IL. Case 3 analyzes the impacts of fixing one type of input energy on the flexibility of the other input energies. Case 4 analyzes the factors in the IL that affect the IFR of the DMSI, including subtask types and production capacities.

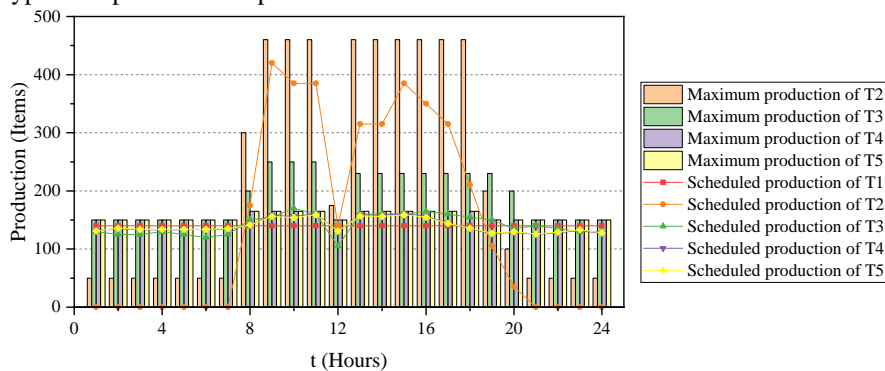


Fig. 10.12. The maximum production and the day-ahead production schedule of subtasks at different times

2) Case 1: the verification of accuracy compared with a benchmark method

In this case, in order to verify the accuracy of the proposed method for describing the boundaries of the integrated flexibility, the proposed method (M_I) is compared with a numerical sampling method (M_II). The numerical sampling method can find feasible solutions by testing all solutions, although the computational efficiency is usually very low. In specific, the M_II discretizes all variables in a certain step and calculates all the numerical feasible points. The convex hull formed by all feasible points is the IFR found by the M_II.

The IFRs of the test system at time ten calculated by the M_I and the M_II are shown in Fig. 10.13. It can be concluded that the IFRs calculated by the two methods are the same within a limited error. In specific, the volume difference between the two IFRs is 0.26%. If the discrete step in the M_II is small enough, the two IFRs should completely coincide.

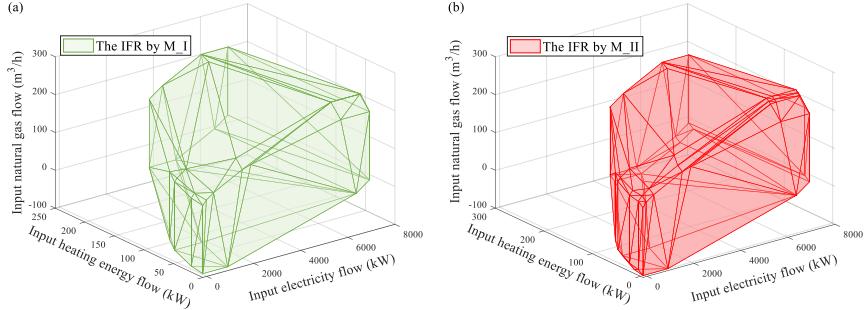


Fig. 10.13. The IFRs at time ten calculated by (a) the vertex enumeration method (M_I) and (b) the numerical sampling method (M_{II})

3) Case 2: the contribution of the IL and the DESS to the IFR of the DMSI

In this case, in order to compare IFRs of the DESS and the IL with that of the DMSI, three scenarios are presented.

Scenario 1 only considers the flexibility of the DESS, while the terminal load, i.e. the IL, is fixed.

Scenario 2 only considers the flexibility of the IL, while the operation of equipment in the DESS is not adjustable.

Scenario 3 takes both the flexibility of the DESS and that of the IL into consideration.

Fig. 10.14 illustrates IFRs of the DESS, the IL, and the DMSI at time ten. The conclusion can be drawn that the integration of the DESS and the IL can provide more flexibility than a single section. The IFR of the IL and the IFR of the DESS complement each other to form a comprehensive IFR of the DMSI. As shown in Fig. 10.14(c) and Fig. 10.14(d), the IL's IFR and the DESS's IFR are part of the IFR of the DMSI. The IFR of the DMSI is not a simple sum of those of the DESS and the IFR, but a superposition in various dimensions. In order to compare the size of each IFR more intuitively, after converting and normalizing different energy inputs in proportion, the volume of the DMSI's IFR is 12.7 times that of the DESS's IFR and 15.1 times that of the IL's IFR.

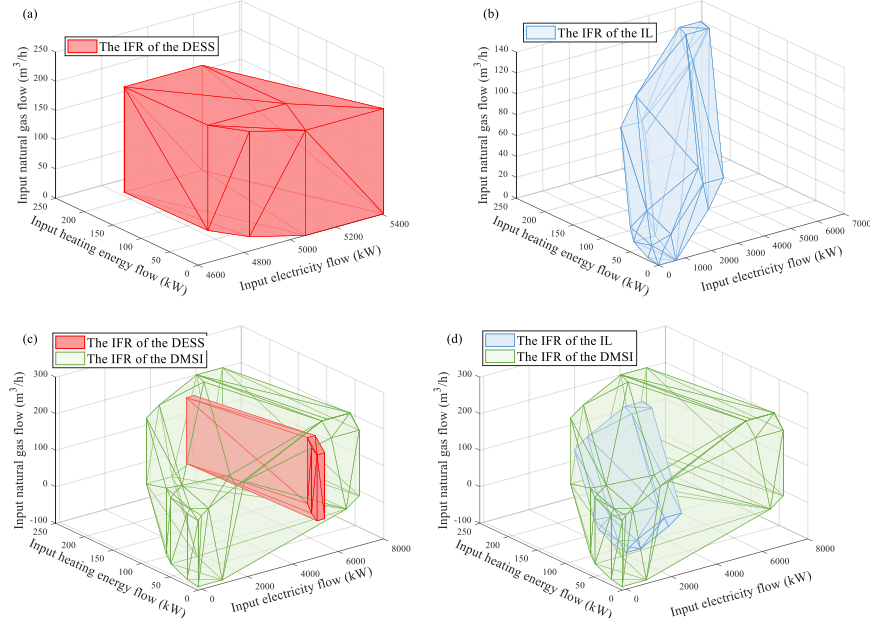


Fig. 10.14. The IFRs at time ten in different scenarios: (a) the IFR of the DESS; (b) the IFR of the IL; (c) the IFRs of the DESS and the DMSI; (d) the IFRs of the IL and the DMSI

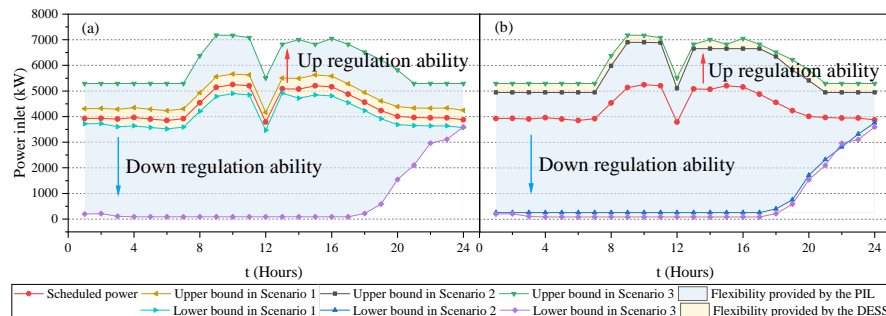


Fig. 10.15. The IFRs projected to the input electricity flow during a whole production planning cycle (a) in Scenarios 1 and 3; (b) in Scenarios 2 and 3

Fig. 10.15 shows the IFRs projected to the input electricity flow during a whole production planning cycle. It also indicates that the input energy can be adjusted in a wider range after considering the integrated flexibility of the DESS and the IL. Moreover, it can be found that the flexibility of the DMSI is reduced during the last time period of the production cycle, especially the down regulation ability. In this context, if the production plan of the DMSI is reduced in the beginning periods, the production cannot be reduced a lot during the last few periods. This is be-

cause if the production is reduced, there will not be enough time to make up for this part of the shortfall and the production target will therefore not be achieved. Furthermore, if the industrial load takes the initiative to increase production in advance, the subsequent production arrangements can be more flexible, enhancing the flexibility during the subsequent time.

4) Case 3: the impact of one fixed input energy on the IFR of the DMSI

In this case, in order to analyze the interaction between the flexibility of various input energy, two scenarios are presented.

In Scenario 1, the heating energy input is fixed. If the terminal IL changes its heating energy demand, the operations of the energy converter in the DESS must be adjusted accordingly.

In Scenario 2, the heating energy input is adjustable.

Since the heating energy input in Scenario 1 is fixed, the IFR in Scenario 1 is a two-dimensional polytope. Moreover, the IFR in Scenario 2 can also be projected onto the same two-dimensional subspace. At time ten, the IFRs in Scenarios 1 and 2 are shown in Fig. 10.16(a). The results show that if the flexibility of one energy input is restricted, the flexible region composed by the other two energy inputs will be reduced accordingly. This is because when a type of energy input is fixed, the production schedule of the IL and the operation of energy converters in the DESS are enforced, resulting in a limitation on the adjustment capabilities. Consequently, the energy demand for electricity and natural gas of the DMSI is less flexible. In order to compare the size of IFRs in different scenarios more intuitively, after converting and normalizing different energy inputs in proportion, the area of the IFR in Scenario 2 is 1.98 times that in Scenario 1.

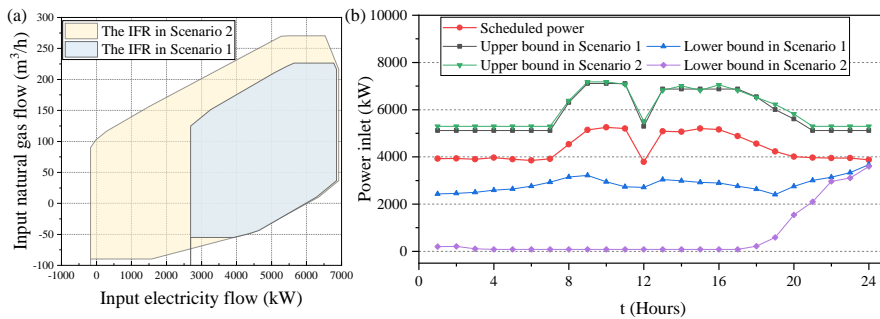


Fig. 10.16. The IFRs in Case 3: (a) The two-dimensional IFRs at time ten in Scenarios 1 and 2; (b) The IFRs projected to the input electricity flow during a whole production planning cycle

Fig. 10.16(b) shows the IFRs projected to the input electricity flow during a whole production planning cycle. In the same way, the fixed heating energy input limits the electric up and down regulation ability of the DMSI. In this case, the lower bound of the flexibility is greatly affected, while the upper bound of the flexibility is less affected. This is because the operation and production of the system must maintain at a certain level to consume the input heating energy. Corre-

spondingly, the electric energy consumed by this part of operation and production cannot be adjusted downward without a lower limit. However, when the system increases the production and the electricity consumption, the corresponding increase in heating energy demand can be supplied by the CHP and the GB in the DESS. Furthermore, it can be concluded that for the multi-energy system on the utility side, the coordinated optimal operation of multi-energy systems can maximize the flexibility of multi-energy loads on the demand side.

5) Case 4: the impacts of IL parameters on the IFR of the DMSI

In this case, the impacts of the hourly maximum production and the type of subtasks of the IL on the IFR of the DMSI are discussed. In this context, four scenarios are conducted and their details are presented in Table 10.3. Scenarios 1-3 have the same types of subtasks but different production capacities. Scenarios 1 and 4 have the same production capacity but different types of subtasks.

Table 10.3. The parameters of different scenarios in Case 4.

Scenarios	Maximum production of different subtasks	Type of subtasks
1	Base	T1-DS, T2-CS, T3-CS, T4-FS, T5-FS, Ta-AS
2	0.85 Base	T1-DS, T2-CS, T3-CS, T4-FS, T5-FS, Ta-AS
3	1.15 Base	T1-DS, T2-CS, T3-CS, T4-FS, T5-FS, Ta-AS
4	Base	T1-DS, T2-DS, T3-DS, T4-DS, T5-DS, Ta-AS

* DS is discreet subtask, CS is continuous subtask, FS is flexible subtask, and AS is ancillary subtask

To analyze the impact of the hourly maximum production on the IFR, Figs. 10.17(a)-(c) show IFRs of the DMSI in scenarios 1-3 at time ten. It indicates that relaxing the hourly maximum production limit of each subtask in industry contributes to an increase in the flexible region for the DMSI. After converting and normalizing different energy inputs in proportion, the volume of the IFR in Scenario 1 is 1.56 times that in Scenario 2 and 0.83 times that in Scenario 3. Fig. 10.18 shows the IFRs projected to the input electricity flow during a whole production planning cycle. Increasing the hourly maximum production of each subtask can directly increase the upper bound of the IFR. On the other hand, since the upper bound of the IFR increases, the DMSI has more capacity to make up for the possible margin due to the reduced production contributing to an increase of the lower bound for the IFR. In addition, the lower bound in Scenario 2 begins to increase very early, while that in Scenario 3 begins to increase in the last few hours. This also indicates that the down regulation ability of the DMSI depends on the maximum production of subtasks.

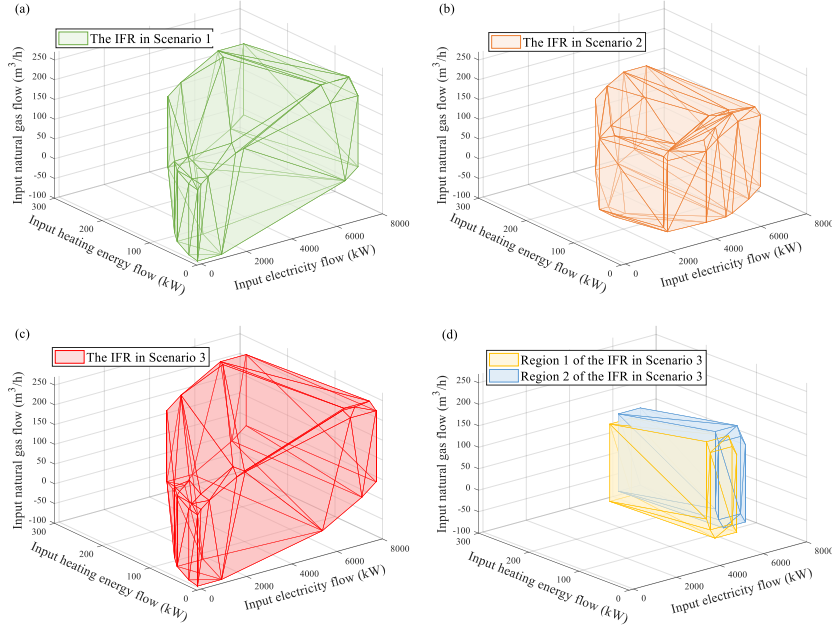


Fig. 10.17. The IFRs (a) at time ten in Scenarios 1-3; (b) at time five in Scenarios 1 and 4

To analyze the impact of the types of subtasks on the IFR, Fig. 10.17(a) and (d) show IFRs of the DMSI in Scenarios 1 and 4 at time ten. It can be seen that the IFR in Scenario 4 is not a polytope, but a combination of two polytopes. In Scenario 4, all subtasks except the ancillary subtask are discreet subtasks. Therefore, if the flexibility of the DESS and the Ta is not considered, the IFR is just a few points in the three-dimensional space. The operating states of the industrial loads can only be switched between several feasible points. With the flexibility provided by the DESS, the IFR of the DMSI has been greatly expanded. When the DESS, continuous subtasks, and flexible subtasks provide sufficient flexibility for the DMSI, the non-convex polyhedron can also be approximately regarded as a polytope with a limited error.

When the system operators on the utility side schedule the coordinated operation for the multi-energy system, whether the scheduled operating point of the demand side system is inside the polytope determines whether the schedule is feasible. So far, the scheduling on the utility side can make full use of the flexibility on the demand side without collecting the specific parameters and operating conditions of the demand side system.

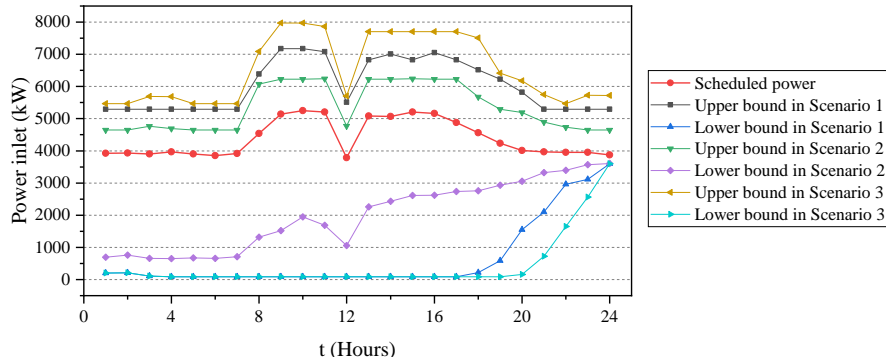


Fig. 10.18. The IFRs projected to the input electricity flow during a whole production planning cycle in Scenarios 1-3

10.5 Outlook of incorporating integrated demand response in risk control of multi-energy systems

Through the IFR, the interaction between the utility system and the DMSI can be divided into the following steps:

Step 1. First of all, the DMSI makes a production plan within a production cycle based on self-interest factors such as energy price and production target. With the formulated plan, the scheduled multi-energy demand of the DMSI is the red point in Fig. 10.19. On this basis, with the help of energy converters in the DESS and adjustable subtasks in the IL, the multi-energy demand of the DMSI can be strategically adjusted within a certain region rather than fixed at a point. Therefore, the DMSI could construct its IFR considering the energy conversion constraints and production targets and then submit it to the utility system.

Step 2. When a contingency happens, the utility operators can dispatch flexible resources to keep the energy balancing for the MES. Taking the scenario of renewable energy's uncertainties in power systems as an example, the hourly fluctuation of renewable energy could cause a power shortage which is the gray part of the histogram shown in Fig. 10.19. It can be observed that the power shortage is greater than the conventional flexibility provided by the supply side. If the flexible resources on the demand side remain undetected and unexcavated, energy imbalance in power systems could cause frequency drop and widespread outages. Similarly, energy imbalance in natural gas systems or thermal energy systems could also contribute to severe load shedding. Therefore, after mastering the IFR of the DMSI, the system can strengthen its flexibility and avoid such serious consequences. The utility operators dispatch the conventional flexible resources and the flexibility provided by the DMSI to lead a new energy balance for the MES.

Step 3. Utility operators send the regulation signals to DMSIs and the DMSI can adjust its multi-energy demand from the scheduled point to the rescheduled point as shown in Fig. 10.19.

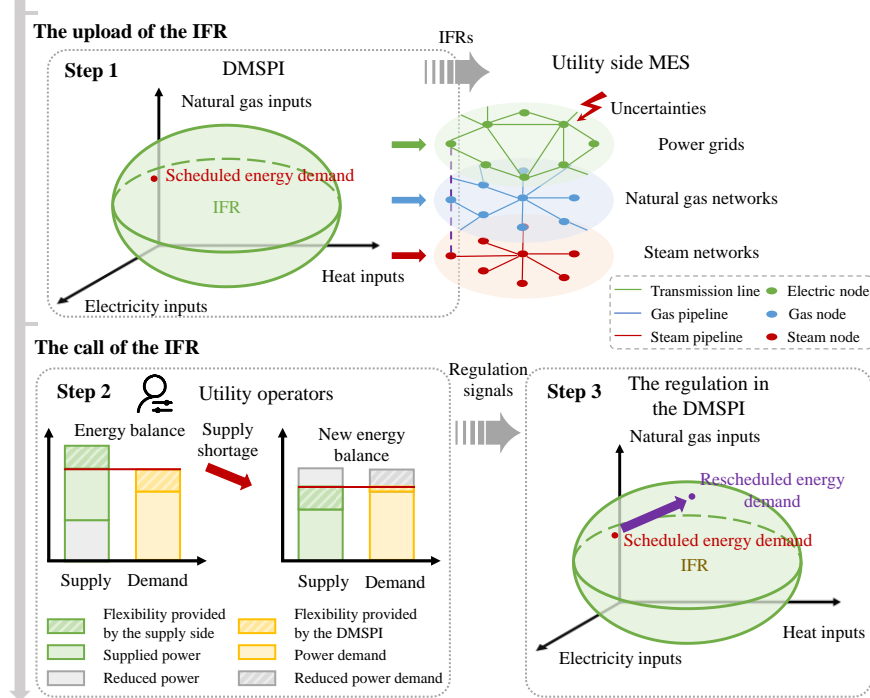


Fig. 10.19. The application of the IFR

This chapter proposes a novel method to explore the integrated flexible region of distributed multi-energy systems with industrial loads (DMSI). At first, the adjustable components in the industrial load (IL) are summarized into four categories of subtasks according to their respective load characteristics. On this basis, an energy-material integrated model is proposed to couple the energy converters in the district energy supply system (DESS) and the subtasks in the IL considering the production targets. After modeling the DMSI, the mathematical expression for the integrated flexibility is represented by an integrated flexible region (IFR) based on the polytopic projection. The calculation method based on vertex enumeration for the IFR is then proposed. Case studies show the effectiveness of the proposed evaluation method and analyze different factors that affect the IFR. In specific, the adjustabilities of the DESS and the IL both make a great effort to the IFR of the DMSI.

In this chapter, the IFR composed of the electricity input, the natural gas input, and the heat input to the DMSI is mainly considered. To achieve the net-zero carbon emission target, the use of natural gas in industrial loads may reduce and be replaced by cleaner energy sources, such as hydrogen [39]. Under this circumstance, the proposed method could also be utilized to excavate the IFR of electricity, heat, and hydrogen inputs. In other words, the proposed method to explore the integrated flexibility of multi-energy vectors is a general method and not limited

to specific energy sources. In general, the proposed flexibility exploring scheme constructs a bridge for the demand-side flexible resources to interact with the operation of the multi-energy systems (MES) and excavate enormous flexibility for the MES to accommodate more renewable energy. With more interactions between end-users and the utility system, the feasible operating states of MES can be effectively expanded and more renewable energy can be accommodated, contributing to the reliable, economic, and environmentally friendly development for future energy systems.

Reference

- [1] Mancarella P. MES (multi-energy systems): An overview of concepts and evaluation models. *Energy* 2014;65:1–17. <https://doi.org/10.1016/j.energy.2013.10.041>.
- [2] Guelpa E, Bischi A, Verda V, Chertkov M, Lund H. Towards future infrastructures for sustainable multi-energy systems: A review. *Energy* 2019;184:2–21. <https://doi.org/10.1016/j.energy.2019.05.057>.
- [3] Mavromatis G, Orehounig K, Bollinger LA, Hohmann M, Marquant JF, Miglani S, et al. Ten questions concerning modeling of distributed multi-energy systems. *Building and Environment* 2019;165:106372. <https://doi.org/10.1016/j.buildenv.2019.106372>.
- [4] U.S. Energy Information Administration (EIA). International Energy Outlook 2021. 2021.
- [5] Alizadeh MI, Parsa Moghaddam M, Amjadi N, Siano P, Sheikh-El-Eslami MK. Flexibility in future power systems with high renewable penetration: A review. *Renewable and Sustainable Energy Reviews* 2016;57:1186–93. <https://doi.org/10.1016/j.rser.2015.12.200>.
- [6] Wang J, Zhong H, Ma Z, Xia Q, Kang C. Review and prospect of integrated demand response in the multi-energy system. *Applied Energy* 2017;202:772–82. <https://doi.org/10.1016/j.apenergy.2017.05.150>.
- [7] Lund PD, Lindgren J, Mikkola J, Salpakari J. Review of energy system flexibility measures to enable high levels of variable renewable electricity. *Renewable and Sustainable Energy Reviews* 2015;45:785–807. <https://doi.org/10.1016/j.rser.2015.01.057>.
- [8] Ding Y, Shao C, Yan J, Song Y, Zhang C, Guo C. Economical flexibility options for integrating fluctuating wind energy in power systems: The case of China. *Applied Energy* 2018;228:426–36. <https://doi.org/10.1016/j.apenergy.2018.06.066>.
- [9] Bahrami S, Sheikhi A. From Demand Response in Smart Grid Toward Integrated Demand Response in Smart Energy Hub. *IEEE Transactions on Smart Grid* 2016;7:650–8. <https://doi.org/10.1109/TSG.2015.2464374>.
- [10] Shao C, Wang X, Shahidehpour M, Wang X, Wang B. An MILP-Based Optimal Power Flow in Multicarrier Energy Systems. *IEEE Transactions on*

- Sustainable Energy 2017;8:239–48.
<https://doi.org/10.1109/TSTE.2016.2595486>.
- [11] Shao C, Ding Y, Wang J, Song Y. Modeling and Integration of Flexible Demand in Heat and Electricity Integrated Energy System. *IEEE Transactions on Sustainable Energy* 2018;9:361–70.
<https://doi.org/10.1109/TSTE.2017.2731786>.
- [12] Montuori L, Alcázar-Ortega M, Álvarez-Bel C. Methodology for the evaluation of demand response strategies for the management of natural gas systems. *Energy* 2021;234:121283.
<https://doi.org/10.1016/j.energy.2021.121283>.
- [13] Tan Z, Zhong H, Wang X, Tang H. An efficient method for estimating the capability curve of a virtual power plant. *CSEE Journal of Power and Energy Systems* 2020;1–9. <https://doi.org/10.17775/CSEJPES.2020.00400>.
- [14] Wang Y, Cheng J, Zhang N, Kang C. Automatic and linearized modeling of energy hub and its flexibility analysis. *Applied Energy* 2018;211:705–14.
<https://doi.org/10.1016/j.apenergy.2017.10.125>.
- [15] Tan Z, Zhong H, Xia Q, Kang C, Dai H. Exploiting Integrated Flexibility from a Local Smart Energy Hub, Montreal, QC, Canada: 2020, p. 6.
<https://doi.org/10.1109/PESGM41954.2020.9281984>.
- [16] Nistor S, Wu J, Sooriyabandara M, Ekanayake J. Capability of smart appliances to provide reserve services. *Applied Energy* 2015;138:590–7.
<https://doi.org/10.1016/j.apenergy.2014.09.011>.
- [17] D'huist R, Labeeuw W, Beusen B, Claessens S, Deconinck G, Vanthournout K. Demand response flexibility and flexibility potential of residential smart appliances: Experiences from large pilot test in Belgium. *Applied Energy* 2015;155:79–90. <https://doi.org/10.1016/j.apenergy.2015.05.101>.
- [18] Yi P, Dong X, Iwayemi A, Zhou C, Li S. Real-Time Opportunistic Scheduling for Residential Demand Response. *IEEE Transactions on Smart Grid* 2013;4:227–34. <https://doi.org/10.1109/TSG.2012.2225155>.
- [19] Hui H, Ding Y, Liu W, Lin Y, Song Y. Operating reserve evaluation of aggregated air conditioners. *Applied Energy* 2017;196:218–28.
<https://doi.org/10.1016/j.apenergy.2016.12.004>.
- [20] Good N, Karangelos E, Navarro-Espinosa A, Mancarella P. Optimization Under Uncertainty of Thermal Storage-Based Flexible Demand Response With Quantification of Residential Users' Discomfort. *IEEE Transactions on Smart Grid* 2015;6:2333–42. <https://doi.org/10.1109/TSG.2015.2399974>.
- [21] Beier J, Thiede S, Herrmann C. Energy flexibility of manufacturing systems for variable renewable energy supply integration: Real-time control method and simulation. *Journal of Cleaner Production* 2017;141:648–61.
<https://doi.org/10.1016/j.jclepro.2016.09.040>.
- [22] Contador JC, Satyro WC, Contador JL, Spinola M de M. Flexibility in the Brazilian Industry 4.0: Challenges and Opportunities. *Global Journal of Flexible Systems Management* 2020;21:15–31. <https://doi.org/10.1007/s40171-020-00240-y>.

- [23] Priore P, Ponte B, Puente J, Gómez A. Learning-based scheduling of flexible manufacturing systems using ensemble methods. *Computers & Industrial Engineering* 2018;126:282–91. <https://doi.org/10.1016/j.cie.2018.09.034>.
- [24] Girbea A, Suciu C, Nechifor S, Sisak F. Design and Implementation of a Service-Oriented Architecture for the Optimization of Industrial Applications. *IEEE Transactions on Industrial Informatics* 2014;10:185–96. <https://doi.org/10.1109/TII.2013.2253112>.
- [25] Lombardi P, Komarnicki P, Zhu R, Liserre M. Flexibility options identification within Net Zero Energy Factories. 2019 IEEE Milan PowerTech, 2019, p. 1–6. <https://doi.org/10.1109/PTC.2019.8810494>.
- [26] Caro-Ruiz C, Lombardi P, Richter M, Pelzer A, Komarnicki P, Pavas A, et al. Coordination of optimal sizing of energy storage systems and production buffer stocks in a net zero energy factory. *Applied Energy* 2019;238:851–62. <https://doi.org/10.1016/j.apenergy.2019.01.125>.
- [27] Ding YM, Hong SH, Li XH. A Demand Response Energy Management Scheme for Industrial Facilities in Smart Grid. *IEEE Transactions on Industrial Informatics* 2014;10:2257–69. <https://doi.org/10.1109/TII.2014.2330995>.
- [28] Choobineh M, Mohagheghi S. Optimal Energy Management in an Industrial Plant Using On-Site Generation and Demand Scheduling. *IEEE Transactions on Industry Applications* 2016;52:1945–52. <https://doi.org/10.1109/TIA.2015.2511094>.
- [29] Huang X, Hong SH, Li Y. Hour-Ahead Price Based Energy Management Scheme for Industrial Facilities. *IEEE Transactions on Industrial Informatics* 2017;13:2886–98. <https://doi.org/10.1109/TII.2017.2711648>.
- [30] Reka SS, Ramesh V. Industrial demand side response modelling in smart grid using stochastic optimisation considering refinery process. *Energy and Buildings* 2016;127:84–94. <https://doi.org/10.1016/j.enbuild.2016.05.070>.
- [31] Zhang Y, Xu Y. Optimization of Distributed Integrated Multi-energy System Considering Industrial Process Based on Energy Hub. *Journal of Modern Power Systems and Clean Energy* 2020;8:11.
- [32] Hui H, Bao M, Ding Y, Song Y. Exploring the integrated flexible region of distributed multi-energy systems with process industry. *Applied Energy* 2022;311:118590. <https://doi.org/10.1016/j.apenergy.2022.118590>.
- [33] U.S. Energy Information Administration (EIA). Use of natural gas 2021. <https://www.eia.gov/energyexplained/natural-gas/use-of-natural-gas.php> (accessed November 16, 2021).
- [34] U.S. Environmental Protection Agency (EPA). Renewable Industrial Process Heat 2014. <https://www.epa.gov/rhc/renewable-industrial-process-heat> (accessed November 1, 2021).
- [35] Khan MS, Chaniago YD, Getu M, Lee M. Energy saving opportunities in integrated NGL/LNG schemes exploiting: Thermal-coupling common-utilities and process knowledge. *Chemical Engineering and Processing: Process Intensification* 2014;82:54–64. <https://doi.org/10.1016/j.cep.2014.06.001>.

- [36] Wang Y, Kirschen DS, Yang J, Xia Q. Standardized Matrix Modeling of Multiple Energy Systems. *IEEE Transactions on Smart Grid* 2019;10:14.
- [37] Abiri-Jahromi A, Bouffard F. On the Loadability Sets of Power Systems—Part II: Minimal Representations. *IEEE Transactions on Power Systems* 2017;32:146–56. <https://doi.org/10.1109/TPWRS.2016.2547938>.
- [38] Barber CB, Dobkin DP, Huhdanpaa H. The quickhull algorithm for convex hulls. *ACM Transactions on Mathematical Software* 1996;22:469–83. <https://doi.org/10.1145/235815.235821>.
- [39] Rissman J, Bataille C, Masanet E, Aden N, Morrow WR, Zhou N, et al. Technologies and policies to decarbonize global industry: Review and assessment of mitigation drivers through 2070[J]. *Applied Energy*, 2020, 266: 114848.